Distribution Agreement

Signature:

__________________________________ ________________

Qiushi Yin Date

Studies of Electronically Perturbed Polyoxometalate Catalysts

By

Qiushi Yin
Doctor of Philosophy

Chemistry

Craig L. Hill, Ph.D.
Advisor

Tianquan Lian, Ph.D.
Committee Member

Djamaladdin G. Musaev, Ph.D.
Committee Member

Cora MacBeth, Ph.D.
Committee Member

Accepted:

Lisa A. Tedesco, Ph.D.
Dean of the James T. Laney School of Graduate Studies

Date

Studies of Electronically Perturbed Polyoxometalate Catalysts

By

Qiushi Yin
Master of Science

Advisor: Craig L. Hill, Ph.D.

An abstract of a dissertation submitted to the Faculty of the James T. Laney School of Graduate Studies of Emory University in partial fulfillment of the requirements for the degree of Doctor of Philosophy in Chemistry

2021

Abstract

Studies of Electronically Perturbed Polyoxometalate Catalysts

By

Qiushi Yin

Polyoxometalates (POMs) are polyanionic metal-oxo species that are closely related to metal oxides and capable of a large number of catalytic reactions. However, due to their discrete molecular nature, POMs are suitable for everything from unitary atomic modification to larger scale bulk polymerization. Utilizing this unique aspect of POMs, we devise synthetic strategies that modulate existing POM catalysts through atomic substitution, counterion permutations, and ligand framework adaptation. This is all done in the context of the prominent catalytic reaction of water oxidation, ultimately achieving a number of electronically perturbed POM water oxidation catalysts (WOCs).

The synthesis of these POM WOCs allows us to directly study the effect of electronic perturbation on the reaction mechanism of these catalysts and how that relates to their observed catalytic performance. This degree of atomic control is not generally available to analogous bulk and crystalline heterogeneous metal oxides and provides new insights for both the oxygen evolution reaction (OER) catalysis and for metal-oxo based reactions. Moreover, the molecular nature of these POM WOCs gives additional handles with which we can use for characterization.

Chapter 1 gives the broader scope for which this work is relevant. Chapter 2 and 3 proposes the rational design, synthesis, and characterization of an atomically modified mixed-metal POM catalyst. Chapter 4 examines an unprecedented observed trend in counter-cation identity and catalytic reactivity. Chapter 5 investigates the role of ligands in copper-oxo cluster WOCs and the accompanying stabilization that results. Chapter 6 looks at common characterization techniques for probing the catalytic performance of molecular WOCs and reevaluates their broad adaptation in the context of electrochemistry to couple thermodynamics and kinetics and give additional mechanistic insights.

Studies of Electronically Perturbed Polyoxometalate Catalysts

By

Qiushi Yin

Master of Science

Advisor: Craig L. Hill, Ph.D.

A dissertation submitted to the Faculty of the James T. Laney School of Graduate Studies of
Emory University in partial fulfillment of the requirements for the degree of
Doctor of Philosophy in Chemistry

2021

Acknowledgements

I want to thank my committee for taking the time to read this. I want to sincerely thank Dr. Craig Hill for being my advisor and for being the nicest person I have ever had the privilege of knowing. I want to thank Dr. Tim Lian for his intellectual rigor. I want to thank Dr. Jamal Musaev for his discerning mind. I want to thank Dr. Cora MacBeth for being a wonderful person. I want to thank my friends and family, and if you happen to be reading this, I want to thank you specifically.

Table of Contents

Chapter 1

The Basics

Overview

Life on Earth is one of the most interesting phenomena that has preoccupied thinkers from antiquity to modern day scientists. One of the main thrusts of life is the completion of thermodynamic work cycles. Specifically, this manifests as the acquisition of external resources for a life system to maintain thermodynamic equilibrium. Naturally, acquisition of external resources is also one of the main impetus for humanity. As human society advances technologically, our demand for resources has also increased both in quantity and complexity. Resource scarcity is, therefore, a fundamental issue for human societies throughout their history. Within this framework, most of the problems humanity faces are basically issues of resource acquisition and distribution.

Whether it's to maintain life, or to drive our technological amenities, energy is the common currency upon which human societies are built. Our access to ever greater amounts of energy also underlies the expansion of civilizations and access to improved technologies. The current mode of energy acquisition comes predominantly from fossil fuels.[1-4] Specifically, of the world's total energy supply, 81.3% originate from fossil fuels (26.9% come from coal, 31.6% come from petroleum, and 22.8% come from natural gas).[1] The issue of resource scarcity presents in a few different ways as a result of our current energy economy. The most obvious problem is the limited supply of fossil fuels. As its name suggests, fossil fuels are buried carbonaceous fuel sources mainly the result of millions of years of transformation of organic matter.[5-7] While the overall supply of fossil fuels appear quite abundant, economically accessible deposits differ vastly based on geography.[8] Energy independence of nation-states are thus not guaranteed, often leading to potential geopolitical conflicts.

The far more pressing issue is the scarcity of our atmospheric carbon budget.[9-13] The utilization of fossil fuels as energy sources outputs a tremendous amount of greenhouse gasses mainly in the form of carbon dioxide, leading to global climate change. The impacts of climate change are varied and generally negative.[9, 14-16] We can already observe some of its effects in the form of sea level rise, deoxygenation of lakes,[17] extreme weather patterns, and higher temperatures in all biomes.[9-17] The anticipated effect in the coming century includes, but are not limited to, food and water crises, rising human health issues, ocean acidification, and loss of biodiversity.[9, 14-16] Adaptations will be required in all aspects of human societies, the direct cost of which alone is estimated to be $8 trillion dollars per year by 2050.[1-2] The solution to such a large scale problem would likely require multifaceted approaches, with the ultimate objective being the lowering of carbon emissions to zero and below. The main stated goal of the International Energy Agency including its 38 member and association countries is to achieve zero emissions by 2050.[1-2] The only way to achieve this goal is to drastically alter our energy source and emancipate ourselves from fossil fuels.

If we trace the sources of energy used by modern human civilization to its roots, about 90% of it comes from our Sun. This includes all fossil fuels, hydropower, biofuels, wind, tide/wave/ocean, and direct solar energy. Of these, the most promising mode of energy acquisition is direct solar energy conversion. It is the only fuel source that would be zero emission and represents a likely growth potential that could match humanity's energy demands.[1-4, 9, 18-20] Additional advantages of this energy source include wide availability and off-the-grid compatibility.[18-20] The 2021 US annual energy outlook predicts that about 10% of all the annual energy supply could come from direct solar energy by 2050.[3] In these predictive models, the direct solar energy conversion is assumed to be solar photovoltaic technology. Photovoltaics are the most technologically mature solar conversion technology, converting light energy to electric potential energy. Its main drawbacks include the storage of energy as current solutions center around constructing large arrays of batteries. An alternative proposed method of direct solar energy conversion is the photoelectrochemical cell (PEC).[18-21] A photovoltaic-electrolyzer combination will readily convert sunlight to hydrogen and oxygen. However, it does suffer from a few drawbacks when compared to potential PEC systems. Chiefly, photovoltaic-electrolyzers have an intrinsically lower upper limit on energy conversion efficiency than PECs, much of this is due to the high operating current density of electrolyzers. In addition, PECs are potentially more versatile in their deployment and compatibility with CO_2 reduction reactions. Moreover, PECs present a number of tractable challenges across many different areas of chemistry and chemical engineering that require advances in fundamental science. As such, PEC systems continue to be attractive for research among scientists.[19, 21]

Photoelectrochemical cells differ from traditional photovoltaics in a few aspects. Most importantly, PECs typically include a p-type photocathode and an n-type photoanode. The electric potential generated from the photoelectric effect is directly converted to chemical energy, eliminating the need for battery storage. A basic example of PEC design is shown in Figure 1.1. Typically, water splitting is the primary reaction used to achieve chemical energy storage. Its two component half-reactions, water oxidation and water reduction, can be seen in Figure 1. As the US Department of Energy reevaluated PEC research as a long term research target rather than an imminent technology for a hydrogen economy, recent efforts in PEC research have shifted the focus onto CO_2 reduction in conjunction with water oxidation.[21] Unsurprisingly, such a system would mimic natural photosynthesis, the main mode of energy acquisition underlying most life on Earth. Unfortunately, mere mimicry will not be sufficient. Our artificial photosynthesis must beat nature’s photosynthesis by a large margin to be competitive with other renewables.[19-21] In any case, water oxidation appears to be a cornerstone reaction involved in the future of PEC research and construction.

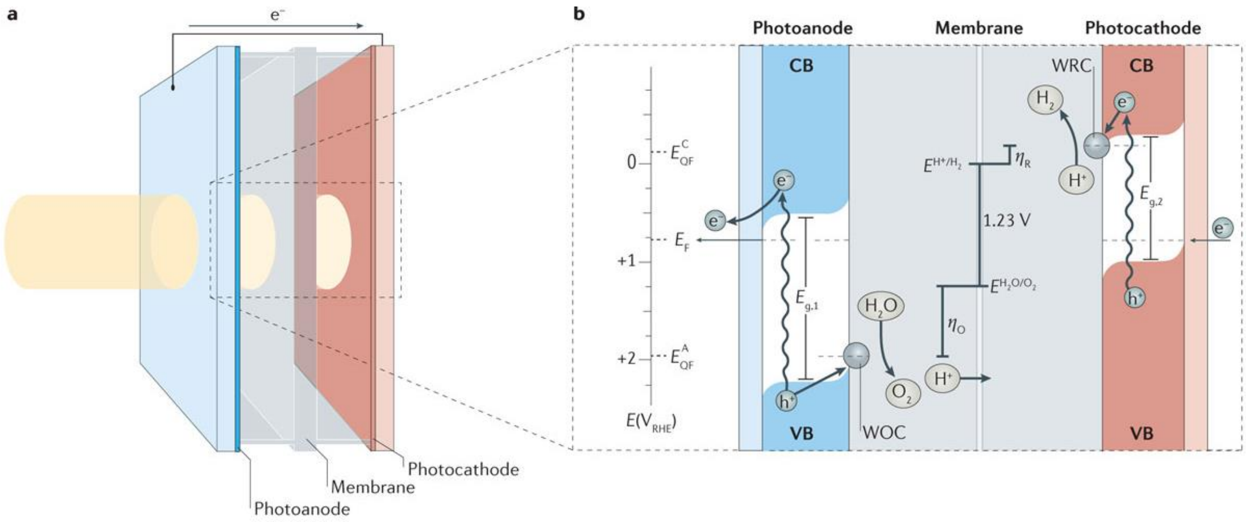

Figure 1.1 A simplified scheme for a PEC containing all the basic requisite components for a functional device. The major components (a) and a more detailed cross-section (b) are shown. This figure is taken from Sivula *et al*. and reproduced with permission.[22]

Water oxidation reaction

Water oxidation is a seemingly straightforward reaction, with the O^{2-} atoms in water consuming four holes sequentially, ultimately leading towards the evolution of molecular oxygen. This process is well studied and have been known for a long time. However, its thermodynamics and kinetics makes the catalysis of the oxygen evolution reaction (OER) non-trivial. Three main half-cell reactions are typically discussed when examining water oxidation:

One-electron oxidation:

$$H_2O \rightarrow \cdot OH(aq) + (H^+ + e^-) \qquad E° = 2.73\ V \qquad (1.1)$$

Two-electron oxidation:

$2H_2O \rightarrow H_2O_2 + 2(H^+ + e^-)$ $E° = 1.76$ V (1.2)

Four-electron oxidation:

$2H_2O \rightarrow O_2 + 4(H^+ + e^-)$ $E° = 1.23$ V (1.3)

Though reactions 1.1-1.3 all lead to stable or semi-stable products, the four-electron process in equation 1.3 is usually the desired reaction in PECs as it has the lowest reduction potential. Realistically, reactions 1.2 and 1.3 require catalysts to proceed at potentials close to the standard reduction potentials due to their multi-electron kinetics. A conspicuous question arises at this point. What determines the selectivity of the products among reactions 1.1-1.3? A qualitative thermodynamic analysis will suffice in understanding the underlying issue.[23-25] Consider a typical metal oxide water oxidation catalyst. In a generalized scheme, the following reaction steps would occur in water oxidation:

One-election oxidation:

$H_2O \rightarrow \cdot OH(aq) + (H^+ + e^-)$ $\Delta G_{\cdot OH}$ (1.4)

Two-electron oxidation:

$M\text{-}OH_2 \rightarrow M\text{-}OH + (H^+ + e^-)$ ΔG_{MOH} (1.5)

$2M\text{-}OH + 2(H^+ + e^-) \rightarrow 2M + H_2O_2 + 2(H^+ + e^-)$ ΔG_{H2O2} (1.6)

Four-electron oxidation:

$M\text{-}OH_2 \rightarrow M\text{-}OH + (H^+ + e^-)$ ΔG_{MOH} (1.5)

$M\text{-}OH + (H^+ + e^-) \rightarrow M\text{-}O + 2(H^+ + e^-)$ ΔG_{MO} (1.7)

$M\text{-}O + 2(H^+ + e^-) \rightarrow M\text{-}OOH + 3(H^+ + e^-)$ ΔG_{MOOH} (1.8)

$M\text{-}OOH + 3(H^+ + e^-) \rightarrow M + O_2 + 4(H^+ + e^-)$ ΔG_{O2} (1.9)

Here, hydroxyl radical formation (equation 1.4) occurs when $\Delta G_{\cdot OH} < \Delta G_{MOH}$. Otherwise, reaction 1.5 is preferred and either a two-electron oxidation or four-electron oxidation occurs.

Similarly, the four-electron oxidation reaction will only occur when $\Delta G_{\cdot OH} < \Delta G_{MOH}$ and $\Delta G_{MO} < \Delta G_{H2O2}$. This insight demonstrates that the critical function of a four-electron water oxidation catalyst vs a one-electron or two-electron water oxidation catalyst is lowering the Gibbs free energy of the bound oxygen atom. Descriptively, we can say that a four-electron oxidation catalyst must be able to bind a water molecule and deprotonate it completely. Experimental measurements on the binding energies of metal oxide/hydroxide species and density function theory (DFT) calculations confirm this line of reasoning.[23-25]

A picture of the exact pathway of OER at transition-metal centers only emerged in the last decade. Most of the advances came as a result of studying molecular water oxidation catalysts.[26-27] Much work has been done on ruthenium-based molecular catalysts.[26] The discovery of mononuclear transition-metal water oxidation catalysts in particular demonstrated that it is not necessary to have four consecutive oxidation events on the transition-metal centers in order to effectuate OER catalysis. A generalized scheme for water oxidation catalysis can be seen in Figure 1.2. Typically, a water molecule is activated through a series of electron transfers (ET) and proton transfers (PT) or proton-coupled electron transfers (PCET) to form oxidized metal oxyl/oxo species. This metal oxyl/oxo will then proceed to an oxygen-oxygen bond formation step, either through a water nucleophilic attack (WNA) from the aqueous solvent or through a radical-coupling interaction with another metal oxyl/oxo (I2M). Further ET and PT or disproportionation will then lead to oxygen evolution to complete the catalytic cycle.

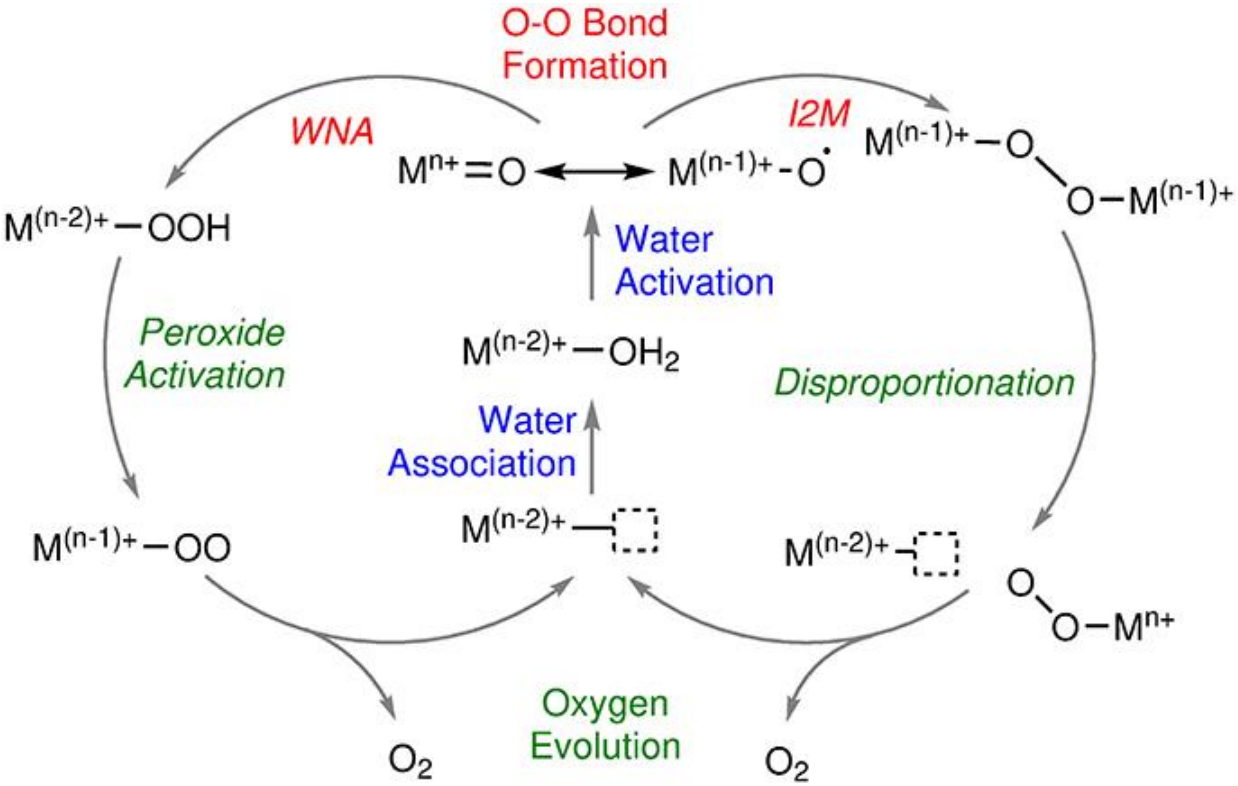

Figure 1.2 General reaction schemes of some key possible reactive intermediates. This summarizes the two major pathways of WNA and I2M. This figure is taken from Schilling and Luber (open access).[27]

Figure 1.2 illustrates two key points. Firstly, multinuclear transition metal centers are not obligatory for a four-electron water oxidation catalyst. Only three accessible oxidation states are necessary for a catalyst to perform OER. Secondly, two main classifications exist for molecular OER mechanisms. WNA and I2M describe two different modes of the O-O bond formation. This step is critical for all OER catalysts and often determines the catalytic rate. A number of variations of the WNA and I2M mechanisms can be found in Figure 1.3.[26] A cursory inspection shows that a WNA from a hydroxide and an intramolecular I2M should result in the most facile O-O bond formation for the respective mechanisms under general conditions. These insights are typically in line with what we observe for both homogeneous and heterogeneous OER catalysts.

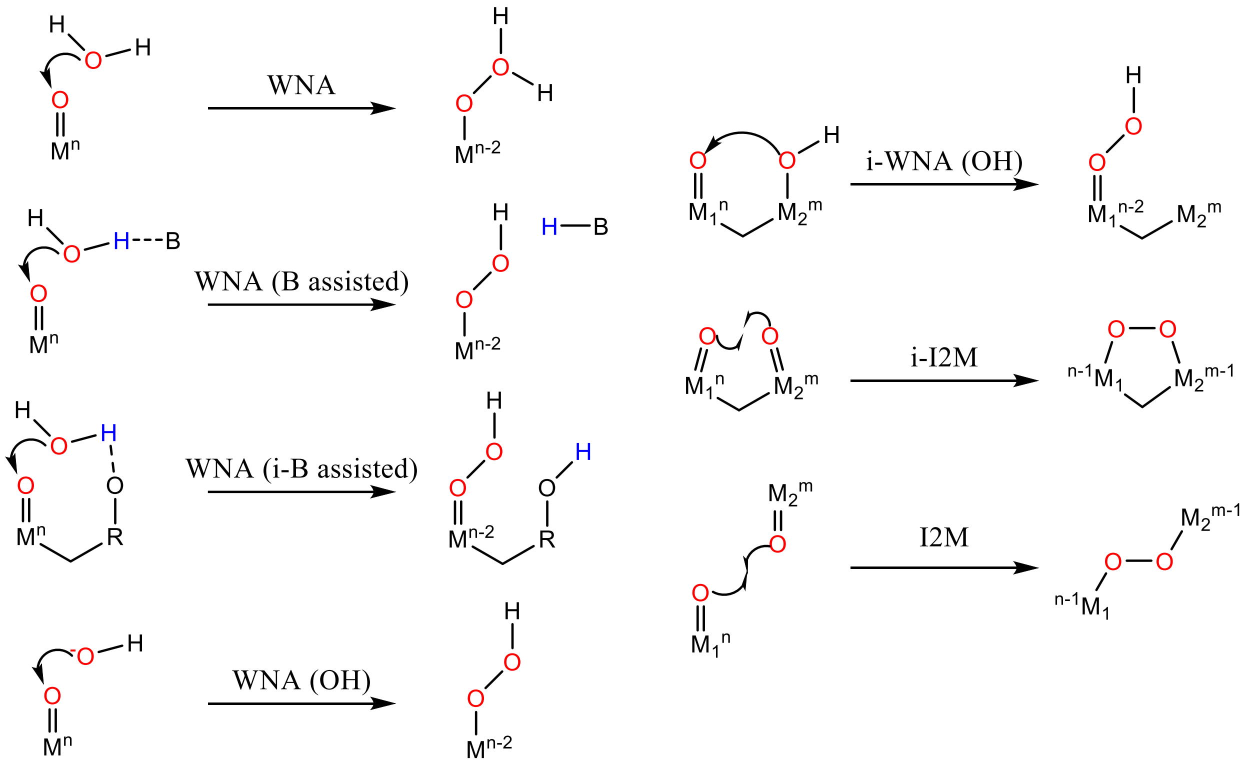

Figure 1.3 Some of the more common possible mechanistic variations of the typical rate determining step of O-O bond formation.

In actuality, the precise mechanism of water oxidation may not always fit so nicely into this paradigm. This is especially evident when we examine heterogeneous OER catalysts. Heterogeneous OER catalysts are most likely necessary for the construction of a function PEC.[19, 21, 28-29] While there are different formulations of them, in general, the majority of viable heterogeneous OER catalysts are electrocatalysts or photoelectrocatalysts for water oxidation. Most promising OER electrocatalysts are metal oxides. Of these, the best performing catalysts are ruthenium oxides and iridium oxides.[29-32] They have some of the lowest overpotentials for four-electron water oxidation at all pH ranges and current densities. For these reasons, formulations of

Ru and/or Ir materials are widely employed in current commercial electrolyzers. For PECs, however, Ru and Ir based OER catalysts are less attractive mainly due to the scarcity of ruthenium and iridium on Earth. Catalysts that are able to oxidize water at a reasonable overpotential are also much more widely available at the much lower current densities that PECs typically operate at compared to electrolyzers. Some of the most researched OER catalysts include cobalt compounds and nickel compounds. A large array of varying structures, ligands, morphologies, and dopings of cobalt and nickel compounds have been explored as OER catalysts.[27, 30, 33-87] While the scheme in Figure 3 is generally applicable, nuances in each step necessitates greater understanding of the possible mechanisms and especially interactions on multinuclear systems such as cobalt oxides/hydroxide electrocatalysts. In particular, cobalt centers show great versatility in possible reaction mechanisms. A number of molecular cobalt complexes have been shown to undergo the WNA pathway, while other experiments have demonstrated the possibility for the I2M mechanism or even the possibility of the μ-oxo superoxide formation.[65] Complicating the matter even more, cobalt oxides/hydroxides may participate in a mixture of mechanisms with differing rate determining steps depending on the local catalyst environment, the solvent conditions, and current density. Nickel OER catalysts have been less well studied compared to cobalt catalysts. Nonetheless, a large body of literature exists and generally show the mechanism being consistent with a WNA pathway.

A more accurate understanding of how the local environment of the reactive transition metal centers affects the reaction mechanism and the reaction rates in metal oxide water oxidation will be very useful for the study and development of OER catalysts and their implementation in PECs. An in-depth understanding of the relevant water oxidation catalysis mechanism would be crucial to improving the catalytic performance and the operating stability of the catalysts. And while much progress has been made clarifying the actual mechanism of water oxidation catalysis, the exact mechanism is always dependent on the transition metal centers, the associated oxidation states, the ligands, and the reactive environment. Transition metal-oxygen cluster polyanions, otherwise known as polyoxometalates (POMs), are ideal molecular analogues for studying bulk metal oxides.[88-93] POMs are widely diverse in composition, synthetically accessible, and are essentially soluble metal oxides. Some giant POMs also exist on the boundaries of discrete molecules and nanoparticles. Most importantly, many POMs allow us atomic level control over the chemical composition. Most POMs are also redox active. This rich redox chemistry is made more tunable with substitutions of different metal atoms as well as adjustable acid-base properties. These properties have made POMs very successful as redox catalysts. Unsurprisingly, there are a number of POMs that can act as OER catalysts.

Water oxidation catalysts comprised of POMs have advanced the general field of OER catalysis research by providing an increasing number of active molecular OER catalysts and by acting as ideal models of their heterogeneous and often amorphous counterparts.[49, 88, 93-96] In general, POMs are relatively straightforward to synthesize as they are often the thermodynamic products of aqueous metal chemistry. The ease of synthesis, on balance, means that more time and effort can be spent in the characterization, analysis, and further development of catalysts. It is in this fertile playground of soluble metallates that I will begin the next chapter.

References

1. Agency, I. E., Key World Energy Statistics 2020. **2021**.

2. Agency, I. E., World Energy Outlook 2020.

3. Adminstration, U. S. E. I., Annual Energy Outlook 2021. **2021**.

4. BP *Statistical Review of World Energy*; 2020.

5. Berner, R. A., The long-term carbon cycle, fossil fuels and atmospheric composition. *Nature* **2003,** *426* (6964), 323-326.

6. Ourisson, G.; Albrecht, P.; Rohmer, M., The Microbial Origin of Fossil Fuels. *Scientific American* **1984,** *251* (2), 44-51.

7. Schobert, H. H., *Chemistry of Fossil Fuels and Biofuels*. Cambridge University Press: 2013.

8. Oakleaf, J. R.; Kennedy, C. M.; Baruch-Mordo, S.; Gerber, J. S.; West, P. C.; Johnson, J. A.; Kiesecker, J., Mapping global development potential for renewable energy, fossil fuels, mining and agriculture sectors. *Scientific Data* **2019,** *6* (1), 101.

9. IPCC *AR5 Synthesis Report: Climate Change 2014*; IPCC: Geneva, Switzerland, 2014; p 151.

10. Rogelj, J.; Schaeffer, M.; Friedlingstein, P.; Gillett, N. P.; van Vuuren, D. P.; Riahi, K.; Allen, M.; Knutti, R., Differences between carbon budget estimates unravelled. *Nature Climate Change* **2016,** *6* (3), 245-252.

11. Friedlingstein, P.; Jones, M. W.; O'Sullivan, M.; Andrew, R. M.; Hauck, J.; Peters, G. P.; Peters, W.; Pongratz, J.; Sitch, S.; Le Quéré, C.; Bakker, D. C. E.; Canadell, J. G.; Ciais, P.; Jackson, R. B.; Anthoni, P.; Barbero, L.; Bastos, A.; Bastrikov, V.; Becker, M.; Bopp, L.;

Buitenhuis, E.; Chandra, N.; Chevallier, F.; Chini, L. P.; Currie, K. I.; Feely, R. A.; Gehlen, M.; Gilfillan, D.; Gkritzalis, T.; Goll, D. S.; Gruber, N.; Gutekunst, S.; Harris, I.; Haverd, V.; Houghton, R. A.; Hurtt, G.; Ilyina, T.; Jain, A. K.; Joetzjer, E.; Kaplan, J. O.; Kato, E.; Klein Goldewijk, K.; Korsbakken, J. I.; Landschützer, P.; Lauvset, S. K.; Lefèvre, N.; Lenton, A.; Lienert, S.; Lombardozzi, D.; Marland, G.; McGuire, P. C.; Melton, J. R.; Metzl, N.; Munro, D. R.; Nabel, J. E. M. S.; Nakaoka, S. I.; Neill, C.; Omar, A. M.; Ono, T.; Peregon, A.; Pierrot, D.; Poulter, B.; Rehder, G.; Resplandy, L.; Robertson, E.; Rödenbeck, C.; Séférian, R.; Schwinger, J.; Smith, N.; Tans, P. P.; Tian, H.; Tilbrook, B.; Tubiello, F. N.; van der Werf, G. R.; Wiltshire, A. J.; Zaehle, S., Global Carbon Budget 2019. *Earth Syst. Sci. Data* **2019,** *11* (4), 1783-1838.

12. Le Quéré, C.; Andres, R. J.; Boden, T.; Conway, T.; Houghton, R. A.; House, J. I.; Marland, G.; Peters, G. P.; van der Werf, G. R.; Ahlström, A.; Andrew, R. M.; Bopp, L.; Canadell, J. G.; Ciais, P.; Doney, S. C.; Enright, C.; Friedlingstein, P.; Huntingford, C.; Jain, A. K.; Jourdain, C.; Kato, E.; Keeling, R. F.; Klein Goldewijk, K.; Levis, S.; Levy, P.; Lomas, M.; Poulter, B.; Raupach, M. R.; Schwinger, J.; Sitch, S.; Stocker, B. D.; Viovy, N.; Zaehle, S.; Zeng, N., The global carbon budget 1959–2011. *Earth Syst. Sci. Data* **2013,** *5* (1), 165-185.

13. Houghton, R. A., Balancing the Global Carbon Budget. *Annual Review of Earth and Planetary Sciences* **2007,** *35* (1), 313-347.

14. IPCC *Special Report on the Ocean and Cryosphere in a Changing Climate*; IPCC: 2019.

15. IPCC *Climate Change and Land*; IPCC: Geneva, Switzerland, 2019.

16. IPCC *Managing the Risks of Extreme Events and Disasters to Advance Climate Change Adaptation*; IPCC
Geneva, Switzerland, 2012.

17. Jane, S. F.; Hansen, G. J. A.; Kraemer, B. M.; Leavitt, P. R.; Mincer, J. L.; North, R. L.; Pilla, R. M.; Stetler, J. T.; Williamson, C. E.; Woolway, R. I.; Arvola, L.; Chandra, S.; DeGasperi, C. L.; Diemer, L.; Dunalska, J.; Erina, O.; Flaim, G.; Grossart, H.-P.; Hambright, K. D.; Hein, C.; Hejzlar, J.; Janus, L. L.; Jenny, J.-P.; Jones, J. R.; Knoll, L. B.; Leoni, B.; Mackay, E.; Matsuzaki, S.-I. S.; McBride, C.; Müller-Navarra, D. C.; Paterson, A. M.; Pierson, D.; Rogora, M.; Rusak, J. A.; Sadro, S.; Saulnier-Talbot, E.; Schmid, M.; Sommaruga, R.; Thiery, W.; Verburg, P.; Weathers, K. C.; Weyhenmeyer, G. A.; Yokota, K.; Rose, K. C., Widespread deoxygenation of temperate lakes. *Nature* **2021,** *594* (7861), 66-70.

18. IPCC *Renewable Energy Sources and Climate Change Mitigation*; IPCC: Geneva, Switzerland, 2011.

19. Lewis, N. S., Toward Cost-Effective Solar Energy Use. *Science* **2007,** *315* (5813), 798-801.

20. Kannan, N.; Vakeesan, D., Solar energy for future world: - A review. *Renewable and Sustainable Energy Reviews* **2016,** *62*, 1092-1105.

21. Miller, E. L., Solar Hydrogen Production by Photoelectrochemical Water Splitting: The Promise and Challenge. In *On Solar Hydrogen & Nanotechnology*, 2010; pp 1-35.

22. Sivula, K.; van de Krol, R., Semiconducting materials for photoelectrochemical energy conversion. *Nature Reviews Materials* **2016,** *1* (2), 15010.

23. Shi, X.; Siahrostami, S.; Li, G.-L.; Zhang, Y.; Chakthranont, P.; Studt, F.; Jaramillo, T. F.; Zheng, X.; Nørskov, J. K., Understanding activity trends in electrochemical water oxidation to form hydrogen peroxide. *Nature Communications* **2017,** *8* (1), 701.

24. Seh, Z. W.; Kibsgaard, J.; Dickens, C. F.; Chorkendorff, I. B.; Norskov, J. K.; Jaramillo, T. F., Combining theory and experiment in electrocatalysis: Insights into materials design. *Science* **2017,** *355* (6321), 1.

25. Siahrostami, S.; Li, G.-L.; Viswanathan, V.; Nørskov, J. K., One- or Two-Electron Water Oxidation, Hydroxyl Radical, or H2O2 Evolution. *The Journal of Physical Chemistry Letters* **2017,** *8* (6), 1157-1160.

26. Shaffer, D. W.; Xie, Y.; Concepcion, J. J., O–O bond formation in ruthenium-catalyzed water oxidation: single-site nucleophilic attack vs. O–O radical coupling. *Chemical Society Reviews* **2017,** *46* (20), 6170-6193.

27. Schilling, M.; Luber, S., Computational Modeling of Cobalt-Based Water Oxidation: Current Status and Future Challenges. *Frontiers in Chemistry* **2018,** *6* (100).

28. McKone, J. R.; Lewis, N. S.; Gray, H. B., Will Solar-Driven Water-Splitting Devices See the Light of Day? *Chemistry of Materials* **2014,** *26* (1), 407-414.

29. Hunter, B. M.; Gray, H. B.; Müller, A. M., Earth-Abundant Heterogeneous Water Oxidation Catalysts. *Chemical Reviews* **2016,** *116* (22), 14120-14136.

30. Dau, H.; Limberg, C.; Reier, T.; Risch, M.; Roggan, S.; Strasser, P., The Mechanism of Water Oxidation: From Electrolysis via Homogeneous to Biological Catalysis. *ChemCatChem* **2010,** *2* (7), 724-761.

31. Reier, T.; Oezaslan, M.; Strasser, P., Electrocatalytic Oxygen Evolution Reaction (OER) on Ru, Ir, and Pt Catalysts: A Comparative Study of Nanoparticles and Bulk Materials. *Acs Catalysis* **2012,** *2* (8), 1765-1772.

32. Lee, Y.; Suntivich, J.; May, K. J.; Perry, E. E.; Shao-Horn, Y., Synthesis and Activities of Rutile IrO2 and RuO2 Nanoparticles for Oxygen Evolution in Acid and Alkaline Solutions. *J. Phys. Chem. Lett.* **2012,** *3* (3), 399-404.

33. Reath, A. H.; Ziller, J. W.; Tsay, C.; Ryan, A. J.; Yang, J. Y., Redox Potential and Electronic Structure Effects of Proximal Nonredox Active Cations in Cobalt Schiff Base Complexes. *Inorganic Chemistry* **2017,** *56* (6), 3713-3718.

34. Fukuzumi, S.; Ohkubo, K., Quantitative Evaluation of Lewis Acidity of Metal Ions Derived from the g Values of ESR Spectra of Superoxide: Metal Ion Complexes in Relation to the Promoting Effects in Electron Transfer Reactions. *Chemistry – A European Journal* **2000,** *6* (24), 4532-4535.

35. Blasco-Ahicart, M.; Soriano-López, J.; Carbó, J. J.; Poblet, J. M.; Galan-Mascaros, J. R., Polyoxometalate electrocatalysts based on earth-abundant metals for efficient water oxidation in acidic media. *Nature Chemistry* **2018,** *10* (1), 24-30.

36. Soriano-López, J.; Goberna-Ferrón, S.; Carbó, J. J.; Poblet, J. M.; Galán-Mascarós, J. R., Chapter Six - $[Co_9(H_2O)_6(OH)_3(HPO_4)_2(PW_9O_{34})_3]^{16-}$: A Highly Efficient Catalyst for Water Oxidation. In *Advances in Inorganic Chemistry*, van Eldik, R.; Cronin, L., Eds. Academic Press: 2017; Vol. 69, pp 155-179.

37. Folkman, S. J.; Soriano-Lopez, J.; Galán-Mascarós, J. R.; Finke, R. G., Electrochemically Driven Water-Oxidation Catalysis Beginning with Six Exemplary Cobalt Polyoxometalates: Is It Molecular, Homogeneous Catalysis or Electrode-Bound, Heterogeneous CoOx Catalysis? *Journal of the American Chemical Society* **2018,** *140* (38), 12040-12055.

38. Smith, R. D. L.; Prévot, M. S.; Fagan, R. D.; Trudel, S.; Berlinguette, C. P., Water Oxidation Catalysis: Electrocatalytic Response to Metal Stoichiometry in Amorphous Metal

Oxide Films Containing Iron, Cobalt, and Nickel. *Journal of the American Chemical Society* **2013,** *135* (31), 11580-11586.

39. Gerken, J. B.; McAlpin, J. G.; Chen, J. Y. C.; Rigsby, M. L.; Casey, W. H.; Britt, R. D.; Stahl, S. S., Electrochemical Water Oxidation with Cobalt-Based Electrocatalysts from pH 0–14: The Thermodynamic Basis for Catalyst Structure, Stability, and Activity. *Journal of the American Chemical Society* **2011,** *133* (36), 14431-14442.

40. Zidki, T.; Zhang, L.; Shafirovich, V.; Lymar, S. V., Water Oxidation Catalyzed by Cobalt(II) Adsorbed on Silica Nanoparticles. *Journal of the American Chemical Society* **2012,** *134* (35), 14275-14278.

41. Zhang, R. R.; Zhang, Y. C.; Pan, L.; Shen, G. Q.; Mahmood, N.; Ma, Y. H.; Shi, Y.; Jia, W. Y.; Wang, L.; Zhang, X. W.; Xu, W.; Zou, J. J., Engineering Cobalt Defects in Cobalt Oxide for Highly Efficient Electrocatalytic Oxygen Evolution. *Acs Catalysis* **2018,** *8* (5), 3803-+.

42. Pijpers, J. J.; Winkler, M. T.; Surendranath, Y.; Buonassisi, T.; Nocera, D. G., Light-induced water oxidation at silicon electrodes functionalized with a cobalt oxygen-evolving catalyst. *Proc Natl Acad Sci U S A* **2011,** *108* (25), 10056-61.

43. Kanan, M. W.; Nocera, D. G., In Situ Formation of an Oxygen-Evolving Catalyst in Neutral Water Containing Phosphate and Co^{2+}. *Science* **2008,** *321* (5892), 1072-1075.

44. Jiao, F.; Frei, H., Nanostructured cobalt oxide clusters in mesoporous silica as efficient oxygen-evolving catalysts. *Angew Chem Int Ed Engl* **2009,** *48* (10), 1841-4.

45. Chauhan, M.; Reddy, K. P.; Gopinath, C. S.; Deka, S., Copper Cobalt Sulfide Nanosheets Realizing a Promising Electrocatalytic Oxygen Evolution Reaction. *Acs Catalysis* **2017,** *7* (9), 5871-5879.

46. Brodsky, C. N.; Hadt, R. G.; Hayes, D.; Reinhart, B. J.; Li, N.; Chen, L. X.; Nocera, D. G., In situ characterization of cofacial Co(IV) centers in Co₄O₄ cubane: Modeling the high-valent active site in oxygen-evolving catalysts. *Proceedings of the National Academy of Sciences* **2017,** *114* (15), 3855-3860.

47. Pegis, M. L.; Wise, C. F.; Martin, D. J.; Mayer, J. M., Oxygen Reduction by Homogeneous Molecular Catalysts and Electrocatalysts. *Chemical Reviews* **2018,** *118* (5), 2340-2391.

48. Landon, J.; Demeter, E.; Inoglu, N.; Keturakis, C.; Wachs, I. E.; Vasic, R.; Frenkel, A. I.; Kitchin, J. R., Spectroscopic Characterization of Mixed Fe-Ni Oxide Electrocatalysts for the Oxygen Evolution Reaction in Alkaline Electrolytes. *Acs Catalysis* **2012,** *2* (8), 1793-1801.

49. Yin, Q.; Tan, J. M.; Besson, C.; Geletii, Y. V.; Musaev, D. G.; Kuznetsov, A. E.; Luo, Z.; Hardcastle, K. I.; Hill, C. L., A Fast Soluble Carbon-Free Molecular Water Oxidation Catalyst Based on Abundant Metals. *Science* **2010,** *328* (5976), 342.

50. Zhu, C. Z.; Wen, D.; Leubner, S.; Oschatz, M.; Liu, W.; Holzschuh, M.; Simon, F.; Kaskel, S.; Eychmuller, A., Nickel cobalt oxide hollow nanosponges as advanced electrocatalysts for the oxygen evolution reaction. *Chemical Communications* **2015,** *51* (37), 7851-7854.

51. Xu, Y. F.; Gao, M. R.; Zheng, Y. R.; Jiang, J.; Yu, S. H., Nickel/Nickel(II) Oxide Nanoparticles Anchored onto Cobalt(IV) Diselenide Nanobelts for the Electrochemical Production of Hydrogen. *Angew. Chem.-Int. Edit.* **2013,** *52* (33), 8546-8550.

52. Gerken, J. B.; Landis, E. C.; Hamers, R. J.; Stahl, S. S., Fluoride-Modulated Cobalt Catalysts for Electrochemical Oxidation of Water under Non-Alkaline Conditions. *Chemsuschem* **2010,** *3* (10), 1176-1179.

53. Ndambakuwa, W.; Ndambakuwa, Y.; Choi, J.; Fernando, G.; Neupane, D.; Mishra, S. R.; Perez, F.; Gupta, R. K., Nanostructured nickel-cobalt oxide and sulfide for applications in supercapacitors and green energy production using waste water. *Surf. Coat. Technol.* **2021,** *410*, 10.

54. Peng, Z.; Jia, D.; Al-Enizi, A. M.; Elzatahry, A. A.; Zheng, G., From Water Oxidation to Reduction: Homologous Ni–Co Based Nanowires as Complementary Water Splitting Electrocatalysts. *Adv. Energy Mater.* **2015,** *5* (9), 1402031.

55. Surendranath, Y.; Dincă, M.; Nocera, D. G., Electrolyte-Dependent Electrosynthesis and Activity of Cobalt-Based Water Oxidation Catalysts. *Journal of the American Chemical Society* **2009,** *131* (7), 2615-2620.

56. Young, E. R.; Nocera, D. G.; Bulović, V., Direct formation of a water oxidation catalyst from thin-film cobalt. *Energy & Environmental Science* **2010,** *3* (11), 1726-1728.

57. Huang, Z.; Luo, Z.; Geletii, Y. V.; Vickers, J. W.; Yin, Q.; Wu, D.; Hou, Y.; Ding, Y.; Song, J.; Musaev, D. G.; Hill, C. L.; Lian, T., Efficient Light-Driven Carbon-Free Cobalt-Based Molecular Catalyst for Water Oxidation. *Journal of the American Chemical Society* **2011,** *133* (7), 2068-2071.

58. Wee, T.-L.; Sherman, B. D.; Gust, D.; Moore, A. L.; Moore, T. A.; Liu, Y.; Scaiano, J. C., Photochemical Synthesis of a Water Oxidation Catalyst Based on Cobalt Nanostructures. *Journal of the American Chemical Society* **2011,** *133* (42), 16742-16745.

59. Kanan, M. W.; Yano, J.; Surendranath, Y.; Dincă, M.; Yachandra, V. K.; Nocera, D. G., Structure and Valency of a Cobalt−Phosphate Water Oxidation Catalyst Determined by in Situ X-ray Spectroscopy. *Journal of the American Chemical Society* **2010,** *132* (39), 13692-13701.

60. Kim, H.; Park, J.; Park, I.; Jin, K.; Jerng, S. E.; Kim, S. H.; Nam, K. T.; Kang, K., Coordination tuning of cobalt phosphates towards efficient water oxidation catalyst. *Nature Communications* **2015,** *6* (1), 8253.

61. Lv, H.; Song, J.; Geletii, Y. V.; Vickers, J. W.; Sumliner, J. M.; Musaev, D. G.; Kögerler, P.; Zhuk, P. F.; Bacsa, J.; Zhu, G.; Hill, C. L., An Exceptionally Fast Homogeneous Carbon-Free Cobalt-Based Water Oxidation Catalyst. *Journal of the American Chemical Society* **2014,** *136* (26), 9268-9271.

62. Deng, X.; Tüysüz, H., Cobalt-Oxide-Based Materials as Water Oxidation Catalyst: Recent Progress and Challenges. *ACS Catalysis* **2014,** *4* (10), 3701-3714.

63. Du, P. W.; Eisenberg, R., Catalysts made of earth-abundant elements (Co, Ni, Fe) for water splitting: Recent progress and future challenges. *Energy & Environmental Science* **2012,** *5* (3), 6012-6021.

64. Burke, M. S.; Kast, M. G.; Trotochaud, L.; Smith, A. M.; Boettcher, S. W., Cobalt-Iron (Oxy)hydroxide Oxygen Evolution Electrocatalysts: The Role of Structure and Composition on Activity, Stability, and Mechanism. *Journal of the American Chemical Society* **2015,** *137* (10), 3638-3648.

65. Moysiadou, A.; Lee, S.; Hsu, C.-S.; Chen, H. M.; Hu, X., Mechanism of Oxygen Evolution Catalyzed by Cobalt Oxyhydroxide: Cobalt Superoxide Species as a Key Intermediate and Dioxygen Release as a Rate-Determining Step. *Journal of the American Chemical Society* **2020,** *142* (27), 11901-11914.

66. Fan, J.; Chen, Z.; Shi, H.; Zhao, G., In situ grown, self-supported iron–cobalt–nickel alloy amorphous oxide nanosheets with low overpotential toward water oxidation. *Chemical Communications* **2016,** *52* (23), 4290-4293.

67. Wang, Y.; Yang, C.; Huang, Y.; Li, Z.; Liang, Z.; Cao, G., Nickel induced electronic structural regulation of cobalt hydroxide for enhanced water oxidation. *Journal of Materials Chemistry A* **2020,** *8* (14), 6699-6708.

68. Chou, N. H.; Ross, P. N.; Bell, A. T.; Tilley, T. D., Comparison of Cobalt-based Nanoparticles as Electrocatalysts for Water Oxidation. *ChemSusChem* **2011,** *4* (11), 1566-1569.

69. Enman, L. J.; Stevens, M. B.; Dahan, M. H.; Nellist, M. R.; Toroker, M. C.; Boettcher, S. W., Operando X-Ray Absorption Spectroscopy Shows Iron Oxidation Is Concurrent with Oxygen Evolution in Cobalt–Iron (Oxy)hydroxide Electrocatalysts. *Angewandte Chemie International Edition* **2018,** *57* (39), 12840-12844.

70. Nguyen, A. I.; Ziegler, M. S.; Oña-Burgos, P.; Sturzbecher-Hohne, M.; Kim, W.; Bellone, D. E.; Tilley, T. D., Mechanistic Investigations of Water Oxidation by a Molecular Cobalt Oxide Analogue: Evidence for a Highly Oxidized Intermediate and Exclusive Terminal Oxo Participation. *Journal of the American Chemical Society* **2015,** *137* (40), 12865-12872.

71. Carroll, G. M.; Zhong, D. K.; Gamelin, D. R., Mechanistic insights into solar water oxidation by cobalt-phosphate-modified α-Fe2O3 photoanodes. *Energy & Environmental Science* **2015,** *8* (2), 577-584.

72. Ertem, M. Z.; Cramer, C. J., Quantum chemical characterization of the mechanism of a supported cobalt-based water oxidation catalyst. *Dalton Transactions* **2012,** *41* (39), 12213-12219.

73. Ullman, A. M.; Brodsky, C. N.; Li, N.; Zheng, S.-L.; Nocera, D. G., Probing Edge Site Reactivity of Oxidic Cobalt Water Oxidation Catalysts. *Journal of the American Chemical Society* **2016,** *138* (12), 4229-4236.

74. Zhang, M.; de Respinis, M.; Frei, H., Time-resolved observations of water oxidation intermediates on a cobalt oxide nanoparticle catalyst. *Nature Chemistry* **2014,** *6* (4), 362-367.

75. Brunschwig, B. S.; Chou, M. H.; Creutz, C.; Ghosh, P.; Sutin, N., Mechanisms of water oxidation to oxygen: cobalt(IV) as an intermediate in the aquocobalt(II)-catalyzed reaction. *Journal of the American Chemical Society* **1983,** *105* (14), 4832-4833.

76. Feizi, H.; Bagheri, R.; Jagličić, Z.; Singh, J. P.; Chae, K. H.; Song, Z.; Najafpour, M. M., A nickel(ii) complex under water-oxidation reaction: what is the true catalyst? *Dalton Transactions* **2019,** *48* (2), 547-557.

77. Singh, A.; Chang, S. L. Y.; Hocking, R. K.; Bach, U.; Spiccia, L., Highly active nickel oxide water oxidation catalysts deposited from molecular complexes. *Energy & Environmental Science* **2013,** *6* (2), 579-586.

78. Menezes, P. W.; Indra, A.; Levy, O.; Kailasam, K.; Gutkin, V.; Pfrommer, J.; Driess, M., Using nickel manganese oxide catalysts for efficient water oxidation. *Chemical Communications* **2015,** *51* (24), 5005-5008.

79. Luo, G.-Y.; Huang, H.-H.; Wang, J.-W.; Lu, T.-B., Further Investigation of a Nickel-Based Homogeneous Water Oxidation Catalyst with Two cis Labile Sites. *ChemSusChem* **2016,** *9* (5), 485-491.

80. Wang, D.; Ghirlanda, G.; Allen, J. P., Water Oxidation by a Nickel-Glycine Catalyst. *Journal of the American Chemical Society* **2014,** *136* (29), 10198-10201.

81. Moreno-Hernandez, I. A.; MacFarland, C. A.; Read, C. G.; Papadantonakis, K. M.; Brunschwig, B. S.; Lewis, N. S., Crystalline nickel manganese antimonate as a stable water-oxidation catalyst in aqueous 1.0 M H_2SO_4. *Energy & Environmental Science* **2017,** *10* (10), 2103-2108.

82. Zhu, G.; Glass, E. N.; Zhao, C.; Lv, H.; Vickers, J. W.; Geletii, Y. V.; Musaev, D. G.; Song, J.; Hill, C. L., A nickel containing polyoxometalate water oxidation catalyst. *Dalton Transactions* **2012,** *41* (42), 13043-13049.

83. Diaz-Morales, O.; Ferrus-Suspedra, D.; Koper, M. T. M., The importance of nickel oxyhydroxide deprotonation on its activity towards electrochemical water oxidation. *Chemical Science* **2016,** *7* (4), 2639-2645.

84. González-Flores, D.; Fernández, G.; Urcuyo, R., Spectroelectrochemical Experiment for Studying Water Oxidation with a Nickel Oxide Catalyst. *Journal of Chemical Education* **2021,** *98* (2), 607-613.

85. Zhang, L.-H.; Yu, F.; Shi, Y.; Li, F.; Li, H., Base-enhanced electrochemical water oxidation by a nickel complex in neutral aqueous solution. *Chemical Communications* **2019,** *55* (43), 6122-6125.

86. Ng, J. W. D.; García-Melchor, M.; Bajdich, M.; Chakthranont, P.; Kirk, C.; Vojvodic, A.; Jaramillo, T. F., Gold-supported cerium-doped NiOx catalysts for water oxidation. *Nature Energy* **2016,** *1* (5), 16053.

87. Kalantarifard, S.; Allakhverdiev, S. I.; Najafpour, M. M., Water oxidation by a nickel complex: New challenges and an alternative mechanism. *International Journal of Hydrogen Energy* **2020,** *45* (58), 33563-33573.

88. Song, Y. F.; Tsunashima, R., Recent advances on polyoxometalate-based molecular and composite materials. *Chemical Society Reviews* **2012,** *41* (22), 7384-7402.

89. Pope, M. T.; Muller, A., POLYOXOMETALATE CHEMISTRY - AN OLD FIELD WITH NEW DIMENSIONS IN SEVERAL DISCIPLINES. *Angew. Chem.-Int. Edit. Engl.* **1991,** *30* (1), 34-48.

90. Long, D. L.; Burkholder, E.; Cronin, L., Polyoxometalate clusters, nanostructures and materials: From self assembly to designer materials and devices. *Chemical Society Reviews* **2007,** *36* (1), 105-121.

91. Long, D. L.; Tsunashima, R.; Cronin, L., Polyoxometalates: Building Blocks for Functional Nanoscale Systems. *Angew. Chem.-Int. Edit.* **2010,** *49* (10), 1736-1758.

92. Hill, C. L.; Prossermccartha, C. M., HOMOGENEOUS CATALYSIS BY TRANSITION-METAL OXYGEN ANION CLUSTERS. *Coord. Chem. Rev.* **1995,** *143*, 407-455.

93. Sullivan, K. P.; Yin, Q.; Collins-Wildman, D. L.; Tao, M.; Geletii, Y. V.; Musaev, D. G.; Lian, T.; Hill, C. L., Multi-Tasking POM Systems. **2018,** *6* (365).

94. Sumliner, J. M.; Lv, H. J.; Fielden, J.; Geletii, Y. V.; Hill, C. L., Polyoxometalate Multi-Electron-Transfer Catalytic Systems for Water Splitting. *European Journal of Inorganic Chemistry* **2014,** (4), 635-644.

95. Lv, H. J.; Geletii, Y. V.; Zhao, C. C.; Vickers, J. W.; Zhu, G. B.; Luo, Z.; Song, J.; Lian, T. Q.; Musaev, D. G.; Hill, C. L., Polyoxometalate water oxidation catalysts and the production of green fuel. *Chemical Society Reviews* **2012,** *41* (22), 7572-7589.

96. Lauinger, S. M.; Yin, Q.; Geletii, Y. V.; Hill, C. L., Chapter Five - Polyoxometalate Multielectron Catalysts in Solar Fuel Production. In *Advances in Inorganic Chemistry*, van Eldik, R.; Cronin, L., Eds. Academic Press: 2017; Vol. 69, pp 117-154.

Chapter 2

Electronic Perturbation of Transition-Metal Catalytic Water Oxidation Sites of Isostructural and Isocharge Polyoxometalates

This study is the result of a collaborative effort with significant experimental contributions from Meilin Tao, John Bacsa, and Yurii Geletii, as well as significant computational contributions from Alexey Kaledin.

Introduction

In Chapter 1, we touched upon the research focus on cobalt-based and nickel-based OER catalysts.[1-41] A number of these catalysts, either molecular or heterogeneous, have been employed to carry out water oxidation catalysis in both model systems and prototypical photoelectrochemical cells. The reason these two elements have received such attention from the scientific community is due to their relative cheap cost being earth-abundant metals, and due to their relatively high efficiency for OER in a number of systems. These compounds continue to show great promise for use in PECs. Further tuning of the metal oxides and oxyhydroxides have been done in the form of morphology modulation, doping, defect generation, etching, etc. In particular, doping metal oxides to create mixed-metal oxides/oxyhydroxides is seen as an extremely valuable strategy as this allows the most direct modification of the active site electronic structures in these catalytic systems. Efficient systems with improved OER performances have been synthesized using this strategy. Currently, most of the best performing OER catalysts are doped or mixed-metal oxides/oxyhydroxides. Among these, cobalt-nickel mixed-metal oxyhydroxides have shown some of the highest OER activity.[2, 6-7, 9-10, 17, 19, 21, 24, 26, 29] Most importantly, the mixing of cobalt and nickel have a synergistic effect that allows the resulting Co-Ni oxyhydroxides to perform much better than either cobalt oxides/oxyhydroxides or nickel oxides/oxyhydroxides. However, the relationship between these changes to catalyst composition and catalytic activity is still unclear. A molecular analogue of these systems could prove to be useful in elucidating the underlying factors at play.

A respectable molecular analogue for cobalt oxide/oxyhydroxides exist in the compound $[Co_4(PW_9O_{34})_2]^{10-}$ (**Co_4P_2**). **Co_4P_2** is a well-documented OER catalyst.[42-43] Atomic level substitution of the cobalt atoms with nickel would thus present an isostructural compound to **Co_4P_2**

that has a mixed-metal core with neighboring cobalt and nickel atoms. This would be an exemplary molecular analogue of the previously described mixed Co-Ni oxide/oxyhydroxides. Moreover, this would give us unprecedented control over the electronic structure of the active site.

In this Chapter, I will detail the collaborative efforts done to synthesize and characterize a new POM, $[Co_2Ni_2(PW_9O_{34})_2]^{10-}$ (**$Co_2Ni_2P_2$**). As seen in Figure 2.1, **$Co_2Ni_2P_2$** is an isostructural analogue of **Co_4P_2**, in which the two buried cobalt atoms in the cobalt-oxo core are replaced by nickel. This represents the first molecular modification of its kind that allows for a one-to-one comparative study of two multinuclear OER catalysts isolating the effects of substituting the transition metal element on an active site neighbor.

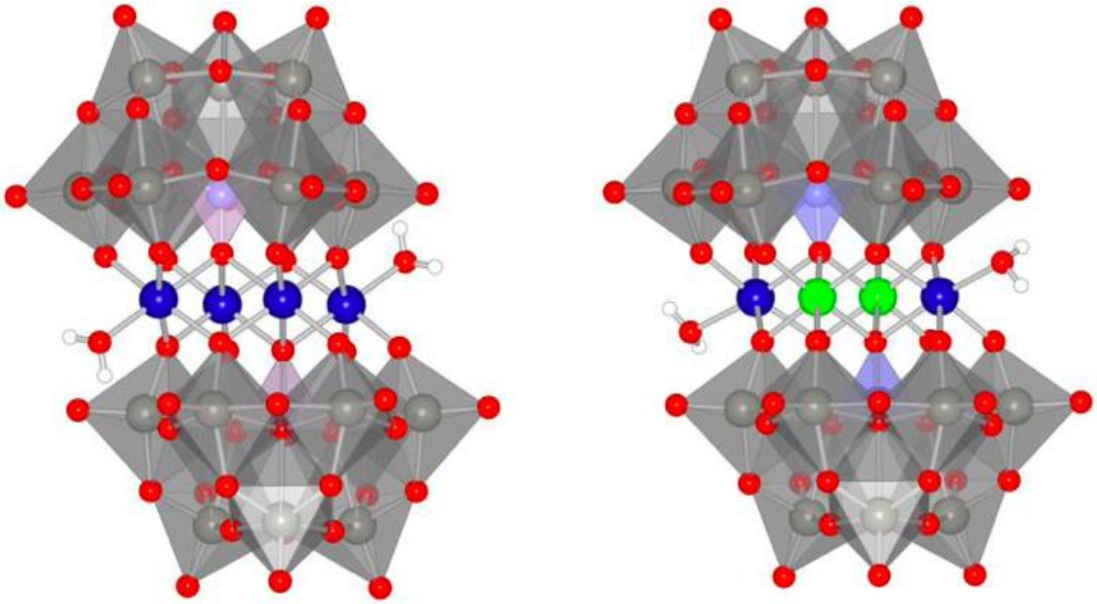

$[Co(OH_2)_2Co_2(\alpha\text{-}PW_9O_{34})_2]^{10-}$
(Co_4P_2)

$[Co(OH_2)_2Ni_2(\alpha\text{-}PW_9O_{34})_2]^{10-}$
($Co_2Ni_2P_2$)

Figure 2.1 Structures of polyoxometalate water oxidation catalysts that have the same cobalt active site structures, overall structures, and molecular charges: **Co_4P_2** and **$Co_2Ni_2P_2$**. Co: blue; Ni: green; WO_6, gray octahedra.

Results and Discussion

Synthesis of $\mathbf{Co_2Ni_2P_2}$

The synthesis of $\mathbf{Co_2Ni_2P_2}$ is summarized in Figure 5. Both the intermediate structures were confirmed by X-ray crystallography, and the final product structure was confirmed by synchrotron multi-wavelength X-ray anomalous scattering (XRAS). Stepwise, reaction with the sodium salt of both tungstate and phosphate in the presence of a select amount of nickel nitrate yields the structural analogue of $\mathbf{Co_4P_2}$, namely $[Na_2(Ni)_2(PW_9O_{34})_2]^{12-}$ ($\mathbf{Na_2Ni_2P_2}$), a complex with extremely labile sodium centers on the outside of the central belt and Ni(II) centers installed in the symmetry-equivalent internal, buried positions. Single crystal X-ray diffraction can be used to confirm the occupancy of the Na and Ni centers because Na^+ and Ni(II) have sufficiently different electron densities.[44] Exchange of the Na^+ positions with Co(II) is achieved by treating $\mathbf{Na_2Ni_2P_2}$ with Co(II) salts at pH 5.5 in the presence of KCl, forming the desired $\mathbf{Co_2Ni_2P_2}$ in good yield but with $[Co(H_2O)_6]^{2+}$ counterions. Nevertheless, these counter-cations must be removed because $[Co(H_2O)_6]^{2+}$ are known pre-catalysts for water oxidation. That is, under oxidizing conditions, $[Co(H_2O)_6]^{2+}$ forms multi-cobalt polyhydroxo complexes of low molecular weight that are active OER catalysts and would thus convolute comparative studies of the OER activity of $\mathbf{Co_2Ni_2P_2}$. To this end, slow re-crystallization from concentrated (0.27 M) KCl effectively replaces the $[Co(H_2O)_6]^{2+}$ counter-cations with redox-inactive K^+ cations. The single crystal X-ray diffraction, elemental analysis (Table 2.1), and the TGA results indicate that the complete structural formula of the ion-exchanged final crystalline complex is a mixed potassium, sodium salt: $K_8Na_2Co_2Ni_2P_2W_{18}O_{68}\cdot 30H_2O$ (KNa$\mathbf{Co_2Ni_2P_2}$).

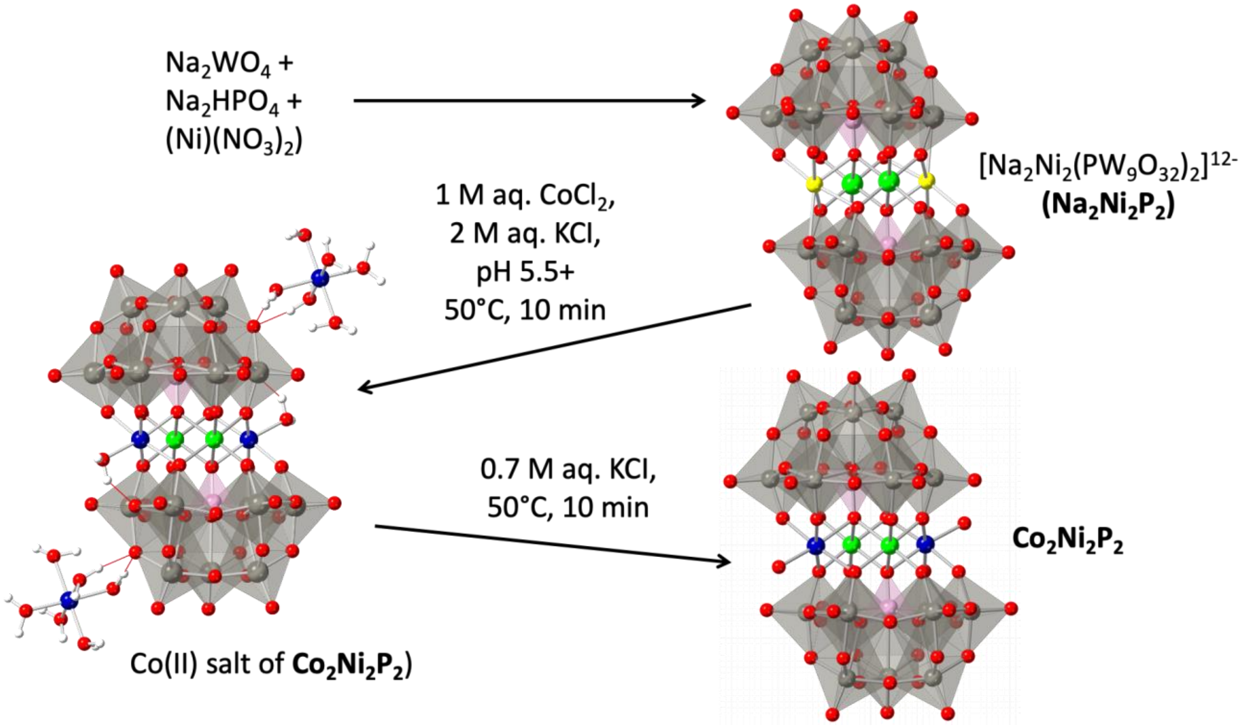

Figure 2.2 Synthesis of a two-transition-metal POM water oxidation catalyst (WOC), X-ray crystal structures of intermediates and products are shown in ball-and-stick figures (W: gray, O: red, P: magenta, Co: blue, Ni: green, Ni: yellow).

The X-ray crystal structures of **$Co_2Ni_2P_2$** reveal that the **$Co_2Ni_2P_2$** polyanion is isomorphic to **Co_4P_2**, and is identically composed of four redox active 3d transition metals within the central belt sandwiched by two trivacant B-α-$[PW_9O_{34}]^{9-}$ Keggin moieties. This structural motif is well-known, having been first reported by Weakley et al. in 1972[45] and remains one of the more utilized structures in POM chemistry. Whereas, the structure of **Co_4P_2** contains two chemically equivalent Co(II) centers buried in the internal belt positions in an overall C_i symmetry polyanion, the structure of **$Co_2Ni_2P_2$** contains two chemically equivalent Ni(II) centers in those same positions instead. Both **Co_4P_2** and **$Co_2Ni_2P_2$** similarly contain two additional chemically equivalent Co(II) centers in the external positions of the belt defining an almost-rhombic Co_2Ni_2 tetrad (Figure 2.1, 2.2). Each Co(II) in **$Co_2Ni_2P_2$** coordinates to six oxygen atoms of the two B-α-$[PW_9O_{34}]^{9-}$ units. **Co_4P_2** and **$Co_2Ni_2P_2$** both have two accessible Co binding coordinates, one on each external Co(II). These are the water oxidation sites. Thus, the active site element in both complexes is the same. Structurally, the buried Co and Ni can not access external water molecules, and thus would only impact the water oxidation reaction by affecting the geometric and electronic structures of the outside "active-site" cobalt centers.

Structural characterization

Structural characterization of **$Co_2Ni_2P_2$** proved to be quite difficult solely due to one factor. Differentiating between Co(II) and Ni(II) in a mixed-metal POM complex in otherwise completely isostructural complexes is very difficult to achieve using traditional X-ray crystallography. Standard, single-wavelength X-ray diffraction is generally not sensitive enough to unequivocally distinguish the electron densities of neighboring transition-metal atoms in the periodic table in a molecule.

Elemental analysis of **$Co_2Ni_2P_2$** provides a basal check for the composition of the synthesized complex. Inductively coupled plasma - atomic emission (ICP-AE) spectroscopy and inductively coupled plasma - mass spectrometry (ICP-MS) were used to characterize the elemental composition of **$Co_2Ni_2P_2$**. Table 2.1 shows that the molar ratio of Ni and Co is very close to the theoretical 1:1 value that we would expect in the structures shown in Figures 2.1 and 2.2. Crucially, the measured weight percentages of Co, Ni, P, and W are all very close to the theoretical value.

Table 2.1. Elemental analysis of $Na_2K_8Co_2Ni_2P_2W_{18}O_{68}$•$30H_2O$

Elements	weight % (found)	weight % (estimated)	stoichiometry (found)	stoichiometry (estimated)
Co	2.00	2.22	2.0	2.0
Ni	2.11	2.21	2.1	2.0
P	1.04	1.15	2.0	2.0
W	61.70	62.46	18.7	18.0

FT-IR spectra are also able to distinguish between **Co_4P_2** and **$Co_2Ni_2P_2$**. However, these differences are slight and qualitative. Significantly, the FT-IR spectra can at best be used as a fingerprint tool and cannot be used to assign structural details in these molecules. Figure 2.3 shows the FT-IR spectra of **Ni_4P_2**, **$Na_2Ni_2P_2$**, **Co_4P_2**, and **$Co_2Ni_2P_2$** in the P-O, W-O, and W-O-W stretch regions. These regions are quite similar to each other, which is consistent with all these POMs being isostructural. Additionally, the triply degenerate ν_3 vibrational mode (1000 cm^{-1}) of the central PO_4 unit in **Co_4P_2** is broadened but not split. Compare that to those of **$Co_2Ni_2P_2$** and the precursor complex **$Na_2Ni_2P_2$**. Both have split peaks, indicating a greater structural distortion and a consequent lowering of symmetry around this central heteroatom unit compared to **Co_4P_2**. The peaks in the lower energy (<1000 cm^{-1}) region are attributed to the characteristic ν(W-O_t), ν(W-O_b-W) and ν(W-O_c-W) absorptions, where O_b = double-bridging oxygen; O_c = central oxygen; and O_t = terminal oxygen.

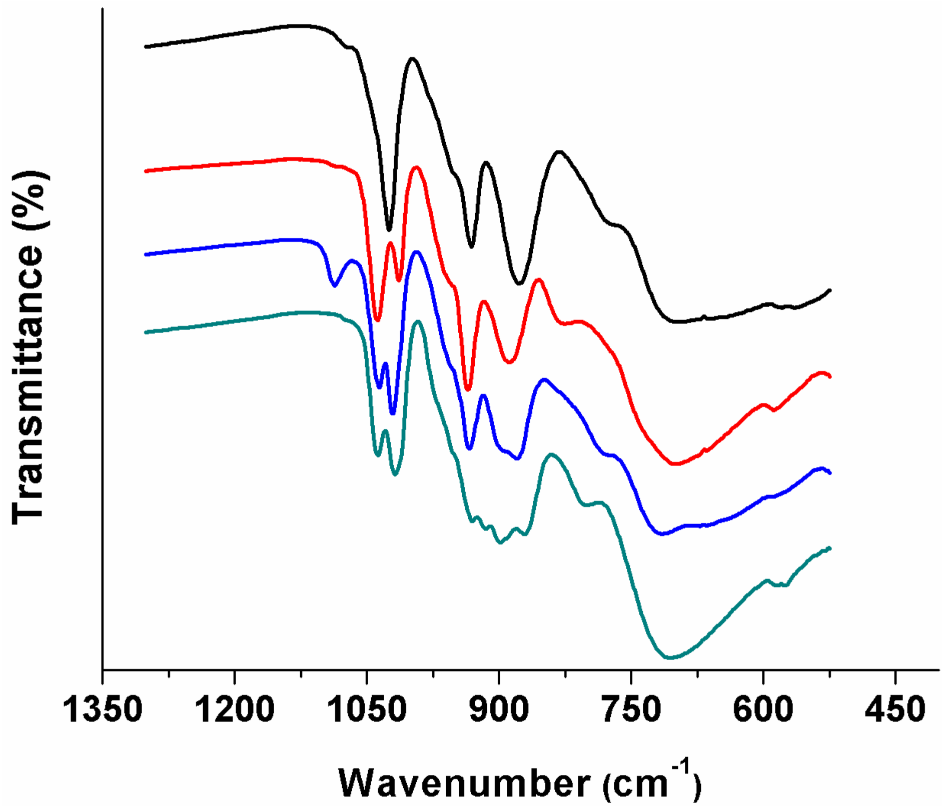

Figure 2.3 Comparison of FTIR spectra of **Co_4P_2** (black), **$Co_2Ni_2P_2$** (red), **Ni_4P_2** (blue), and **$Na_2Ni_2P_2$** (green).

Synchrotron XRAS: confirmation of transition metal positions and occupancies in $Co_2Ni_2P_2$

Collectively, the single crystal X-ray structure of **$Co_2Ni_2P_2$**, the FT-IR spectral data, and the elemental analysis suggest the presence of a Co_2Ni_2 unit in the central belt of the complex. However, precise occupancy assignment of the individual Co(II) and Ni(II) atoms remain uncertain because of their similar Z values. Unequivocal and quantitative assignment of the adjacent 3d elements in the periodic table is made all the more difficult when there are a large number of adjoining heavy metal elements. In a structure that also contains 18 heavily-scattering tungsten ions, **$Co_2Ni_2P_2$** defines a major challenge for precise positional assignment even with up-to-date conventional X-ray diffractometers equipped with strong X-ray sources and improved detectors. If we are to proceed with comparative studies focusing on the isolated effect of altering neighboring elements of the active site in an OER catalyst, quantification of Co and Ni occupancy in the belt cluster is imperative. Consequently, we turned to the use of synchrotron XRAS to address this issue. Synchrotron XRAS is an X-ray diffraction technique that utilizes the anomalous dispersion effect in optics. This methodology had previously not been applied to POM systems. However, in our case, it is uniquely suited to quantify the abundance and locate the positions of the two proximal 3-d transition metals, Co and Ni, in **$Co_2Ni_2P_2$**. The application of this technique to differentiate between similar Z-value metals could potentially be generalized to other complexes beyond **$Co_2Ni_2P_2$**.

In conventional X-ray crystallography, the typical measurements are the angles and intensities of diffracted X-ray beams. The intensities are proportional the square of the structure factor amplitude, $|F(hkl)^2|$. When the incident X-ray energy is low (not approaching any transition edge energy), the scattering process is similar for all atoms and Friedel's law is fulfilled. In other words, structural factors are mirrored across the real axis and diffracted intensities are the same for Friedel pairs: $|F(h, k, l)| = |F(-h, -k, -l)|$.

Consider the scattering factor:

$$f = f_o + \Delta f' + i\Delta f'' \qquad (2.1)$$

f_o is the normal scattering factor, and $\Delta f'$ and $i\Delta f''$ are the real and imaginary components of the correction factors for anomalous scattering. Components of $\Delta f'$ are out of phase with normal scattering factor by π, and components of $\Delta f''$ are out of phase with normal scattering factor by $\pi/2$. The normal scattering factor, f_o, is usually used to calculate the charge density distribution with wave-functions. However, when the incident X-ray beam has sufficient energy to promote electronic transitions in a non-centrosymmetric crystal, anomalous scattering occurs ($\Delta f'$ and $i\Delta f''$

in equation 2.1 becomes non-zero) and Friedel's law is broken. Anomalous scattering becomes appreciable when the frequency of the radiation closely matches that of the natural frequencies of the absorption edges of the electronic shells. At X-ray energies above the absorption edge, we expect to see fluorescence to occur. In XRAS, the anomalous dispersions attenuates the Bragg X-ray peaks, leading to $|F(h, k, l)| \neq |F(-h, -k, -l)|$. Using this inequality, the differences in equation 2.1 can be plotted as a function of incident wavelength. This plot is unique to each element within the crystal and their K edge energy (Figure 2.4). Thus identifying the different elements.

Measurements were acquired over a wide range of wavelengths that included the two K-edges of cobalt and nickel. Data collections were displaced at either side of the two K-edges (Figure 2.4). GSAS-II[46] was used to facilitate processing of all the multiple wavelength data to refine the populations of cobalt and nickel atoms at these specific metal sites. High-resolution data (30 keV) gave us an optimal structural model for the refinement of the fractions of both metals. The results are presented in Table 2.2. In short, the Co(II) centers are confirmed to be located in 97% at the outer, solvent-accessible positions; and Ni(II) centers are confirmed to be located in 96% at the inner solvent-inaccessible positions of the central belt of **$Co_2Ni_2P_2$** (Figure 1). These results confirm not only the Co, Ni atom sites, but also showed that there is no mixing between the sites.

Table 2.2. GSAS-II refinement results of $Na_2K_8Co_2Ni_2P_2W_{18}O_{68}$•$30H_2O$

Outer M atoms	Inner M atoms
Co 0.97(1) Ni 0.03(1)	Ni 0.96(1) Co 0.04(1)

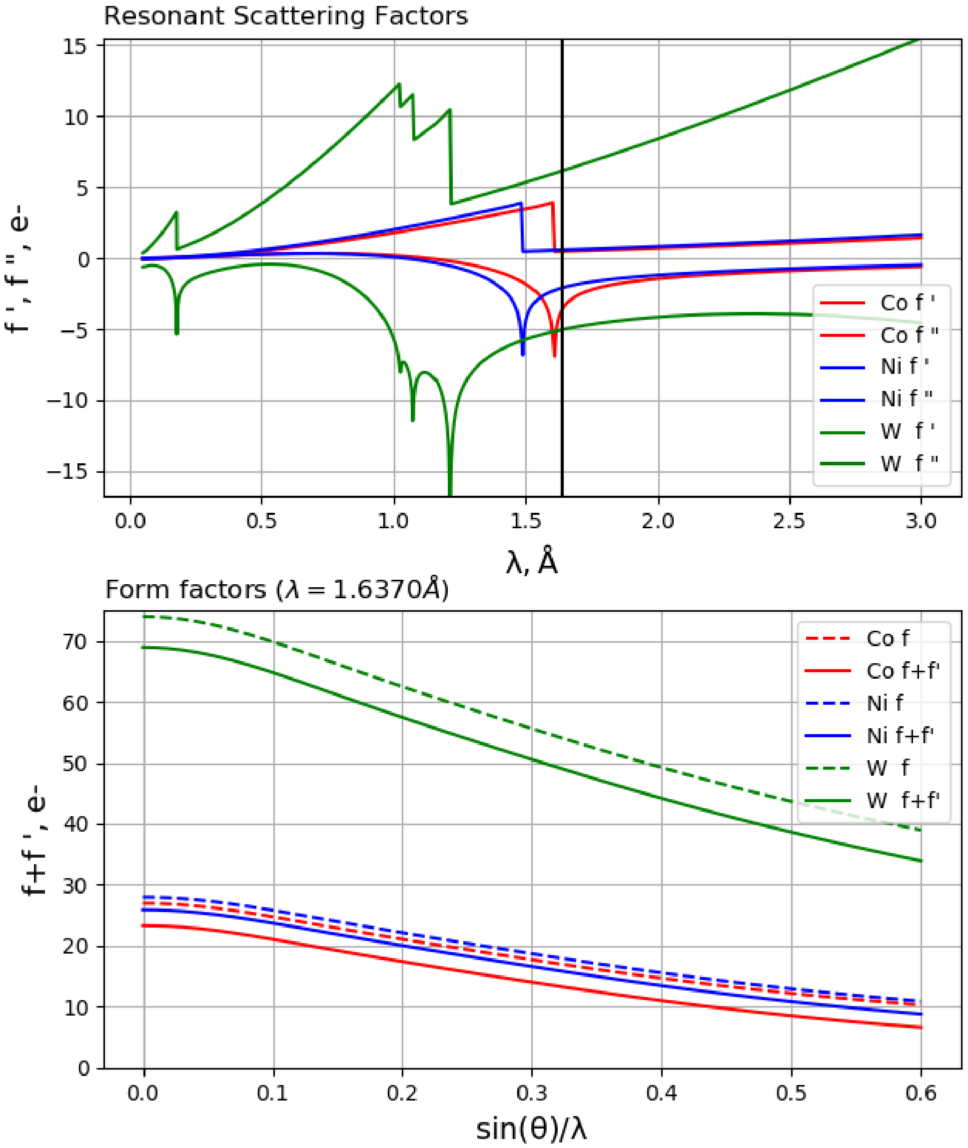

Figure 2.4. The resonant scattering signals for W, Ni and Co in $Co_2Ni_2P_2$ used by GSAS-II[46] for multi-wavelength refinements. Both M^{II} = Co, Ni atom site fractions were refined with the resonant data. The 30 keV data was used to refine the entire structure along with the site fractions to provide the best overall result.

Impact of electronic perturbation on the OER activity of $\mathbf{Co_2Ni_2P_2}$ and $\mathbf{Co_4P_2}$

The catalytic efficiency of $\mathbf{Co_4P_2}$**,** $\mathbf{Ni_4P_2}$**,** $\mathbf{Na_2Ni_2P_2}$, and $\mathbf{Co_2Ni_2P_2}$ for water oxidation were evaluated in dark homogeneous, photodriven homogeneous, and electrocatalytic conditions. The dark reactions used $[Ru(bpy)_3](ClO_4)_3$ as a stoichiometric oxidant (equation 2.2) and were monitored by the UV-Vis spectroscopic kinetics of $[Ru(bpy)_3]^{3+}$ (ε_{670}= 420 M^{-1} cm^{-1})[47] consumption in 80 mM borate buffer at pH 8.0 using the stopped-flow technique.

$$4[Ru(bpy)_3]^{3+} + 2H_2O \rightarrow 4[Ru(bpy)_3]^{2+} + O_2 + 4H^+ \qquad (2.2)$$

Typical kinetic curves, shown in Figure 2.5, are not exponential. The addition of 1.0 μM $\mathbf{Co_2Ni_2P_2}$ results in almost complete $[Ru(bpy)_3]^{3+}$ consumption in less than 0.5 s, which is an order of magnitude faster than with 1.0 μM $\mathbf{Co_4P_2}$ and more than 60 times faster than the self-decomposition rate of $[Ru(bpy)_3]^{3+}$, also shown in Figure 2.5. For comparison, we also recorded the kinetics of $[Ru(bpy)_3]^{3+}$ reduction catalyzed by 5 μM $Co(NO_3)_2$ (brown) and by 5 μM $\mathbf{Na_2Ni_2P_2}$ (green). The oxygen yields, based on the initial concentration of the oxidant, $[Ru(bpy)_3{}^{3+}]$, increase with catalyst concentrations and reach a plateau of about 70-80% at 5.0 μM catalyst ($\mathbf{Co_2Ni_2P_2}$ or $\mathbf{Co_4P_2}$). In the presence of $\mathbf{Ni_4P_2}$ or $\mathbf{Na_2Ni_2P}$, the rate of $[Ru(bpy)_3]^{3+}$ consumption is the same as in the absence of a catalyst.

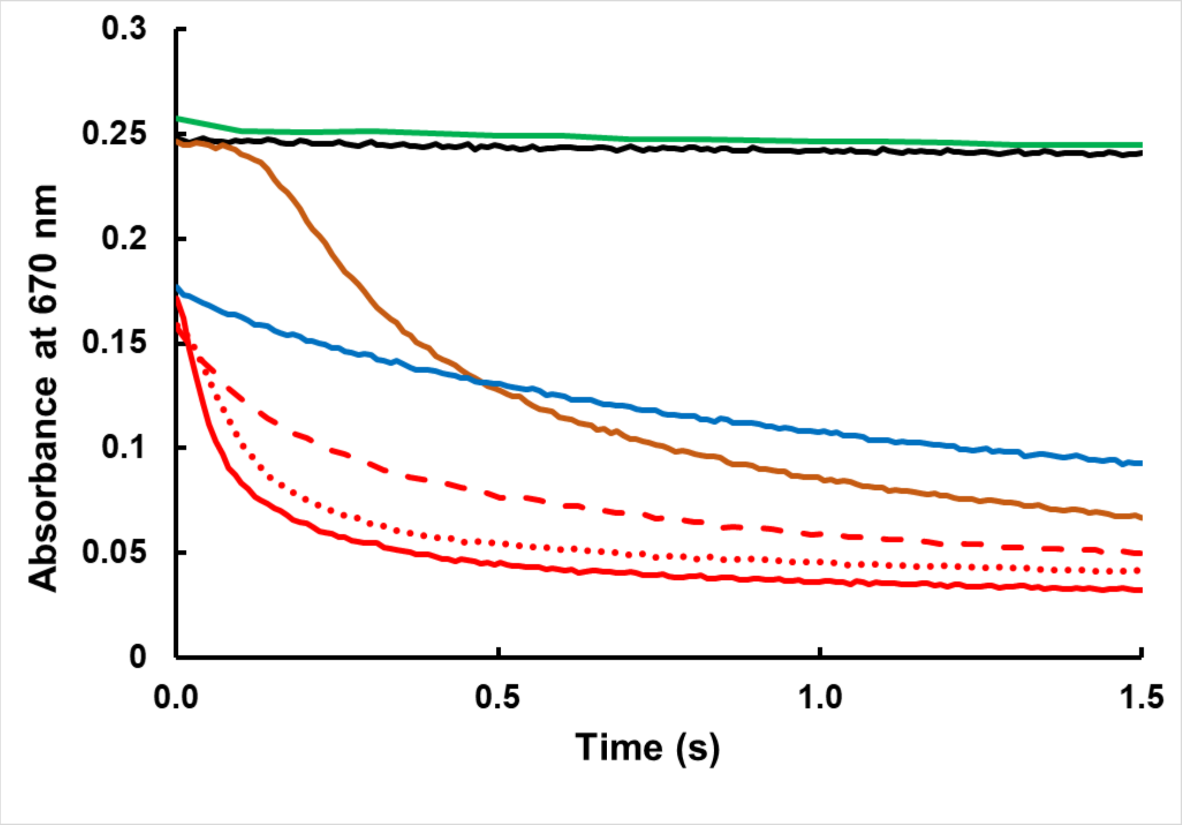

Figure. 2.5 Kinetics of [Ru(bpy)$_3$]$^{3+}$ reduction measured as the decrease in absorbance at 670 nm. Black - no catalyst, green - 5 µM **Na_2Ni_2**, brown - 5 µM Co(NO$_3$)$_2$, blue - 1 µM **Co_4P_2**, red - 1 µM **$Co_2Ni_2P_2$** with 0 (solid), 9 µM bpy (dotted), 40 µM bipyridine (dashed); Conditions: 0.43 mM (red and blue) or 0.6 mM [Ru(bpy)$_3$]$^{3+}$ (brown, black, and green), 80 mM sodium borate buffer at pH 8.0, 298 K.

Light-driven catalytic water oxidation

The activity of **$Co_2Ni_2P_2$** in visible-light-driven catalytic water oxidation was assessed using a standard approach with [Ru(bpy)$_3$]Cl$_2$ as the photosensitizer and persulfate, $Na_2S_2O_8$, as a sacrificial electron acceptor (Figure 2.6).[48-49] The initial rate of O_2 formation is commonly, but incorrectly, considered as a direct measure of the catalytic activity, but in actuality this slope is a measure of the initial quantum yield. Under the conditions in Figure 2.6, the O_2 yields and quantum yields in the presence of **$Co_2Ni_2P_2$** are approximately 23% higher than those in the presence of **Co_4P_2**. The O_2 yields in the **Ni_4P_2** and **$Na_2Ni_2P_2$** reactions are the same as those without a catalyst. The light-induced oxidative decomposition of the photosensitizer, $[Ru(bpy)_3]^{2+}$, by persulfate is the main side-reaction in the absence of a WOC.

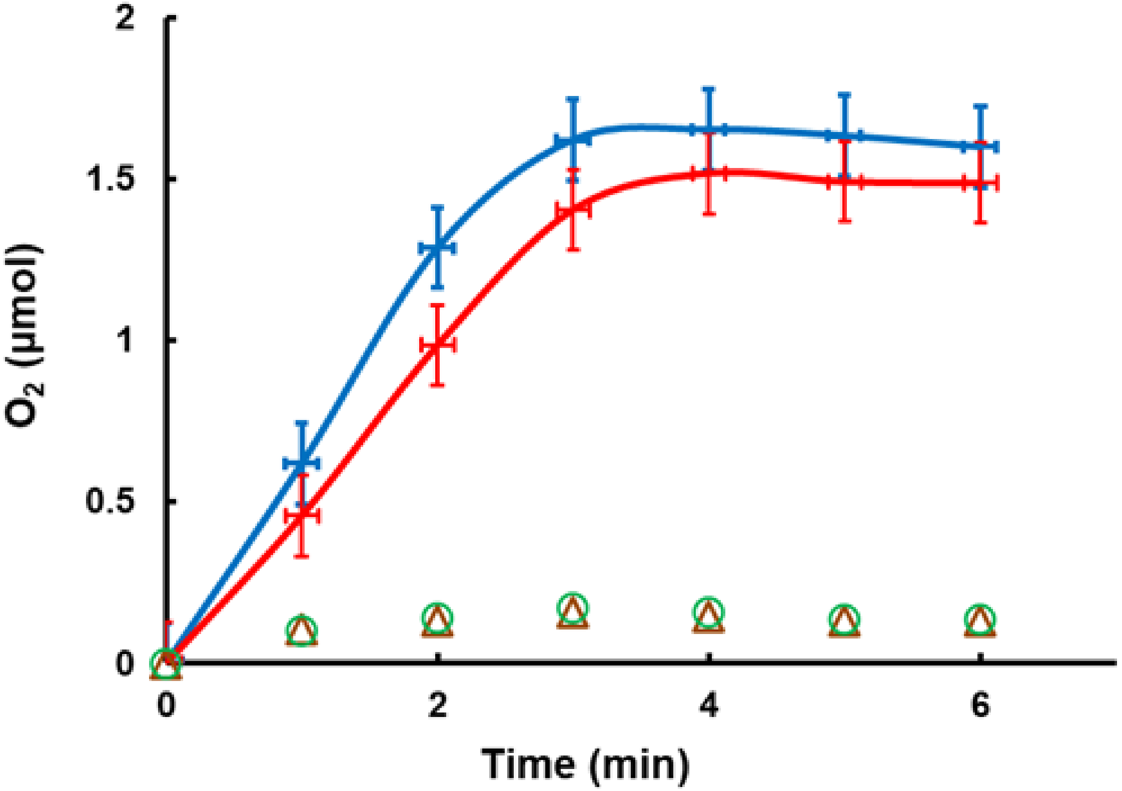

Figure 2.6 Kinetics of O_2 evolution in the light driven reactions with 1.0 mM $[Ru(bpy)_3]Cl_2$ and 5.0 mM $Na_2S_2O_8$ catalyzed by 10 µM of **$Co_2Ni_2P_2$** (blue), **Co_4P_2** (red), **Ni_4P_2** (green), and **$Na_2Ni_2P_2$** (brown). Conditions: 455 nm LED light (17 mW, beam diameter *ca.* 0.4 cm), 80 mM sodium borate buffer, initial pH 8.0, total solution volume 2.0 mL.

Electrocatalytic water oxidation

Previous studies showed that prolonged exposure to the high overpotential conditions required for electrochemical water oxidation tends to decompose cobalt-containing Keggin-sandwich POMs by electrodepositing cobalt oxide species on the working electrode.[50] [51] [52] [53] Embedding Co-POM OER catalysts in carbon paste has been reported to greatly reduce the hydrolytic decomposition of these catalysts.[54-55] Nevertheless, short timescale homogeneous cyclic voltammetry experiments illuminate aspects of the catalytic water oxidation activity of **$Co_2Ni_2P_2$**. At 1.0 μM this POM produces a rising anodic current from the catalytic oxidation of water with no corresponding reductive current (Figure 2.7). More importantly, atom-equivalent concentrations of aqueous Co^{2+} and Ni^{2+} (2.0 μM each) result in a lower oxidative currents. Given that aqueous Co^{2+} is a known active OER catalyst (active precursor) and Ni^{2+} is not, this observation strongly suggests that **$Co_2Ni_2P_2$** is a much faster OER catalyst than Co^{2+}. These results are also consistent with the stopped-flow kinetic studies, where we see not only a much faster initial rate of reaction associated with **$Co_2Ni_2P_2$** but also a delayed reaction onset for aqueous Co^{2+} that is nonexistent in the early-time water oxidations catalyzed by POM OER catalysts (Figure 2.5).

The catalytic current density attributed to water oxidation is generally proportional to the catalyst concentration (Figures 2.7 and 2.8). However, the oxidative current for **$Co_2Ni_2P_2$** plateaus after about 10 μM, possibly due to limited solubility. Interestingly, at higher concentrations of the catalysts, aqueous Co^{2+} may result in a higher oxidative current under these conditions, reversing the earlier trend. Much of this is attributable to electrodeposition of cobalt oxides in the presence of aqueous Co^{2+}. This is consistent with a higher observed oxidative current on subsequent scans in the case of the aqueous cations (Figure 2.8). Little change is observed in the case of **$Co_2Ni_2P_2$**. Furthermore, using the same working electrode in a fresh electrochemical solution containing no electroactive materials resulted in no additional oxidative current in the case of 10.0 μM **$Co_2Ni_2P_2$** but a visible increase in the case of 20.0 μM $Co(NO_3)_2$ + 20.0 μM $Ni(NO_3)_2$. This suggests that cobalt oxide is formed in the oxidation of aqueous Co^{2+} and Ni^{2+} and is at least partially responsible for their catalytic activity. On the other hand, it appears that molecular **$Co_2Ni_2P_2$** is responsible for the observed water oxidation and is not forming significant amounts of cobalt oxides at these timescales.

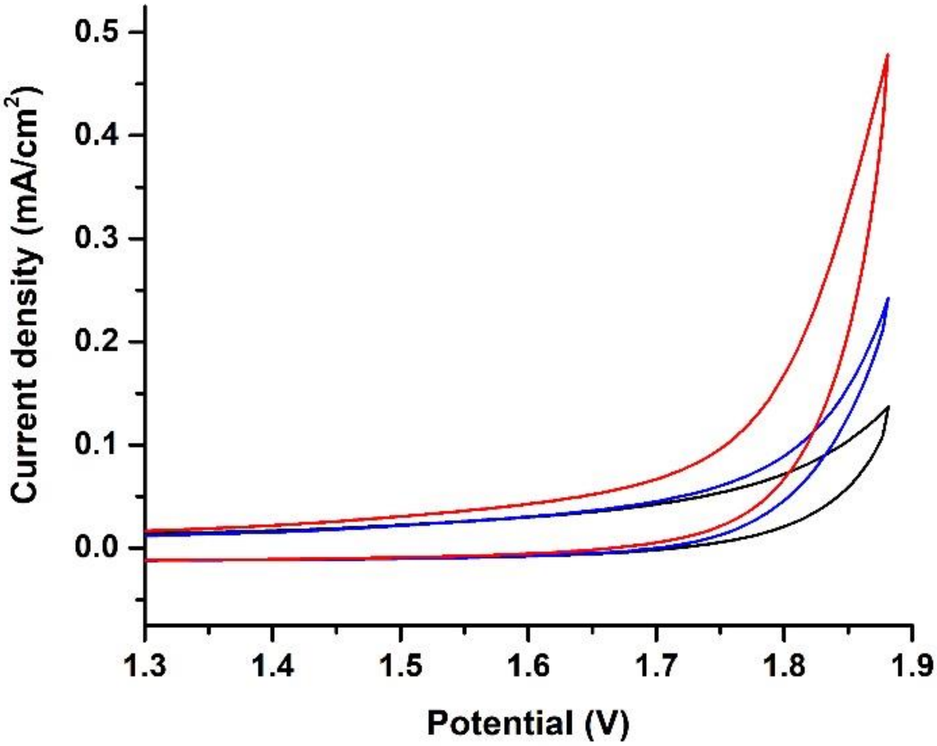

Figure 2.7 Cyclic voltammetry of different catalytic species. No catalyst (black), 1.0 μM **$Co_2Ni_2P_2$** (red), and 2.0 μM $Co(NO_3)_2$ + 2.0 μM Ni $Co(NO_3)_2$ (blue). Conditions: 0.1 M pH 8.0 borate buffer with 0.1 M of KNO_3 as the electrolyte; glassy carbon working electrode; Ag/AgCl reference electrode; 50 mV/s scan rate. The plotted potential is relative to the reversible hydrogen electrode.

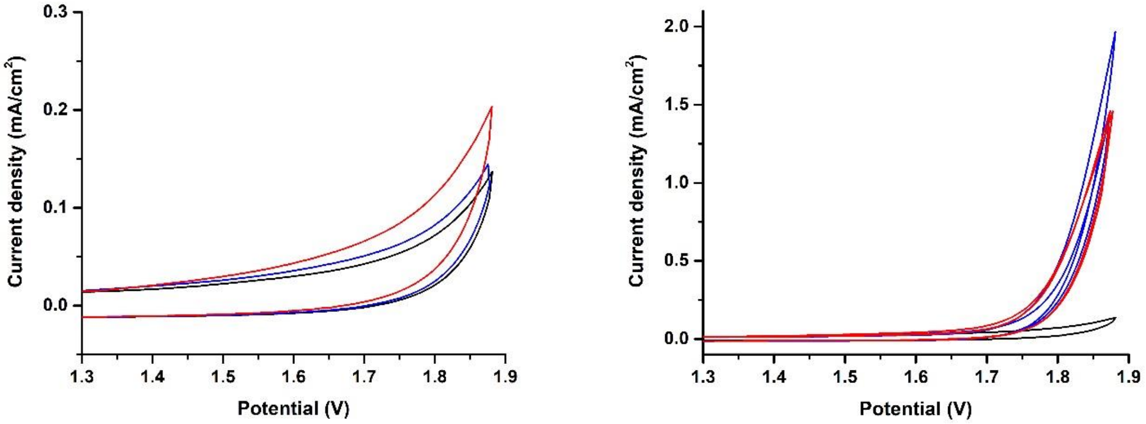

Figure 2.8 Cyclic voltammetry in a 0.1 M pH 8.0 borate buffer with 0.1 M of KNO_3 as the electrolyte. Left: Comparisons of no catalyst (black), 0.10 μM $\mathbf{Co_2Ni_2P_2}$ (red), and 0.20 μM $Co(NO_3)_2$ + 0.20 μM $Ni(NO_3)_2$ (blue) shows the highest oxidative activity attributed to $\mathbf{Co_2Ni_2P_2}$. Right: Comparisons of no catalyst (black), 10.0 μM $\mathbf{Co_2Ni_2P_2}$ (red), and 20.0 μM $Co(NO_3)_2$ + 20.0 μM $Ni(NO_3)_2$ (blue) over two scan cycles. Ag/AgCl was used as the reference electrode. 50 mV/s scan rate. The plotted potential is relative to the reversible hydrogen electrode.

Stability of the $\mathbf{Co_2Ni_2P_2}$ water oxidation catalyst in solution

The stability of any catalyst is a concern as we consider the reactive species responsible for catalysis. For molecular OER catalysts, this is an even more prominent issue. Water oxidation necessitates, by its very nature, generation of very oxidizing chemical environments that would react with many other species. POMs have an advantage in stability by having a fully inorganic and oxidized frameworks, especially when compared with catalysts with oxidizable organic ligands. Nevertheless, even $\mathbf{Co_4P_2}$ can decompose under harsh enough electrochemical conditions. Since the possible decomposition products of $\mathbf{Co_2Ni_2P_2}$ contain Co(II), a known WOC pre-catalyst, it is important to establish the hydrolytic and thermodynamic stability of $\mathbf{Co_2Ni_2P_2}$ under relevant conditions to confirm the identity of the true active species in the observed water oxidation.

A quick discussion of the speciation of Co(II) at pH 8 in borate and phosphate buffers is necessary here. By convention, Co(II) in aqueous solution is denoted as "Co^{2+}(aq)" or "$[Co(H_2O)_6]^{2+}$." However, borate and phosphate buffers were used to control pH in the catalysis and stability studies described here. Their presence replace some of aqua ligands bound to divalent cobalt, thus writing "$[Co(H_2O)_6]^{2+}$" in the buffered solution studies is somewhat misleading. Consequently, divalent cobalt is often referred to as "Co(II)" for these studies which encompasses the different hydrolysis and association species of cobalt. The Co(II)-buffer association equilibria are discussed and, where possible, quantified.[56] [57] In water, $[Co(H_2O)_6]^{2+}$ is in a pH-dependent equilibrium with $[Co(OH)]^+$ and $Co(OH)_2$, $pK_1 = 9.65$ and $pK_2 = 9.15$.[56] At pH 8.0, aqueous cobalt is the dominant species, whereas the molar fraction of $Co(OH)_2$ is only 0.0013.

In borate buffer at pH 8.0, the dominant borate species is $B(OH)_3$, which weakly binds aqueous Co(II). At pH 9.0, the concentration of $B(OH)_4^-$ increases, and the molar fraction of $Co[B(OH)_4]_n^{(n-2)-}$ may reach a low but significant level.

The extremely low solubility of $Co_3(PO_4)_2$, $K_{sp} = [Co^{2+}{}_{aq}]^3[PO_4^{3-}]^2 = 2x10^{-35}$, raises the question whether the solution of Co(II) in phosphate buffer remains strictly homogeneous. At pH 8.0, the upper bound concentration of Co^{2+}(aq) in 0.1 M sodium phosphate buffer would be only 0.01 µM. However, the formation constant of $Co(HPO_4)$ is $\log_{10}(K_c) = 2.21$,[57] which significantly decreases the concentration of Co^{2+}(aq) and makes $Co(HPO_4)$ the dominant species, to about 90-93%, in 0.1 M sodium phosphate buffer at pH 8.0.

Keeping these factors in mind, we proceed to address the stability of the **$Co_2Ni_2P_2$** with regard to its possible decomposition into, or simply leaching of, fully solvated Co(II). A suite of techniques have been previously developed to analyze the stability of $\mathbf{Co_4P_2}$ that can be translated to a similar analysis of $\mathbf{Co_2Ni_2P_2}$.[51]

The $\mathbf{Co_2Ni_2P_2}$ polyanion can be extracted by tetra-*n*-heptylammonium (THpA)NO_3 from the aqeous solution into toluene. The aqueous cobalt remains in the aqueous layer. The aqueous layer can then be evaluated by cathodic adsorptive stripping voltammetry to quantify the amount of Co^{2+}(aq) from POM decomposition. Doing so, we are able to evaluate the long-term hydrolytic stability of $\mathbf{Co_2Ni_2P_2}$. The concentration of Co^{2+}(aq) in sodium borate buffer (100 mM, pH = 8.0) 1and sodium phosphate buffer (100 mM, pH = 8.0) was 5% and 10%. These concentrations are far too low to account for the observed catalytic activity of $\mathbf{Co_2Ni_2P_2}$.[50-51]

Another methodology was recently developed to quantify the amount of Co(II) in a phosphate buffer solution at micromolar concentrations in the presence of $\mathbf{Co_2Ni_2P_2}$. Utilizing a ^{31}P NMR line broadening analysis, we were able to determine the concentration of leached Co(II) present in aged $\mathbf{Co_2Ni_2P_2}$ solutions. Using procedures described in the experimental section, we found that the decomposition of 5 μM $\mathbf{Co_2Ni_2P_2}$ to Co^{2+}(aq) after 1 h in 0.1 M sodium phosphate at pH 8.0 did not exceed 14%.[53,58]

We further assessed the stability of $\mathbf{Co_2Ni_2P_2}$ by measuring the dependence of catalytic activity on the storage time of $\mathbf{Co_2Ni_2P_2}$ in stock solution in 160 mM sodium borate buffer at pH 8.0 by stopped flow kinetics analysis (Figure 2.9). The catalyst, $\mathbf{Co_2Ni_2P_2}$, was kept a desired time in a stock solution, then freshly prepared $Ru(bpy)_3^{3+}$ was used in each measurement. After 1 hour of storage, the activity of $\mathbf{Co_2Ni_2P_2}$ did not change drastically. With perhaps ~5% decomposition, which is in line with the previous measurements. This again suggesting the relative hydrolytic stability of $\mathbf{Co_2Ni_2P_2}$ in borate buffer at pH 8.0.

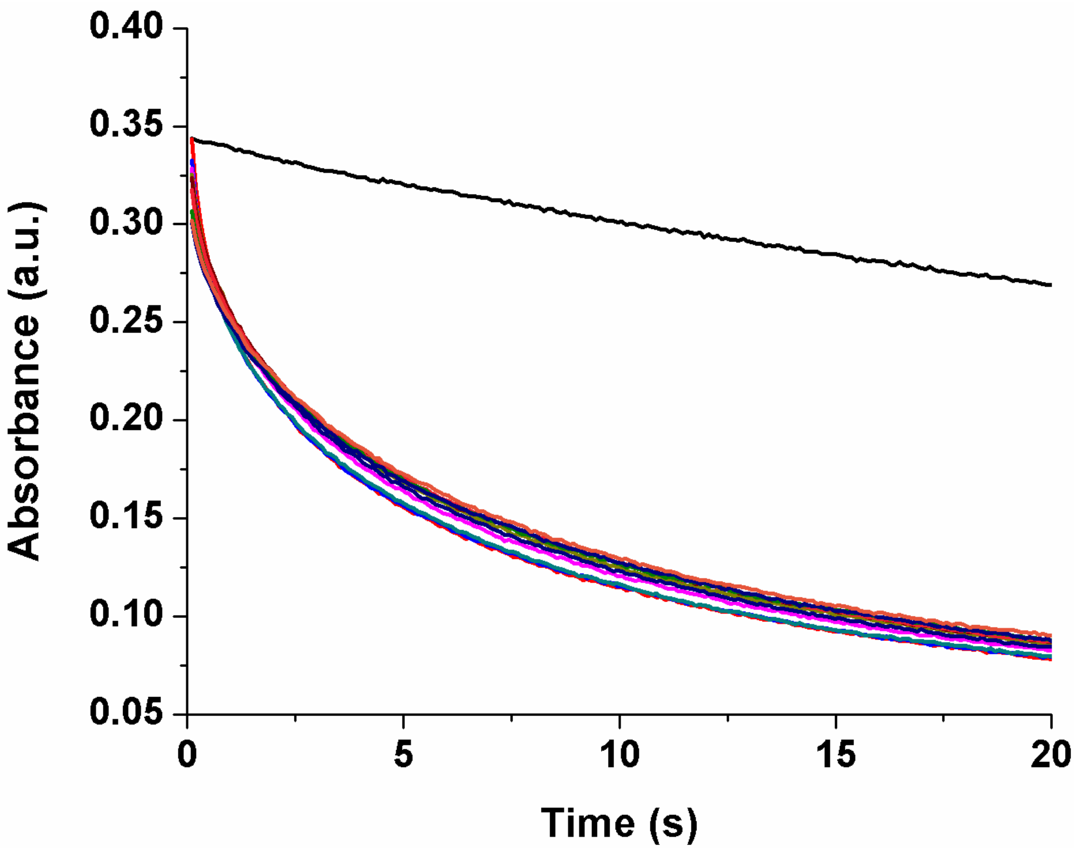

Figure 2.9 $\mathbf{Co_2Ni_2P_2}$ catalyst stability probed by stopped-flow kinetics of $Ru(bpy)_3^{3+}$ reduction. No catalyst (black curve); other curves are recorded over the course of an hour. Conditions: 0.8 mM $[Ru(bpy)_3]^{3+}$, 10 µM of $\mathbf{Co_2Ni_2P_2}$, 80 mM sodium borate buffer at pH 8.0, 298 K.

The addition of bipyridine to the solution of Co^{2+}(aq) results in the formation of mono, bis, and tris-bpy complexes of Co(II) with $\log_{10}(\beta_i)$ values of 5.65, 11.25, and 16.05.[59] In a solution of 1.0 µM of Co^{2+} and 9.0 µM of bipyridine, the concentration of free Co^{2+} is lower than 0.02 µM. The addition of small amounts of bipyridine to the Co^{2+}-catalyzed water oxidation using $[Ru(bpy)_3]^{3+}$ as an oxidant completely shuts down the OER. However, when 9.0 µM of bpy is added to the reaction catalyzed by 1.0 µM of $\mathbf{Co_2Ni_2P_2}$, a decrease in $[Ru(bpy)_3]^{3+}$ consumption correlating to a decrease in catalytic performance is observed (Figure 2.5). However, the remaining catalytic activity is still far larger than would be expected if all $\mathbf{Co_2Ni_2P_2}$ decomposes to Co(II). This confirms that Co^{2+}(aq) cannot be the true catalyst in the $\mathbf{Co_2Ni_2P_2}$ solution. The function of bipyridine as a chelating agent for Co^{2+} implies that it is capable of destabilizing the POM framework. In other words, it should be capable of binding and removing Co(II) as it does in the case of $[Co_4(VW_9O_{34})_2]^{10-}$.[53] It is also possible that the bipyridine simply deactivates $\mathbf{Co_2Ni_2P}$ as an OER catalyst simply by competitively binding to the active Co sites and not extracting the externally positioned Co(II). However, given the previously observed behavior of $[Co_4(VW_9O_{34})_2]^{10-}$ and $\mathbf{Co_4P_2}$, we deem this unlikely. In contrast, the OER activity of $\mathbf{Co_4P_2}$ does not appreciably decrease with the addition of bipyridine.[51] This implies that the cobalt atoms located at the external belt positions in $\mathbf{Co_2Ni_2P_2}$ is more labile than those in $\mathbf{Co_4P_2}$. This is consistent with all other measurements described previously. This effect likely stems from the fact that Ni(II) is more electron-withdrawing than Co(II). Thus, the substitution of the internal cobalt atoms in $\mathbf{Co_2Ni_2P_2}$ increases the μ-oxo bond distances of the two external Co, consistent with weaker bonding of the O_5 ligand sphere of the POM framework to the Co and a commensurate increase in Co lability.

Kinetic model and fitting

In order to explain the order of magnitude higher OER activity of $\mathbf{Co_2Ni_2P_2}$ compared to $\mathbf{Co_4P_2}$, we studied the kinetics of catalytic $[Ru(bpy)_3]^{3+}$ consumption in detail. First, we attempted to estimate the standard reduction potentials of these POMs. Most common electrochemical techniques do not work in this case. Neither POMs show any electroactive redox behavior prior to their water oxidation catalytic current. Accordingly, we performed potentiometric titration by $[Ru(bpy)_3]^{3+}$ (E = 1.26 V) using a stopped-flow technique and measured the $[Ru(bpy)_3]^{2+}$

concentration at 450 nm (ε = 1.42x10^4 M^{-1}cm^{-1}). The addition of 0.8-3.0 equivalents of [Ru(bpy)$_3$]$^{3+}$ to 50 µM of either **$Co_2Ni_2P_2$** or **Co_4P_2** resulted in an immediate (0 – 0.1 s) increase of absorbance at 450 nm due to the presence of [Ru(bpy)$_3$]$^{2+}$ in the injected stock solution. The absorbance grows exponentially with a rate constant of ~0.15 s^{-1}. The rate constant of [Ru(bpy)$_3$]$^{3+}$ self-decomposition is between 0.002-0.0025 s^{-1}. In order to account for the effects of [Ru(bpy)$_3$]$^{3+}$ self-decomposition, we measured the concentration of [Ru(bpy)$_3$]$^{2+}$ 2.0 seconds after mixing in the titration procedure. In the presence of 50 µM **$Co_2Ni_2P_2$**, the yield of [Ru(bpy)$_3$]$^{2+}$ formed was about 15-20% of added [Ru(bpy)$_3$]$^{3+}$ (Figure 2.10). Correspondingly, the first redox potential of **$Co_2Ni_2P_2$** accessible to the oxidant, [Ru(bpy)$_3$]$^{3+}$, must be 20-40 mV higher than the Ru(II/III) reduction potential of [Ru(bpy)$_3$]$^{3+}$ by the Nearnst equation (a more in-depth discussion involving this type of analysis can be found in Chapter 6). Similar results, within experimental error, were obtained for a titration of **Co_4P_2**.

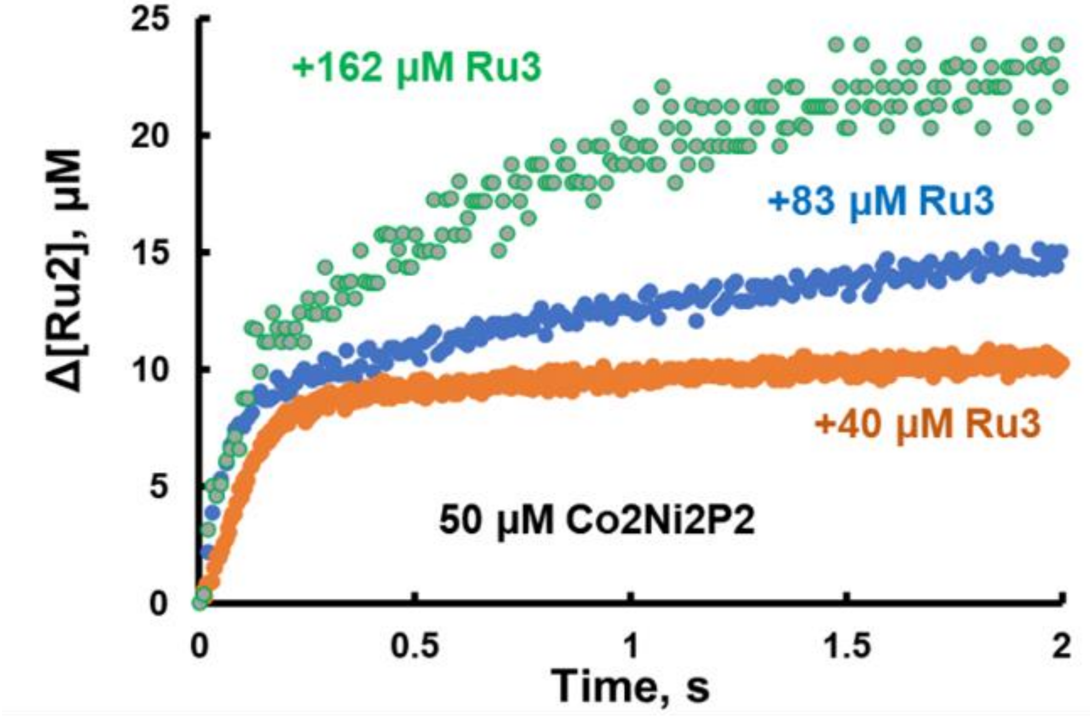

Figure 2.10 Titration of **$Co_2Ni_2P_2$** by $[Ru(bpy)_3]^{3+}$. The stock solution used for titration was a mixture of $[Ru(bpy)_3]^{3+}$ and $[Ru(bpy)_3]^{2+}$ in 6:1 ratio.

Building upon this finding, we constructed a kinetic model for the catalytic reduction of $[Ru(bpy)_3]^{3+}$. Unlike the reaction mechanism that we previously assigned to a ruthenium-based POM OER catalyst, here, we rule out a four-electron sequential oxidation as preceding the rate-determining O-O bond formation step. There are a few good reasons for this rationalization. Usually, the oxidation potentials increase with the number of removed electrons. Even with redox leveling, four sequential oxidation steps would result in either a very low first oxidation potential or a very high final oxidation potential. However, both **$Co_2Ni_2P_2$** and **Co_4P_2** already have high first Co(II/III) oxidation potentials and we empirically observe that the OER catalysis can still be driven by $[Ru(bpy)_3]^{3+}$ as an oxidant or electrochemically at low overpotential (Figures 2.7 and 2.8). Therefore, the oxidant, $[Ru(bpy)_3]^{3+}$, is unlikely to be able to remove three additional electrons sequentially from the OER catalysts, **$Co_2Ni_2P_2$** and **Co_4P_2**. Instead, we assume that two molecules of $[Ru(bpy)_3]^{3+}$ oxidize one POM to form a 2-electron-oxidized intermediate, which then reacts with water. The resulting peroxy-like species is rapidly oxidized subsequently by two $[Ru(bpy)_3]^{3+}$ to form O_2 and regenerates the initial form of the POM. This proposed mechanism is also in line with the WNA mechanism shown in Figure 1.2. The simplified kinetic model is as follows:

$$\text{POM} + [\text{Ru(bpy)}_3]^{3+} \leftrightarrows \text{POM(1)} + [\text{Ru(bpy)}_3]^{2+} \qquad K_1, \Delta G_1 \tag{2.3}$$

$$\text{POM(1)} + [\text{Ru(bpy)}_3]^{3+} \leftrightarrows \text{POM(2)} + [\text{Ru(bpy)}_3]^{2+} \qquad K_2, \Delta G_2 \tag{2.4}$$

$$\text{POM(2)} \rightarrow \text{HO-O-CoPOM} \qquad k_c \tag{2.5}$$

$$\text{HO-O-CoPOM} + 2\,[\text{Ru(bpy)}_3]^{3+} \rightarrow \text{POM} + 2\,[\text{Ru(bpy)}_3]^{2+} + O_2 \qquad \text{fast} \tag{2.6}$$

The self-decomposition of $[Ru(bpy)_3]^{3+}$ is a complex process. The decay of absorbance at 670 nm is exponential, but the yield of $[Ru(bpy)_3]^{2+}$ product is higher than 95% based on initial $[Ru(bpy)_3]^{3+}$. The self-decomposition of the bipyridine ligands on $[Ru(bpy)_3]^{3+}$ in oxidative processes has been thoroughly studied in previously. These show that the oxidatively damaged bipyridine ligand (bpy'), which is almost always more electron-rich than bipyridine itself, is ultimately oxidized to CO_2.[47] To take into account the stoichiometry of the side reaction of bipyridine self-decomposition, we add the reactions 2.7 and 2.8 to the kinetic model:

$[Ru(bpy)_3]^{3+} \rightarrow [Ru(bpy')(bpy)_2]^{2+}$ self-decomposition (2.7)

$10\ [Ru(bpy)_3]^{3+} + [Ru(bpy')(bpy)_2]^{2+} \rightarrow 10\ [Ru(bpy)_3]^{3+}$ + side products (2.8)

The experimental data were fitted using the simplified kinetic model in equations 2.3-2.8. The initial concentrations of $[Ru(bpy)_3]^{3+}$ were calculated from the 0-second absorbance at 670 nm ($\varepsilon = 420\ M^{-1}cm^{-1}$). $[Ru(bpy)_3]^{3+}$ in the stock solutions undergoes slow decomposition to produce $[Ru(bpy)_3]^{2+}$ at *ca.* 90% yield with an apparent $[Ru(bpy)_3]^{3+}$ decomposition rate constant of $2.5x10^{-3}\ s^{-1}$. The initial concentrations of $[Ru(bpy)_3]^{2+}$ was calculated using the added $[Ru(bpy)_3]^{2+}$ and the measured absorbance at 670 nm. We also took into account that the yield of oxygen per four $[Ru(bpy)_3]^{3+}$ did not exceed a theoretical maximum of 80%. To prevent convolution that could occur as a result of multivariable fitting of stochastic kinetics and ordinary differential equations, we reduced the number of variables in the fitting model to three. For the thermodynamically favorable reactions in the equilibrium shown in 2.3 and 2.4 ($k_{reverse}$ in reaction 2.3, and $k_{forward}$ in reaction 2.4), the reaction rate constants can be taken as the diffusion controlled upper limit of $1\times10^{10}\ M^{-1}s^{-1}$. Thus, only the values of K_1 in reaction 2.3 and K_2 in reaction 2.4 as well as of k_c were set as variable parameters. Furthermore, the kinetic model is found to be not very sensitive to variations in K_1 and K_2. A global minimum was found with our understanding of the initial oxidation potentials derived from titration experiments shown in Figure 2.10. Analysis of this model using COPASI affords the following values for **$Co_2Ni_2P_2$** and **Co_4P_2**, respectively: ΔG_1 = 29, 21 mV, ΔG_2 = -34, -33 mV, k_c = 1.1×10^3, 20 s^{-1}. The standard deviations of K_1 and K_2 are about 30% and less than 20% for k_c. The results of the fitting are displayed in Figure 2.11. Given the close values of ΔG_1 and ΔG_2 for **$Co_2Ni_2P_2$** and **Co_4P_2**, the main reason for the significant difference in observed catalytic activity between the two POMs is found to be the difference in the rate of reaction 2.5, which includes O-O bond formation. As such, our model is found to be consistent with a general WNA pathway in which O-O bond formation between a solvent water molecule and a Co(IV)-oxo species is the rate-determining step in this catalytic system. This is analogous to the rate-determining step proposed in other 3d-metal-oxide-based oxidations[60-61] [62]

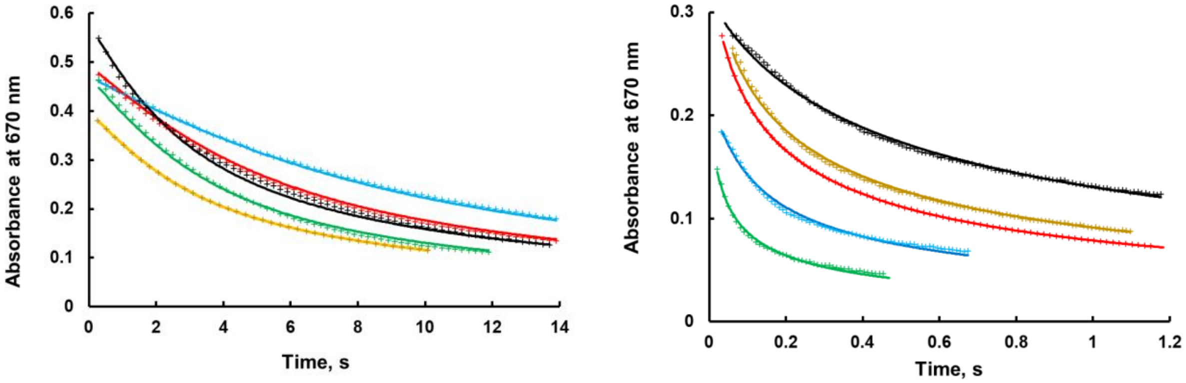

Figure 2.11 Global fitting results using the values derived from a stochastic kinetics for **Co_4P_2** (left) and **$Co_2Ni_2P_2$** (right). The detailed initial concentrations of the reactants are tabulated below.

Right Figure	$[Ru(bpy)_3]^{3+}$, mM	$[Ru(bpy)_3]^{2+}$, mM	**$Co_2Ni_2P_2$**, µM
Black	0.70	0.80	1.0
Dark yellow	0.80	0.50	2.5
Red	0.20	0.20	1.5
Blue	0.52	0.90	0.5
Green	0.46	0.015	1.5
Left Figure			**Co_4P_2**, µM
Black	1.38	0.2	5.0
Blue	1.1	0.01	1.0
Red	1.2	0.02	2.0
Green	1.15	0.01	3.0
Yellow	0.95	0.01	5.0

Theoretical considerations

To further elucidate the impact of **$Co_2Ni_2P_2$** and **Co_4P_2** electronic structures resulting from the isostructural substitution of Co by Ni, we performed quantum-chemical calculations of the thermodynamic properties of the **$Co_2Ni_2P_2$** and **Co_4P_2** intermediates most likely involved in the catalytic cycle. The details are described in the experimental section. The simplified energy diagram is presented as Figure 2.12 which shows that the OER intermediates of **$Co_2Ni_2P_2$** have lower Gibbs free energy across the board than those of **Co_4P_2**. The largest difference in ΔG comes at the peroxo (O-O) forming step. Accordingly, the higher OER catalytic activity of the newly synthesized **$Co_2Ni_2P_2$** derives primarily from the more favorable thermodynamics of **$Co_2Ni_2P_2$** compared to that of **Co_4P_2**.

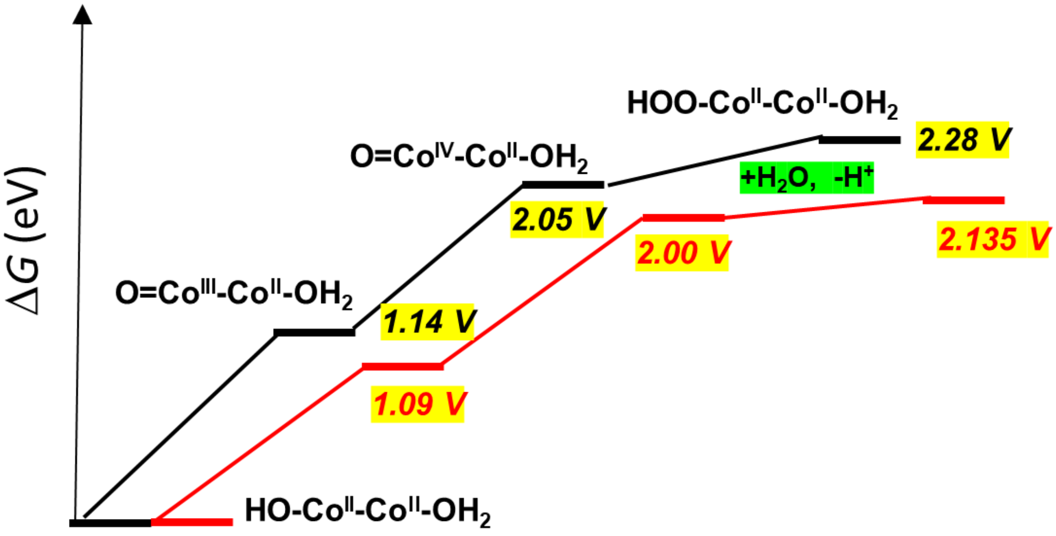

Figure 2.12 Calculated thermodynamics of the CoO-OH hydroperoxo and other intermediates that form with **Co$_2$Ni$_2$P$_2$** (red) and **Co$_4$P$_2$** (black).

One key insight from the computations is that the internal and external metal atoms in the central belt of the POM are strongly antiferromagnetically coupled through superexchange (through the bridging oxo ligands) rather than via direct exchange. This critical interaction explains, at least in part, the observed difference in reaction rates between **Co$_2$Ni$_2$P$_2$** and **Co$_4$P$_2$**. This difference in molecular orbital energy can be observed in the ground state UV-Vis spectroscopy of the two POMs (Figure 2.13). In fact, the difference in their d-d transition absorption peaks (565 nm and 600 nm, respectively), corresponds to an energy difference of 0.128 eV or 2.95 kcal/mol. This is very consistent with the calculated values as well as the kinetic rate differences observed from stopped-flow spectroscopy. Furthermore, a detailed analysis of the theoretical calculations shows very good quantitative agreement with kinetic parameters we derived from our experimental measurements. A summary of the possible reaction pathways along with the experimental and theoretical values are laid out in Figure 2.14.

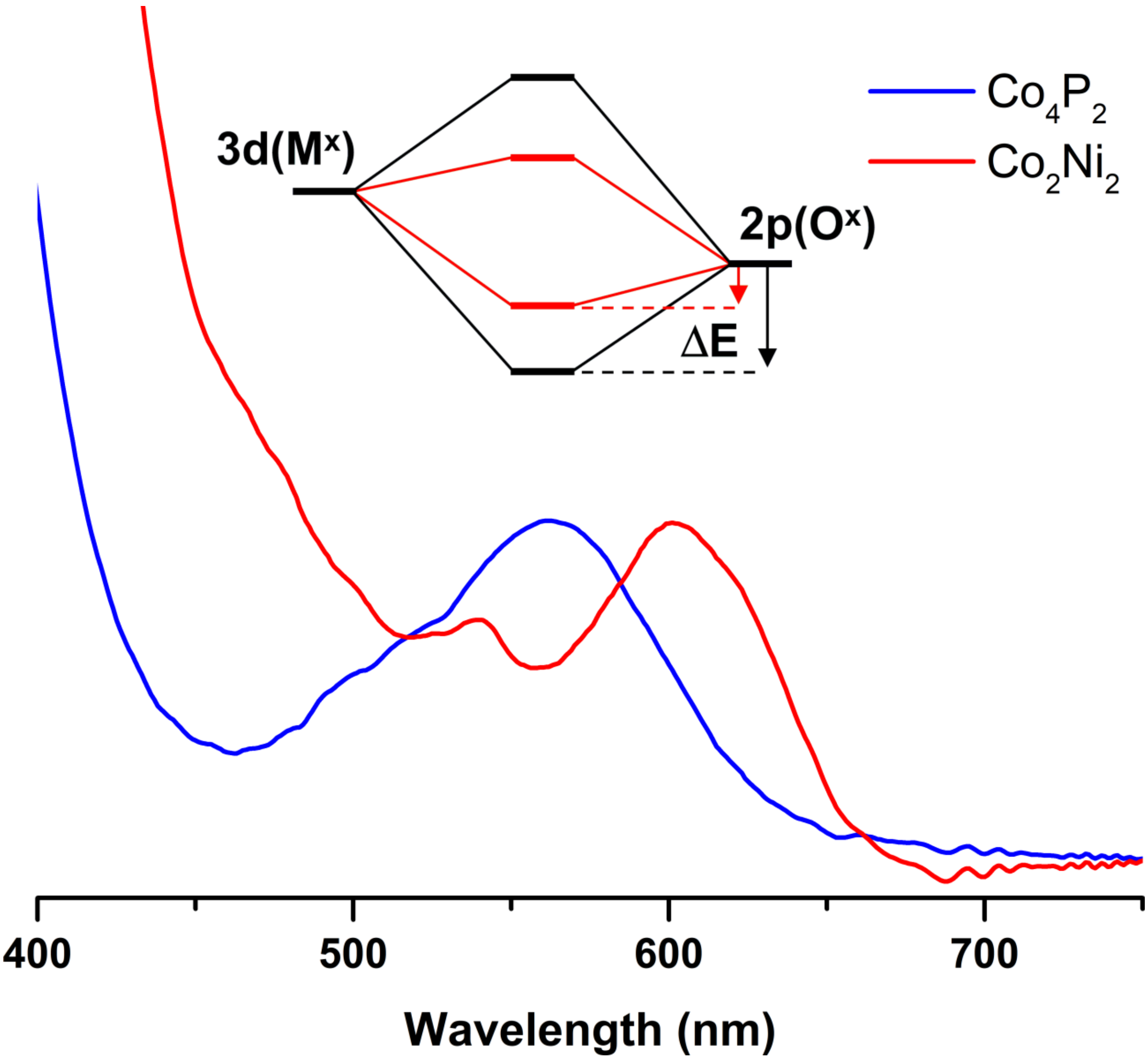

Figure 2.13 Normalized UV-vis spectra of **$Co_2Ni_2P_2$** (red) and **Co_4P_2** (blue) and the associated 3d-metal-based HOMOs and LUMOs responsible for the observed transition.

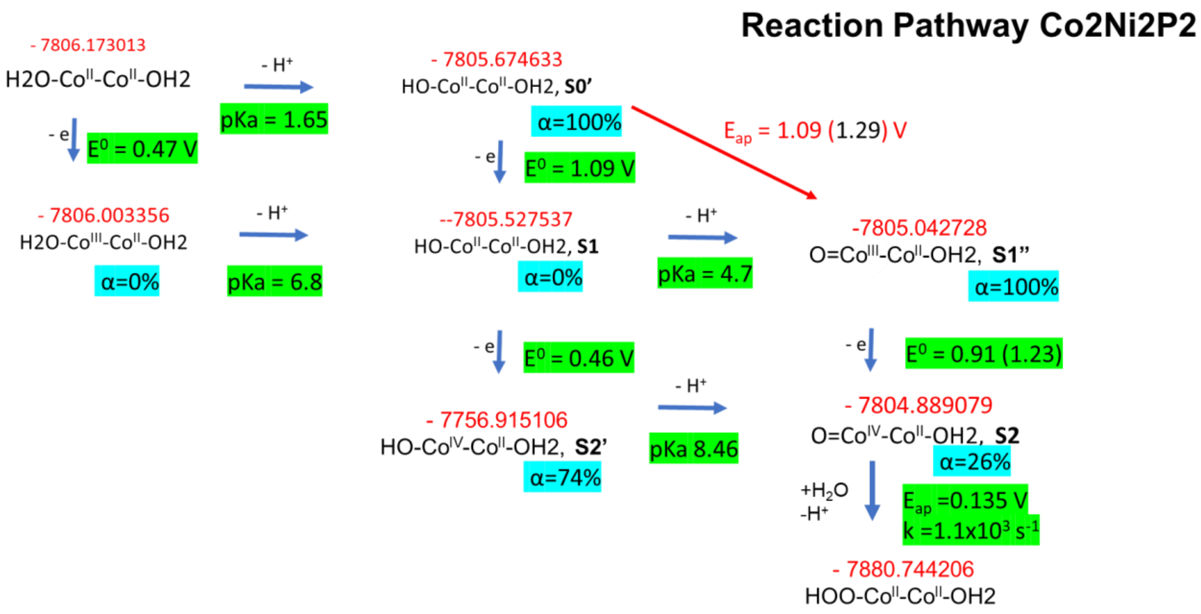

Figure 2.14 Possible reaction pathways in the oxidation of water by the Co active site at the external position of the central belt of **$Co_2Ni_2P_2$**.

Experimental

General methods and materials

All common laboratory chemicals used in synthesis were reagent grade, purchased from commercial sources, and used without further purification. All chemicals used in electrochemistry were high-purity grade, unless otherwise stated. The FT-IR spectra were measured on a Thermo Nicolet 6700 spectrometer. Elemental analyses were performed by Galbraith Lab Inc., Knoxville, TN, 37921. Thermogravimetric (TGA) data were collected on an Instrument Specialists Incorporated TGA 1000 instruments.

Synthesis of $K_8Na_4[Na_2Ni_2(PW_9O_{34})_2]$•$30H_2O$ ($Na_2Ni_2P_2$)

$Na_2WO_4 \cdot 2H_2O$ (5 g, 15.2 mmol) and Na_2HPO_4 (0.24 g, 1.7 mmol) were dissolved in 50 mL of H_2O followed by the addition of $Ni(NO_3)_2 \cdot 6H_2O$ (0.32 g, 1.1 mmol), resulting in a cloudy suspension. The pH was adjusted to 7.5 by dropwise addition of 6 M HCl, and a yellow-green solution formed. The solution was heated at 90 ^{o}C for 1 h and then was allowed to cool to room temperature. Powdered KCl (0.6 g, 8.0 mmol) was added, and the solution was allowed to evaporate for several days at room temperature generating 0.2 g of yellow-green needles (7% yield based on W).

Synthesis of $K_{10}[Co_2Ni_2(PW_9O_{34})_2]$•$28H_2O$ ($Co_2Ni_2P_2$).

$Na_2Ni_2P_2$ (0.04 g) was dissolved in 4 mL of 1 M $CoCl_2$ aqueous solution. KCl (0.08 g in 1 mL of solution) was added with stirring at 50 °C to accelerate the crystallization. Dark purple-brown crystals with two $[Co(H_2O)_6]^{2+}$ as counterions to the deca-anion, **$Co_2Ni_2P_2$**, were obtained overnight upon slow evaporation (0.028 g, 70 % yield). The two $[Co(H_2O)_6]^{2+}$ counterions were quantitatively removed by recrystallization as follows: 5 mg of the above crystals were dissolved in 4 mL of water, and 1 mL of KCl solution (0.1 g•mL^{-1}) was added with stirring at 50 °C. Single crystals suitable for X-ray crystallography were obtained overnight upon slow evaporation (yield 2.5 mg, 50%). FTIR data (cm^{-1}): 1039(s), 1012(s), 936(sh), 889(sh), 700(s). The TGA measurement indicated 30 water molecules of crystallization. Elemental analysis calculated (wt%) for **$Co_2Ni_2P_2$**: Co, 2.22; Ni, 2.21; P, 1.15; W, 62.46; Found (wt%): Co, 2.00; Ni, 2.11; P, 1.04; W, 61.70 (Table 2.1).

$Na_{10}[Co_4(H_2O)_2(PW_9O_{34})_2]\cdot 27H_2O$ (Co_4P_2)

Co_4P_2 was synthesized according to literature procedures: $Na_2WO_4\cdot 2H_2O$ (35.62 g, 108 mmol), $Na_2HPO_4\cdot 7H_2O$ (3.22 g, 12 mmol), and $Co(NO_3)_2\cdot 6H_2O$ (6.98 g, 24 mmol) were mixed in 100 mL water. The pH of this solution was then adjusted from 9 to 7. The resulting purple suspension was then refluxed for two hours. After reflux, the dark purple solution was saturated with NaCl and allowed to cool to room temperature. The subsequent purple crystals were collected, rinsed with water, and recrystallized from hot water (35% yield).

$Na_6K_4[Ni_4(H_2O)_2(PW_9O_{34})_2]\cdot 32H_2O$ (Ni_4P_2)

Ni_4P_2 was synthesized according to a modified literature procedures[63-64]: $Na_2WO_4\cdot 2H_2O$ (33 g, 100 mmol) and Na_2HPO_4 (1.57 g, 11 mmol) were dissolved in 100 mL 18.2 MΩ water, and the pH was adjusted to 7.0 using concentrated acetic acid. With vigorous stirring, a solution of $Ni(OOCCH_3)_2\cdot 4H_2O$ (5.5 g, 22 mmol) in 50 mL 18.2 MΩ water was slowly added to the previous solution. The resulting mixture was refluxed for 2.5 hours and filtered hot to remove all precipitates. $K(OOCCH_3)$ (4 g) was then added to the yellow solution and left to crystallize overnight. The resulting crystals were collected via filtration (75% yield).

Synthesis of $Ru(bpy)_3(ClO_4)_3$

$Ru(bpy)_3(ClO_4)_3$ was prepared as was described in literature.[47] Solid PbO_2 (1.5 g) was added to a solution of $[Ru(bpy)_3]Cl_2{\cdot}6H_2O$ (300 mg, 0.4 mmol) in 10 mL of 0.6 M sulfuric acid, then the resulting orange-red solution was vigorously stirred until it turned green. After removing the solid PbO_2 powder via a filter with fine porosity frit, the solution was cooled in ice-bath and then 2.2 mL of 70% (11.6 M) $HClO_4$ was slowly added. The resulting dark green precipitate was filtered through a medium-sized frit and then dried under water pump vacuum to remove most of the water. The samples were further dried under high-vacuum for 3-6 hrs and stored in a sealed glass container at 5 °C until use. Yield: ~ 200 mg.

Synthesis of tetraheptylammonium nitrate ($THpANO_3$)

$THpANO_3$ was synthesized by reacting tetra-*n*-heptylammonium bromide (THpABr) with $AgNO_3$. Typically, an aqueous solution of $AgNO_3$ (40 mg $AgNO_3$ dissolved in 10 mL of H_2O) was added to a solution of THpABr (110 mg) in toluene. The resulting mixture was shaken vigorously forming light yellow AgBr. The colorless organic layer was filtered to remove AgBr precipitate before use.

X-Ray Crystallography

Suitable crystals were selected and mounted on a loop on a Bruker APEX-IICCD diffractometer. The crystals were kept at 110(2)K during data collection. The structures were refined with the ShelXL refinement package using Least Squares minimization.

X-ray structure of $Co_2Ni_2P_2$

Further refinements using Shelx on single wavelength data provided strong evidence that the outer sites were cobalt. The refined population of atom cobalt is only 81% of the occupancy of the main component at the outer sites (with data close to the K-edges of Co) but the high resolution (30 keV) data does not discriminate between Ni and Co sites. Therefore, this is strong evidence that this site is cobalt not Ni. However, the program GSAS-II allowed us to use all the multiple wavelength data to refine the populations of cobalt and nickel atoms at these specific metal sites. The high-resolution data (30 keV) gave us an optimal structural model for the refinement of the fractions of both metals. The 30 keV atomic positions and thermal parameters were frozen and only the occupancies and scale factors were refined. The results are presented in Table 2.3.

Table 2.3. Crystal data and structure refinement for $\mathbf{Co_2Ni_2P_2}$.

Identification code	$\mathbf{Co_2Ni_2P_2}$	Formula weight	5591.76
Empirical formula	$Co_2H_{60}K_8Na_2Ni_2O_{98}P_2W_{18}$	Temperature/K	100
Crystal system	monoclinic	Space group	C2/m
a/Å	12.1762(3)	α/°	90
b/Å	21.5100(5)	β/°	104.896(3)
c/Å	16.9887(5)	γ/°	90
Crystal size/mm^3	0.418 × 0.215 × 0.033	Volume/Å^3	4299.99(19)
Radiation	MoKα (λ = 0.71073)	ρ_{calc}g/cm^3	4.319
2Θ range for data collection/°	3.788 to 67.082	F(000)	4976.0
Index ranges	$-18 \leq h \leq 18$, $-31 \leq k \leq 32$, $-25 \leq l \leq 26$	Goodness-of-fit on F^2	1.162
Reflections collected	54212	μ/mm^{-1}	25.332
Independent reflections	7915 [R_{int} = 0.0746, R_{sigma} = 0.0377]	Largest diff. peak/hole / e Å^{-3}	6.92/-5.08
Data/restraints/parameters	7915/338/333	Z	2
Final R indexes [I>=2σ (I)]	R_1 = 0.0732, wR_2 = 0.1815	Final R indexes [all data]	R_1 = 0.0802, wR_2=0.1848

Multiwavelength synchrotron X-radiation anomalous dispersion scattering (synchrotron XRAS)

We collected six data sets at the Advanced Photon Source (15-ID-B) using radiation close to the K-edges of cobalt and nickel to explicitly determine the exact nature of the metal atoms in the central belt of **$Co_2Ni_2P_2$**. Specifically, measurements were performed at and displaced at both sides of the K-edges of Co (1.608 Å, 7.71 keV) and Ni (1.488 Å, 8.33 keV). The conditions available at 15-ID-B enabled collection of extremely high-resolution, multi-wavelength, and complete data sets that are responsive to the exact composition of the Co/Ni atom sites in the crystal.

Electrochemistry

Electrochemical analyses were carried out using standard three-electrode measurements on a Pine Research Instrument WaveDriver 20 bipotentiostat and a BAS CV-50W potentiostat. All potentials were measured using glassy carbon electrodes against 1 M KCl Ag/AgCl reference electrodes (+0.235 V vs. NHE) purchased from CH Instruments. The counter electrodes were either a platinum wire or a graphite rod. Electrochemical cells were either cylindrical or conical electrochemical glassware or three-necked round-bottom flasks. All electrochemical measurements were done with the reference and working electrodes in proximity and clear from obstructions that would hinder contact with the reaction solution.

Dioxygen measurement and quantification

The catalytic activity towards water oxidation was evaluated using the techniques described earlier[48, 65] and also addressed below. The O_2 yield in water oxidation by $[Ru(bpy)_3]^{3+}$ was measured in a custom-built apparatus, that was described in detail earlier.[66] The oxygen concentration was measured by an Ocean Optics Neofox Phase Measurement System containing a calibrated FOXY-R probe with a FOXY-AFMG coating. The measurements were performed until the oxygen reading was constant for 3-5 consecutive experiments. Analysis of oxygen in the reaction headspace in the light-driven system was performed using a HP7890A model gas chromatograph (GC) equipped with thermal conductivity detector (TCD) and a 5Å molecular sieve capillary column. The kinetics and the O_2 yields in this system are strongly dependent on the stirring rate, light intensity, configuration of a light source and reactor.[51, 65] Therefore, this technique is applicable only for determining the relative catalytic activities of different complexes under strictly identical conditions.

Stopped-flow UV-Vis spectroscopy

The rapid kinetics of catalytic $[Ru(bpy)_3]^{3+}$ decay was monitored using a Hi-Tech Stopped Flow SF-61SX2 instrument equipped with a diode array spectrophotometer (400-700 nm). One of the feeding syringes was filled with a solution of $[Ru(bpy)_3](ClO_4)_3$ in water at pH 3 and the second with a freshly prepared buffer solution of the catalyst. All concentrations are given after 1:1 mixing of solutions in the feeding syringes. The consumption of $[Ru(bpy)_3]^{3+}$ was followed by a decrease in absorbance at 670 nm ($\varepsilon_{670} = 4.2 \times 10^2$ M^{-1} cm^{-1}) with optical path length $l = 10$ mm (Figure 2.15). The data were acquired and treated using KinetAsyst^{TM} 3.0 software.

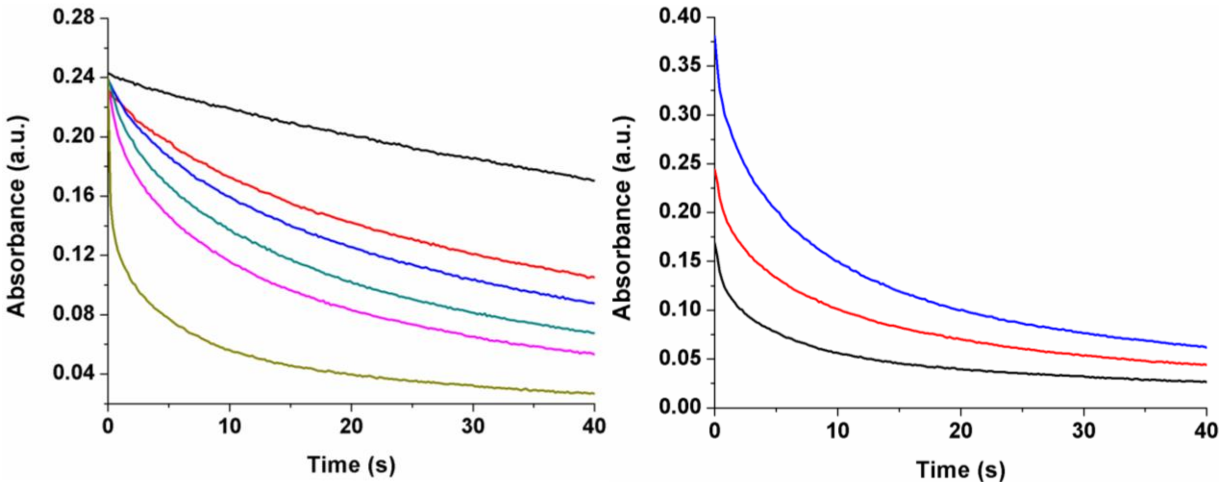

Figure 2.15 Left: effect of **$Co_2Ni_2P_2$** at different final concentrations on the consumption of $[Ru(bpy)_3]^{3+}$: 0 μM (black), 2.5 μM (red), 3.75 μM (blue), 5 μM (green) and 7.5 μM (pink), 10 μM (brown). Conditions: 0.6 mM $[Ru(bpy)_3]^{3+}$, 80 mM sodium borate buffer at pH 8.0, 298 K. Right: effect of $[Ru(bpy)_3]^{3+}$ at different concentrations: 0.4 mM (black), 0.6 mM (red), 0.8 mM (blue). **$Co_2Ni_2P_2$** was 5 μM in 80 mM sodium borate buffer at pH 8.0, 298 K.

Light-driven catalytic water oxidation

The overall light-driven catalytic water oxidation reaction is given in reaction 2.9.

$$2\ S_2O_8^{2-} + 2\ H_2O \rightarrow 4\ SO_4^{2-} + O_2 + 4\ H^+ \qquad (2.9)$$

The experiment was performed in a cylindrical cuvette (NSG, 32UV10) with a total volume of ~2.5 mL. The cell was filled with 2.0 mL of reaction solution with 1.0 mM $Ru(bpy)_3Cl_2 \cdot 6H_2O$, 5.0 mM $Na_2S_2O_8$, 0.2–6.0 μM catalyst in 80 mM sodium borate buffer and pH 9.0. The reaction cell was sealed with a rubber septum, carefully deaerated and filled with Ar. All procedures were performed with minimum exposure to ambient light. The reaction was initiated by turning on the LED-light source (λ = 455 nm; light intensity 17 mW, beam diameter ~0.4 cm). A magnetically-coupled stirring system (SYS 114, SPECTROCELL) was used to the mix reaction solutions (4×103 RPM). The O_2 concentration in the headspace was quantified by GC. The solution pH was measured after the reaction.

Analysis of dioxygen in the reaction headspace was performed using a computer-controlled Agilent 6850 model gas chromatograph equipped with a thermal conductivity detector and a HP-MOLESIEVE capillary GC column (30m × 0.535 mm × 25.00 μm); argon was the carrier gas. Typically, the O_2 yield was quantified by withdrawing a gas sample from the headspace without stopping the reaction. Contamination of the head-space with air was corrected by quantification of N_2 present in the head-space (from the N_2 peak in the GC traces).

Extraction of $Co_2Ni_2P_2$ from aqueous cobalt

After aging 0.2 mM of **$Co_2Ni_2P_2$** in 80 mM, pH 8.0 borate buffer and 80 mM, pH 8.0 phosphate buffer, 1.0 mL of a concentrated (50 mM) toluene solution of tetra-*n*-heptylammonium (THpA)NO_3 was added to the aged solution. This extracts >99% of the POM into the toluene layer.[51] The aqueous layer was evaluated by CAdSV to confirm the amount [Co(II) from POM decomposition. The concentration determined from the calibration curve (Figure 2.16), and the hydrolytic transformation of Co(II) in sodium borate buffer (100 mM, pH 8.0) and sodium phosphate buffer (100 mM, pH 8.0) was 5% and 10%, in separate reproducible experiments.

Cathodic adsorptive stripping voltammetry

Cathodic adsorptive stripping voltammetry (CAdSV) was performed with slight modifications to the literature method.[67] A bismuth film glassy carbon (GC) electrode was prepared by applying a -0.26 V potential (vs Ag/AgCl (3 M NaCl) for 45 s under stirring, and the electrolyte was 10 mL 1 M HCl solution containing 0.02 M $Bi(NO_3)_3$•$5H_2O$ and 0.5 M LiBr. The electrode was then rinsed with water and dried under a flow of air. Differential pulse voltammetry (DPV) was then performed with the following parameters: chronoamperometry at -1.3 V, for 15 s with stirring at 300 rpm. The voltammogram was then recorded from -0.7 V to -1.3 V at ν = 4mV/s without stirring, a pulse potential = 50 mV, 0.1s pulse width, 0.0167 s sampling width, 0.2 s pulse period, and 2 s quiet time. Calibration curves using $Co(NO_3)_2$•$6H_2O$ as the source of aqueous Co(II) were prepared for NaPi and borate buffers (Figure 2.16). In all cases, the peak current (i_p) was used to determine the concentration of cobalt present.

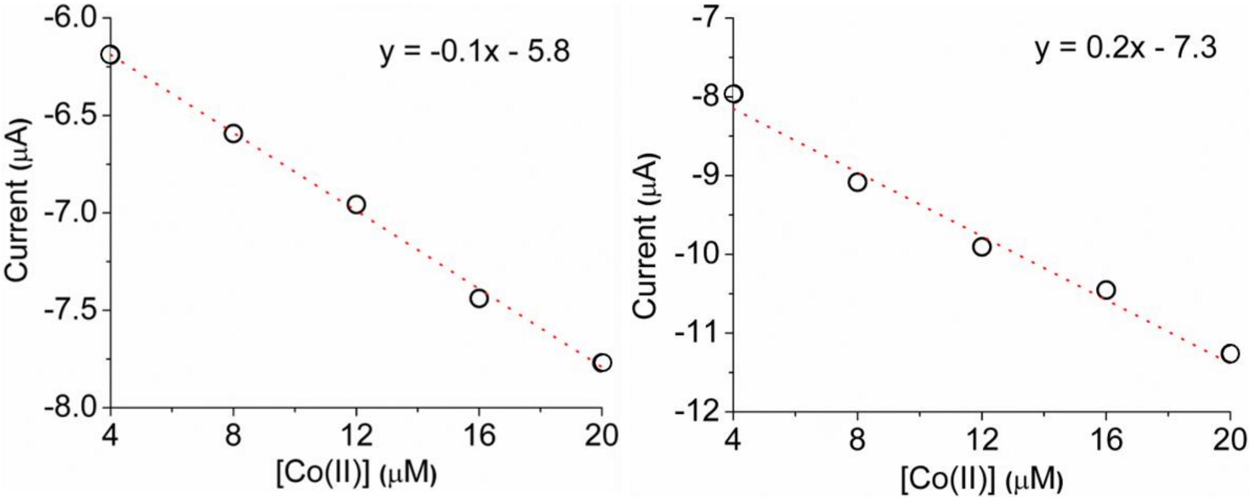

Figure 2.16 CAdSV calibration curves (left: sodium borate buffer; right, sodium phosphate buffer). Cathodic adsorptive stripping voltammetry with bismuth film glassy carbon electrode and 0.4 mM dimethyl glyoxime (DMG). Voltammogram peak current (i_p) recorded from -0.7 V to -1.3 V at $\nu = 4$ mV/s, pulse potential = 50 mV and step potential = 2 mV. With $Co(NO_3)_2$ in sodium borate buffer (100 mM).

Quantification of Co^{2+}(aq) present determined by ^{31}P NMR line broadening analysis

Co^{2+}(aq)-induced line broadening was used to determine the amount of Co(II) leached from the POM. To generate a calibration curve, standard solutions were prepared by diluting stock solutions of $Co(NO_3)_2$, $Ni(NO_3)_2$, 0.2 M sodium phosphate (sodium phosphate, pH 8.0), and 99.9% D_2O to the concentrations used in the calibration curves to yield 1.0 mL of 0.1 M sodium phosphate solution with 25% D_2O. The probe was tuned to the ^{31}P signal of the 0.1 M sodium phosphate containing no added cobalt and nickel. The full widths at half-maximum (fwhm) of the peaks were determined using a Bruker Ascend™ 600 MHz NMR with VnmrJ software and plotted against Co(II) to obtain the calibration curves and corresponding linear regressions (Figure 2.17). For the stability determination of **$Co_2Ni_2P_2$**, a 5 μL solution of **$Co_2Ni_2P_2$** in 1 mM buffer was mixed with

245 µL of water, 250 µL of D_2O, and 500 µL of the appropriate 0.2 M phosphate buffer to yield a final 1.0 mL solution containing 5 µM **$Co_2Ni_2P_2$** and 0.1 M sodium phosphate at pH 8.0 and 25% D_2O. The time, t = 0, was set upon the addition of buffer to the POM powder; typically about 10 minutes elapse between sample mixing and the first ^{31}P NMR spectrum acquisition. Spectra were then obtained approximately every 6 min for 1 h. The exact time of acquisition were variable due to delays in the autosampler. Therefore, the reported time in the NMR file log was used to determine the exact elapsed time. The [Co(II)] vs time profiles for **$Co_2Ni_2P_2$** in 0.1 M sodium borate pH 8.0 are shown in Figure 2.18.

The experiments were conducted twice to assess error (Figure 2.18). The generation of Co(II) from **$Co_2Ni_2P_2$** was 1.0×10^{-3} mM at the first measurement and *ca.* 1.4×10^{-3} mM after 1 hour, which means that after 1 hour in 100 mM sodium phosphate at pH = 8.0, about 14% of the **$Co_2Ni_2P_2$** decomposes to Co(II). This is not surprising given the speciation studies of **Co_4P_2** as a function of pH and in different buffers (including sodium phosphate) under these pH and concentration conditions.[51, 68-71] [53] The concentrations of Co(II) cease changing after 45-50 min. This is consistent with the recent study showing that Co(II) and Co-containing OER catalysts reach a hydrolytic equilibrium in the presence of buffer in a limited pH range.[53] In these experiments, if we assume that **$Co_2Ni_2P_2$** decomposition produces at most equimolar Co(II) and Ni(II) instead of just Co(II), the estimated Co(II) leaching percentage would be even lower. In conclusion, the maximal possible decomposition was ~14%.

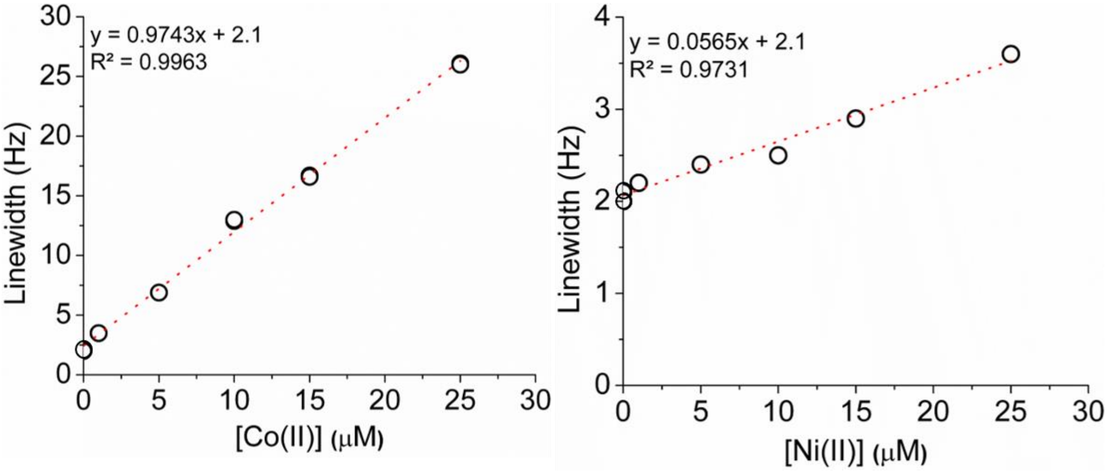

Figure 2.17 ^{31}P NMR line broadening calibration curves for pH 8.0 (100 mM of sodium phosphate).

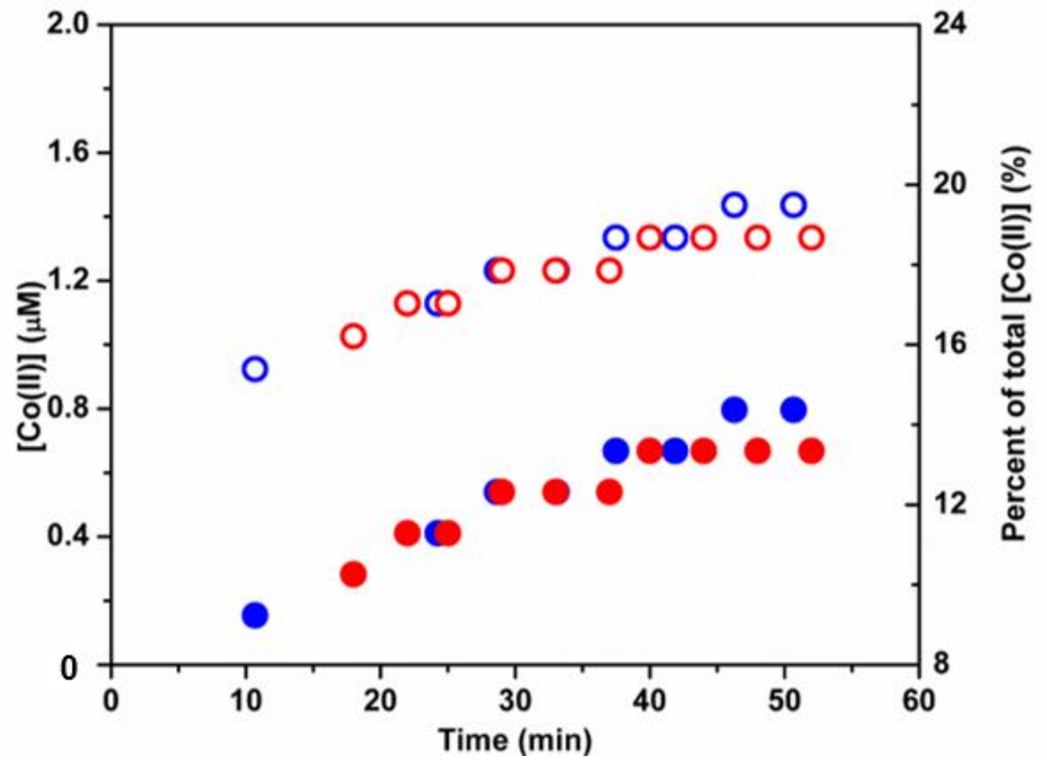

Figure 2.18 Co(II) concentration (open circles) and the percent of total Co(II) dissociated (solid circles) vs. time for **$Co_2Ni_2P_2$** determined using ^{31}P NMR line broadening analysis. The experiment was repeated; first measurement (blue), second measurement (red).

Theoretical calculations of the POM catalytic OER reaction pathways

Conversion of computed potentials in Hartrees to potentials vs SHE and pKa.

Given: Red → Ox + e^-

Abbreviations: H_r – a potential of Red in Hartrees

H_{ox} – a potential of Ox in Hartrees

H_e – a potential of hydrated electrons in Hartrees H_e = -0.104 Hartrees or -2.83 eV

The potential of SHE is based on the half reaction

1 hartree = 27.21 eV

$2\ H^+(aq) + 2\ e^- \rightarrow H_2(g)$

Its absolute electrode potential is 4.44 ± 0.02 V at 25 °C, or 2.22 eV = 0.08158 Hartrees

Thus, the oxidation potential of Ox/Red couple vs SHE is

E^0 (V vs SHE) = $-27.21 \times (H_r - H_{ox}) + (2.83 + 2.22)$

Given: $HA = A^- + H^+$

$pK_a = \log_{10}([HA]/[A^-]) + pH$, thus pK_a = pH at which $[HA] = [A^-]$

$\Delta G_1 = G(A^-) + G(H^+) – G(HA)$

Absolute $G^o(H^+)$ at $[H^+]$ = 1M is -0.4205 Hatrees

$G(H^+)$ at pH = pK_a is $[G^o(H^+) – 0.06\times pK_a]$; in addition, $G(H^+)$ should be used vs SHE

ΔG_1(in eV) = $G(A^-) + G^o(H^+) – 0.06\times pK_a – G(HA) – 0.08158 = 27.21 \times [G(A^-) – G(AH)] – 2.22 – 0.06\times pK_a$

At the same time, $\Delta G_1 = 0.06\times pK_a$, and we have

$pK_a = \{27.21 \times [G(A^-) – G(AH)] – 2.22\}/0.12$

The distribution of different protonated forms as a function of pH was calculated using Curtipot software[72]

Conclusion

Chemists have long wished for precise atomic control over chemical structures. This Chapter describes the development and the application of such control over a particular class of chemicals. Specifically, we were able to replace two inaccessible buried Co(II) centers in a catalytically active tetra-metal core. By turning $\mathbf{Co_4P_2}$ into $\mathbf{Co_2Ni_2P_2}$ while leaving all other features of this OER catalyst unaltered, we are able to gain control over the tuning of the catalytic active site via elemental doping at an atomic scale.

In doing so, we are able to purposefully perturb the electronic structure of a well-studied OER catalyst. This not only resulted in the increase in catalytic performance that we hoped for, it also opened the door to answering the question of why such a permutation results in an increase in OER activity. It raises brand new questions about the various aspects of such a perturbation: why do the outer cobalts become more labile? Is the lability related to water oxidation reactivity? How does the OER mechanism of $\mathbf{Co_2Ni_2P_2}$ differ from that of $\mathbf{Co_4P_2}$? We have at least partially answered some of these questions in this chapter.

Crucially, we were able to gain key insights into not just the reaction mechanism of the newly synthesized $\mathbf{Co_2Ni_2P_2}$ but also that of $\mathbf{Co_4P_2}$. Thus, we fulfill one of the main aims of this study. Due to the analogous properties that these two molecular metal oxides have to the large number of heterogeneous cobalt and nickel oxide electrocatalysts, the particular insights gained here should serve to inform the broader research community.

While the combination of theoretical calculations and stopped-flow experiments have unveiled many of the elementary interactions affecting the thermodynamics and kinetics of $\mathbf{Co_2Ni_2P_2}$ and $\mathbf{Co_4P_2}$, there is still much that is unclear about the intricacies of the possible reactive pathways. Going forward, direct characterization of the electronic structure that results from controlled perturbation of these kinds of touchstone complexes would be indispensable.

References

1. Blasco-Ahicart, M.; Soriano-López, J.; Carbó, J. J.; Poblet, J. M.; Galan-Mascaros, J. R., Polyoxometalate electrocatalysts based on earth-abundant metals for efficient water oxidation in acidic media. *Nature Chemistry* **2018,** *10* (1), 24-30.

2. Burke, M. S.; Kast, M. G.; Trotochaud, L.; Smith, A. M.; Boettcher, S. W., Cobalt-Iron (Oxy)hydroxide Oxygen Evolution Electrocatalysts: The Role of Structure and Composition on Activity, Stability, and Mechanism. *Journal of the American Chemical Society* **2015,** *137* (10), 3638-3648.

3. Carroll, G. M.; Zhong, D. K.; Gamelin, D. R., Mechanistic insights into solar water oxidation by cobalt-phosphate-modified α-Fe_2O_3 photoanodes. *Energy & Environmental Science* **2015,** *8* (2), 577-584.

4. Chou, N. H.; Ross, P. N.; Bell, A. T.; Tilley, T. D., Comparison of Cobalt-based Nanoparticles as Electrocatalysts for Water Oxidation. *ChemSusChem* **2011,** *4* (11), 1566-1569.

5. Deng, X.; Tüysüz, H., Cobalt-Oxide-Based Materials as Water Oxidation Catalyst: Recent Progress and Challenges. *ACS Catalysis* **2014,** *4* (10), 3701-3714.

6. Du, P. W.; Eisenberg, R., Catalysts made of earth-abundant elements (Co, Ni, Fe) for water splitting: Recent progress and future challenges. *Energy & Environmental Science* **2012,** *5* (3), 6012-6021.

7. Enman, L. J.; Stevens, M. B.; Dahan, M. H.; Nellist, M. R.; Toroker, M. C.; Boettcher, S. W., Operando X-Ray Absorption Spectroscopy Shows Iron Oxidation Is Concurrent with Oxygen Evolution in Cobalt–Iron (Oxy)hydroxide Electrocatalysts. *Angewandte Chemie International Edition* **2018,** *57* (39), 12840-12844.

8. Ertem, M. Z.; Cramer, C. J., Quantum chemical characterization of the mechanism of a supported cobalt-based water oxidation catalyst. *Dalton Transactions* **2012,** *41* (39), 12213-12219.

9. Fan, J.; Chen, Z.; Shi, H.; Zhao, G., In situ grown, self-supported iron–cobalt–nickel alloy amorphous oxide nanosheets with low overpotential toward water oxidation. *Chemical Communications* **2016,** *52* (23), 4290-4293.

10. Gerken, J. B.; Landis, E. C.; Hamers, R. J.; Stahl, S. S., Fluoride-Modulated Cobalt Catalysts for Electrochemical Oxidation of Water under Non-Alkaline Conditions. *Chemsuschem* **2010,** *3* (10), 1176-1179.

11. Gerken, J. B.; McAlpin, J. G.; Chen, J. Y. C.; Rigsby, M. L.; Casey, W. H.; Britt, R. D.; Stahl, S. S., Electrochemical Water Oxidation with Cobalt-Based Electrocatalysts from pH 0–14: The Thermodynamic Basis for Catalyst Structure, Stability, and Activity. *Journal of the American Chemical Society* **2011,** *133* (36), 14431-14442.

12. Huang, Z.; Luo, Z.; Geletii, Y. V.; Vickers, J. W.; Yin, Q.; Wu, D.; Hou, Y.; Ding, Y.; Song, J.; Musaev, D. G.; Hill, C. L.; Lian, T., Efficient Light-Driven Carbon-Free Cobalt-Based Molecular Catalyst for Water Oxidation. *Journal of the American Chemical Society* **2011,** *133* (7), 2068-2071.

13. Kanan, M. W.; Yano, J.; Surendranath, Y.; Dincă, M.; Yachandra, V. K.; Nocera, D. G., Structure and Valency of a Cobalt−Phosphate Water Oxidation Catalyst Determined by in Situ X-ray Spectroscopy. *Journal of the American Chemical Society* **2010,** *132* (39), 13692-13701.

14. Kim, H.; Park, J.; Park, I.; Jin, K.; Jerng, S. E.; Kim, S. H.; Nam, K. T.; Kang, K., Coordination tuning of cobalt phosphates towards efficient water oxidation catalyst. *Nature Communications* **2015,** *6* (1), 8253.

15. Lv, H.; Song, J.; Geletii, Y. V.; Vickers, J. W.; Sumliner, J. M.; Musaev, D. G.; Kögerler, P.; Zhuk, P. F.; Bacsa, J.; Zhu, G.; Hill, C. L., An Exceptionally Fast Homogeneous Carbon-Free Cobalt-Based Water Oxidation Catalyst. *Journal of the American Chemical Society* **2014,** *136* (26), 9268-9271.

16. Moysiadou, A.; Lee, S.; Hsu, C.-S.; Chen, H. M.; Hu, X., Mechanism of Oxygen Evolution Catalyzed by Cobalt Oxyhydroxide: Cobalt Superoxide Species as a Key Intermediate and Dioxygen Release as a Rate-Determining Step. *Journal of the American Chemical Society* **2020,** *142* (27), 11901-11914.

17. Ndambakuwa, W.; Ndambakuwa, Y.; Choi, J.; Fernando, G.; Neupane, D.; Mishra, S. R.; Perez, F.; Gupta, R. K., Nanostructured nickel-cobalt oxide and sulfide for applications in supercapacitors and green energy production using waste water. *Surf. Coat. Technol.* **2021,** *410*, 10.

18. Nguyen, A. I.; Ziegler, M. S.; Oña-Burgos, P.; Sturzbecher-Hohne, M.; Kim, W.; Bellone, D. E.; Tilley, T. D., Mechanistic Investigations of Water Oxidation by a Molecular Cobalt Oxide Analogue: Evidence for a Highly Oxidized Intermediate and Exclusive Terminal Oxo Participation. *Journal of the American Chemical Society* **2015,** *137* (40), 12865-12872.

19. Peng, Z.; Jia, D.; Al-Enizi, A. M.; Elzatahry, A. A.; Zheng, G., From Water Oxidation to Reduction: Homologous Ni–Co Based Nanowires as Complementary Water Splitting Electrocatalysts. *Adv. Energy Mater.* **2015,** *5* (9), 1402031.

20. Schilling, M.; Luber, S., Computational Modeling of Cobalt-Based Water Oxidation: Current Status and Future Challenges. *Frontiers in Chemistry* **2018,** *6* (100).

21. Smith, R. D. L.; Prévot, M. S.; Fagan, R. D.; Trudel, S.; Berlinguette, C. P., Water Oxidation Catalysis: Electrocatalytic Response to Metal Stoichiometry in Amorphous Metal

Oxide Films Containing Iron, Cobalt, and Nickel. *Journal of the American Chemical Society* **2013,** *135* (31), 11580-11586.

22. Surendranath, Y.; Dincă, M.; Nocera, D. G., Electrolyte-Dependent Electrosynthesis and Activity of Cobalt-Based Water Oxidation Catalysts. *Journal of the American Chemical Society* **2009,** *131* (7), 2615-2620.

23. Ullman, A. M.; Brodsky, C. N.; Li, N.; Zheng, S.-L.; Nocera, D. G., Probing Edge Site Reactivity of Oxidic Cobalt Water Oxidation Catalysts. *Journal of the American Chemical Society* **2016,** *138* (12), 4229-4236.

24. Wang, Y.; Yang, C.; Huang, Y.; Li, Z.; Liang, Z.; Cao, G., Nickel induced electronic structural regulation of cobalt hydroxide for enhanced water oxidation. *Journal of Materials Chemistry A* **2020,** *8* (14), 6699-6708.

25. Wee, T.-L.; Sherman, B. D.; Gust, D.; Moore, A. L.; Moore, T. A.; Liu, Y.; Scaiano, J. C., Photochemical Synthesis of a Water Oxidation Catalyst Based on Cobalt Nanostructures. *Journal of the American Chemical Society* **2011,** *133* (42), 16742-16745.

26. Xu, Y. F.; Gao, M. R.; Zheng, Y. R.; Jiang, J.; Yu, S. H., Nickel/Nickel(II) Oxide Nanoparticles Anchored onto Cobalt(IV) Diselenide Nanobelts for the Electrochemical Production of Hydrogen. *Angew. Chem.-Int. Edit.* **2013,** *52* (33), 8546-8550.

27. Young, E. R.; Nocera, D. G.; Bulović, V., Direct formation of a water oxidation catalyst from thin-film cobalt. *Energy & Environmental Science* **2010,** *3* (11), 1726-1728.

28. Zhang, M.; de Respinis, M.; Frei, H., Time-resolved observations of water oxidation intermediates on a cobalt oxide nanoparticle catalyst. *Nature Chemistry* **2014,** *6* (4), 362-367.

29. Zhu, C. Z.; Wen, D.; Leubner, S.; Oschatz, M.; Liu, W.; Holzschuh, M.; Simon, F.; Kaskel, S.; Eychmuller, A., Nickel cobalt oxide hollow nanosponges as advanced

electrocatalysts for the oxygen evolution reaction. *Chemical Communications* **2015,** *51* (37), 7851-7854.

30. Diaz-Morales, O.; Ferrus-Suspedra, D.; Koper, M. T. M., The importance of nickel oxyhydroxide deprotonation on its activity towards electrochemical water oxidation. *Chemical Science* **2016,** *7* (4), 2639-2645.

31. Feizi, H.; Bagheri, R.; Jagličić, Z.; Singh, J. P.; Chae, K. H.; Song, Z.; Najafpour, M. M., A nickel(ii) complex under water-oxidation reaction: what is the true catalyst? *Dalton Transactions* **2019,** *48* (2), 547-557.

32. González-Flores, D.; Fernández, G.; Urcuyo, R., Spectroelectrochemical Experiment for Studying Water Oxidation with a Nickel Oxide Catalyst. *Journal of Chemical Education* **2021,** *98* (2), 607-613.

33. Kalantarifard, S.; Allakhverdiev, S. I.; Najafpour, M. M., Water oxidation by a nickel complex: New challenges and an alternative mechanism. *International Journal of Hydrogen Energy* **2020,** *45* (58), 33563-33573.

34. Luo, G.-Y.; Huang, H.-H.; Wang, J.-W.; Lu, T.-B., Further Investigation of a Nickel-Based Homogeneous Water Oxidation Catalyst with Two cis Labile Sites. *ChemSusChem* **2016,** *9* (5), 485-491.

35. Menezes, P. W.; Indra, A.; Levy, O.; Kailasam, K.; Gutkin, V.; Pfrommer, J.; Driess, M., Using nickel manganese oxide catalysts for efficient water oxidation. *Chemical Communications* **2015,** *51* (24), 5005-5008.

36. Moreno-Hernandez, I. A.; MacFarland, C. A.; Read, C. G.; Papadantonakis, K. M.; Brunschwig, B. S.; Lewis, N. S., Crystalline nickel manganese antimonate as a stable water-

oxidation catalyst in aqueous 1.0 M H2SO4. *Energy & Environmental Science* **2017,** *10* (10), 2103-2108.

37. Ng, J. W. D.; García-Melchor, M.; Bajdich, M.; Chakthranont, P.; Kirk, C.; Vojvodic, A.; Jaramillo, T. F., Gold-supported cerium-doped NiOx catalysts for water oxidation. *Nature Energy* **2016,** *1* (5), 16053.

38. Singh, A.; Chang, S. L. Y.; Hocking, R. K.; Bach, U.; Spiccia, L., Highly active nickel oxide water oxidation catalysts deposited from molecular complexes. *Energy & Environmental Science* **2013,** *6* (2), 579-586.

39. Wang, D.; Ghirlanda, G.; Allen, J. P., Water Oxidation by a Nickel-Glycine Catalyst. *Journal of the American Chemical Society* **2014,** *136* (29), 10198-10201.

40. Zhang, L.-H.; Yu, F.; Shi, Y.; Li, F.; Li, H., Base-enhanced electrochemical water oxidation by a nickel complex in neutral aqueous solution. *Chemical Communications* **2019,** *55* (43), 6122-6125.

41. Zhu, G.; Glass, E. N.; Zhao, C.; Lv, H.; Vickers, J. W.; Geletii, Y. V.; Musaev, D. G.; Song, J.; Hill, C. L., A nickel containing polyoxometalate water oxidation catalyst. *Dalton Transactions* **2012,** *41* (42), 13043-13049.

42. Lauinger, S. M.; Yin, Q.; Geletii, Y. V.; Hill, C. L., Chapter Five - Polyoxometalate Multielectron Catalysts in Solar Fuel Production. In *Advances in Inorganic Chemistry*, van Eldik, R.; Cronin, L., Eds. Academic Press: 2017; Vol. 69, pp 117-154.

43. Yin, Q.; Tan, J. M.; Besson, C.; Geletii, Y. V.; Musaev, D. G.; Kuznetsov, A. E.; Luo, Z.; Hardcastle, K. I.; Hill, C. L., A Fast Soluble Carbon-Free Molecular Water Oxidation Catalyst Based on Abundant Metals. *Science* **2010,** *328* (5976), 342.

44. Hou, Y.; Xu, L.; Cichon, M. J.; Lense, S.; Hardcastle, K. I.; Hill, C. L., A New Family of Sandwich-Type Polytungstophosphates Containing Two Types of Metals in the Central Belt: $M'_2M_2(PW_9O_{34})_2^{12-}$ (M' = Na or Li, M = Mn^{2+}, Co^{2+}, Ni^{2+},and Zn^{2+}). *Inorg. Chem.* **2010,** *49*, 4125-4132.

45. Weakley, T. J. R.; Evans, H. T., Jr.; Showell, J. S.; Tourné, G. F.; Tourné, C. M., 18-Tungstotetracobalto(II)diphosphate and related Anions: a Novel Structural Class of Heteropolyanions. *J. Chem. Soc., Chem. Commun.* **1973,** *4*, 139-140.

46. Toby, B. H.; Dreele, R. B. V., GSAS-II: the genesis of a modern open-source all purpose crystallography software package *J. Appl. Crystallography* **2013,** *46* (Part 2), 544-549.

47. Ghosh, P. K.; Brunschwig, B. S.; Chou, M.; Creutz, C.; Sutin, N., Thermal and Light-Induced Reduction of $Ru(bpy)_3^{3+}$ in Aqueous Solution. *J. Am. Chem. Soc.* **1984,** *106*, 4772-4783.

48. Geletii, Y. V.; Huang, Z.; Hou, Y.; Musaev, D. G.; Lian, T.; Hill, C. L., Homogeneous Light-Driven Water Oxidation Catalyzed by a Tetraruthenium Complex with All Inorganic Ligands. *J. Am. Chem. Soc.* **2009,** *131*, 7522-7523.

49. White, H. S.; Becker, W. G.; Bard, A. J., Photochemistry of the Tris(2,2'-bipyridine)ruthenium(II)-Peroxydisulfate System in Aqueous and Mixed Acetonitrile-Water Solutions. Evidence for a Long-Lived Photoexcited Ion Pair. *J. Phys. Chem.* **1984,** *88* (9), 1840-1846.

50. Stracke, J. J.; Finke, R. G., Electrocatalytic Water Oxidation Beginning with the Cobalt Polyoxometalate $[Co_4(H_2O)_2(PW_9O_{34})_2]^{10-}$: Identification of Heterogeneous CoO_x as the Dominant Catalyst. *J. Am. Chem. Soc.* **2011,** *133*, 14872-14875.

51. Vickers, J. W.; Lv, H.; Sumliner, J. M.; Zhu, G.; Luo, Z.; Musaev, D. G.; Geletii, Y. V.; Hill, C. L., Differentiating Homogeneous and Heterogeneous Water Oxidation Catalysis:

Confirmation that $[Co_4(H_2O)_2(\alpha\text{-}PW_9O_{34})_2]^{10-}$ Is a Molecular Water Oxidation Catalyst. *J. Am. Chem. Soc.* **2013,** *135* (38), 14110-14118.

52. Lv, H.; Song, J.; Geletii, Y. V.; Vickers, J. W.; Sumliner, J. M.; Musaev, D. G.; Kögerler, P.; Zhuk, P. F.; Bacsa, J.; Zhu, G.; Hill, C. L., An Exceptionally Fast Homogeneous Carbon-free Cobalt-based Water Oxidation Catalyst. *J. Am. Chem. Soc.* **2014,** *136* (26), 9268-9271.

53. Sullivan, K. P.; Wieliczko, M.; Kim, M.; Yin, Q.; Collins-Wildman, D. L.; Mehta, A. K.; Bacsa, J.; Lu, X.; Geletii, Y. V.; Hill, C. L., Speciation and Dynamics in the $[Co_4V_2W_{18}O_{68}]^{10-}$/ $CO(II)_{aq}$ / CoC_x Catalytic Water Oxidation System. *ACS Catal.* **2018,** *8* (12), 11952-11959.

54. Blasco-Ahicart, M.; Soriano-López, J.; Carbó, J. J.; Poblet, J. M.; Galan-Mascaros, J. R., Polyoxometalate electrocatalysts based on earth-abundant metals for efficient water oxidation in acidic media. *Nat. Chem.* **2018,** *10* (1), 24-30.

55. Arens, J. T.; Blasco-Ahicarta, M.; Azmania, K.; Soriano-López, J.; García-Eguizábal, A.; Poblet, J. M.; Galan-Mascaros, J. R., Water oxidation electrocatalysis in acidic media with Co-containing polyoxometalates. *J. Catal.* **2020,** *389*, 345-351.

56. Richens, D. T., *The Chemistry of Aqua Ions: Synthesis, Structure, and Reactivity: A Tour through the Periodic Table of the Elements*. John Wiley & Sons: Chichester, 1997; p 592.

57. Abu-Shandi, K.; Al-Wedian, F., Estimation of composition, coordination model, and stability constant of some metal/phosphate complexes using spectral and potentiometric measurements. *Chem. Papers* **2009,** *63* (4), 420-425.

58. Folkman, S. J.; Kirner, J. T.; Finke, R. G., Cobalt Polyoxometalate $Co_4V_2W_{18}O_{68}^{10-}$: A Critical Investigation of Its Synthesis, Purity, and Observed ^{51}V Quadrupolar NMR. *Inorg. Chem.* **2016,** *55* (11), 5343-5355.

59. *Critical Stability Constants: First Supplement*. Springer US: New York, 1982; Vol. 5, p 604, Arthur E. Martell and Robert M. Smith, Eds.

60. Haschke, S.; Mader, M.; Schlicht, S.; Roberts, A. M.; Angeles-Boza, A. M.; Barth, J. A. C.; Bachmann, J., Direct oxygen isotope effect identifies the rate-determining step of electrocatalytic OER at an oxidic surface *Nat. Commun.* **2018,** *9* (1, Article number 4565), 1-8.

61. Dau, H.; Limberg, C.; Reier, T.; Risch, M.; Roggan, S.; Strasser, P., The Mechanism of Water Oxidation: From Electrolysis via Homogeneous to Biological Catalysis. *ChemCatChem* **2010,** *2*, 724-761.

62. Man, I. C.; Su, H.-Y.; Calle-Vallejo, F.; Hansen, H. A.; nez, J. I. M.; Inoglu, N. G.; Kitchin, J.; Jaramillo, T. F.; Nørskov, J. K.; Rossmeisl, J., Universality in Oxygen Evolution Electrocatalysis on Oxide Surfaces. *ChemCatChem* **2011,** *3*, 1159-1165.

63. Yin, Q.; Tan, J. M.; Besson, C.; Geletii, Y. V.; Musaev, D. G.; Kuznetsov, A. E.; Luo, Z.; Hardcastle, K. I.; Hill, C. L., A fast soluble carbon-free molecular water oxidation catalyst based on abundant metals. *Science* **2010,** *328*, 342-345.

64. Lv, H.; Guo, W.; Wu, K.; Chen, Z.; Bacsa, J.; Musaev, D. G.; Geletii, Y. V.; Lauinger, S. M.; Lian, T.; Hill, C. L., A Noble-Metal-Free, Tetra-nickel Polyoxotungstate Catalyst for Efficient Photocatalytic Hydrogen Evolution. *J. Am. Chem. Soc.* **2014,** *136* (40), 14015-14018.

65. Huang, Z.; Luo, Z.; Geletii, Y. V.; Vickers, J.; Yin, Q.; Wu, D.; Hou, Y.; Ding, Y.; Song, J.; Musaev, D. G.; Hill, C. L.; Lian, T., Efficient Light-Driven Carbon-Free Cobalt-Based Molecular Catalyst for Water Oxidation. *J. Am. Chem. Soc.* **2011,** *133*, 2068-2071.

66. Vickers, J. W.; Sumliner, J. M.; Lv, H.; Morris, M.; Geletii, Y. V.; Hill, C. L., Collecting meaningful early-time kinetic data in homogeneous catalytic water oxidation with a sacrificial oxidant. *Phys. Chem. Chem. Phys.* **2014,** *16* (24), 11942-11949.

67. Krolicka, A.; Bobrowski, A.; Kalcher, K.; Mocak, J.; Svancara, I.; Vytras, K., Study on Catalytic Adsorptive Stripping Voltammetry of Trace Cobalt at Bismuth Film Electrodes. *Electroanalysis* **2003,** *15* (23-24), 1859-1863.

68. Ohlin, C. A.; Harley, S. J.; McAlpin, J. G.; Hocking, R. K.; Mercado, B. Q.; Johnson, R. L.; Villa, E. M.; Fidler, M. K.; Olmstead, M. M.; Spiccia, L.; Britt, R. D.; Casey, W. H., Rates of Water Exchange for Two Cobalt(II) Heteropolyoxotungstate Compounds in Aqueous Solution. *Chem. Eur. J.* **2011,** *17*, 4408-4417.

69. Lieb, D.; Zahl, A.; Wilson, E. F.; Streb, C.; Nye, L. C.; Meyer, K.; Ivanović-Burmazović, I., Water Exchange Reactivity and Stability of Cobalt Polyoxometalates under Catalytically Relevant pH Conditions: Insight into Water Oxidation Catalysis. *Inorg. Chem.* **2011,** *50* (18), 9053-9058.

70. Stracke, J. J.; Finke, R. G., Water Oxidation Catalysis Beginning with 2.5 μM $[Co_4(H_2O)_2(PW_9O_{34})_2]^{10-}$: Investigation of the True Electrochemically Driven Catalyst at ≥600 mV Overpotential at a Glassy Carbon Electrode. *ACS Catal.* **2013,** *3* (6), 1209-1219.

71. Folkman, S. J.; Soriano-Lopez, J.; Galán-Mascarós, J. R.; Finke, R. G., Electrochemically Driven Water-Oxidation Catalysis Beginning with Six Exemplary Cobalt Polyoxometalates: Is It Molecular, Homogeneous Catalysis or Electrode-Bound, Heterogeneous CoO_x Catalysis? *J. Am. Chem. Soc* **2018,** *140*, 12040-12055.

72. Gutz, I. G. R., CurTiPot – pH and Acid–Base Titration Curves:
Analysis and Simulation freeware, version 4.3.1
http://www.iq.usp.br/gutz/Curtipot_.html

Chapter 3

Electronic Spectroscopy of the Effect of Elemental Substitution in Isostructural Polyoxometalate Water Oxidation Catalysts

This study is the result of a collaborative effort with significant experimental contributions from Michael Mara

Introduction

While material science has come a long way, and methods for surface characterization of heterogeneous materials have advanced tremendously over the years, inherent difficulties still exist regarding the probing of specific atomic moieties.[1-5] Most notably, precise atomic control, characterization, and thus in-depth mechanistic studies stll reside largely in the realm of homogeneous catalysis.[1, 3, 6-33]

In Chapter 2, **$Co_2Ni_2P_2$**, a new POM isostructural to the well-established **Co_4P_2**, was synthesized. They allow for investigating an isolated change in the electronic structure of an OER catalyst. Together, **$Co_2Ni_2P_2$** and **Co_4P_2** constitute the best discrete analogues of important heterogeneous Co-based and CoNi mixed-metal oxide film electrocatalytic active sites in terms of both function and structure. The synthesis of structurally well-defined mixed-metal **$Co_2Ni_2P_2$** allows the first X-ray absorption spectroscopy (XAS) studies to be performed on this class of OER catalysts. Characterization of the electronic and geometric changes in these two isostructural POM OER catalysts with respect to each other in both resting (reduced) and oxidized states will not only elucidate the differences of the two POM WOCs as a result of hole injection but also will allow correlations to be made regarding different redox-active metals in a multi-metal OER active site and OEC properties. No such studies have been done on metal oxide OER catalyst films, as analogous materials are difficult to synthesize and characterize.

Studying the component steps of water oxidation reactions on surfaces is nearly impossible due to the nature of bulk materials. Painstaking efforts to clarify reaction steps on materials surfaces abound.[3, 23, 25, 29, 34-37] As such, **$Co_2Ni_2P_2$** and **Co_4P_2** are touchstone tractable, molecular model compounds for such heterogeneous OER catalysis. The only difference between **$Co_2Ni_2P_2$** and **Co_4P_2** are two elemental substitutions. It would be quite useful to correlate this compositional change with any electronic change. With the goal of then correlating the electronic change to reactivity changes and decoding the mechanistic steps in their OER catalysis.

Every attempt at rational catalyst design starts with a full theoretical understanding of the fundamental scientific principles governing the relevant reaction. The issues of electron transfer, proton transfer, proton-coupled electron transfer, charge separation, and charge delocalization lie at the heart of dark and light-driven redox catalysis.[13, 38-43] XAS provides a unique opportunity to study the electronic structure of **$Co_2Ni_2P_2$** and **Co_4P_2** in detail.[44-45] A direct one-to-one comparison has never been more apt. An XAS characterization would potentially answer questions regarding the role that all of the aforementioned phenomena play in the oxidation chemistry of **$Co_2Ni_2P_2$** and **Co_4P_2**.

Results and Discussion

Ozonation of Co_4P_2 and $Co_2Ni_2P_2$

Clean oxidation of **Co_4P_2** and **$Co_2Ni_2P_2$** are difficult to achieve. Since both compounds are electrochemically silent until water oxidation currents are seen, higher-valent intermediate cobalt states are not easily accessible by electrochemistry. Few chemical oxidants have the requisite oxidation potential and stability to oxidize **Co_4P_2** and **$Co_2Ni_2P_2$**, and even fewer are available that do not significantly perturb the larger reaction. One oxidant with minimal influence on other reaction species and conditions is ozone. With an oxidation potential of 2.07,[46] it is more than capable of oxidizing **Co_4P_2** and **$Co_2Ni_2P_2$**. Furthermore, ozone is often an atom-transfer oxidant, and thus its reduction side products in an aqueous environment can be dioxygen, hydrogen peroxide, and or water.

Ozonation of **Co_4P_2** quickly yields a dark red solution. Sufficient exposure of **Co_4P_2** to ozone yields a semi-stable solution. We can characterize this ozonated solution using UV-Vis spectroscopy. More importantly, we can titrate this oxidizing solution with a reductant to determine the solution's oxidizing equivalents. Figure 3.1 shows one such titration, in which 0.5 mM **Co_4P_2** dissolved in pH 8 borate buffer is oxidized using ozone, and then reversibly titrated back to resting state using ascorbic acid as a reductant. From Figure 3.1, we see that the semi-stable solution of ozonated **Co_4P_2** gains significant transition probability and the main peak shifts to a lower wavelength. This change in the Co-based HOMO-LUMO transition is consistent with an asymmetric oxidation of Co(II) in **Co_4P_2** to Co(III). Reductive titration confirms that this semi-stable product is oxidized by at least one electron. The semi-stable nature of the ozonated product merits further consideration. From Figure 3.1, we can see that a relatively fast self-reduction occurs (~2% reduction in 5 seconds) even after about 30 seconds of delay between ozonation and UV-vis measurement. This implies that whatever oxidized intermediate we are left with, it is likely not the rate limiting species in OER catalysis. Nevertheless, electronic characterization of these higher-valent cobalt species would shed light on the oxidation chemistry of cobalt-oxo species especially with regard to water oxidation.

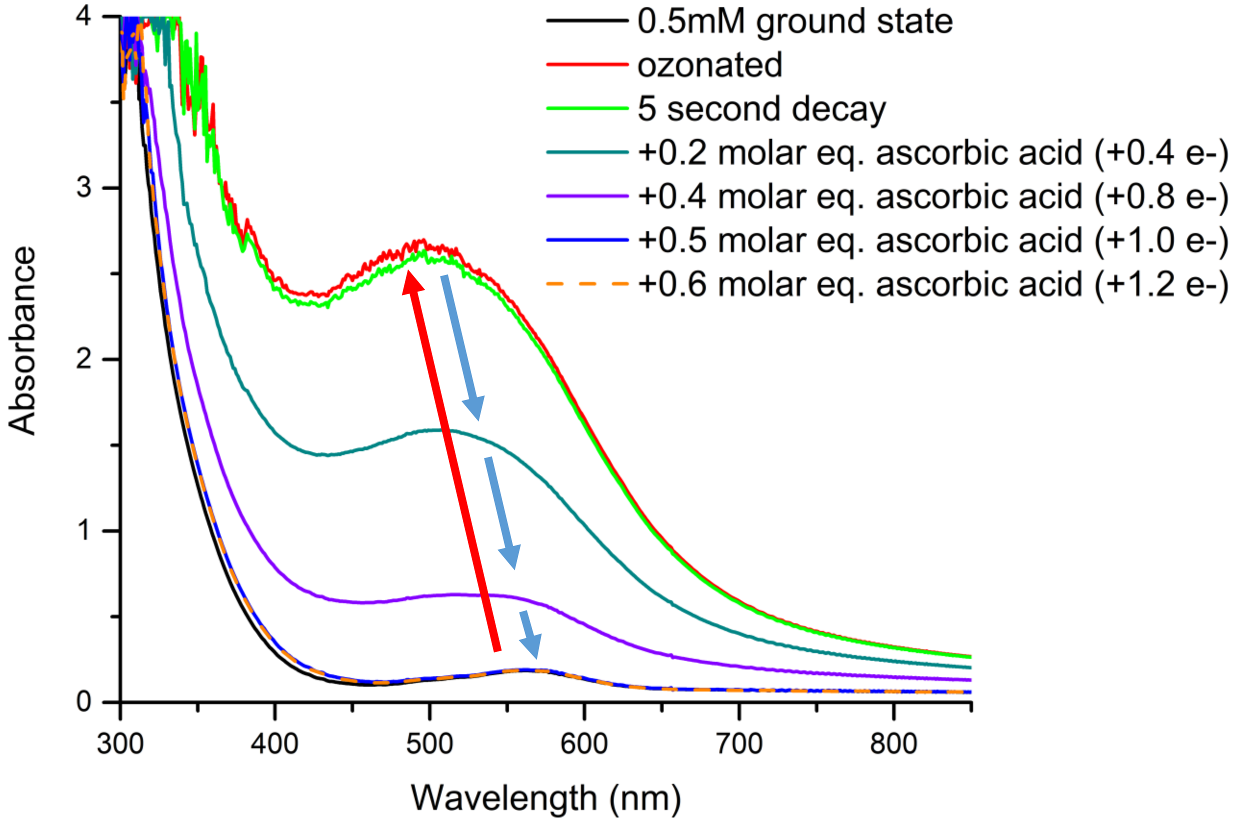

Figure 3.1 UV-Vis spectra of the reversible oxidation and reduction **Co_4P_2** by ozone and ascorbic acid.

A similar process can be conducted using our electronically perturbed **$Co_2Ni_2P_2$** instead of **Co_4P_2**. We observe very analogous behavior (Figure 3.2). A few key differences bear mentioning. Overall, the ozonated **$Co_2Ni_2P_2$** appears slightly more stable towards self-reduction n compared to **Co_4P_2**. In addition, we are very clearly able to access a two-electron oxidized semi-stable solution. However, the reductive reversibility of **$Co_2Ni_2P_2$** after ozonation appears slightly worse than that of **Co_4P_2**. Some deviations in the resting state spectra can be observed. This is not surprising and is consistent with the observed trend in the oxidative and hydrolytic stability of **Co_4P_2** and **$Co_2Ni_2P_2$** that we discussed in the previous chapter.

More interestingly, the auto-reduction may have implications on the catalytic OER mechanisms of the POMs. After ozonation, the only species present in solution are the POM, sodium borate, and water. For either of the POMs to reduce over time, they must be slowly oxidizing water. This suggests that the one-or-more-electron oxidized form of **Co_4P_2** and the two-or-more-electron oxidized form of **$Co_2Ni_2P_2$** are prone to disproportionation and are thermodynamically capable of water oxidation via this disproportionation pathway. This finding appears consistent with theoretical calculations summarized in Figure 2.12.

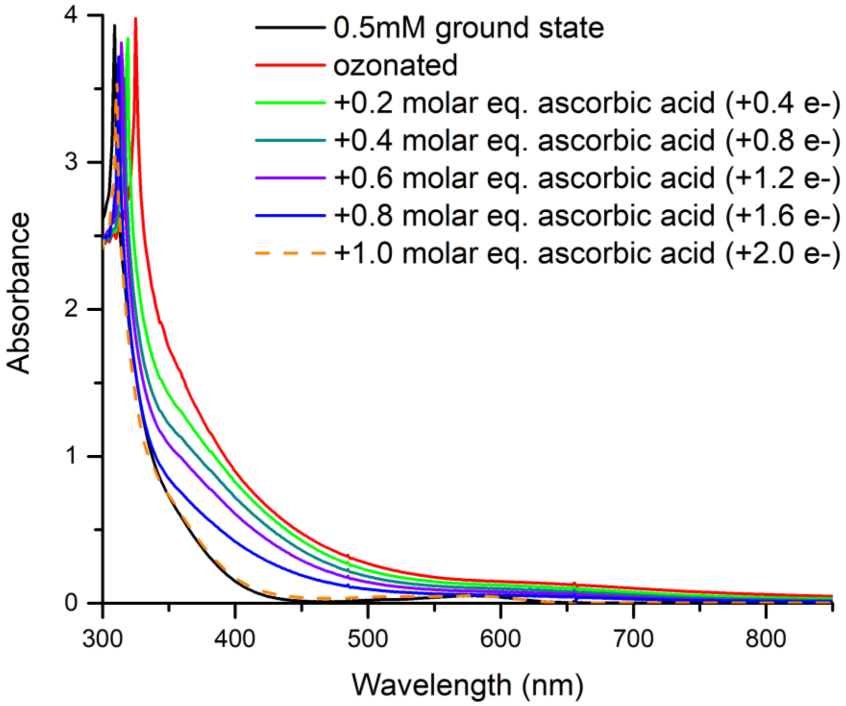

Figure 3.2 UV-Vis spectra of the reversible oxidation and reduction **$Co_2Ni_2P_2$** by ozone and ascorbic acid.

X-ray absorption spectroscopy

Long term stabilization of the ozonated/oxidized POM species can be achieved through flash freezing using liquid nitrogen. Frozen samples retain almost all oxidized absorption spectroscopy characteristics upon thawing after a week of storage. Using this technique, we set out to characterize **Co_4P_2** and **$Co_2Ni_2P_2$** using XAS. Using frozen samples of **Co_4P_2** and **$Co_2Ni_2P_2$**, we are able to characterize their resting, reduced and semi-stable, oxidized states by X-ray absorption near edge structure (XANES) and extended X-ray absorption fine structure (EXAFS).

Since XAS spectra are sums of all metal sites, we should be able to extract information on the oxidized species by subtracting out the ground-state spectra or by reconstructing from a linear combination of components. For this, it is essential to have a pertinent reference sample. We used a known Keggin POM that share structural elements with **Co_4P_2** and **$Co_2Ni_2P_2$** but is electronically much simpler: $[Co(II)SiW_{10}O_{34}]^{6-}$ (**Co(II)Si**, Figure 3.3). Moreover, this complex has a stable one electron oxidized form: $[Co(III)SiW_{10}O_{34}]^{5-}$ (**Co(III)Si**) that is also known and characterized in the literature.

Figure 3.3 Polyhedral representation of **Co(II)Si** and **Co(III)Si**. WO_6: gray; SiO_4: yellow; $CoO_5(H_2O)$: magenta.

XAS measurements at a synchrotron source provided the full range X-ray absorption spectra of **Co_4P_2**, **$Co_2Ni_2P_2$**, **Co(II)Si**, and **Co(III)Si**. K-edge XANES should readily allow us to assign oxidation states to the cobalt atoms in all four POMs (Figure 3.4). Clearly, the resting state **Co_4P_2** consists of all Co(II) sites, as the XANES edge energy and white line energy of resting state **Co_4P_2** matches up well with that of our reference POM, **Co(II)Si**. However, very little change is observed upon oxidation via ozone. Figure 3.4 shows a very minor edge shift of the oxidized **Co_4P_2** compared to resting **Co_4P_2**. A white line shift does still occur, which indicates structural changes. This unexpected result seems to suggest that the tetra-cobalt core in **Co_4P_2** is not oxidized by even one equivalent, which contradicts our UV-Vis spectroscopic titration experiments. To further confirm this finding, we must take into account the fact that **Co_4P_2** has four cobalts and that holes could be delocalized across the central belt. Subtracting the resting state of **$Co(II)_4P_2$** gives us a better quantification of the oxidation (Figure 3.5). However, even when 75% of the resting state was subtracted, we could not account for over 50% of the oxidized charge.

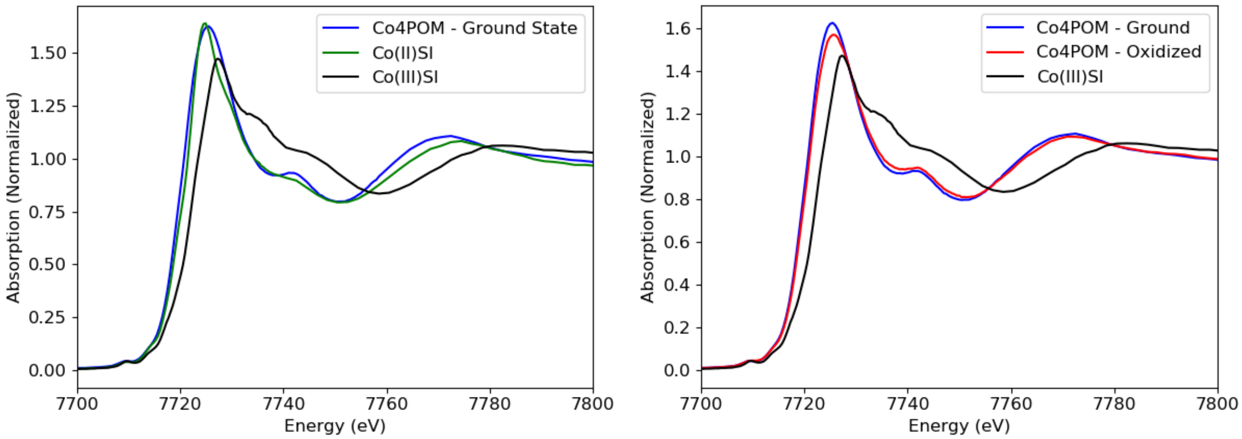

Figure 3.4 Normalized cobalt K-edge XANES of (left) resting state **Co_4P_2**, **Co(II)Si**, and **Co(III)Si**; (right) resting state **Co_4P_2**, ozonated, flash frozen **Co_4P_2**, and **Co(III)Si** at liquid nitrogen temperatures. POM concentration, 1 mM.

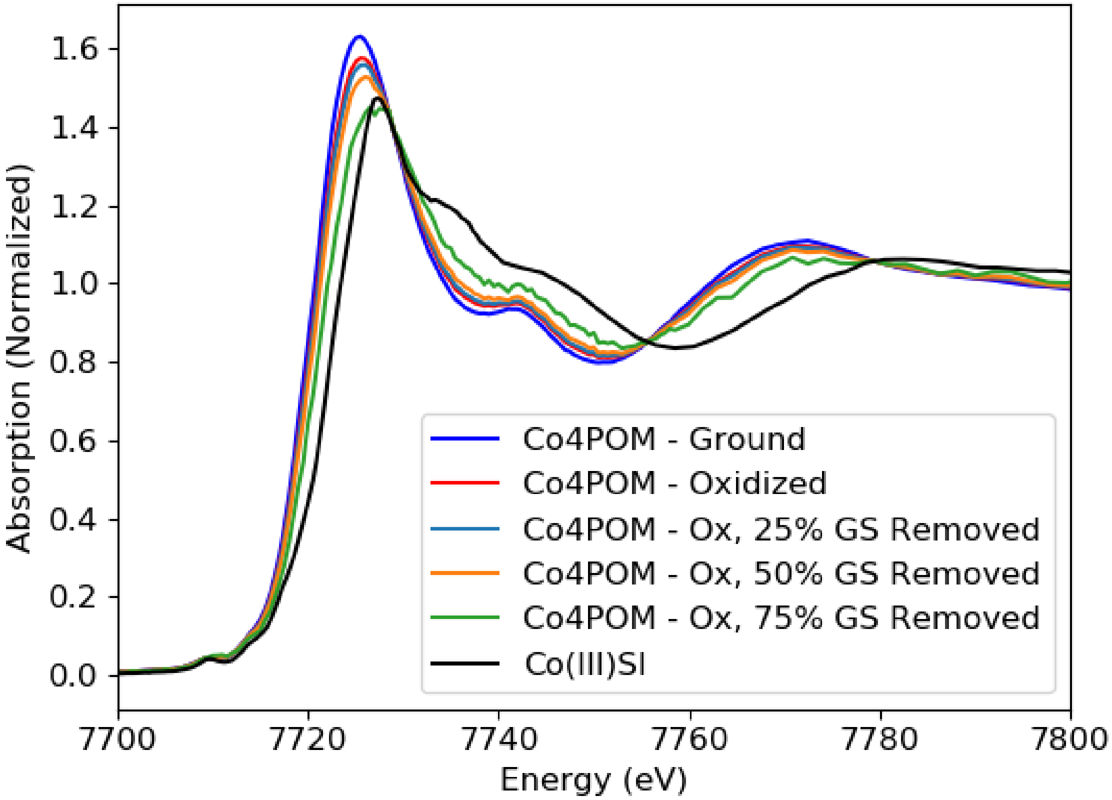

Figure 3.5 Normalized cobalt K-edge XANES of resting, reduced state corrected for the ozonated **Co_4P_2** (navy, yellow, and green) compared to the reference **Co(III)Si** K-edge XANES.

The behavior of oxidized **$Co_2Ni_2P_2$** is quite distinct from that of oxidized **Co_4P_2**. We find that the cobalt centers on the initial resting, reduced state of **$Co_2Ni_2P_2$** is, unsurprisingly, Co(II) and matches well with both **Co_4P_2** and **Co(II)Si** (Figure 3.6). However, the ozone-oxidized form of **$Co_2Ni_2P_2$** has a large shift in both edge energy and white line energy (Figure 3.7), illustrating full oxidation of both Co(II) centers to Co(III). Accompanying this is a corresponding increase in the pre-edge amplitude, another feature that's muted in the case of **Co_4P_2** (Figure 3.7). This pre-edge feature in **$Co_2Ni_2P_2$** indicates a lower symmetry at the cobalt centers. Any observed change on the external cobalt centers on **$Co_2Ni_2P_2$** is not translated to the internal nickel atoms. The XANES of Ni K-edge shows no shift (Figure 3.8). This suggests that the redox equivalents from the ozone oxidation of **$Co_2Ni_2P_2$** are localized on the cobalt centers with no delocalization of holes over the buried Ni(II) centers. This finding could mean that the presence of Ni may impede the delocalization of holes on the tetra-metal core. Considering the general mechanism of OER catalysis in Figure 1.2, one possible explanation for the higher OER activity of **$Co_2Ni_2P_2$** vs **Co_4P_2** derives from this localization of charge on the external cobalt centers in **$Co_2Ni_2P_2$**.

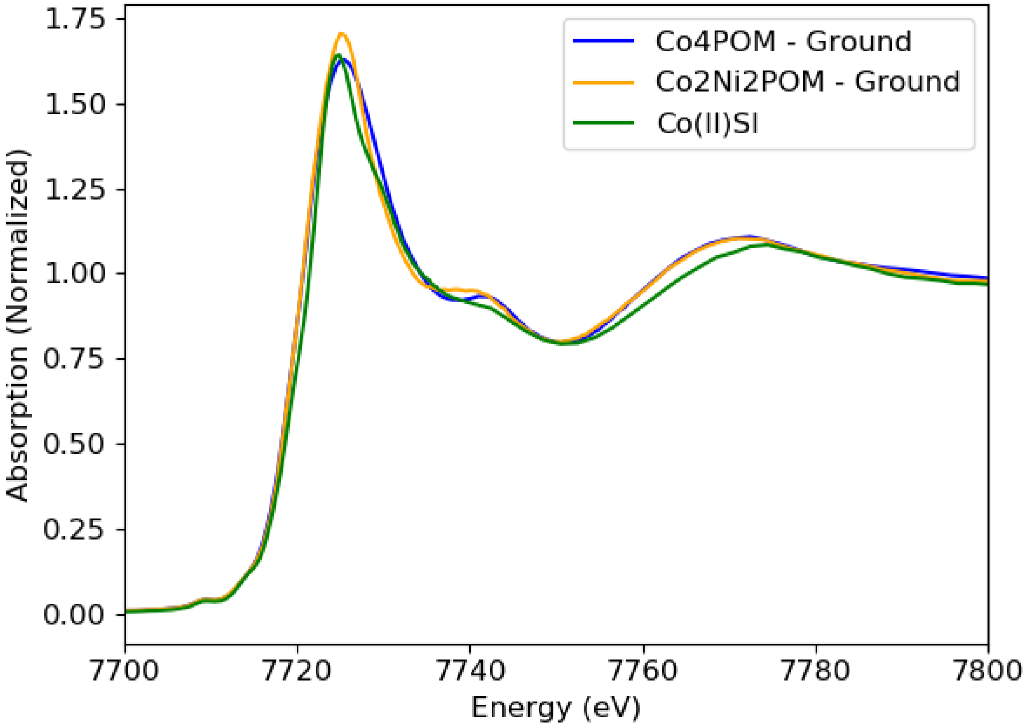

Figure 3.6 Normalized cobalt K-edge XANES of the initial resting states of **Co_4P_2**, **$Co_2Ni_2P_2$**, and **Co(II)Si** at liquid nitrogen temperatures. POM concentration = 1 mM.

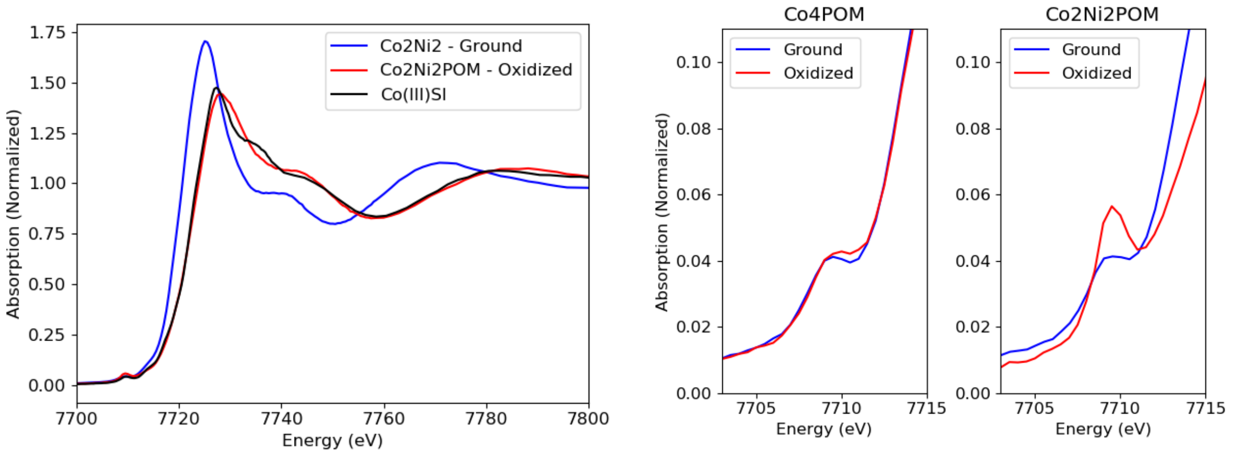

Figure 3.7 Left: Normalized cobalt K-edge XANES of the initial resting states of **$Co_2Ni_2P_2$**, ozonated **$Co_2Ni_2P_2$**, and the reference **Co(III)Si** at liquid nitrogen temperatures. POM concentration = 1 mM. Right: comparison of the change in the pre-edge features in **Co_4P_2** and **$Co_2Ni_2P_2$**.

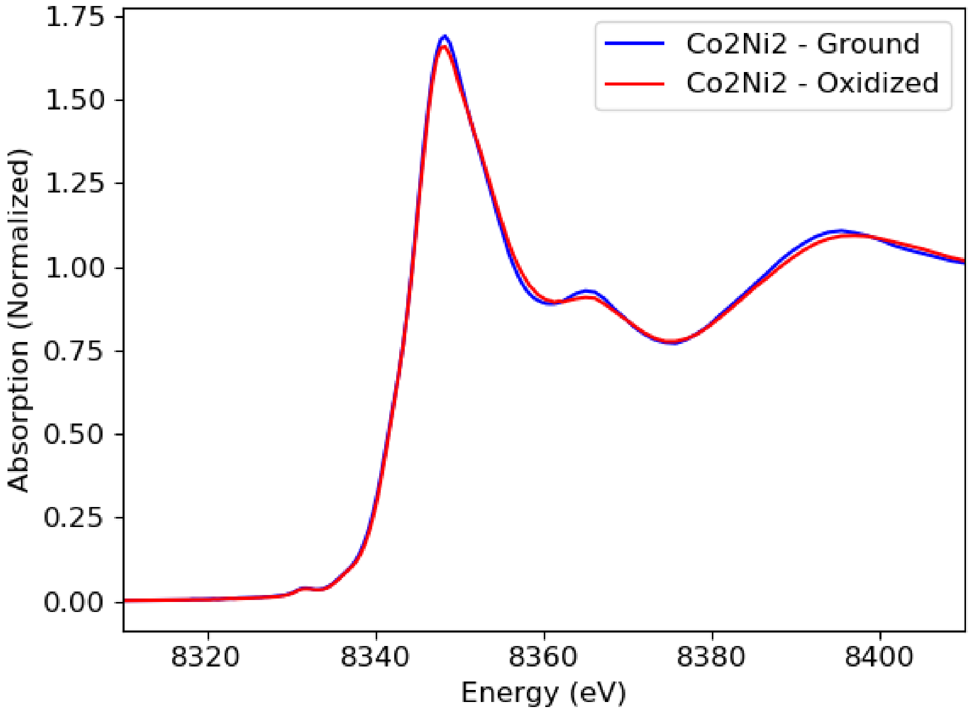

Figure 3.8 Normalized nickel K-edge XANES of the initial resting, reduced and oxidized states of **$Co_2Ni_2P_2$** and the ozonated **$Co_2Ni_2P_2$**.

Analysis of the Co EXAFS, again, shows very little difference between the resting state and the ozonated oxidation state **Co_4P_2**: contractions are observed in the first shell Co-O bonds but only very minor changes are seen at longer distances (Figure 3.9). Similarly, the Ni EXAFS of **$Co_2Ni_2P_2$** exhibits only small changes (Figure 3.10), the ozone oxidation of **$Co_2Ni_2P_2$** has very little impact on the nickel-related scattering paths (Ni-O, Ni-Ni, and Ni-Co).

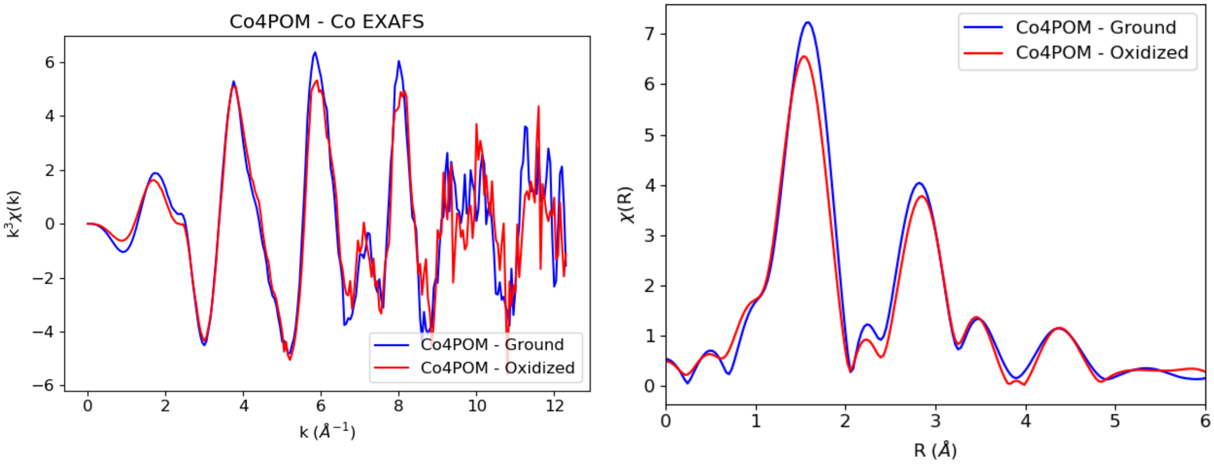

Figure 3.9 Normalized cobalt EXAFS in k-space (left) and its Fourier transformation (right) at liquid nitrogen temperatures. **Co_4P_2** concentration = 1 mM.

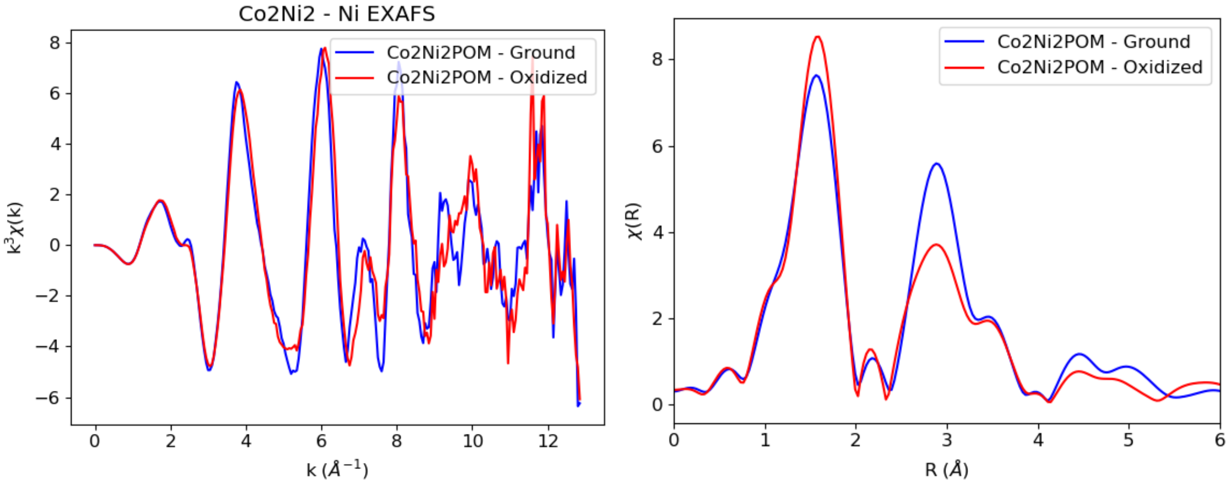

Figure 3.10 Normalized nickel EXAFS in k-space (left) and its Fourier transformation (right) at liquid nitrogen temperatures. **$Co_2Ni_2P_2$** concentration = 1 mM.

In contrast, very significant changes are observed in the Co EXAFS of **$Co_2Ni_2P_2$** (Figure 3.11). Not only are there major contractions in the Co-O bonds typical of oxidation, additional changes are very evident at higher scattering distances. In particular, a new feature appears at ~2.4Å. This feature is likely not related to Co-Ni or Co-O scattering paths as that would be require a considerable contraction of ~0.3Å in the Co-Ni scattering. It could be compatible with a peroxo species in the case of Co-O scattering. Since the formation of a peroxo on the external cobalt should essentially lead to oxygen evolution, the possibility of a semi-stable Co-OOH in a fast OER catalyst is highly unlikely. One possible scenario is dimerization whereby another cobalt atom binds to form a Co-O-Co bond. Furthermore, the large Co-O contractions we observe in Figure 3.11 may be due to the formation of Co(III)-OH leading with a spin state change whereby high-spin Co(II) becomes low-spin Co(III). Finally, we can probably characterize the observed intermediate as such: in **$Co_2Ni_2P_2$**, exposure to ozone oxidizes the aqua ligands to hydroxo ligands, leading to a major contraction of the Co-OH bond but smaller contractions in the other Co-O bonds. Specifically, a likely ~0.1Å contraction in the other 5 Co-μ-oxo bonds occur as a result of conversion to a low-spin state from high-spin state (Figure 3.12a). In **Co_4P_2**, Co-O contraction in is ~0.04-0.05Å, which may indicate a Co-OH bond at one of the cobalt centers. The structural change with change in oxidation state is much smaller than in to **$Co_2Ni_2P_2$** (Figure 3.12b). This raises a few possible explanations. It's possible that the sample is reduced from XAS measurement. This is unlikely because the reductive rate of the X-ray can be seen and is carefully controlled by moving the beam acquisition spot. Moreover, the isostructural **$Co_2Ni_2P_2$** does not have this issue and has fully localized oxidized Co(III) centers. The much more intriguing possibility is that the oxidized equivalent is actually fully delocalized over the entire **Co_4P_2** polyanion structure. This explanation would be consistent with small changes we see in the XAS and explain the OER activity differences between **Co_4P_2** and **$Co_2Ni_2P_2$**. Forced localization of charge on the external cobalts in **$Co_2Ni_2P_2$** facilitates access to higher-valent cobalt centers and associated higher rates of OER.

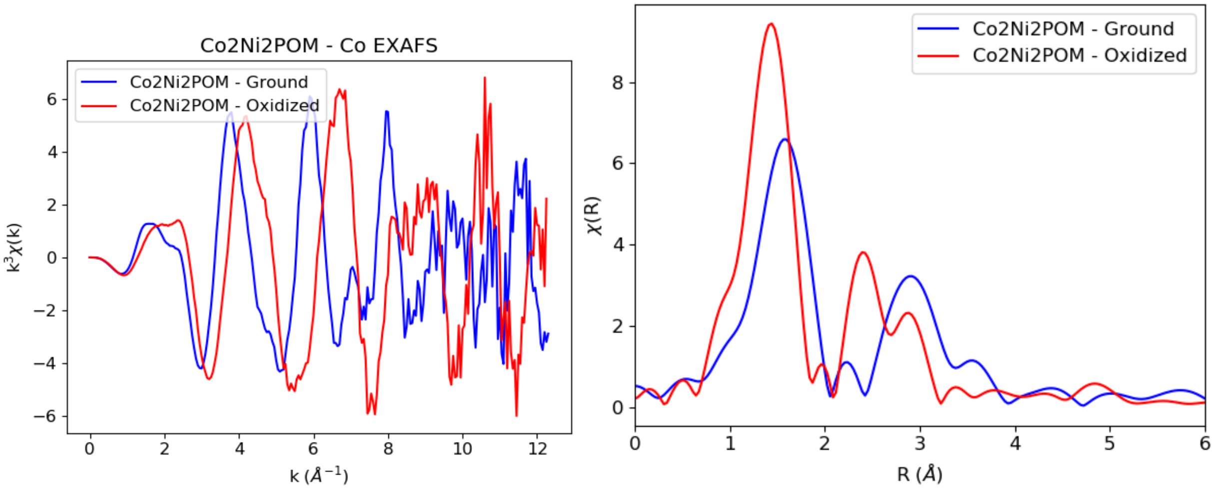

Figure 3.11 Normalized cobalt EXAFS in k-space (left) and its Fourier transformation (right) at liquid nitrogen temperatures. **$Co_2Ni_2P_2$** concentration = 1 mM.

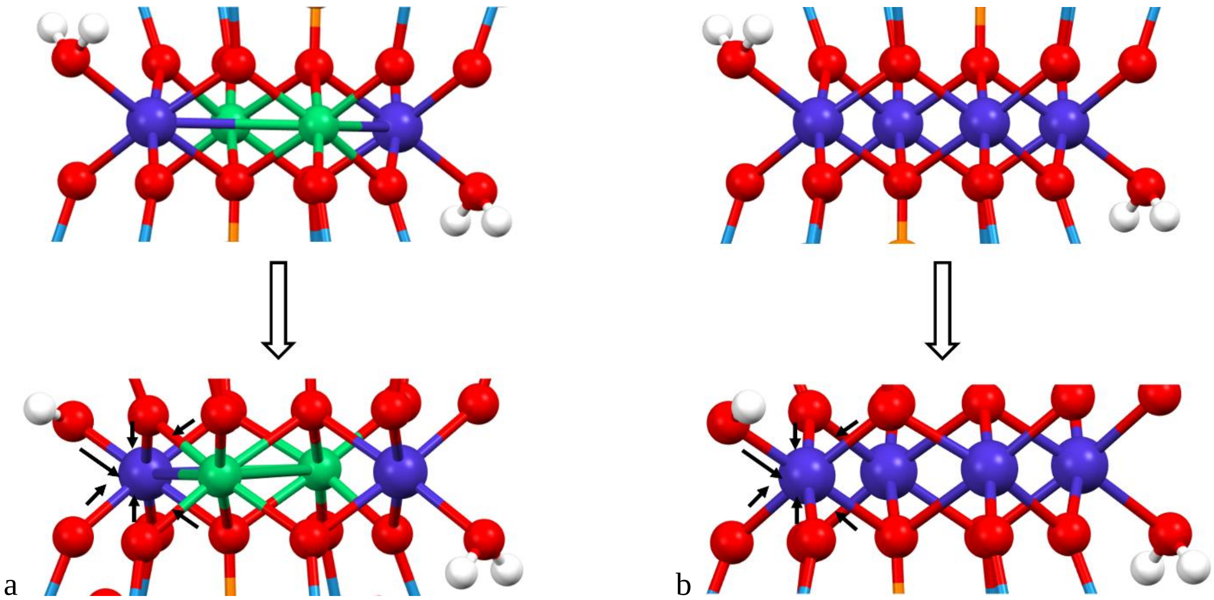

Figure 3.12 Likely structural changes that lead to the intermediates observed using XAS for (a) **$Co_2Ni_2P_2$** and (b) **Co_4P_2**.

Experimental

General methods and materials

All common laboratory chemicals used in synthesis were reagent grade, purchased from commercial sources, and used without further purification. The FT-IR spectra were measured on a Thermo Nicolet 6700 spectrometer. All solutions were prepared using Milli-Q nanopure water (18.2 MΩ.cm resistivity) unless stated otherwise.

Titration of ozonated POMs

Millimolar concentration range of solutes are ozonated in 0.1 M pH 8 sodium borate buffer. Ozone is directly extracted from the ozone generator through a glass pipette nozzle into the desired solution. Typical exposure time for a 5 mL solution of 1mM POM is 5 minutes at maximum ozone yield. Known concentrations of ascorbic acid solution are made using nitrogen-purged solvents and kept under nitrogen flow to prevent air oxidation. This stock solution is then used immediately after sample oxidation for stoichiometry titration of any ozonated samples at the UV-Vis spectrometer. All UV-Vis spectroscopy was performed with an Agilent 8453 spectrometer using a quartz cell with a 1 cm path length.

Frozen sample handling

Upon completion of ozonation procedure, the ozonated sample is immediately purged with nitrogen for ~10 seconds in order to expel excess ozone. Said sample is titrated as soon as possible. In the case of preparing samples for XAS analysis, once the UV-Vis titration results are consistent, fresh solutions are immediately processed and frozen after ozonation to allow for least amounts of auto-reduction time. After purging with nitrogen, the solutions are quickly deposited dropwise onto an optical cell constructed from Kapton polyimide tape with a PTFE washer, sealed, and flash frozen by submerging into liquid nitrogen. The frozen samples are then handled with forceps and are either directly mounted for XAS measurement or packed into a dry ice container and shipped overnight to Advanced Photon Source (APS) at Argonne National Laboratory (ANL).

Conclusion

We have performed the first XAS studies on **$Co_2Ni_2P_2$** and **Co_4P_2**, two isostructural POM OER catalysts. Despite their structural similarity, they behave very differently. **$Co_2Ni_2P_2$** is an order of magnitude faster at catalyzing water oxidation than **Co_4P_2**. Underlying this performance enhancement is a vastly different electronic structure. Chapter 2 already addressed the possiblity that **$Co_2Ni_2P_2$** and **Co_4P_2** have different reaction mechanisms in OER catalysis.

Here, it is shown that **$Co_2Ni_2P_2$** and **Co_4P_2** have drastically different oxidative chemistry. Whereas **$Co_2Ni_2P_2$** is semi-stable after being oxidized by two electron equivalents, **Co_4P_2** shows little oxidative character after exposure to ozone. The replacement of the two buried cobalt centers by nickel appears to force charge localization onto their neighboring outside cobalts, thus allowing them easier access to higher-valent states. This could potentially account for the differences in OER catalytic activity.

Perhaps more interesting is how little oxidative character is observed in the oxidized **Co_4P_2**. Both the XANES and the EXAFS show very little change from the resting $Co(II)_4$ states to the oxidized state. One possibility is very significant delocalization of the hole across the entire POM including its fully oxidized tungstate framework. While work still remains to demonstrate this possibility, the unprecedented nature of this observation makes it fascinating.

References

1. Burke, M. S.; Kast, M. G.; Trotochaud, L.; Smith, A. M.; Boettcher, S. W., Cobalt-Iron (Oxy)hydroxide Oxygen Evolution Electrocatalysts: The Role of Structure and Composition on Activity, Stability, and Mechanism. *Journal of the American Chemical Society* **2015,** *137* (10), 3638-3648.

2. Lauinger, S. M.; Piercy, B. D.; Li, W.; Yin, Q.; Collins-Wildman, D. L.; Glass, E. N.; Losego, M. D.; Wang, D.; Geletii, Y. V.; Hill, C. L., Stabilization of Polyoxometalate Water Oxidation Catalysts on Hematite by Atomic Layer Deposition. *ACS Applied Materials & Interfaces* **2017,** *9* (40), 35048-35056.

3. Yang, X. F.; Wang, A. Q.; Qiao, B. T.; Li, J.; Liu, J. Y.; Zhang, T., Single-Atom Catalysts: A New Frontier in Heterogeneous Catalysis. *Accounts Chem. Res.* **2013,** *46* (8), 1740-1748.

4. Young, E. R.; Nocera, D. G.; Bulović, V., Direct formation of a water oxidation catalyst from thin-film cobalt. *Energy & Environmental Science* **2010,** *3* (11), 1726-1728.

5. Zhang, M.; de Respinis, M.; Frei, H., Time-resolved observations of water oxidation intermediates on a cobalt oxide nanoparticle catalyst. *Nature Chemistry* **2014,** *6* (4), 362-367.

6. Barnett, S. M.; Goldberg, K. I.; Mayer, J. M., A soluble copper-bipyridine water-oxidation electrocatalyst. *Nat Chem* **2012,** *4* (6), 498-502.

7. Du, P. W.; Eisenberg, R., Catalysts made of earth-abundant elements (Co, Ni, Fe) for water splitting: Recent progress and future challenges. *Energy & Environmental Science* **2012,** *5* (3), 6012-6021.

8. Geletii, Y. V.; Besson, C.; Hou, Y.; Yin, Q.; Musaev, D. G.; Quiñonero, D.; Cao, R.; Hardcastle, K. I.; Proust, A.; Kögerler, P.; Hill, C. L., Structural, Physicochemical, and

Reactivity Properties of an All-Inorganic, Highly Active Tetraruthenium Homogeneous Catalyst for Water Oxidation. *Journal of the American Chemical Society* **2009,** *131* (47), 17360-17370.

9. Geletii, Y. V.; Yin, Q.; Hou, Y.; Huang, Z.; Ma, H.; Song, J.; Besson, C.; Luo, Z.; Cao, R.; O'Halloran, K. P.; Zhu, G.; Zhao, C.; Vickers, J. W.; Ding, Y.; Mohebbi, S.; Kuznetsov, A. E.; Musaev, D. G.; Lian, T.; Hill, C. L., Polyoxometalates in the Design of Effective and Tunable Water Oxidation Catalysts. **2011,** *51* (2), 238-246.

10. Luo, G.-Y.; Huang, H.-H.; Wang, J.-W.; Lu, T.-B., Further Investigation of a Nickel-Based Homogeneous Water Oxidation Catalyst with Two cis Labile Sites. *ChemSusChem* **2016,** *9* (5), 485-491.

11. Lv, H.; Song, J.; Geletii, Y. V.; Vickers, J. W.; Sumliner, J. M.; Musaev, D. G.; Kögerler, P.; Zhuk, P. F.; Bacsa, J.; Zhu, G.; Hill, C. L., An Exceptionally Fast Homogeneous Carbon-Free Cobalt-Based Water Oxidation Catalyst. *Journal of the American Chemical Society* **2014,** *136* (26), 9268-9271.

12. Schilling, M.; Luber, S., Computational Modeling of Cobalt-Based Water Oxidation: Current Status and Future Challenges. *Frontiers in Chemistry* **2018,** *6* (100).

13. Yang, J. H.; Wang, D. G.; Han, H. X.; Li, C., Roles of Cocatalysts in Photocatalysis and Photoelectrocatalysis. *Accounts Chem. Res.* **2013,** *46* (8), 1900-1909.

14. Yin, Q.; Tan, J. M.; Besson, C.; Geletii, Y. V.; Musaev, D. G.; Kuznetsov, A. E.; Luo, Z.; Hardcastle, K. I.; Hill, C. L., A Fast Soluble Carbon-Free Molecular Water Oxidation Catalyst Based on Abundant Metals. *Science* **2010,** *328* (5976), 342.

15. Yin, Q.; Xu, Z.; Lian, T.; Musaev, D. G.; Hill, C. L.; Geletii, Y. V., Tafel Slope Analyses for Homogeneous Catalytic Reactions. *Catalysts* **2021,** *11* (1), 87.

16. Yu, L.; Lin, J.; Zheng, M.; Chen, M.; Ding, Y., Homogeneous electrocatalytic water oxidation at neutral pH by a robust trinuclear copper(II)-substituted polyoxometalate. *Chemical Communications* **2018,** *54* (4), 354-357.

17. Bockris, J. O. M.; Otagawa, T., Mechanism of oxygen evolution on perovskites. *The Journal of Physical Chemistry* **1983,** *87* (15), 2960-2971.

18. Brunschwig, B. S.; Chou, M. H.; Creutz, C.; Ghosh, P.; Sutin, N., Mechanisms of water oxidation to oxygen: cobalt(IV) as an intermediate in the aquocobalt(II)-catalyzed reaction. *Journal of the American Chemical Society* **1983,** *105* (14), 4832-4833.

19. Carroll, G. M.; Zhong, D. K.; Gamelin, D. R., Mechanistic insights into solar water oxidation by cobalt-phosphate-modified α-Fe_2O_3 photoanodes. *Energy & Environmental Science* **2015,** *8* (2), 577-584.

20. Diaz-Morales, O.; Ferrus-Suspedra, D.; Koper, M. T. M., The importance of nickel oxyhydroxide deprotonation on its activity towards electrochemical water oxidation. *Chemical Science* **2016,** *7* (4), 2639-2645.

21. Enman, L. J.; Stevens, M. B.; Dahan, M. H.; Nellist, M. R.; Toroker, M. C.; Boettcher, S. W., Operando X-Ray Absorption Spectroscopy Shows Iron Oxidation Is Concurrent with Oxygen Evolution in Cobalt–Iron (Oxy)hydroxide Electrocatalysts. *Angewandte Chemie International Edition* **2018,** *57* (39), 12840-12844.

22. Ertem, M. Z.; Cramer, C. J., Quantum chemical characterization of the mechanism of a supported cobalt-based water oxidation catalyst. *Dalton Transactions* **2012,** *41* (39), 12213-12219.

23. Gerken, J. B.; Landis, E. C.; Hamers, R. J.; Stahl, S. S., Fluoride-Modulated Cobalt Catalysts for Electrochemical Oxidation of Water under Non-Alkaline Conditions. *Chemsuschem* **2010,** *3* (10), 1176-1179.

24. Huang, Z.-F.; Song, J.; Du, Y.; Xi, S.; Dou, S.; Nsanzimana, J. M. V.; Wang, C.; Xu, Z. J.; Wang, X., Chemical and structural origin of lattice oxygen oxidation in Co–Zn oxyhydroxide oxygen evolution electrocatalysts. *Nature Energy* **2019,** *4* (4), 329-338.

25. Kalantarifard, S.; Allakhverdiev, S. I.; Najafpour, M. M., Water oxidation by a nickel complex: New challenges and an alternative mechanism. *International Journal of Hydrogen Energy* **2020,** *45* (58), 33563-33573.

26. Kang, D.; Kim, T. W.; Kubota, S. R.; Cardiel, A. C.; Cha, H. G.; Choi, K. S., Electrochemical Synthesis of Photoelectrodes and Catalysts for Use in Solar Water Splitting. *Chemical Reviews* **2015,** *115* (23), 12839-12887.

27. Koppenol, W. H., The reduction potential of the couple O_3/O_3^-. Consequences for mechanisms of ozone toxicity. *FEBS Lett* **1982,** *140* (2), 169-72.

28. Lauinger, S. M.; Yin, Q.; Geletii, Y. V.; Hill, C. L., Chapter Five - Polyoxometalate Multielectron Catalysts in Solar Fuel Production. In *Advances in Inorganic Chemistry*, van Eldik, R.; Cronin, L., Eds. Academic Press: 2017; Vol. 69, pp 117-154.

29. Li, J.; Triana, C. A.; Wan, W.; Adiyeri Saseendran, D. P.; Zhao, Y.; Balaghi, S. E.; Heidari, S.; Patzke, G. R., Molecular and heterogeneous water oxidation catalysts: recent progress and joint perspectives. *Chemical Society Reviews* **2021,** *50* (4), 2444-2485.

30. Li, X.; Siegbahn, P. E. M., Water Oxidation Mechanism for Synthetic Co–Oxides with Small Nuclearity. *Journal of the American Chemical Society* **2013,** *135* (37), 13804-13813.

31. Li, Y.-F.; Selloni, A., Mechanism and Activity of Water Oxidation on Selected Surfaces of Pure and Fe-Doped NiOx. *ACS Catalysis* **2014,** *4* (4), 1148-1153.

32. Moysiadou, A.; Lee, S.; Hsu, C.-S.; Chen, H. M.; Hu, X., Mechanism of Oxygen Evolution Catalyzed by Cobalt Oxyhydroxide: Cobalt Superoxide Species as a Key Intermediate and Dioxygen Release as a Rate-Determining Step. *Journal of the American Chemical Society* **2020,** *142* (27), 11901-11914.

33. Suen, N.-T.; Hung, S.-F.; Quan, Q.; Zhang, N.; Xu, Y.-J.; Chen, H. M., Electrocatalysis for the oxygen evolution reaction: recent development and future perspectives. *Chemical Society Reviews* **2017,** *46* (2), 337-365.

34. DuVall, S. H.; McCreery, R. L., Self-catalysis by catechols and quinones during heterogeneous electron transfer at carbon electrodes. *Journal of the American Chemical Society* **2000,** *122* (28), 6759-6764.

35. Hansen, T. W.; Wagner, J. B.; Hansen, P. L.; Dahl, S.; Topsoe, H.; Jacobsen, C. J. H., Atomic-resolution in situ transmission electron microscopy of a promoter of a heterogeneous catalyst. *Science* **2001,** *294* (5546), 1508-1510.

36. Pegis, M. L.; Wise, C. F.; Martin, D. J.; Mayer, J. M., Oxygen Reduction by Homogeneous Molecular Catalysts and Electrocatalysts. *Chemical Reviews* **2018,** *118* (5), 2340-2391.

37. Watzky, M. A.; Finke, R. G., Transition metal nanocluster formation kinetic and mechanistic studies. A new mechanism when hydrogen is the reductant: Slow, continuous nucleation and fast autocatalytic surface growth. *Journal of the American Chemical Society* **1997,** *119* (43), 10382-10400.

38. Bakulin, A. A.; Rao, A.; Pavelyev, V. G.; van Loosdrecht, P. H. M.; Pshenichnikov, M. S.; Niedzialek, D.; Cornil, J.; Beljonne, D.; Friend, R. H., The Role of Driving Energy and Delocalized States for Charge Separation in Organic Semiconductors. *Science* **2012,** *335* (6074), 1340-1344.

39. Huang, H. W.; Tu, S. C.; Zeng, C.; Zhang, T. R.; Reshak, A. H.; Zhang, Y. H., Macroscopic Polarization Enhancement Promoting Photo- and Piezoelectric-Induced Charge Separation and Molecular Oxygen Activation. *Angew. Chem.-Int. Edit.* **2017,** *56* (39), 11860-11864.

40. Jiang, C. R.; Moniz, S. J. A.; Wang, A. Q.; Zhang, T.; Tang, J. W., Photoelectrochemical devices for solar water splitting - materials and challenges. *Chemical Society Reviews* **2017,** *46* (15), 4645-4660.

41. Niu, F. J.; Wang, D. G.; Li, F.; Liu, Y. M.; Shen, S. H.; Meyer, T. J., Hybrid Photoelectrochemical Water Splitting Systems: From Interface Design to System Assembly. *Adv. Energy Mater.* **2020,** *10* (11), 24.

42. Sivula, K.; van de Krol, R., Semiconducting materials for photoelectrochemical energy conversion. *Nature Reviews Materials* **2016,** *1* (2), 15010.

43. Wasielewski, M. R., Energy, charge, and spin transport in molecules and self-assembled nanostructures inspired by photosynthesis. *J. Org. Chem.* **2006,** *71* (14), 5051-5066.

44. Brodsky, C. N.; Hadt, R. G.; Hayes, D.; Reinhart, B. J.; Li, N.; Chen, L. X.; Nocera, D. G., In situ characterization of cofacial Co(IV) centers in Co_4O_4 cubane: Modeling the high-valent active site in oxygen-evolving catalysts. *Proceedings of the National Academy of Sciences* **2017,** *114* (15), 3855-3860.

45. Ullman, A. M.; Brodsky, C. N.; Li, N.; Zheng, S.-L.; Nocera, D. G., Probing Edge Site Reactivity of Oxidic Cobalt Water Oxidation Catalysts. *Journal of the American Chemical Society* **2016,** *138* (12), 4229-4236.

46. Haynes, W. M., Lide, D. R., & Bruno, T. J. , *CRC handbook of chemistry and physics: a ready-reference book of chemical and physical data.* . 97th ed.; CRC Press.: Boca Raton, Florida, 2016.

Chapter 4

Effects of Counter Cations on Polyoxometalates Redox Properties and Oxygen Evolution Catalysis Performance

This study is the result of a collaborative effort with significant experimental contributions from Meilin Tao and Sarah M. Lauinger, as well as significant computational contributions from Alexey Kaledin.

Introduction

In Chapter 2 and Chapter 3, we described the use of model molecular systems for OER at near-neutral pH values. This chapter takes a U-turn and proceeds in the opposite direction. This chapter deals with the immobilization of a known molecular OER catalyst in acidic conditions. For a number of reasons, the solutions used in PEC construction largely benefit from being in either acidic or basic conditions rather than neutral ones.[1-6] Acidic conditions present as an attractive PEC operating environment mainly due to efficient rates of cathodic processes and membrane concerns.[1-6] However, under acidic conditions, water oxidation becomes much more thermodynamically challenging.[6-12] Even more challenging is the fact that the metal oxides of most earth-abundant metal elements dissolve in strongly acidic conditions.[13] Thus, while a number of catalysts are operational in basic and neutral conditions, there are a limited number of good OER catalysts that function in acidic conditions.[2, 8-9, 13-42, 53]

One interesting molecular OER catalyst that has been reported to be acid stable is a POM. Specifically, it is the water solubilized polyanion $[Co_9(H_2O)_6(OH)_3(HPO_4)_2(PW_9O_{34})_3]^{16-}$ (**Co_9**).[14, 41-42] which also catalyzes OER at near neutral conditions. **Co_9** was first reported as a by-product of **Co_4P_2**. Significantly, the cesium salt of **Co_9** was reported to be an active OER catalyst in acidic conditions after it was embedded into a carbon paste electrode.[14]

While we were intrigued by the use of carbon paste as a supporting electrode structure in acid, we were more surprised in the possible conferred acid stability from a supposedly simple metathesis reaction. Furthermore, we are more interested specific counter-cation effects that can affect the electronic and geometric structure of these POM catalysts. In this chapter, we synthesize various salts of **Co_4P_2** using Y, La, Ba, Rb, and Cs, making **YCo_4P_2**, **$LaCo_4P_2$**, **$BaCo_4P_2$**, **$RbCo_4P_2$**, and **$CsCo_4P_2$**. Further, we immobilize these different materials onto anodes. They are then electrochemically characterized and their electrocatalytic OER behaviors analyzed and compared.

Results and Discussion

Synthesis and X-ray crystallography of YCo_9

The synthesis of crystalline nearly-insoluble varying cation salts of $\mathbf{Co_9}$ is difficult by virtue given their requisite nature. Being essentially insoluble in all known solvents, traditional evaporative crystallization methods are not applicable. The small solubility product constant, K_{sp}, also promotes the formation of precipitates rather than crystalline products. Fortunately, we were able to utilize diffusion to crystallize $\mathbf{YCo_9}$ which facilitated structural characterization.

Figure 4.1 shows the X-ray structure of an $\mathbf{YCo_9}$. This crystal structure clearly shows that Y^{3+} cations are more than just simple counter cations of the $\mathbf{Co_9}$ polyanion. In addition to balancing the negative charges of the $\mathbf{Co_9}$ clusters, they are connected to the $\mathbf{Co_9}$ polyanion framework by corner and edge-sharing oxygen atoms. In addition, the crystal structure of $\mathbf{YCo_9}$ shows that none of nitrate anions of the initial Y(III) nitrate synthetic precursor are present. Most of the Y^{3+} cations are 8-coordinate and form weak links to water molecules as well as the terminal tungstate oxygens. One of the Y^{3+} cations is bound to the tetrahedral phosphate cores. This P-O-Y linkage is alternatively and conventionally termed an “inner-sphere ion pair” or a “contact ion pair”. Such covalent linkages implicate significant molecular orbital interactions between the Y(III) cations and the $\mathbf{Co_9}$ POM. Perhaps most interestingly, this crystal structure demonstrates the emergence of a material bordering on a bulk mixed metal oxide, yet synthesized from molecular polyoxometalates, as the Y(III) cations datively bridging the tungstate frameworks in the unit cells.

The result of this is a insoluble material that can be readily utilized as an electrocatalyst material under acidic conditions.

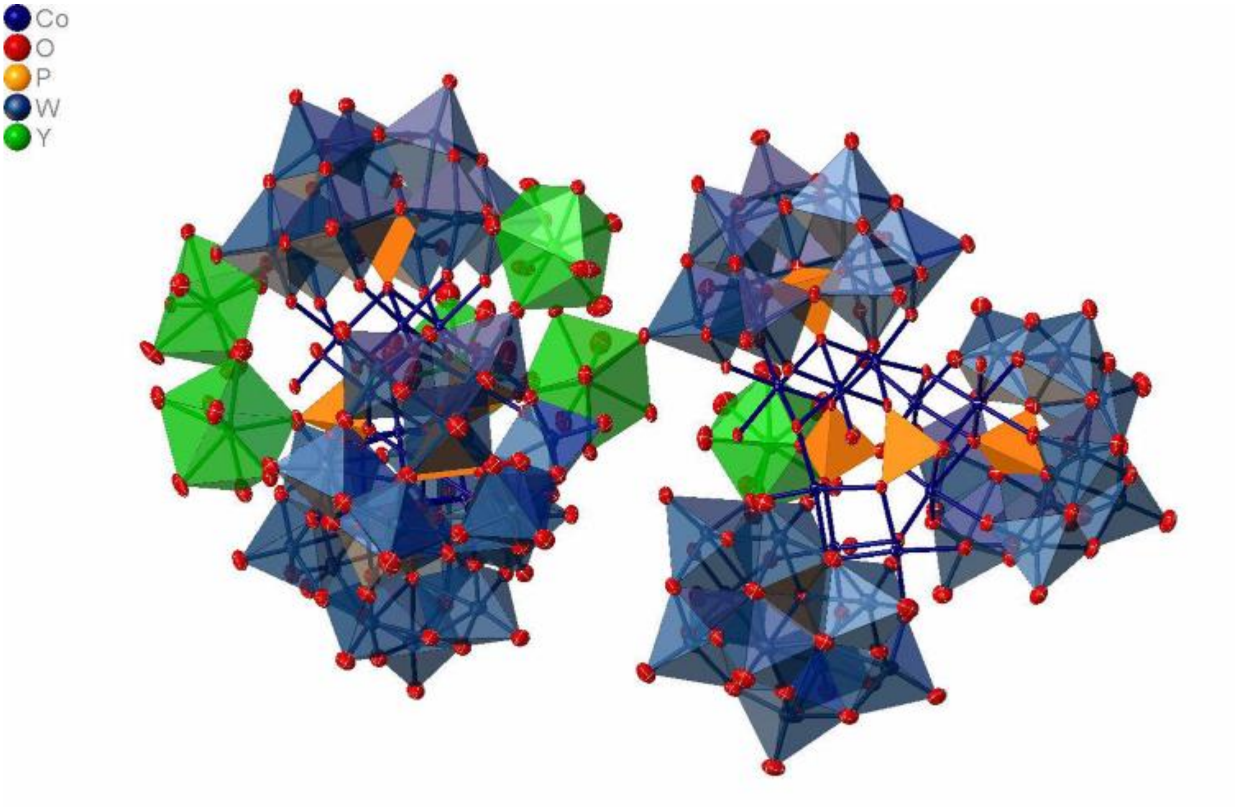

Figure 4.1 A combined polyhedral/thermal ellipsoid representation of two $Y_4K_4[Co_9(H_2O)_6(OH)_3(HPO_4)_2(PW_9O_{34})_3]$ **(YCo9)** clusters from the X-ray structure.

Single crystal X-ray structures of the analogous POM complexes, **LaCo$_9$**, **BaCo$_9$**, **RbCo$_9$**, and **CsCo$_9$**, were not as easily obtained from diffusion crystallization as **YCo$_9$**, because they were even less soluble (smaller K_{sp} values). However, FT-IR and elemental analyses of precipitated samples of **LaCo$_9$**, **BaCo$_9$**, **RbCo$_9$**, and **CsCo$_9$** demonstrate that the **Co$_9$** structure remains intact and that the La(III), Ba(II), Rb(I), and Cs(I) counter-cations were successfully incorporated within the insoluble heterogenous material.

Characterization of YCo$_9$, LaCo$_9$, BaCo$_9$, and CsCo$_9$ as electrocatalysts

The water-insoluble nature of **YCo$_9$**, **LaCo$_9$**, **BaCo$_9$**, **RbCo$_9$**, and **CsCo$_9$** make them perfect candidates for heterogeneous electrocatalysts. Not only can they be readily immobilized onto an electrode surface, but also their insolubility likely improves the reactive stability of the catalysts due to a lack of solution-phase chemistry. Given that the tetra-*n*-butyl ammonium (TBA) salt of **Co$_9$** is a known OER catalyst, we could easily probe the OER activities of **YCo$_9$**, **LaCo$_9$**, **BaCo$_9$**, **RbCo$_9$**, and **CsCo$_9$** as electrocatalysts.

The electrochemical oxidation of water with the different salts of **Co$_9$** as anode materials were evaluated. Figure 4.2a shows linear sweeps corresponding to the anodic current for water oxidation of these materials. All the **Co$_9$** salts were active OER catalysts in acid (pH = 2), and **YCo$_9$** was the most active material for anodic OER. In addition, we also compared these **Co$_9$** anodes with polycrystalline Co_3O_4 in similar electrode setups while accounting for the number of cobalt atoms present per electrode surface area. We show that the observed water oxidation current of Co_3O_4 under the same conditions is less than a tenth than that of **YCo$_9$** (Figure 4.2b). As expected, the ability of polycrystalline Co_3O_4 to catalyze water oxidation is extremely limited under acidic conditions. Similar electrochemical studies using glassy carbon as an electrode substrate demonstrates the behavior for all four salts of **Co$_9$** (Figure 4.3).

Potentiostatic electrolysis of water using FTO anodes containing **YCo$_9$**, **LaCo$_9$**, **BaCo$_9$**, and **CsCo$_9$** were performed for extended periods at an overpotential of 640 mV. Figure 4.4 indicates that the electrocatalytic current leveled out quickly and remained constant over an 8-hour period. All four electrodes show remarkably stable electrochemical activity in strong acid, resulting in less than 1% drop in anodic current after 8 hours. The conferred acid stability of these insoluble counterion versions of **Co$_9$** is particularly interesting. Typically, cobalt oxides are not hydrolytically stable below pH 3.5.[53, 54] The improved acidic OER stability of water-insoluble **Co$_9$**

after pairing with these specific counter-cations is appealing for immobilization modifications of molecular OER catalysts. Moreover, acid-compatible OER electrocatalysts are few in number and there is a significant amount of interest in both new catalysts in acid and possible protection schemes to enable known OER catalysts to function in acid.[10, 14, 35, 53, 54]

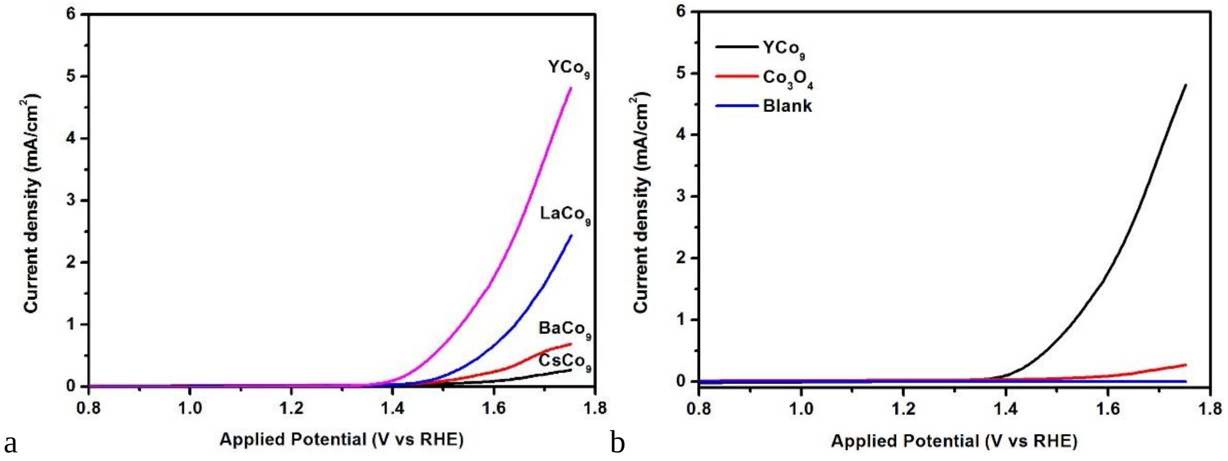

Figure 4.2 a) Linear sweep voltammetry of four salts of **Co$_9$** and b) **YCo$_9$** (blank line) and Co_3O_4 (red line) electrodes using FTO substrates. Conditions: 50 mV scan rate, pH = 2 H_2SO_4 buffer, and 1 M KNO_3 electrolyte. Potentials measured against Ag/AgCl (1 M NaCl) electrode and reported vs the reversible hydrogen electrode.

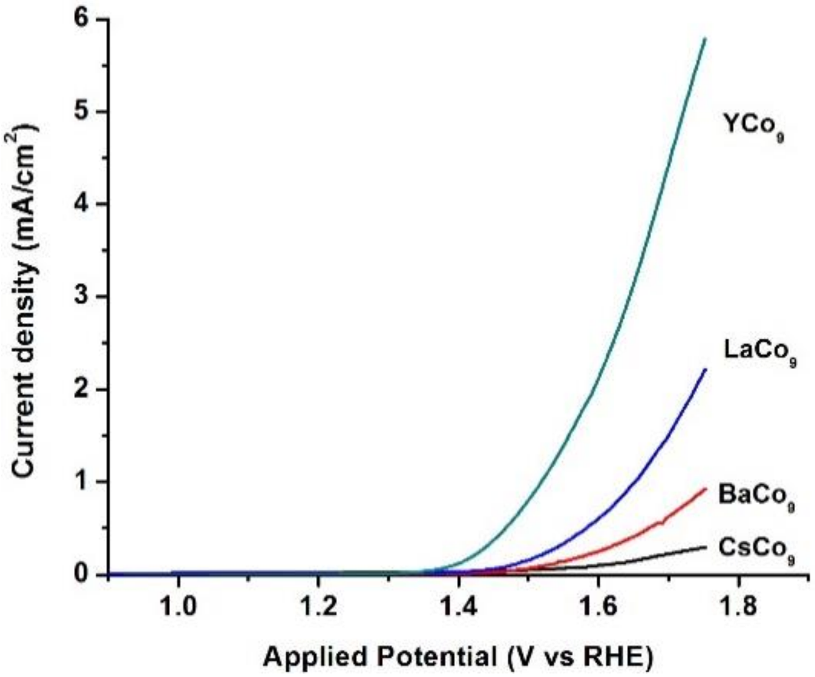

Figure 4.3 Linear sweep voltammetry of four electrodes fabricated using the different salts of **Co9** on glassy carbon (GC) electrodes. Conditions: 50 mV scan rate, pH = 2 H_2SO_4 buffer, and 1 M KNO_3 electrolyte. Potentials reported vs Ag/AgCl (1 M NaCl) electrode.

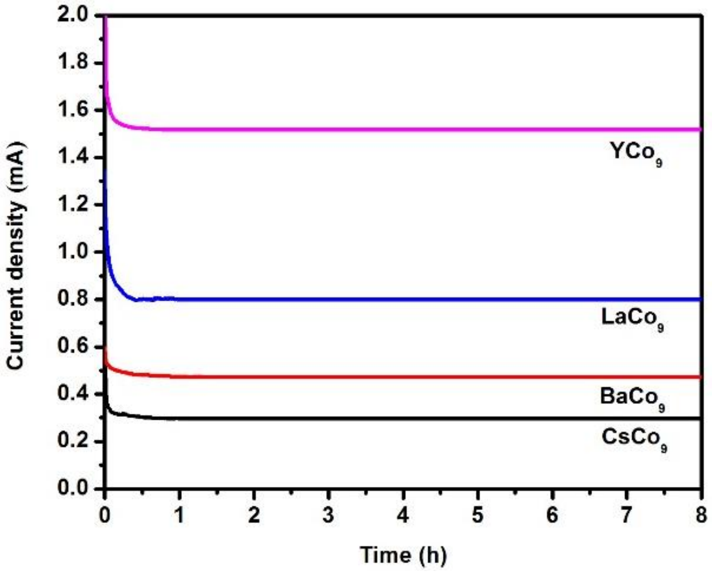

Figure 4.4 Bulk electrolysis at an applied potential of 1.753 V vs RHE in pH = 2 H_2SO_4 buffer and 1 M KNO_3 electrolyte. Conditions: FTO working electrode, Pt wire cathode, and 1.0 M Ag/AgCl reference.

To rule out possible side reactions to OER that could be occurring under experimental conditions, the amount of oxygen evolved during the potentiostatic electrolysis of water were measured with an oxygen fluorescence probe. Figure 4.5 shows the faradaic current of water oxidation and the corresponding amount of dioxygen measured. All four electrode materials display very good faradic yield, consistent with the electrochemical stability observed in Figure 4.4. Compared with the other three salts of **Co$_9$**, **YCo$_9$** produced by far the most oxygen. The order of efficiency for water oxidation is thus observed to be **YCo$_9$** > **LaCo$_9$** > **BaCo$_9$** > **CsCo$_9$**. This is both an expected result and a surprising finding. While we expected some difference in the catalytic capabilities of the different counter-cation salts, we were not expecting such a pronounced variance. This further confirms that extensive inner-sphere interactions between the counter-cations, Y^{3+}, La^{3+}, Ba^{2+}, and Cs^{+} counterions and the **Co$_9$** clusters are present. However, it is the trend of the catalytic efficiency that is most surprising. We observe a periodic trend of the counterions that is giving rise to a very significant effect on the OER catalysis of the **Co$_9$** POM motif.

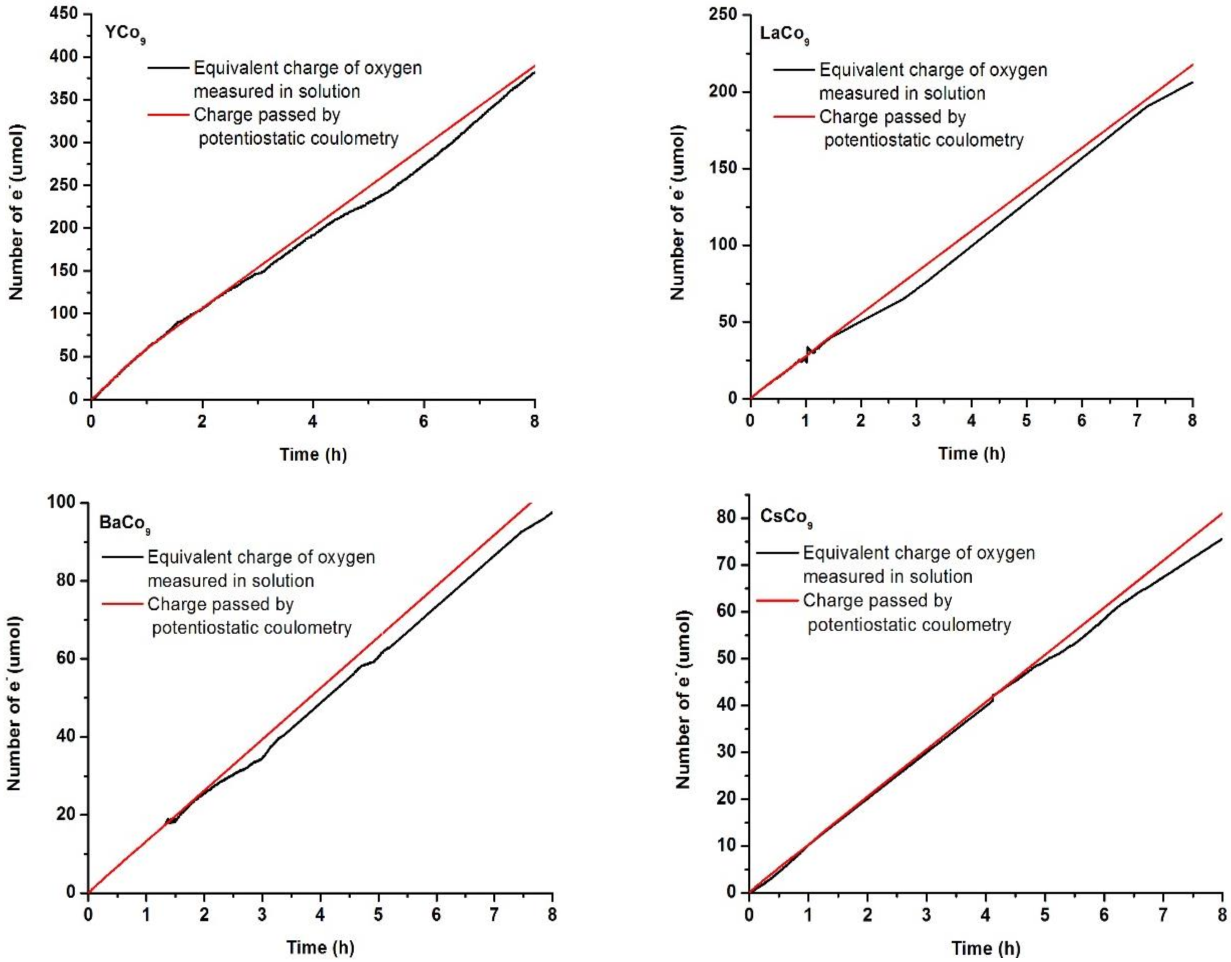

Figure 4.5 Dioxygen measurement using salts of **Co_9** as catalysts. The equivalent charge of O_2 measured in solution tracks well with the charge passed by potentiostatic coulometry. Conditions: sulfuric acid buffer (pH = 2) with KNO_3 (1 M) electrolyte; FTO working electrode, Pt wire cathode, Ag/AgCl (1.0 M) reference. Applied potential = 1.753 V (vs RHE).

Stability of catalysts

Control experiments with Co_3O_4 yielded much less dioxygen measured under the same conditions (Figure 4.6). Especially significant is the unstable nature of Co_3O_4 in acid. In contrast to the Co_9 salts, Co_3O_4 slowly dissolves into the solution and, within hours, we observe structural disintegration of the Co_3O_4 film deposited onto our working electrodes.

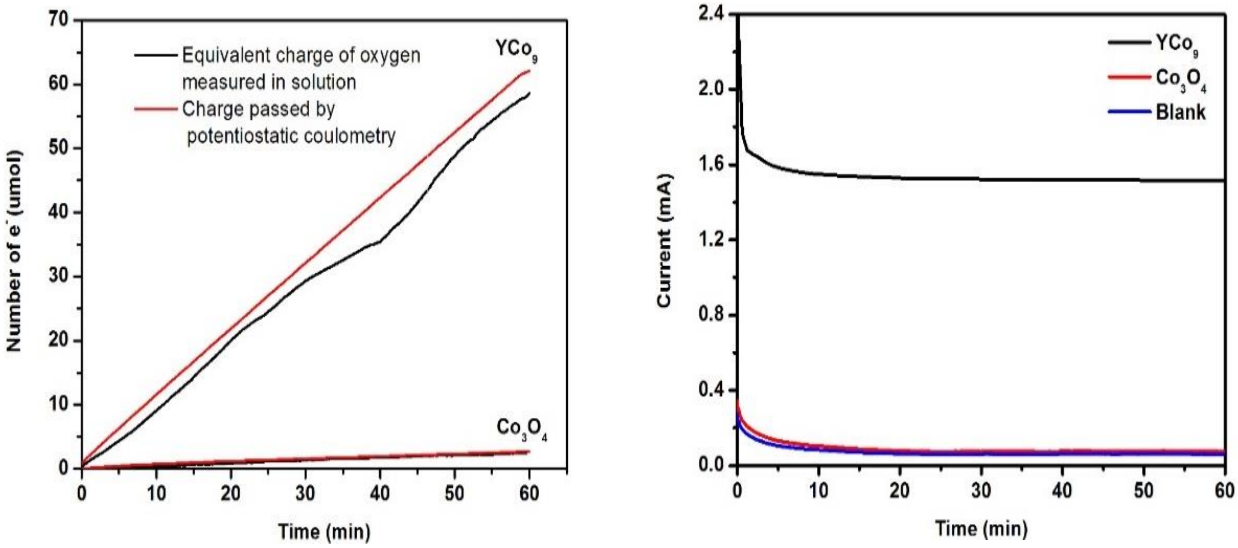

Figure 4.6 Left: O_2 production measured with a fluorescence sensor; right: bulk electrolysis for water oxidation under an applied voltage of 1.753 V vs RHE in a H_2SO_4 buffer with KNO_3 (1 M) as the electrolyte. **YCo_9**/FTO and Co_3O_4/FTO were used as working electrodes.

FT-IR spectroscopy of the catalytic materials before and after electrolysis are shown to be identical, yielding no new peaks or disappearance of existing peaks (Figure 4.7). This includes any potential peaks that could arise from Co_3O_4. These observations demonstrate that the **Co_9** POM remains structurally intact and unchanged after the catalytic oxidation of water. The PXRD patterns of **YCo_9** before and after reaction is also consistent with a stable catalyst material in which the **Co_9** structure remains unchanged following electrocatalytic OER (Figure 4.8).

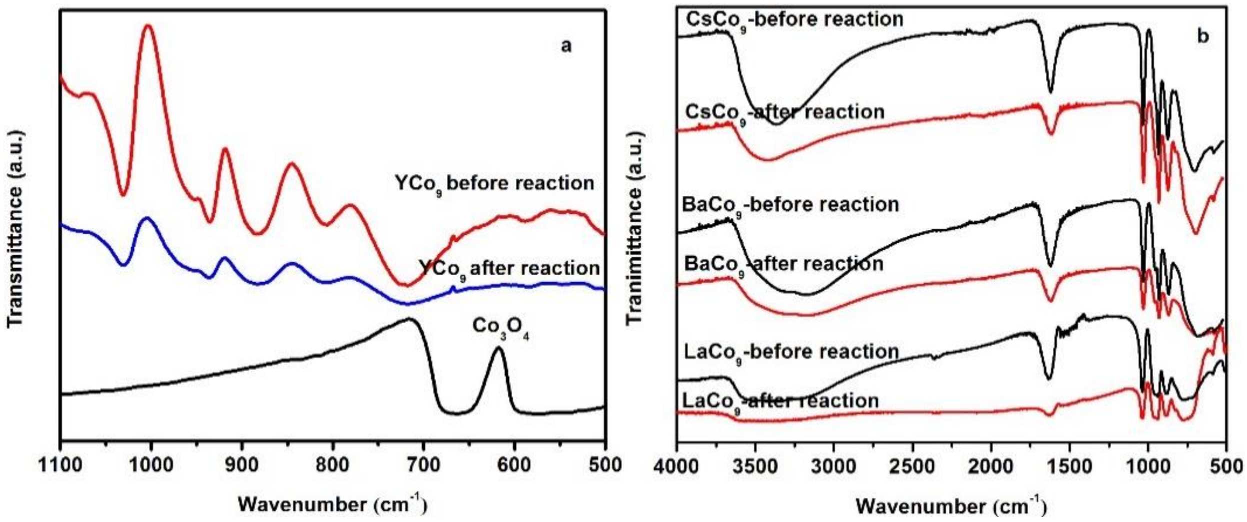

Figure 4.7 FT-IR spectra of **Co$_9$** salts freshly prepared and after one hour of electrocatalytic OER at pH 2, and compared with the corresponding spectra of Co$_3$O$_4$.

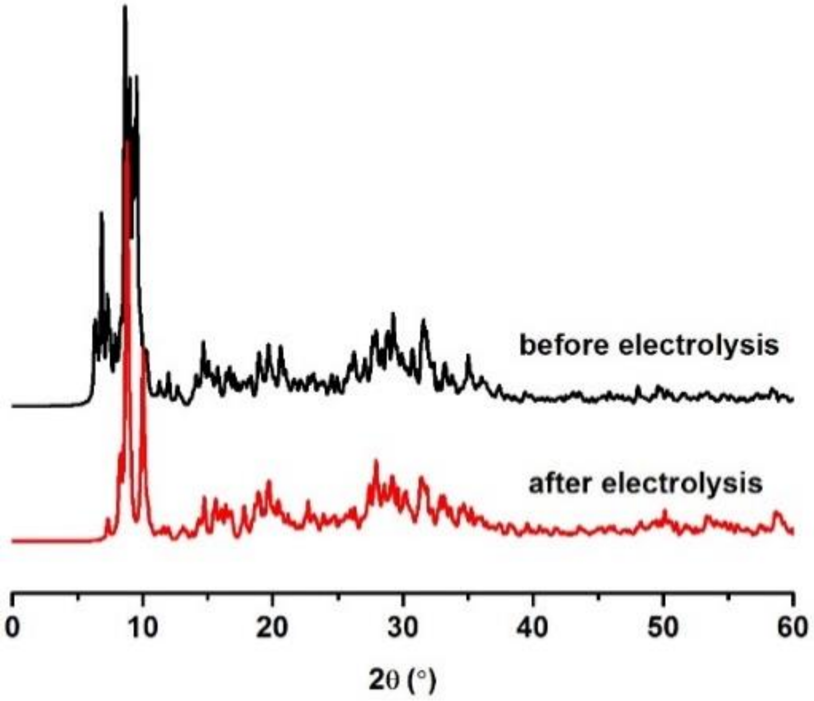

Figure 4.8 PXRD pattern for **YCo$_9$** before (black) and after one hour of electrocatalytic water oxidation (red) in H_2SO_4 (pH 2). Small differences in the <10° range are attributed to differences in the waters of hydration.

The stoichiometry of **YCo9** before and after reaction was determined by Inductively coupled plasma - mass spectrometry (ICP-MS) metal analysis and thermogravimetry (Table 4.1). ICP-MS metal analysis shows a 1:3 Co/W ratio. This ratio is maintained after one hour of electrocatalysis. The stability of **YCo9** after electrochemical reaction was also confirmed by elemental mapping from a scanning electron microscope coupled with energy dispersive X-ray detector (SEM-EDX) (Figure 4.9). Elemental mapping shows that all catalytic materials remain upon the surface. The EDX data confirmed the expected elemental distributions (Figure 4.10 and Table 4.2). The ratio of cobalt to phosphorus agrees with the theoretical ratio of 9:5 and the cobalt to tungsten ratio agrees with the expected 1:3 ratio in **YCo9**. The slight deviation in the EDX quantification of yttrium is attributed to the higher background associated with the heavy element. We further confirmed stability by of **YCo9** via XPS (Figure 4.11). Comparative analyses do not show any significant differences between fresh or used materials, suggesting no major compositional change of the catalyst after one hour of OER. Additionally, the Co2p peaks correspond to Co(II) centers rather than mixed Co(II,III) centers as would be expected for Co_3O_4. All three elemental analysis methods are consistent with the compositional makeup of the crystalline **Co9** materials and show no significant decomposition after one hour of electrocatalytic OER.

Table 4.1 Metal analysis of **YCo9** by ICP-MS before and after electrocatalytic OER

	YCo9 before reaction		**YCo9** after reaction	
	weight % (found)	Stoichiometry (estimated)	weight % (found)	stoichiometry (estimated)
Co	5.44	9.2	5.50	9.3
Y	5.40	6.1	5.43	6.1
W	51.8	28.2	50.7	27.6

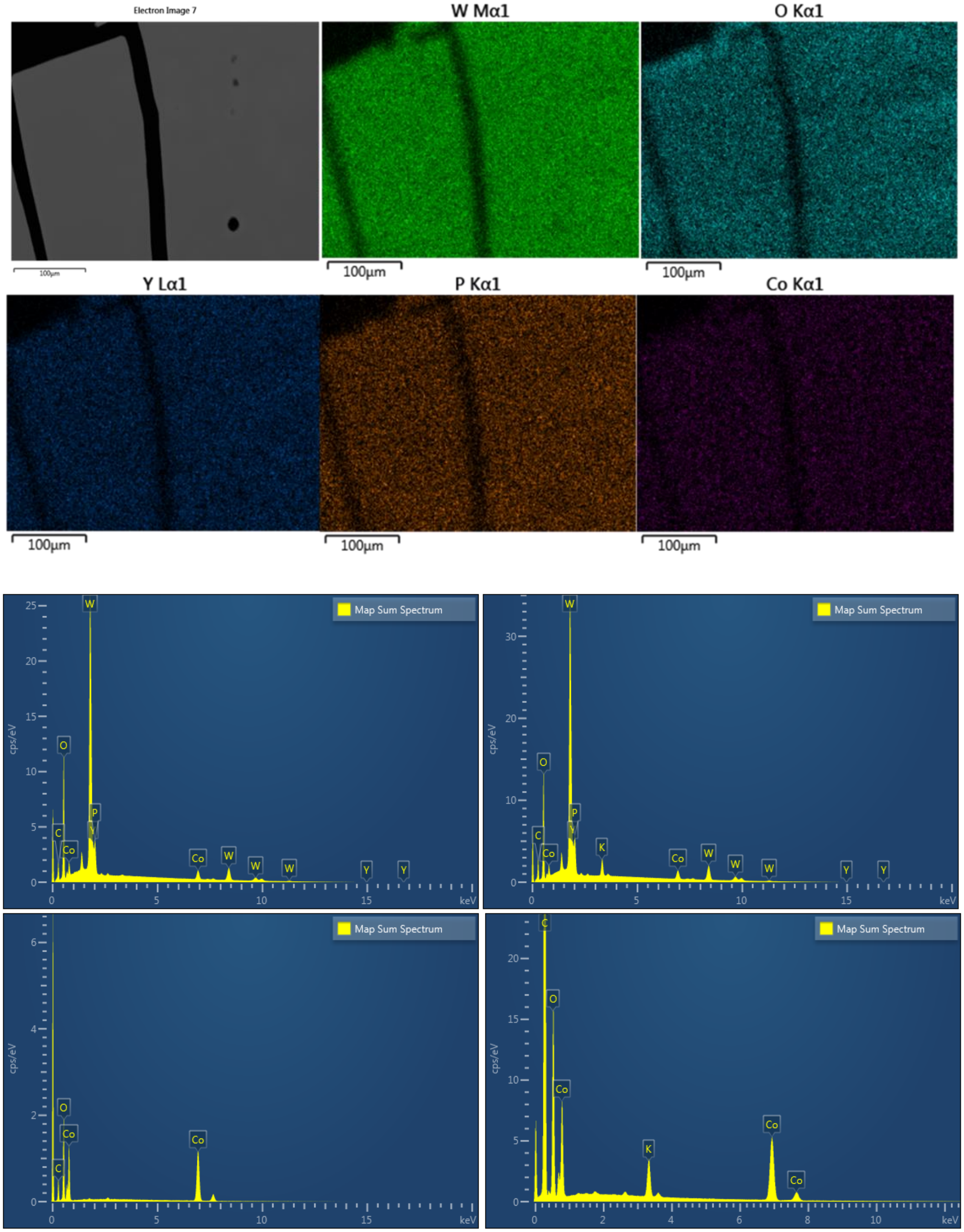

Figure 4.9 Elemental mapping from SEM-EDX of **YCo9** after catalysis.

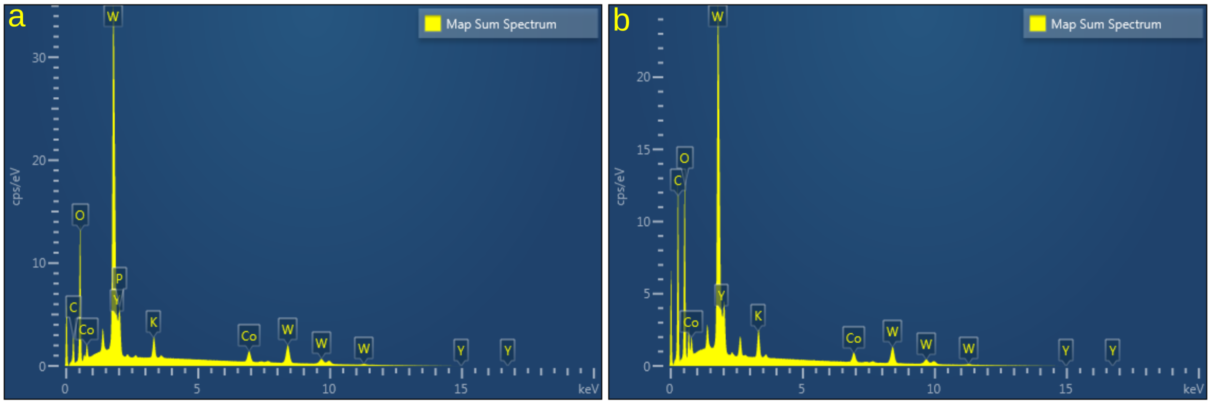

Figure 4.10 EDX of **YCo9** before (a) and after (b) one hour of electrocatalytic OER.

Table 4.2 Elemental abundance for **YCo9** from EDX before and after electrocatalytic OER

	YCo9 before reaction		**YCo9** after reaction	
	atomic %	stoichiometry	atomic %	stoichiometry
Co	4.35	9.0	4.35	8.9
P	2.61	5.4	2.59	5.3
Y	1.98	4.1	2.16	4.4
W	13.36	27.6	13.16	27
O	57.81	119.6	59.24	119.5

Periodic trend

Tafel plots for five immobilized **Co_9** electrocatalysts are shown in Figure 4.12, with steady-state current density values obtained in the $0.3\ V < \eta < 0.8\ V$ range. Not surprisingly, the Tafel slopes of the five **Co_9** salts are the same, consistent with having the same rate determining step and thus a similar water oxidation mechanisms under these reaction conditions. This is not surprising, given that **YCo_9**, **$LaCo_9$**, **$BaCo_9$**, and **$CsCo_9$** all have the same catalytic **Co_9** motif responsible for water oxidation. At the same current densities, **YCo_9** gives the lowest overpotential, thus also yielding the lowest exchange current density. The exchange current density of the other **Co_9** salts also follows the same periodic trend as discussed previously, namely **YCo_9** < **$LaCo_9$** < **$BaCo_9$** < **$RbCo_9$** < **$CsCo_9$**, with the lowest exchange current corresponding to the highest electrocatalytic efficiency.

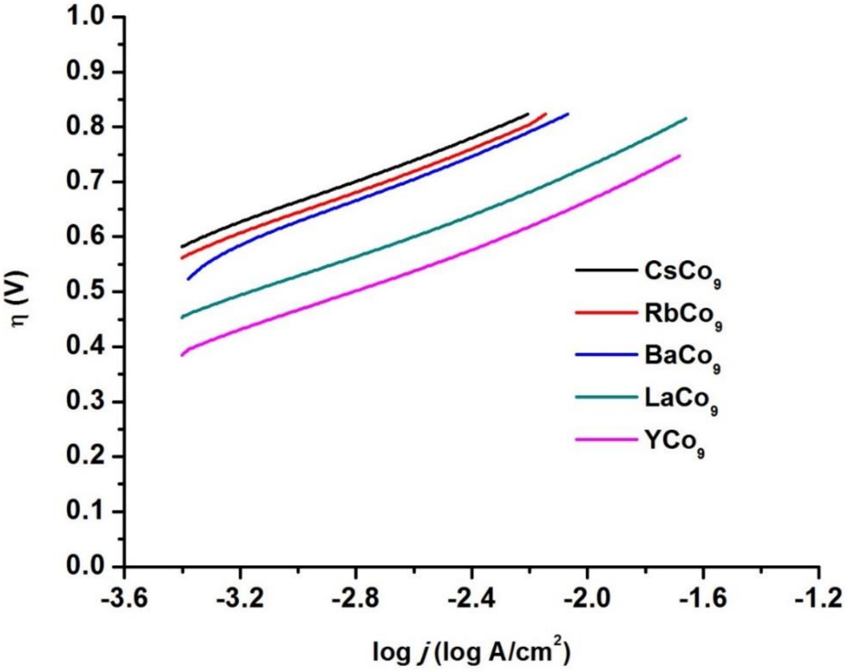

Figure 4.12 Tafel region for **Co_9** salts from steady-state chronopotentiometry experiments in H_2SO_4 (pH = 2) solution. Tafel slope ~120 mV/decade.

We consider several factors that could explain such an observed periodic trend. First, we measure and control for the electroactive surface area of all working electrodes. We measure the double-layer capacitance of all anodes using a similar procedure to those reported by McCrory *et al*.[55, 56] **YCo$_9$**, **LaCo$_9$**, **BaCo$_9$**, and **CsCo$_9$** salts with the same number of Co atoms per unit area were immobilized on the glassy carbon electrodes using the previously reported method. The average current densities in a non-faradaic region (0.335 V to 0.435 V vs RHE) were then measured as a function of scan rate in cyclic voltammetry. The ratios of electroactive surface area to geometric surface area can be derived from the slope and shown to be effectively the same for all four anodes (Figure 4.13). Thus, it is the chemical differences between **YCo$_9$**, **LaCo$_9$**, **BaCo$_9$**, and **CsCo$_9$** that are giving rise to the different water oxidation capabilities rather than any macroscopic morphological differences.

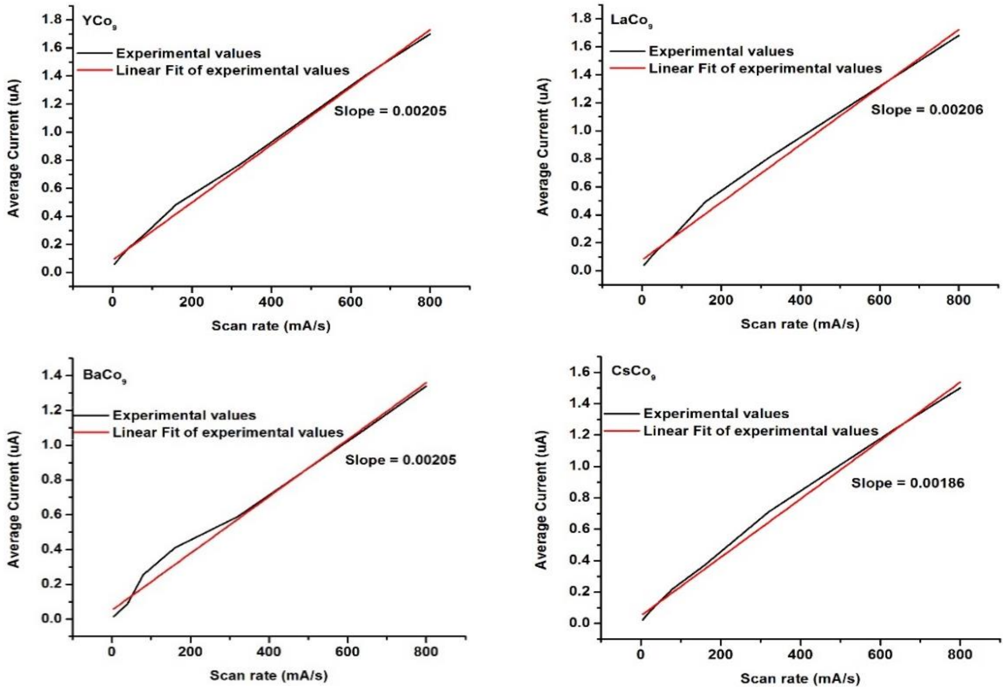

Figure 4.13 Electroactive surface area measurement via double-layer capacitance. Conditions: sulfuric acid buffer (pH = 2) with KNO$_3$ (1 M) electrolyte; glassy carbon working electrode, Pt

cathode, and Ag/AgCl (1.0 M) reference electrode. Applied potential ranges from 0.688 mV vs RHE to 0.788 mV vs RHE.

We can also measure the redox potential of the Co(I/II) couple within these **Co$_9$** salts (Figure 4.14a). Interestingly, the same observed periodic trend holds for all five salts. Indeed, plotting these Co(I/II) redox potentials vs their corresponding water oxidation catalysis exchange current densities yield a linear correlation (Figure 4.14b). This demonstrates a direct correlation between the redox potentials of the cobalt centers and the catalytic water oxidation performance. The more noteworthy aspect of this observation is the order of the periodic trend. While we observe the trend of the redox potentials as **YCo$_9$** < **LaCo$_9$** < **BaCo$_9$** < **RbCo$_9$** < **CsCo$_9$**, this runs counter to the existing observations of the modifications of metal oxide OER centers by Lewis acidic ions.[43-52] Whereas, we should anticipate increasing oxidation potential for increasing Lewis acidity, we observe the opposite trend. The most Lewis acidic cation, Y^{3+}, has the lowest redox potential for Co(I/II). If we infer this trend holds for any possible Co(II/III) and Co(III/IV) couples involved in water oxidation catalysis, and if we assume the discrete **Co$_9$** moiety in all five counter-cation salts proceeds by a similar OER pathway that oxidizes water quickly once high-valent cobalt centers are generated, it follows that the electrochemical oxidation of Co to Co(III) or Co(IV) are the rate-determining steps. Consequently, the lowest overpotential is achieved with the most Lewis acidic form of **Co$_9$**.

Traditionally, higher Lewis acidity causes a stronger electron withdrawing action upon the active metal centers, increasing corresponding redox potentials. However, the opposite observations recorded here is indicative of an effect that runs counter to the previously held explanation given by the Lewis acidity of the counterions. No other OER catalyst has been shown to follow this trend in reactivity. In fact, immobilizing the **Co_4P_2** studied in previous chapters yields the expected result, giving the opposite periodic trend as observed in **Co_9** (Figure 4.15).

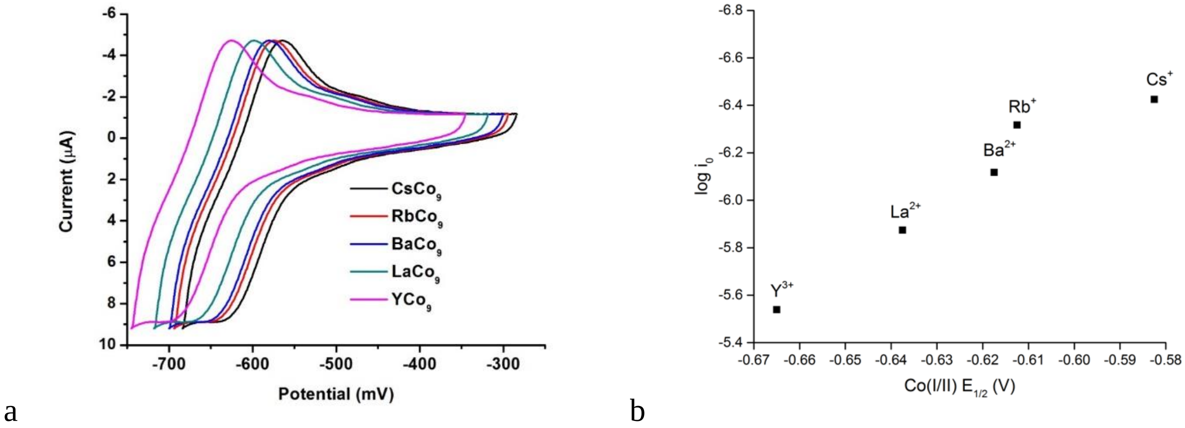

a b

Figure 4.14 a) Cyclic voltammetry of five salts of **Co$_9$** and b) E$_{1/2}$ of Co(I/II) couple plotted vs their corresponding exchange current for water oxidation. Conditions: 50 mV scan rate; pH = 2 H$_2$SO$_4$ buffer, and KNO$_3$ (1 M) as electrolyte. Potentials measured against Ag/AgCl (1 M NaCl) electrode.

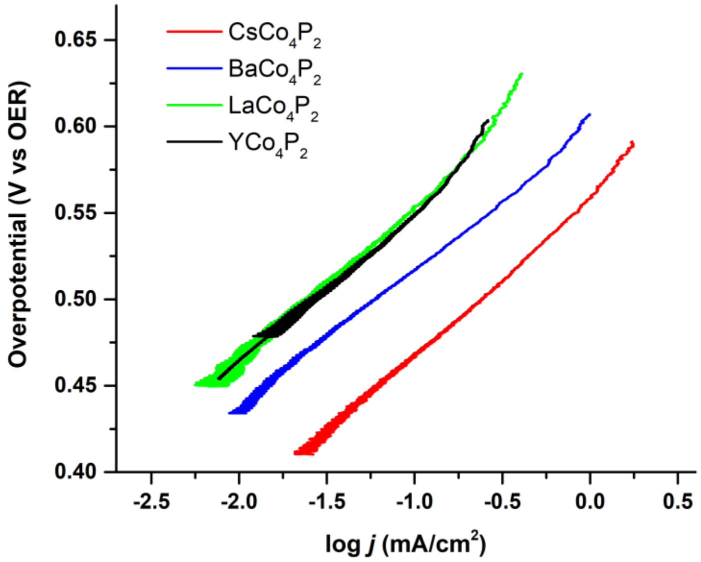

Figure 4.15 Tafel plot of heterogenized **Co$_4$P$_2$** on glassy carbon electrodes with different counterions. Conditions: 1 mV/s iR compensated chronoamperometry in 0.1 M pH 8 sodium

borate buffer and 0.1 M KNO_3 electrolyte solution. Reference electrode, Ag/AgCl (1.0 M KCl); counter electrode, graphite. Tafel slopes of the linear regions are shown to be ~80 mV/decade.

In order to explain this extraordinary result, we turn to theoretical computations. Density function theory (DFT) calculations done using the M06L/6-31++g(d,p)/LanL2dz mixed basis set demonstrates that the HOMO and LUMO energy levels of the cobalt active centers are extensively altered by the electronic structure of the tetrahedral phosphates within **Co9** (Figures 4.16). This, in turn, is strongly influenced by the counter-ions present. Where Y^{3+} lowers the energy levels of the cobalt-based HOMO the least, Cs^+ lowers them the most. Structurally, this can be explained given the extensive interactions we observe between the Y^{3+} and the phosphate in the crystal structure. Similar ion-pairing effects are theoretically expected for other POMs. DFT calculations also indicate that the trends between the HOMO and LUMO levels are maintained, leading to the linear correlation we see in Figure 4.14b and accounting for the overall periodic trends that we observe for our catalysts. In summary, $HOMO_{YCo9} > HOMO_{LaCo9} > HOMO_{CsCo9}$ leads to $E_{1/2}$(**YCo9**) < $E_{1/2}$(**LaCo9**) < $E_{1/2}$(**CsCo9**).

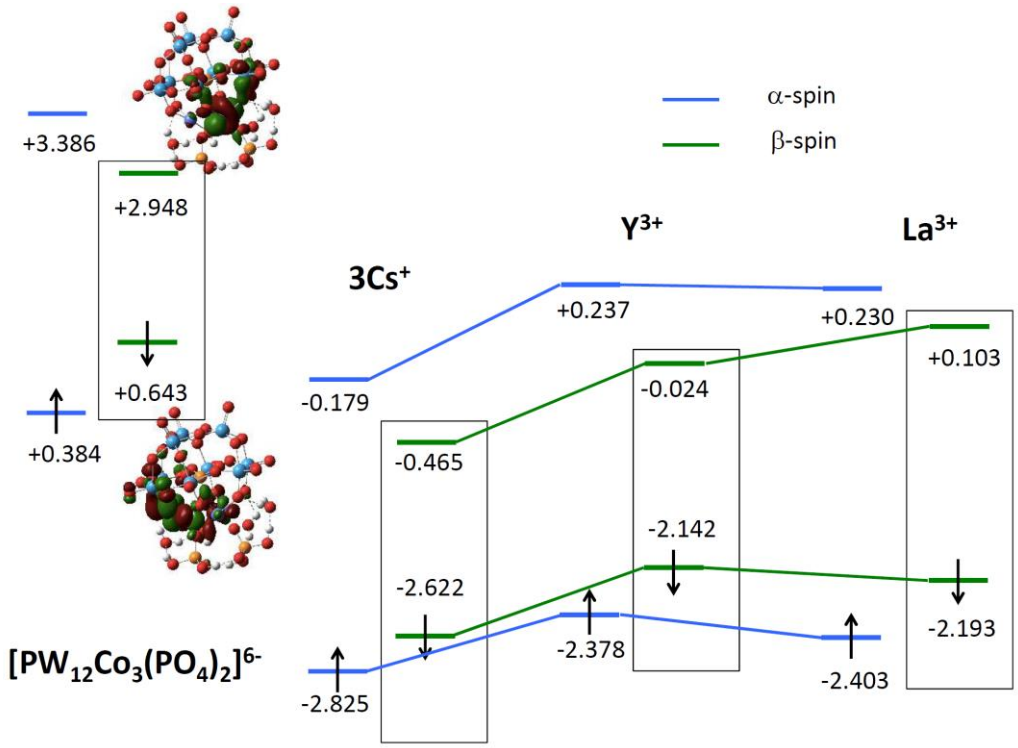

Figure 4.16 Summary of the HOMO/LUMO results from DFT calculations.

Alternatively, it is also possible that the electrocatalytic OER pathway of **Co_9** is rate-limited by the first step of water binding and deprotonation rather than the typical O-O bond formation step. In this case, we would indeed expect a high Lewis acidity counter-cation to increase the reaction rate. The value of the Tafel slopes of the **Co_9** salts are ~120 mV/decade (Figure 4.12). This value matches 2RT/F and is consistent with what we would expect to see if the first step of water oxidation is the rate determining step. Compare this to the Tafel slopes of **Co_4P_2**, which are ~80 mV/decade (Figure 4.15). This value is closer to RT/F, and would be consistent with a mechanism in which O-O bond formation is the rate determining step. Regardless, the observed periodic trend for the insoluble cation-paired series of **Co_9** is unique among known OER catalysts and thus warrant further scrutiny.

Experimental

General methods, materials, and instrumentation

Materials and solvents were purchased as ACS analytical or reagent grade and used as received. Infrared spectra (2% sample in KBr pellet) were recorded on a Nicolet 6700 Fourier-transform infrared (FT-IR) spectrometer. ICP-MS (Y, Co and W) were conducted by Galbraith Laboratories (Knoxville, TN). ^{31}P nuclear magnetic resonance (NMR) spectra were acquired on a Varian INOVA 400 spectrometer using H_3PO_4 (δ 0) as the external standard. Scanning electron microscopy and energy dispersive X-ray spectroscopy (SEM/EDX) data were gathered at the Clemson University Advanced Materials Center using three Hitachi transmission electron microscopes (STEM HD2000, TEM H7600T, and TEM 9500) and scanning electron microscopes (SEM 3400, SU-6600, and S4800) equipped with EDX. X-ray photoelectron spectroscopy was collected on a PHI VersaProbe II spectrometer equipped with a scanning monochromatic Al−Kα

X-ray source (hν = 1486.6 eV). The powder XRD data were collected on a D8 Discover Powder Instrument under monochromatic Cu Kα (γ = 1.54060 Å) radiation. Thermogravimetric analyses (TGA) were acquired on a STA 6000 thermal analyzer.

Diffusion crystallization

$[Co_9(H_2O)_6(OH)_2(HPO_4)_2(PW_9O_{34})_3]^{16-}$ (**Co_9**) was prepared using a synthesis previously reported in literature [8] and recrystallized from water as the $Na_8K_8[Co_9(OH)_3(H_2O)_6(HPO_4)_2(PW_9O_{34})_3]\cdot 43H_2O$ (**$NaKCo_9$**) salt. A solution of **$NaKCo_9$** (0.088 g, 0.01 mmol) in water (2 mL) was placed into a narrow diameter glass tube (1 cm in diameter) as a bottom layer. After this time, a mixed solvent of water and acetonitrile (1:1 volume, 2 mL) was added slowly to the bottom layer forming a middle layer to facilitate slow solvent diffusion. Finally, a solution of of $Y(NO_3)_3 \bullet 6\ H_2O$ (0.015 g, 0.04 mmol) in acetonitrile (2 mL) was carefully added on the middle layer as a top layer. The glass tube was left undisturbed for 3 days or more to collect pink crystals, which were identified crystallographically as **YCo_9**.

X-ray crystallography

Single-crystal X-ray diffraction data for **YCo_9** were collected at 150 K on an Agilent Technologies Gemini A Ultra system, with Mo Kα (λ = 0.71073 Å) radiation. The empirical absorption corrections were applied using spherical harmonics, implemented in the SCALE3 ABSPACK scaling algorithm.

Preparation of POM/FTO electrodes

$[Co_9(H_2O)_6(OH)_2(HPO_4)_2(PW_9O_{34})_3]^{16-}$ (**Co_9**) was prepared using a synthesis previously reported in literature [8] and recrystallized from water as the $Na_8K_8[Co_9(OH)_3(H_2O)_6(HPO_4)_2(PW_9O_{34})_3]\cdot 43H_2O$ (**$NaKCo_9$**) salt. The yttrium salt of **Co_9** was prepared via metathesis. A stoichiometric excess of a 0.1 M solution of $Y(NO_3)_3$ was added to a solution of the **$NaKCo_9$** under stirring. After five minutes, the resultant precipitate and gel were isolated and washed with deionized water three times and dried at room temperature overnight, producing the desired **YCo_9** material. A typical yield of about 80% was obtained. Four other salts using lanthanum, barium, rubidium, and cesium as counter cations were all synthesized using the same metathesis procedure. The salt sources used were $LaCl_3\cdot 7H_2O$, $BaCl_2\cdot 2H_2O$, $RbNO_3$, and $CsNO_3$ yielding insoluble powdered samples of, respectively, **$LaCo_9$**, **$BaCo_9$**, **$RbCo_9$**, and **$CsCo_9$**. An analogous process was used to synthesize **YCo_4P_2**, **$LaCo_4P_2$**, **$BaCo_4P_2$**, and **$CsCo_4P_2$**.

The fluorine-doped tin oxide substrates, FTO (Pilkington TEC15, ~15 Ω/sq resistance), were cleaned by sonicating sequentially in acetone, ethanol, and deionized water for 20 min each time, followed by drying with nitrogen gas. Before coating, the outer area of the FTO substrate was insulated using PTFE tape to create an uncoated FTO surface for electrical contact. The effective surface area of the FTO electrode was measured using ImageJ (Figure 4.17). A compact layer of **YCo_9** (0.15 μmol) was deposited onto the FTO, covered by 5 uL of Nafion perfluorinated resin solution (5 wt. % in mixture of lower aliphatic alcohols and water, containing 45 % water). Subsequently, the substrates were dried under ambient conditions overnight. This same process was repeated to produce the working electrodes containing **$LaCo_9$**, **$BaCo_9$**, **$RbCo_9$**, and **$CsCo_9$**. Glassy carbon electrodes were also used as substrates for the deposition of these electrocatalysts using a similar procedure. $\mathbf{YCo_4P_2}$/FTO, $\mathbf{LaCo_4P_2}$/FTO, $\mathbf{BaCo_4P_2}$/FTO, and $\mathbf{CsCo_4P_2}$/FTO were fabricated in much the same way.

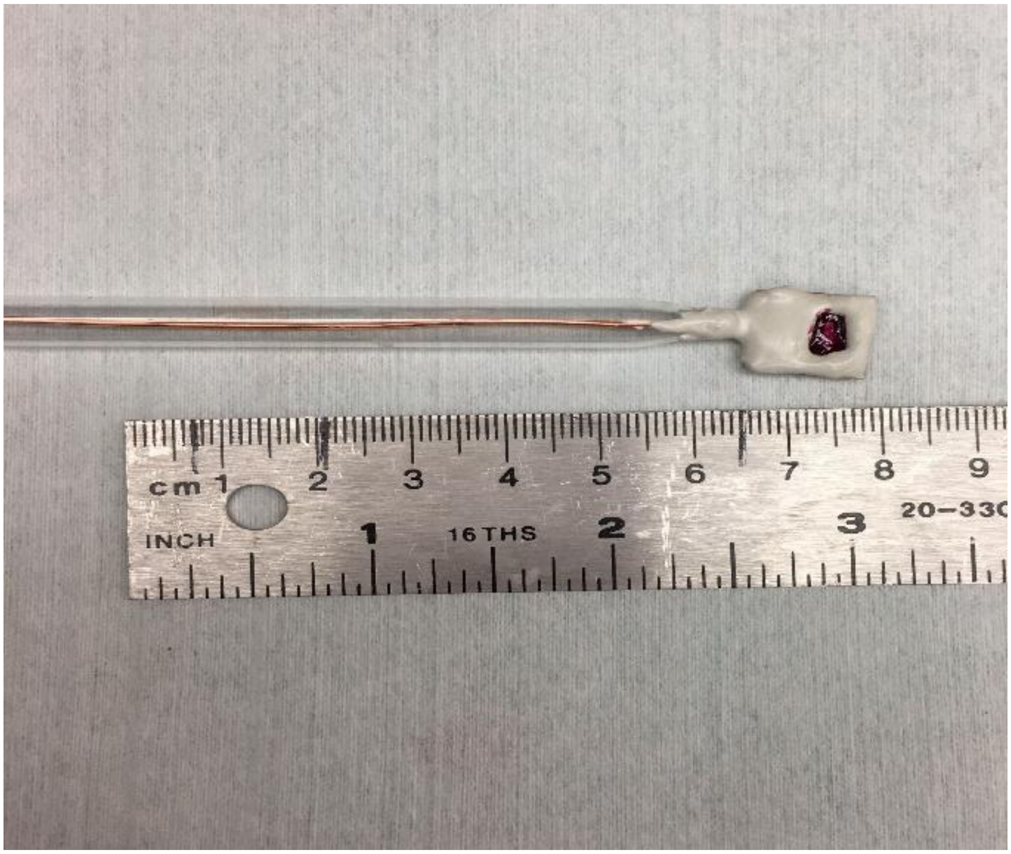

Figure 4.17 A typical photo of a working anode we would use to quantify the effective area of the POM/FTO electrode.

Electrochemical Studies

Electrochemical reactions were carried out using standard three-electrode measurements on a Pine Research Instrument WaveDriver 20 bipotentiostat. All potentials were measured against a 1 M KCl Ag/AgCl reference electrodes (+0.235 V vs NHE) purchased from CH Instruments. Platinum wire was used as the counter electrode. Working electrodes were fabricated from the films discussed above. A copper wire was fixed to the exposed FTO surface using conductive silver adhesive 503 (Electron Microscopy Sciences). The copper wire was then fitted through a glass tube to provide structural support, and the FTO/copper wire was insulated and attached to the glass tube with Epoxy adhesive (Henkel Loctite Hysol 1C Epoxy). Electrodes were dried overnight before testing. Bulk electrolysis and linear scan voltammetry were conducted in a custom rounded 100 mL PEC cell with a flat quartz window and four arms equipped with airtight adaptors for electrodes and headspace access (Tudor Scientific Glass). The cell was purged with argon gas prior to use. All of the experiments were conducted in sulfuric acid buffer of pH 2, with 0.1 M KNO_3 electrolyte.

Conclusion

We were able to synthesize and immobilize **Co₉** with a series of different counter cations. Structurally, some unexpected inner-sphere interactions are present between the **Co₉** polyanion and the cations. **YCo₉**, **LaCo₉**, **BaCo₉**, **RbCo₉**, and **CsCo₉** were all able to be heterogenized and immobilized onto anode surfaces and perform electrocatalytic water oxidation under acidic conditions (pH 2).

Even more interesting is the observed periodic trend in the redox potentials and OER activity of these electrocatalysts. For example, the most Lewis acidic and electron withdrawing cation, Y^{3+} decreases the potentials of the Co redox couples and enhances the OER rate of **Co₉** significantly, while **CsCo₉** has the highest redox potentials and lowest OER rates. We explore this unprecedented correlation using DFT calculations and theoretical considerations.

In sum, it is possible that **Co₉** has a unique reaction mechanism with an unconventional rate determining step that allows it to be idiosyncratically affected by counterion effects. Comprehensively, cation identity has significant influence on the frontier orbitals of the **Co₉** polyanion, leading to differences in catalytic performance. Similar effects are likely much more widespread than we generally assume. Significant care should be taken when considering the choice of counterions used in any catalyst design. Even beyond cation-anion interactions, surface properties of polarizable materials are also likely to be significantly impacted by the different cations they may come in contact with.

References

1. Abdi, F. F.; Gutierrez Perez, R. R.; Haussener, S., Mitigating voltage losses in photoelectrochemical cell scale-up. *Sustainable Energy & Fuels* **2020,** *4* (6), 2734-2740.

2. Alibabaei, L.; Brennaman, M. K.; Norris, M. R.; Kalanyan, B.; Song, W.; Losego, M. D.; Concepcion, J. J.; Binstead, R. A.; Parsons, G. N.; Meyer, T. J., Solar water splitting in a molecular photoelectrochemical cell. *Proceedings of the National Academy of Sciences* **2013,** *110* (50), 20008-20013.

3. McKone, J. R.; Lewis, N. S.; Gray, H. B., Will Solar-Driven Water-Splitting Devices See the Light of Day? *Chemistry of Materials* **2014,** *26* (1), 407-414.

4. Haussener, S.; Xiang, C.; Spurgeon, J. M.; Ardo, S.; Lewis, N. S.; Weber, A. Z., Modeling, simulation, and design criteria for photoelectrochemical water-splitting systems. *Energy & Environmental Science* **2012,** *5* (12), 9922-9935.

5. Hu, S.; Xiang, C.; Haussener, S.; Berger, A. D.; Lewis, N. S., An analysis of the optimal band gaps of light absorbers in integrated tandem photoelectrochemical water-splitting systems. *Energy & Environmental Science* **2013,** *6* (10), 2984-2993.

6. McDonald, M. B.; Ardo, S.; Lewis, N. S.; Freund, M. S., Use of Bipolar Membranes for Maintaining Steady-State pH Gradients in Membrane-Supported, Solar-Driven Water Splitting. *ChemSusChem* **2014,** *7* (11), 3021-3027.

7. Diaz-Morales, O.; Raaijman, S.; Kortlever, R.; Kooyman, P. J.; Wezendonk, T.; Gascon, J.; Fu, W. T.; Koper, M. T. M., Iridium-based double perovskites for efficient water oxidation in acid media. *Nature Communications* **2016,** *7* (1), 12363.

8. Wang, L.-P.; Wu, Q.; Van Voorhis, T., Acid−Base Mechanism for Ruthenium Water Oxidation Catalysts. *Inorganic Chemistry* **2010,** *49* (10), 4543-4553.

9. Vannucci, A. K.; Alibabaei, L.; Losego, M. D.; Concepcion, J. J.; Kalanyan, B.; Parsons, G. N.; Meyer, T. J., Crossing the divide between homogeneous and heterogeneous catalysis in water oxidation. *Proceedings of the National Academy of Sciences* **2013,** *110* (52), 20918-20922.

10. Gerken, J. B.; McAlpin, J. G.; Chen, J. Y. C.; Rigsby, M. L.; Casey, W. H.; Britt, R. D.; Stahl, S. S., Electrochemical Water Oxidation with Cobalt-Based Electrocatalysts from pH 0–14: The Thermodynamic Basis for Catalyst Structure, Stability, and Activity. *Journal of the American Chemical Society* **2011,** *133* (36), 14431-14442.

11. Stevens, M. B.; Enman, L. J.; Batchellor, A. S.; Cosby, M. R.; Vise, A. E.; Trang, C. D. M.; Boettcher, S. W., Measurement Techniques for the Study of Thin Film Heterogeneous Water Oxidation Electrocatalysts. *Chemistry of Materials* **2017,** *29* (1), 120-140.

12. Smith, R. D. L.; Prévot, M. S.; Fagan, R. D.; Trudel, S.; Berlinguette, C. P., Water Oxidation Catalysis: Electrocatalytic Response to Metal Stoichiometry in Amorphous Metal Oxide Films Containing Iron, Cobalt, and Nickel. *Journal of the American Chemical Society* **2013,** *135* (31), 11580-11586.

13. Wang, Z.; Zheng, Y.-R.; Chorkendorff, I.; Nørskov, J. K., Acid-Stable Oxides for Oxygen Electrocatalysis. *ACS Energy Letters* **2020,** *5* (9), 2905-2908.

14. Blasco-Ahicart, M.; Soriano-López, J.; Carbó, J. J.; Poblet, J. M.; Galan-Mascaros, J. R., Polyoxometalate electrocatalysts based on earth-abundant metals for efficient water oxidation in acidic media. *Nature Chemistry* **2018,** *10* (1), 24-30.

15. Deng, X.; Tüysüz, H., Cobalt-Oxide-Based Materials as Water Oxidation Catalyst: Recent Progress and Challenges. *ACS Catalysis* **2014,** *4* (10), 3701-3714.

16. Ertem, M. Z.; Cramer, C. J., Quantum chemical characterization of the mechanism of a supported cobalt-based water oxidation catalyst. *Dalton Transactions* **2012,** *41* (39), 12213-12219.

17. Geletii, Y. V.; Yin, Q.; Hou, Y.; Huang, Z.; Ma, H.; Song, J.; Besson, C.; Luo, Z.; Cao, R.; O'Halloran, K. P.; Zhu, G.; Zhao, C.; Vickers, J. W.; Ding, Y.; Mohebbi, S.; Kuznetsov, A. E.; Musaev, D. G.; Lian, T.; Hill, C. L., Polyoxometalates in the Design of Effective and Tunable Water Oxidation Catalysts. **2011,** *51* (2), 238-246.

18. Gerlach, D. L.; Bhagan, S.; Cruce, A. A.; Burks, D. B.; Nieto, I.; Truong, H. T.; Kelley, S. P.; Herbst-Gervasoni, C. J.; Jernigan, K. L.; Bowman, M. K.; Pan, S.; Zeller, M.; Papish, E. T., Studies of the Pathways Open to Copper Water Oxidation Catalysts Containing Proximal Hydroxy Groups During Basic Electrocatalysis. *Inorganic Chemistry* **2014,** *53* (24), 12689-12698.

19. Hunter, B. M.; Gray, H. B.; Müller, A. M., Earth-Abundant Heterogeneous Water Oxidation Catalysts. *Chemical Reviews* **2016,** *116* (22), 14120-14136.

20. Kanan, M. W.; Yano, J.; Surendranath, Y.; Dincă, M.; Yachandra, V. K.; Nocera, D. G., Structure and Valency of a Cobalt−Phosphate Water Oxidation Catalyst Determined by in Situ X-ray Spectroscopy. *Journal of the American Chemical Society* **2010,** *132* (39), 13692-13701.

21. Kim, H.; Park, J.; Park, I.; Jin, K.; Jerng, S. E.; Kim, S. H.; Nam, K. T.; Kang, K., Coordination tuning of cobalt phosphates towards efficient water oxidation catalyst. *Nature Communications* **2015,** *6* (1), 8253.

22. Lauinger, S. M.; Piercy, B. D.; Li, W.; Yin, Q.; Collins-Wildman, D. L.; Glass, E. N.; Losego, M. D.; Wang, D.; Geletii, Y. V.; Hill, C. L., Stabilization of Polyoxometalate Water

Oxidation Catalysts on Hematite by Atomic Layer Deposition. *ACS Applied Materials & Interfaces* **2017,** *9* (40), 35048-35056.

23. Li, J.; Triana, C. A.; Wan, W.; Adiyeri Saseendran, D. P.; Zhao, Y.; Balaghi, S. E.; Heidari, S.; Patzke, G. R., Molecular and heterogeneous water oxidation catalysts: recent progress and joint perspectives. *Chemical Society Reviews* **2021,** *50* (4), 2444-2485.

24. Luo, G.-Y.; Huang, H.-H.; Wang, J.-W.; Lu, T.-B., Further Investigation of a Nickel-Based Homogeneous Water Oxidation Catalyst with Two cis Labile Sites. *ChemSusChem* **2016,** *9* (5), 485-491.

25. Lv, H.; Geletii, Y. V.; Zhao, C.; Vickers, J. W.; Zhu, G.; Luo, Z.; Song, J.; Lian, T.; Musaev, D. G.; Hill, C. L., Polyoxometalate water oxidation catalysts and the production of green fuel. *Chemical Society Reviews* **2012,** *41* (22), 7572-7589.

26. Lv, H.; Song, J.; Geletii, Y. V.; Vickers, J. W.; Sumliner, J. M.; Musaev, D. G.; Kögerler, P.; Zhuk, P. F.; Bacsa, J.; Zhu, G.; Hill, C. L., An Exceptionally Fast Homogeneous Carbon-Free Cobalt-Based Water Oxidation Catalyst. *Journal of the American Chemical Society* **2014,** *136* (26), 9268-9271.

27. Menezes, P. W.; Indra, A.; Levy, O.; Kailasam, K.; Gutkin, V.; Pfrommer, J.; Driess, M., Using nickel manganese oxide catalysts for efficient water oxidation. *Chemical Communications* **2015,** *51* (24), 5005-5008.

28. Schilling, M.; Luber, S., Computational Modeling of Cobalt-Based Water Oxidation: Current Status and Future Challenges. *Frontiers in Chemistry* **2018,** *6* (100).

29. Singh, A.; Chang, S. L. Y.; Hocking, R. K.; Bach, U.; Spiccia, L., Highly active nickel oxide water oxidation catalysts deposited from molecular complexes. *Energy & Environmental Science* **2013,** *6* (2), 579-586.

30. Sullivan, K. P.; Yin, Q.; Collins-Wildman, D. L.; Tao, M.; Geletii, Y. V.; Musaev, D. G.; Lian, T.; Hill, C. L., Multi-Tasking POM Systems. **2018,** *6* (365).

31. Sumliner, J. M.; Lv, H.; Fielden, J.; Geletii, Y. V.; Hill, C. L., Polyoxometalate Multi-Electron-Transfer Catalytic Systems for Water Splitting. *European Journal of Inorganic Chemistry* **2014,** *2014* (4), 635-644.

32. Surendranath, Y.; Dincă, M.; Nocera, D. G., Electrolyte-Dependent Electrosynthesis and Activity of Cobalt-Based Water Oxidation Catalysts. *Journal of the American Chemical Society* **2009,** *131* (7), 2615-2620.

33. Ullman, A. M.; Brodsky, C. N.; Li, N.; Zheng, S.-L.; Nocera, D. G., Probing Edge Site Reactivity of Oxidic Cobalt Water Oxidation Catalysts. *Journal of the American Chemical Society* **2016,** *138* (12), 4229-4236.

34. Wee, T.-L.; Sherman, B. D.; Gust, D.; Moore, A. L.; Moore, T. A.; Liu, Y.; Scaiano, J. C., Photochemical Synthesis of a Water Oxidation Catalyst Based on Cobalt Nanostructures. *Journal of the American Chemical Society* **2011,** *133* (42), 16742-16745.

35. Yin, Q.; Hill, C. L., Passing the Acid Test. *Nature Chemistry* **2018,** *10*, 6-7.

36. Yin, Q.; Tan, J. M.; Besson, C.; Geletii, Y. V.; Musaev, D. G.; Kuznetsov, A. E.; Luo, Z.; Hardcastle, K. I.; Hill, C. L., A Fast Soluble Carbon-Free Molecular Water Oxidation Catalyst Based on Abundant Metals. *Science* **2010,** *328* (5976), 342.

37. Young, E. R.; Nocera, D. G.; Bulović, V., Direct formation of a water oxidation catalyst from thin-film cobalt. *Energy & Environmental Science* **2010,** *3* (11), 1726-1728.

38. Zhang, L.-H.; Yu, F.; Shi, Y.; Li, F.; Li, H., Base-enhanced electrochemical water oxidation by a nickel complex in neutral aqueous solution. *Chemical Communications* **2019,** *55* (43), 6122-6125.

39. Zhang, T.; Wang, C.; Liu, S.; Wang, J.-L.; Lin, W., A Biomimetic Copper Water Oxidation Catalyst with Low Overpotential. *Journal of the American Chemical Society* **2014,** *136* (1), 273-281.

40. Zhu, G.; Glass, E. N.; Zhao, C.; Lv, H.; Vickers, J. W.; Geletii, Y. V.; Musaev, D. G.; Song, J.; Hill, C. L., A nickel containing polyoxometalate water oxidation catalyst. *Dalton Transactions* **2012,** *41* (42), 13043-13049.

41. Folkman, S. J.; Soriano-Lopez, J.; Galán-Mascarós, J. R.; Finke, R. G., Electrochemically Driven Water-Oxidation Catalysis Beginning with Six Exemplary Cobalt Polyoxometalates: Is It Molecular, Homogeneous Catalysis or Electrode-Bound, Heterogeneous CoOx Catalysis? *Journal of the American Chemical Society* **2018,** *140* (38), 12040-12055.

42. Soriano-López, J.; Goberna-Ferrón, S.; Carbó, J. J.; Poblet, J. M.; Galán-Mascarós, J. R., Chapter Six - $[Co_9(H_2O)_6(OH)_3(HPO_4)_2(PW_9O_{34})_3]^{16-}$: A Highly Efficient Catalyst for Water Oxidation. In *Advances in Inorganic Chemistry*, van Eldik, R.; Cronin, L., Eds. Academic Press: 2017; Vol. 69, pp 155-179.

43. Tsui, E. Y.; Tran, R.; Yano, J.; Agapie, T., Redox-inactive metals modulate the reduction potential in heterometallic manganese–oxido clusters. *Nature Chemistry* **2013,** *5* (4), 293-299.

44. Zhu, S.; Gao, X.; Dong, F.; Zhu, Y.; Zheng, H.; Li, Y., Design of a highly active silver-exchanged phosphotungstic acid catalyst for glycerol esterification with acetic acid. *Journal of Catalysis* **2013,** *306*, 155-163.

45. Emeis, C. A., Determination of Integrated Molar Extinction Coefficients for Infrared Absorption Bands of Pyridine Adsorbed on Solid Acid Catalysts. *Journal of Catalysis* **1993,** *141* (2), 347-354.

46. Ohkubo, K.; Menon, S. C.; Orita, A.; Otera, J.; Fukuzumi, S., Quantitative Evaluation of Lewis Acidity of Metal Ions with Different Ligands and Counterions in Relation to the Promoting Effects of Lewis Acids on Electron Transfer Reduction of Oxygen. *The Journal of Organic Chemistry* **2003,** *68* (12), 4720-4726.

47. Fukuzumi, S.; Ohkubo, K., Quantitative Evaluation of Lewis Acidity of Metal Ions Derived from the g Values of ESR Spectra of Superoxide: Metal Ion Complexes in Relation to the Promoting Effects in Electron Transfer Reactions. *Chemistry – A European Journal* **2000,** *6* (24), 4532-4535.

48. Chen, X.; McCrum, I. T.; Schwarz, K. A.; Janik, M. J.; Koper, M. T. M., Co-adsorption of Cations as the Cause of the Apparent pH Dependence of Hydrogen Adsorption on a Stepped Platinum Single-Crystal Electrode. *Angewandte Chemie International Edition* **2017,** *56* (47), 15025-15029.

49. Reath, A. H.; Ziller, J. W.; Tsay, C.; Ryan, A. J.; Yang, J. Y., Redox Potential and Electronic Structure Effects of Proximal Nonredox Active Cations in Cobalt Schiff Base Complexes. *Inorganic Chemistry* **2017,** *56* (6), 3713-3718.

50. Reddy, C. R.; Bhat, Y. S.; Nagendrappa, G.; Jai Prakash, B. S., Brønsted and Lewis acidity of modified montmorillonite clay catalysts determined by FT-IR spectroscopy. *Catalysis Today* **2009,** *141* (1), 157-160.

51. Boffa, A. B.; Lin, C.; Bell, A. T.; Somorjai, G. A., Lewis acidity as an explanation for oxide promotion of metals: implications of its importance and limits for catalytic reactions. *Catalysis Letters* **1994,** *27* (3), 243-249.

52. Rajagopal, S.; Marzari, J. A.; Miranda, R., Silica-Alumina-Supported Mo Oxide Catalysts: Genesis and Demise of Brønsted-Lewis Acidity. *Journal of Catalysis* **1995,** *151* (1), 192-203.

53. Mondschein, J. S.; Callejas, J. F.; Read, C. G.; Chen, J. Y. C.; Holder, C. F.; Badding, C. K; Schaak, R. E., Crystalline Cobalt Oxide Films for Sustained Electrocatalytic Oxygen Evolution under Strongly Acidic Conditions. *Chemistry of Materials* **2017**, *29* (3), 950-957

54. Brunschwig, B. S.; Chou, M. H.; Creutz, C.; Ghosh, P.; Sutin, N., Mechanisms of water oxidation to oxygen: cobalt(IV) as an intermediate in the aquocobalt(II)-catalyzed reaction. *Journal of the American Chemical Society* **1983,** *105* (14), 4832-4833.

55. McCrory, C. C. L.; Jung, S.; Ferrer, I. M.; Chatman, S. M.; Peters, J. C.; Jaramillo, T. F., Benchmarking Hydrogen Evolving Reaction and Oxygen Evolving Reaction Electrocatalysts for Solar Water Splitting Devices. *Journal of the American Chemical Society* **2015**, *137* (13), 4347-4357.

56. McCrory, C. C. L.; Jung, S.; Peters, J. C.; Jaramillo, T. F., Benchmarking Heterogeneous Electrocatalysts for the Oxygen Evolution Reaction. *Journal of the American Chemical Society* **2013**, *135* (45), 16977-16987.

Chapter 5

Stabilization of a Copper-Oxo Unit in Base Utilizing Polyoxoniobates

This study is the result of a collaborative effort with significant experimental contributions from

Yimu Hu and Elliot Glass

Introduction

Chapter 4 dealt with water oxidation in acidic environments. We now move 11 pH units in the other direction and consider water oxidation in strong base. In contrast to acid, basic environments are much more thermodynamically favorable for water oxidation.[1-4] Consequently, there are a many examples of catalysts in base, mostly of heterogeneous materials or electrocatalysts,[3, 5-25] but also some molecular catalysts.[2, 7, 25-34] However, no POM-based OER catalysts has been found that remains homogeneous and functional in alkaline conditions. For the sake of completion, we are obligated to report in this chapter the first molecular, base-compatible POM OER catalyst, $[H_9Cu_{25.5}O_8(Nb_7O_{22})_8]^{28-}$ (**1**) as its $K_{16}Na_{12}$ salt (**KNa-1**).

Despite the now quite mature field of base-compatible OER catalysts, the number of molecular catalysts available for study under basic conditions are quite limited. Under alkaline conditions, the number of heterogeneous materials that catalyze OER far outnumber homogeneous molecular ones.[24] Much of this is due to the tendency for metal oxides/oxyhydroxides to form under basic conditions. As such, ligands that can stabilize and protect redox-active metal centers in the presence of strong base while allowing the transition metal to remain an active site for water (or more likely hydroxide) oxidation can be quite interesting to study.

Thus far, there have been no other reported base-compatible POM catalysts. This is not surprising, as the nature of polyoxometalate chemistry is closely related to that of metal oxide chemistry. So many of the traditionally active metals, such as cobalt and nickel, will tend to form metal oxyhydroxides in base. Moreover, typical POM frameworks used in 3-d transition metal substituted systems such as polyoxotungstates will dissolve into its component WO_4^{2-} species.

In this chapter, we report the utilization of polyoxoniobates to stabilize cuprates in strong base. Furthermore, we utilize **KNa-1** as an OER catalyst. After serving as a homogeneous OER electrocatalyst, **KNa-1** was subsequently and thoroughly characterized by a number of different techniques to investigate its stability. Through this process, we are able to gain some insights into the nature of polyoxoniobates as stabilizing ligands, and the solution phase chemistry of the **1** poly anion cluster.

Results and Discussion

Structural characterization of KNa-1.

KNa-1 was independently synthesized as previously described in the literature,[35] and was characterized by X-ray crystallography (Figure 5.1). The polyanion, **1**, is a large and structurally complex specie. However, it is highly symmetric, with an O point symmetry. Small deviations are observed due to minor distortions in the crystal unit cell. One way to break down the visualization of **1** is to consider it as a cube with 8 $[Nb_7O_{22}]^{9-}$ units capping each of the corners. These $[Nb_7O_{22}]^{9-}$ units coordinate 24 bridging square planar CuO_4 units and all isopolyniobates are centered by a $Cu_{1.5}O_8$ motif. UV-Vis spectroscopy of **KNa-1** exhibits the characteristic Cu(II) d-d transition at 680 nm (Figure 5.2).

Polyanion, **1**, is shown to be hydrolytically stable under basic conditions (pH 12-13). No changes in the absorption spectrum are observed by aging **1** in a pH 12 solution for a day. In fact, crystals of **1** may be obtained from these basic conditions. Furthermore, no precipitates are observed in base. In contrast, aqueous copper (II) readily precipitates in the presence of base. This results from the miniscule solubility product of $Cu(OH)_2$: $K_{sp} = 2.2\times10^{-20}$.[36]

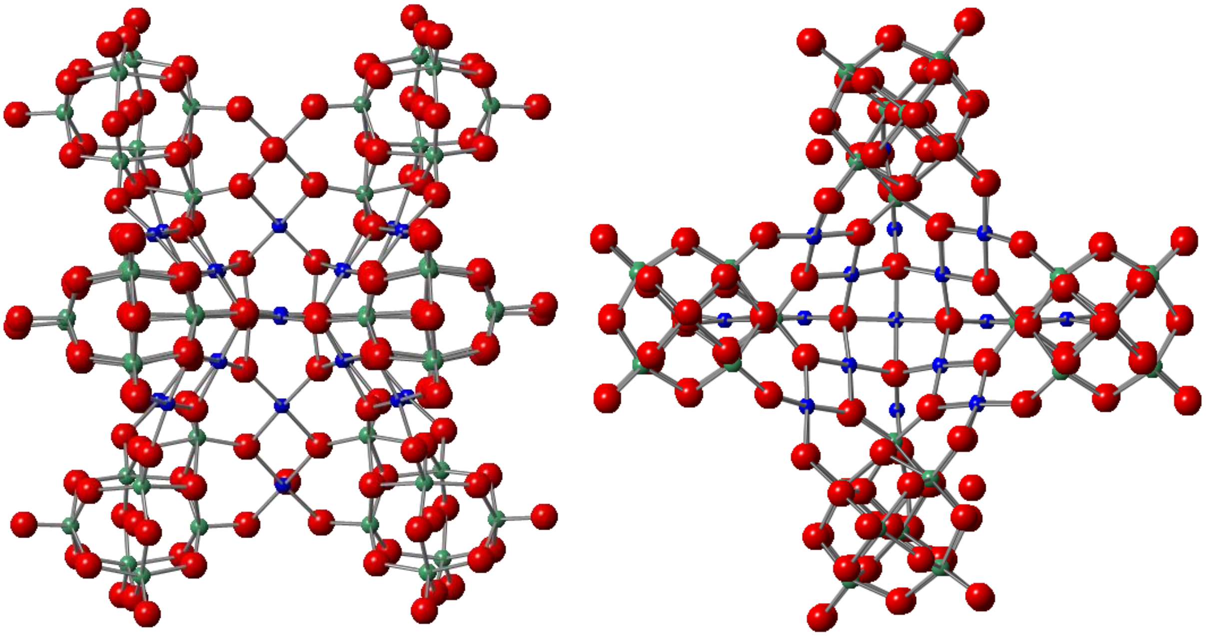

Figure 5.1 The ball-and-stick representations of the polyanion, **1**, from two different vantages. Other discrete K^+, Na^+ cations, and water molecules are omitted for clarity.

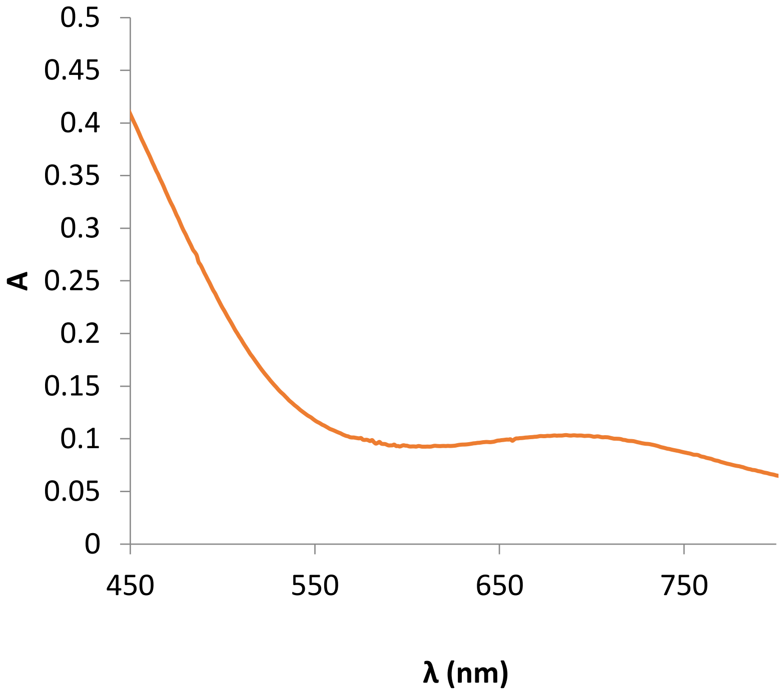

Figure 5.2 The UV-Vis absorption spectrum of 100 μM of **KNa-1** in 0.1 M KOH at pH 13.

Electrochemical solution phase OER catalysis

In order to probe the water oxidation capability of this **KNa-1** in base, we systematically investigated the redox properties of **KNa-1** using electrochemistry in 0.1 M KOH. The cyclic voltammetry (CV) of **KNa-1** exhibited a large, irreversible oxidative wave that corresponds to water oxidation (Figure 5.3). An appreciable catalytic current for water oxidation (≥ 0.1 mA cm^{-2}) became observable at ~0.8 V (onset potential, corresponding to $\eta = 340$ mV), significantly lower than previously reported mono- and di-nuclear Cu-based molecular OER catalysts.[7, 26, 28, 33, 37-41] Upon addition of 2 mM $CuSO_4$ to the buffer, immediate precipitation of $Cu(OH)_2$ was observed, and the resulting suspension exhibits no water oxidation activity. The same control experiment was also carried out for 2 mM $K_7HNb_6O_{19}\cdot 13H_2O$ in 0.1 M KOH, which also showed no activity. That the suspension/solution is catalytically inactive indicates that the catalytic current is likely due to the POM and not from uncomplexed Cu(II) or $Nb_6O_{19}^{8-}$ in solution.[8, 27, 42] Therefore, the incorporation of the Cu(II) centers into the polyoxoniobate architecture is likely essential for the observed electrochemical activity at this pH.

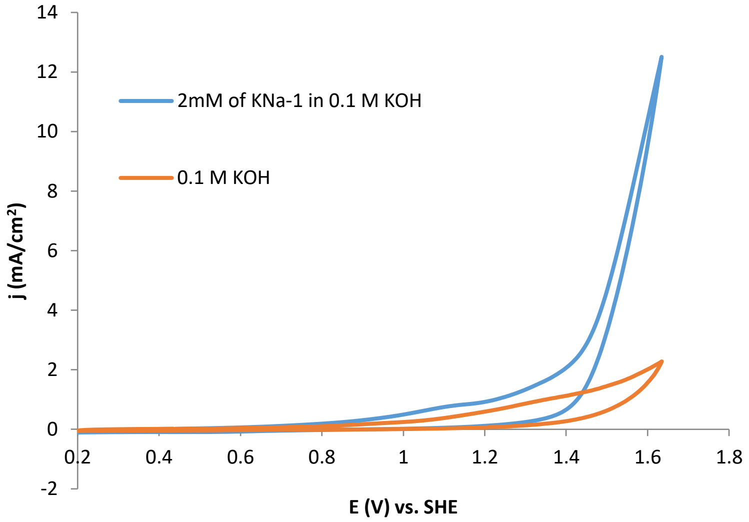

Figure 5.3 CV of solubilized 1 mM **KNa-1** in 0.1 M KOH (pH 13) at a glassy carbon working electrode, 50mV/s scan rate, referenced to 1M Hg/HgO.

The production of oxygen was confirmed and measured quantitatively during chronoamperometry (bulk electrolysis, BE) at 1V vs. 1M Hg/HgO (overpotential η = 0.677 V) with an FTO working electrode (0.56 cm^2) for 24 hours. The experiment was performed in a gas-tight, two-compartment cell with a stirred solution of 1.0 mM **KNa-1** in 0.1 M KOH. A current of ~1 mA/cm^2 was maintained throughout the whole duration of electrolysis (Figure 5.4). In contrast, the current density in the absence of **KNa-1** quickly decays and eventually reaches less than 0.1 mA/cm^2. The amount of O_2 was measured by a calibrated Ocean Optics FOXY probe, with a final Faradaic efficiency of 97% after 10 hours (Figure 5.5). Without the **KNa-1** in solution, the background O_2 formation was negligibly small. Clearly, the **KNa-1** is very active in OER under basic conditions. Importantly, we show that **KNa-1** is active in OER catalysis at pH 13 and pH 12 for up to 24 hours of continuous water/hydroxide oxidation (Figure 5.5). This ultimately corresponds to a turnover number (TON) of ~30.

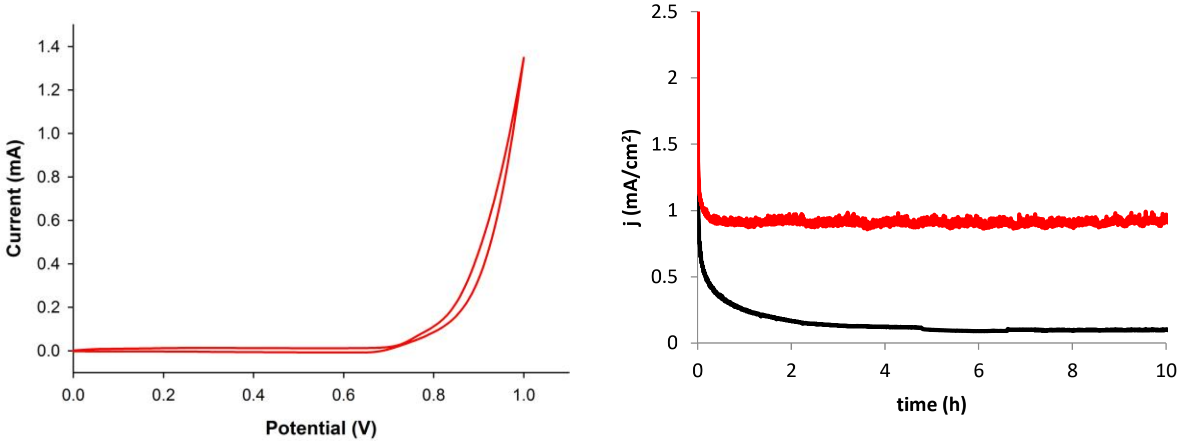

Figure 5.4 Left: CV of solubilized 1 mM **KNa-1** in 0.1 M KOH (pH 13) at an FTO working electrode, 50mV/s scan rate, referenced to 1M Hg/HgO. Right: catalytic current obtained upon chronoamperometry at controlled potential without (black) and with (red) 1 mM **KNa-1** in 0.1 M KOH at 1.25 V vs. SHE using an FTO working electrode (A = 0.56 cm^2).

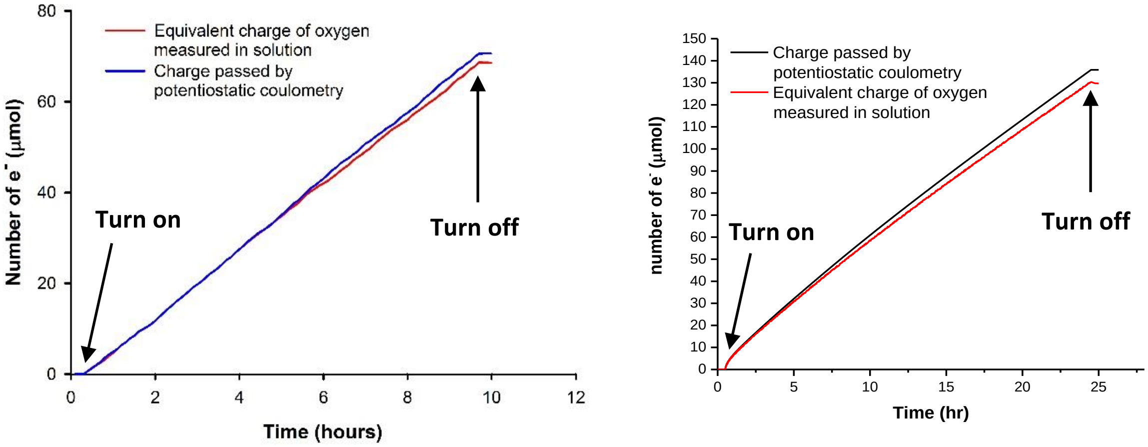

Figure 5.5 Left: plot of detected dioxygen and total charge passed during chronoamperometry, converted to molar equivalents of electrons, over the course of ~10 hours at pH 13, η = 0.677, 97% Faradaic efficiency. Right: plot of detected dioxygen and total charge passed during chronoamperometry, converted to molar equivalents of electrons, over the course of ~24 hours at pH 12, η = 0.618, 95% Faradaic efficiency, 1 mM **KNa-1**, KOH buffer, 1V applied potential vs. 1M Hg/HgO. FTO working electrode.

Kinetics

CVs were recorded with glassy carbon electrodes at different scan rates to investigate the kinetics of the electron transfer process involving **1**. Scanning the solution of **KNa-1**, initially purged with nitrogen, in the cathodic direction shows a quasi-reversible Cu(II/I) couple at $E_{p,a}$ = 0.2 V vs. NHE (Figure 5.6). At pH 13, the reversible diffusive current for the Cu(II/I) couple varies linearly with the square root of the scan rate (Figure 5.6), as described by the Randles-Sevcik equation,

$$i_d = 0.4633nFAC(nF\nu D_{\mathbf{1}}/RT)^{1/2} \qquad (5.1)$$

with n = 1, the electron transferred in the noncatalytic process; F is the Faraday constant, A is the electrode surface area (0.07 cm^2), C is the catalyst concentration (100 μM), ν is the scan rate, D_1 is the diffusion coefficient of **1**, and T is the absolute temperature. The ratio of the catalytic peak current i_{cat} (given by equation 5.2) over the diffusive current, i_d, matches the pure kinetics regime behavior at low scan rate (≤ 10mV/s) and low catalyst concentration (100 μM **KNa-1**, Figure 5.7),

$$i_{cat} = n_{cat}FAC(k_{cat}D_1)^{1/2} \qquad (5.2)$$

in which n_{cat} = 4 as the number of electrons transferred for water oxidation. The division of equation 5.2 by 5.1 gives equation 5.3,

$$i_{cat}/i_d = 1.424(k_{cat}/\nu)^{1/2} \qquad (5.3)$$

Solving for k_{cat} in equation 5.3 for **1** using the highest achieved catalytic OER current gives an apparent rate constant k_{cat} of 40 s^{-1} (Figure 5.7), this value can be interpreted as the turnover frequency (TOF) for catalytic water oxidation in 0.1 M KOH at pH 13 given an overpotential of ~1.1 V. This value is comparable with that of the previously reported copper bipyridine (~100 s^{-1})[26] and copper polypeptide (~33 s^{-1})[37] complexes under comparable catalytic conditions (pH 12.5 and 11, respectively), and significantly higher than those of other reported molecular copper OER catalysts.[20–26] Here, it should be noted that while the behavior of equation 5.3 matches that of the pure kinetics regime, it is not technically applicable, as the catalytic current is not limited only by the water oxidation steps, as shown by the linear shape of the catalytic current. The apparent k_{cat}, and in turn TOF, value of 40 s^{-1} that we derived is thus likely a lower limit. The OER parameters, kinetics, and stability data of **KNa-1** are summarized in Table 1 along with that of select other copper-based molecular OER catalysts. **KNa-1** is noteworthy as a strong-base-stable POM catalyst capable of relatively fast homogeneous OER catalysis.

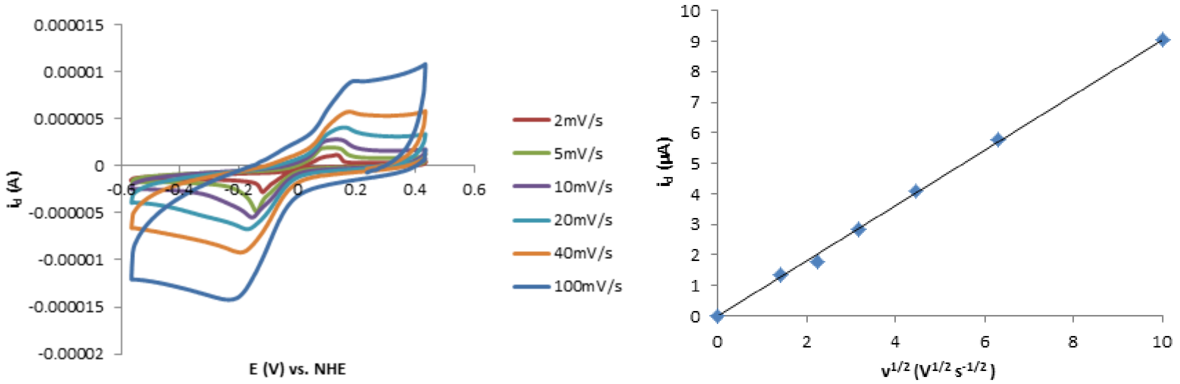

Figure 5.6 Left: CV of the Cu(I/II) couple during a reductive scan, scan rate from 2 to 100 mV/s of 100 μM **KNa-1** in 0.1 M KOH at pH 13 using a glassy carbon working electrode (A = 0.07cm^2). Right: dependence of the peak current for the Cu(I/II) couple at $E_{p,a}$ = 0.1 V vs. NHE.

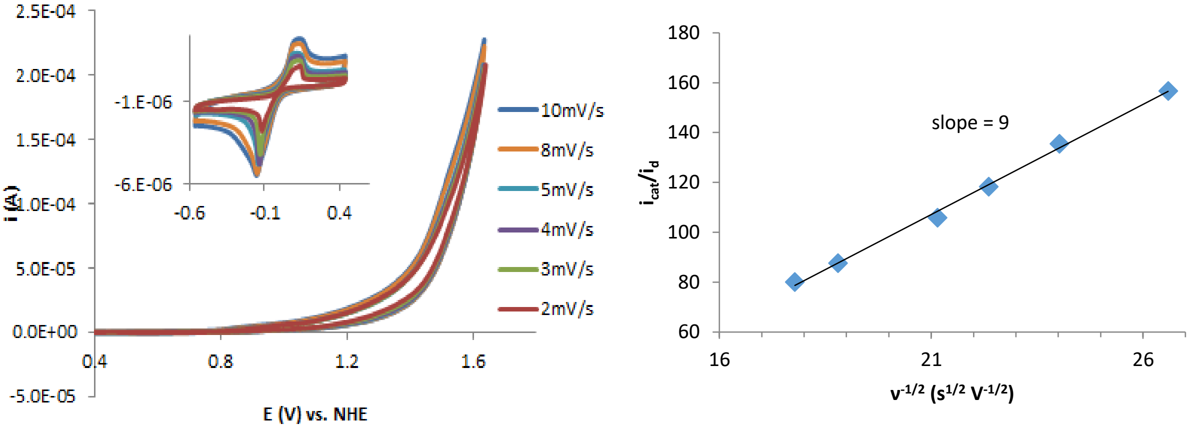

Figure 5.7 Left: CVs of 100 μM **KNa-1** in 0.1 M KOH at pH 13 at different scan rates from 2 to 10 mV/s using a glassy carbon working electrode (A = 0.07cm^2). Insert: CVs of the Cu(I/II) couple during a cathodic scan of **KNa-1**. Right: plot of the ratio of the catalytic current at 1.635 V, i_{cat}, to the oxidative peak current for the Cu(II/I) wave, i_d, vs $v^{-1/2}$ (v = 2, 3, 4, 5, 8, and 10 mV/s).

Table 5.1. Kinetic, electrochemical, and stability data of **KNa-1** and other select copper-based molecular OER catalysts reported in the literature

Entry	Catalyst[b]	pH	Onset[c] (0.1 mA/cm^2) η, mV	k_{cat}, s^{-1}	Stability[d]
1[a]	**KNa-1**	13	380	40	24 h @ 1 mA/cm^2
2[26]	$[(bpy)Cu(OH)_2]$	12.5	750	100	30 min @ 0.5 mA/cm^2
3[37]	$[(TGG)^{4-}\ Cu\text{-}OH_2]^{2-}$	11	520	33	5 h @ 0.8 mA/cm^2
4[41]	$[Cu_2(BPMAN)(\mu\text{-}OH)]^{3+}$	7.0	~1050	0.6	0.5 h @ 0.4 mA/cm^2
5[7]	$[(Py_3P)Cu(OH)]^-$	8.0	~ 500	20	7 h @ 0.2-0.3 mA/cm^2
6	Cu(II)	10.8	~860[42, e]	0.1[27, e]	30 h @ ~ 0.38 mA/cm^2
7[28]	[N1,N1’ – (1,2-phenylene)Cu]-$(NMe)_2$	11.5	700	3.56	1 h 2 0.11 mA/cm^2
8[38]	$[(dhbp)Cu(OH_2)_2]$	12.4	540	0.4	3 h @ 0.15 mA/cm^2
9[32]	$[(\alpha\text{-}SbW_9O_{33})_2Cu_3(H_2O)_3]^{12-}$	7.1	1200	0.7	likely unstable

[a] this work. [b] bpy = 2,2’-bipyridine; TGG = triglycylglycine; BPMAN = 2,7-[bis(2-pyridylmethyl)aminomethyl]-1,8-naphthyridine; Py_3P = *N*,*N*-bis(2-(2-pyridyl)ethyl)pyridine-2,6-dicarboxamidate; dhbp = 6,6′-dihydroxy-2,2′-bpy. [c] Measured by DPV for 7 and 8 and from the initial foot of the electrocatalytic curve or the catalytic current density from CV for the rest. [d] These values generally are not highly informative, as they do not list the TON. In addition, in many cases, these values appear to be lower-bound time frames. [e] For Cu(II), η was measured using $CuSO_4$ as Cu(II) source at pH 10.8,[42] while k_{cat} was measured at pH 6.7 in 1 atm CO_2-saturated 0.1 M $NaHCO_3$[27]

Homogeneous electrocatalyst identity

Aqueous or uncomplexed Cu(II) ions and copper oxide deposits formed from Cu-based precursor complexes under electrocatalytic conditions are known to be OER catalysts.[8, 43-44] Herein, we attempt to elucidate the identity of the active OER electrocatalyst in this system. Is **KNa-1** is a stable molecular catalyst or a pre-catalyst for another homogeneous species for OER electrocatalysis under strong alkaline conditions?

The characteristic copper-based absorption of **KNa-1** at 680 nm remains nearly constant after 24 hours of homogeneous OER catalysis. Little significant changes are observed in the UV-Vis spectra (Figure 5.8). Changes in the structure **KNa-1** during catalysis could result in a shift in the visible spectrum. However, given the conventional nature of the Cu(II) d-d transition bands, we cannot rule out any chemical change that may occur to **KNa-1**.

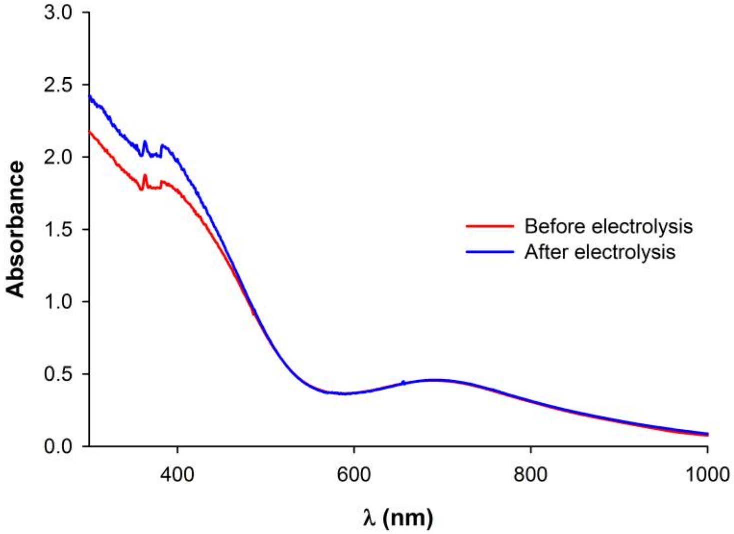

Figure 5.8 UV-Vis spectrum of **KNa-1** before (red line) and after (blue line) 24 h of electrolysis. Conditions: 1 mM **KNa-1** catalyst in 0.1 M KOH (pH = 13) was used in chronoamperometry. The solution was diluted 10 times by 0.1 M KOH for UV-Vis spectroscopy. There was no significant change in the absorption spectrum after a 24 h electrolysis period.

Since KOH is soluble in ethanol, while most other polyionic species present, including **KNa-1**, are minimally soluble, we can use ethanol to extract excess KOH from the reaction solution after electrocatalytic OER. Subsequent centrifugation facilitates isolation of all the copper-containing species as a precipitate. The FT-IR spectrum in the Nb-O region from 400 to 1200 cm^{-1} of the recovered green precipitate is very similar to that of crystalline **KNa-1** (Figure 5.9). However, the disappearance of the peak at 1150 cm^{-1} and the decrease of the peak at 500 cm^{-1} suggest that **KNa-1** may, in fact, have undergone some small changes in its structure.

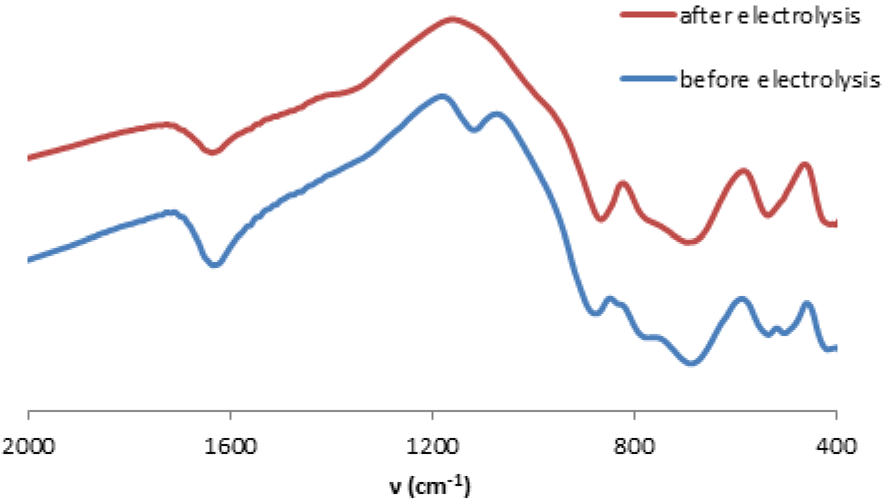

Figure 5.9 FT-Infrared spectrum of **KNa-1** before (blue) and after (red) 24 hours of chronoamperometry. All FT-IR spectroscopy was performed using 1 wt% sample in KBr pellet.

X-ray photoelectron spectroscopy was performed on similar samples as those used for the above-described FT-IR characterization (Figure 5.10). Unfortunately, due to Cu(II) shake-up peaks, there is >50% error on any quantitative fitting we may attempt. Nevertheless, there is some useful information we can infer from Figure 5.10. The Cu 2p$_{3/2}$ and Cu LMM Auger peak energies indicate Cu(II), in line with our expectations. Interestingly, the Cu LMM shape resembles Cu(OH)$_2$

rather than CuO, which could mean that the polyoxoniobate framework in **KNa-1** significantly changes the electronic structures of the bridging CuO_4 moieties to be more akin to copper hydroxides rather than oxides. This may also explain the relative base-stability of **KNa-1**. The Nb 3d$_{5/2}$ energy along with the Cu 2p$_{3/2}$ energy demonstrate that some copper charge density is delocalized into the niobate framework. Nonetheless, these XPS measurements show little change in the electronic structures of K, Cu, and Nb atoms after OER electrocatalysis.

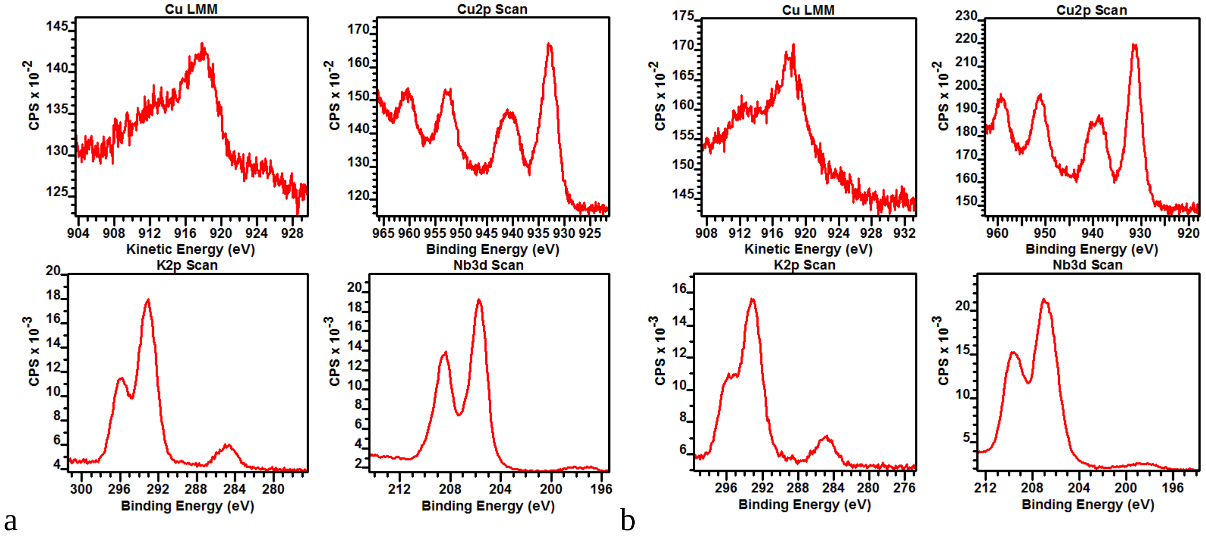

Figure 5.10 High resolution XPS spectra of **KNa-1** before (a) and after (b) 24 hours of chronoamperometry at pH 13. Conditions: 0.1 M KOH, 1 V vs. Hg/HgO, FTO working electrode (0.56 cm^2).

In a multi-segment scan CV of **KNa-1**, the maximum current and the shape of CV curve do not change upon multiple scan cycles (Figure 5.11). We note that the current density decrease between scan cycles is likely attributable to the generation of an observable O_2 gas bubble. The glassy carbon working electrode was shaken slightly to remove the gas bubbles attached on the electrode surface in between the two 8-cycles (green and red). Alternatively, the diffusion of reactive species to the working electrode surface is simply too slow to keep up with the moderate scan rate. CV of **KNa-1** at an FTO electrode before and after 24 hours of chronoamperometry also shows little change (Figure 5.12). Slight differences in the shape of the anisotropic catalytic current can be attributed to innate surface changes on the FTO electrode (Figure 5.15).

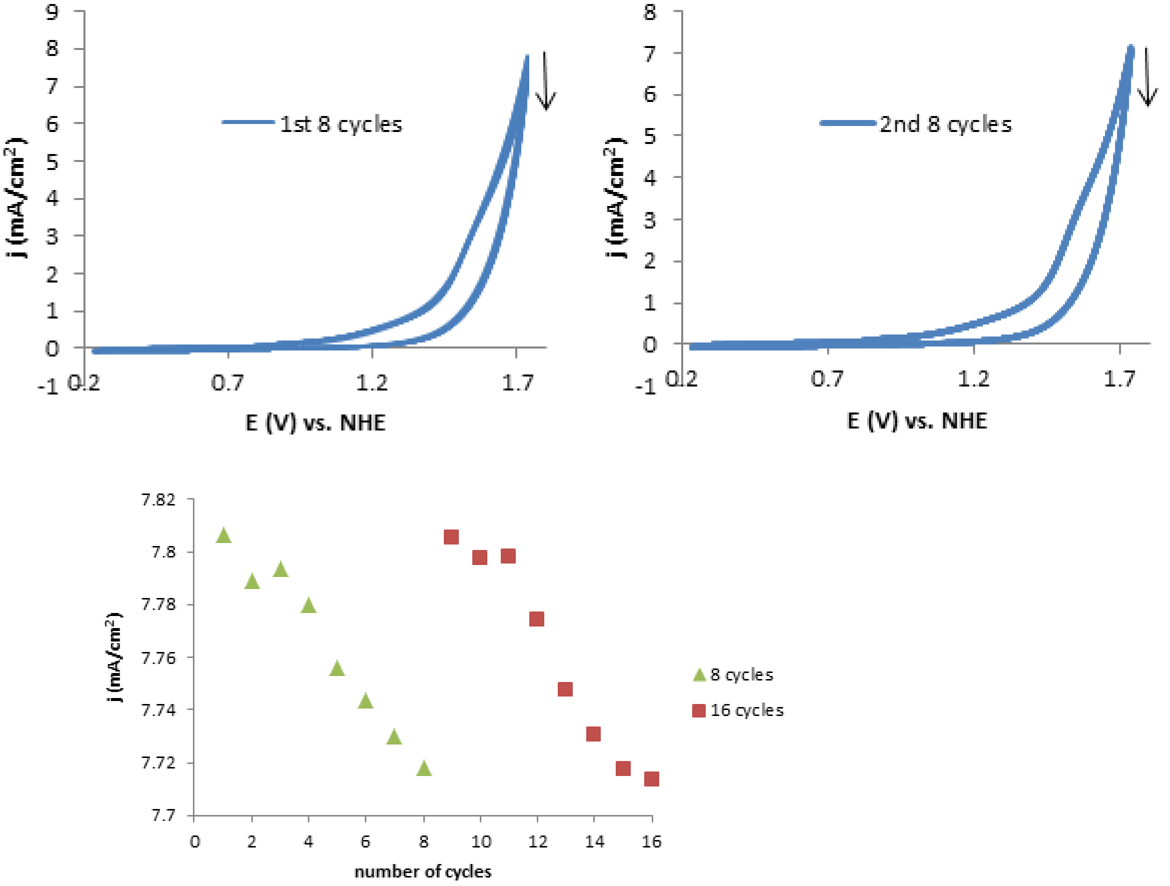

Figure 5.11 Top: two series of 8 continuous scan cycles of 1 mM **KNa-1** in 0.1 M KOH (pH 13). There is little change in CV shape during the multiple scans. Bottom: the plots of peak current density as a function of the scan cycle. Conditions: glassy carbon working electrode (0.071 cm^2); scan rate 50 mV/s.

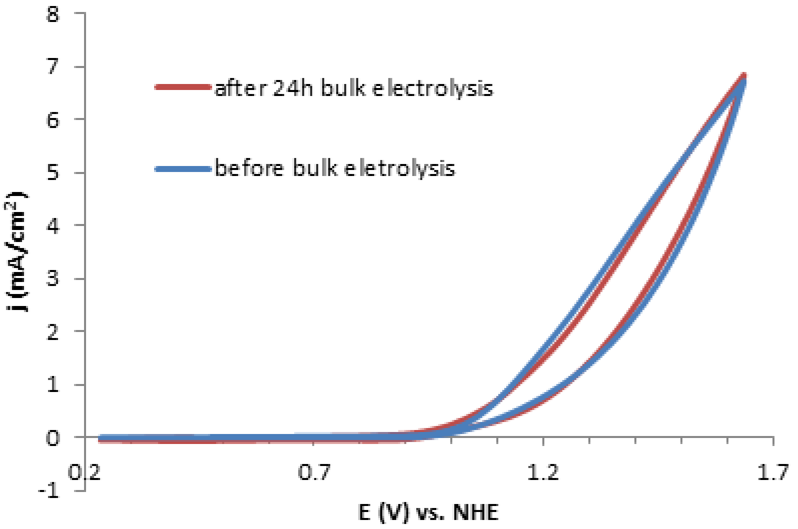

Figure 5.12 CVs of **KNa-1** before (blue) and after (red) 24 hours of chronoamperometry at pH 13. Conditions: 0.1 M KOH, 1.25 V vs. NHE, FTO working electrode, A = 0.56 cm^2.

To rule out electrodeposition of heterogeneous OER catalysts, a FTO electrode that had undergone 24 hours of chronoamperometry at 1.25 V vs. NHE in 0.1 M KOH at pH 13 with 1 mM of **KNa-1** was reused. After chronoamperometry, the electrode was rinsed continuously with DI water for 1 minute but was not polished in any way. The same electrode was then used for chronoamperometry in 0.1 M KOH without catalyst under the same potentiometric conditions. No catalytic current was generated on the reused electrode (Figure 5.13), likely because no electrodeposition had occurred. The difference in the current density profile of the reused electrode compared to that of a fresh FTO electrode is likely due to innate changes on the FTO surface (Figure 5.15). A similar result was also obtained using a GC working electrode (Figure 5.14).

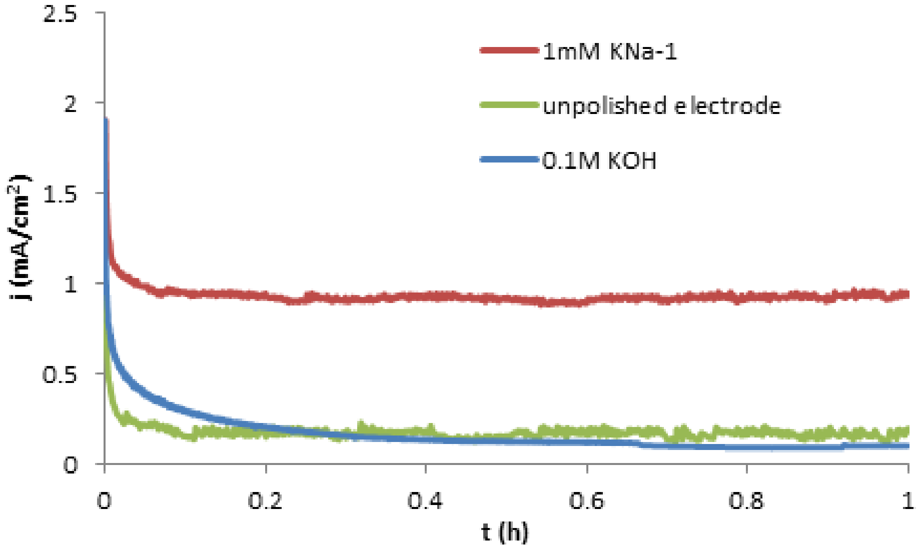

Figure 5.13 Catalytic current obtained with (red) and without (blue) 1 mM **KNa-1** in 0.1 M KOH with an FTO working electrode (A = 0.56 cm^2). The reused electrode (green) shows very little OER activity.

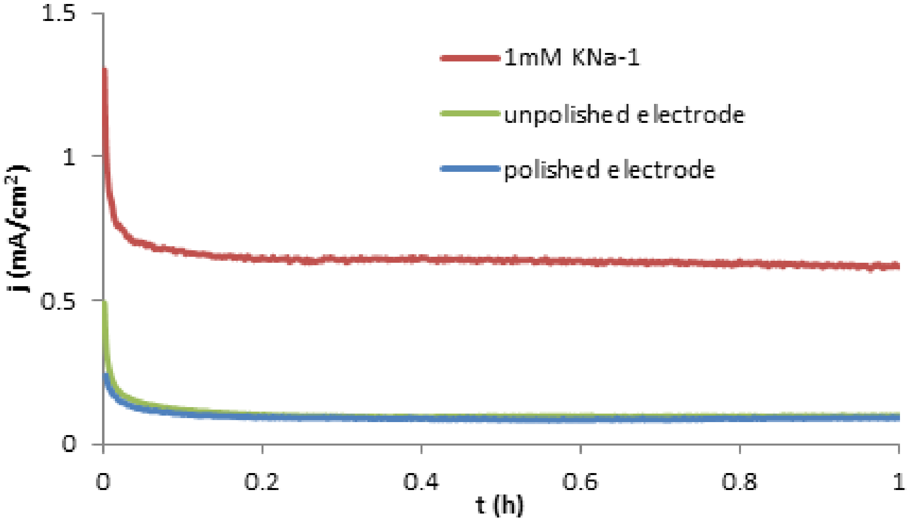

Figure 5.14 Catalytic current obtained with (red) and without (blue) 1 mM **KNa-1** in 0.1 M KOH using a glassy carbon working electrode (A = 0.071 cm^2). The reused electrode (green) shows very little OER activity.

Finally, the morphology and composition of the FTO electrode surface before and after catalysis were analyzed by scanning electron microscopy (SEM) and energy-dispersive X-ray spectroscopy (EDX). No morphology changes from precipitation or deposition film buildup were observed on the electrode surface (Figure 5.15), and the absence of Cu signals for copper oxide deposits in EDX measurement further confirmed that the catalytic system remains homogeneous, even after 24 hours of sustained electrolysis. Overall, these five lines of investigation strongly suggest that **KNa-1** is generally stable to large scale decomposition, precipitation, and electrodeposition under catalytic conditions.

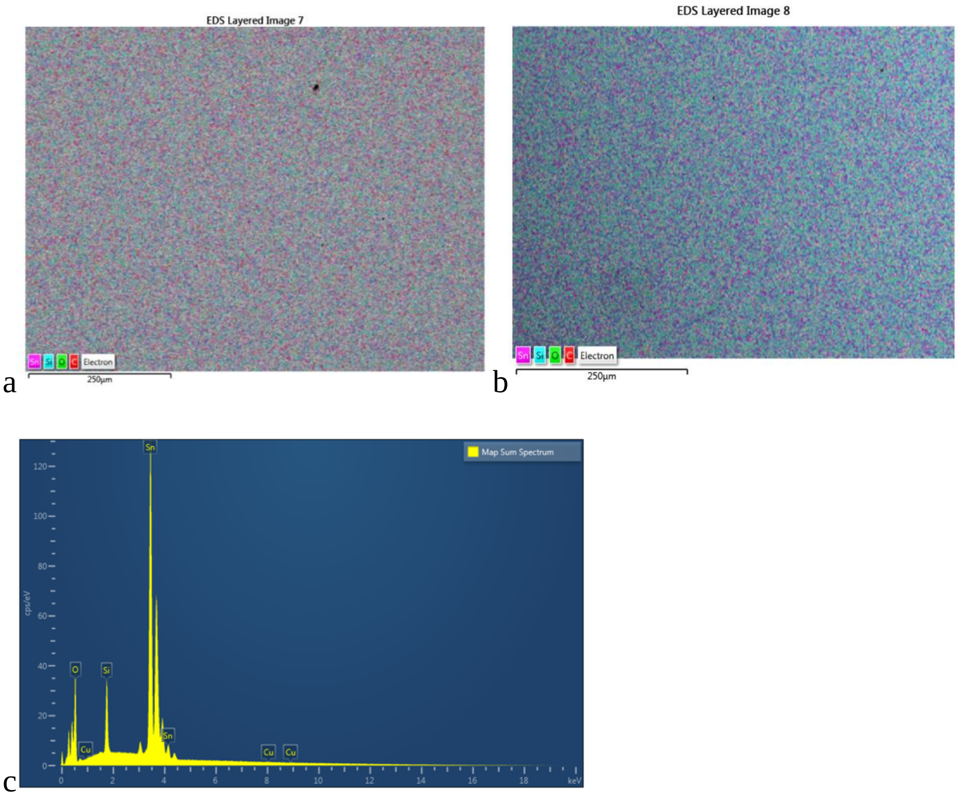

Element	Line Type	Wt%	Wt% Sigma	Atomic %
O	K series	25.32	0.23	67.88
Si	K series	4.40	0.05	6.72
Cu	K series	0.00	0.00	0.00
Sn	L series	70.28	0.22	25.40
Total:		100.00		100.00

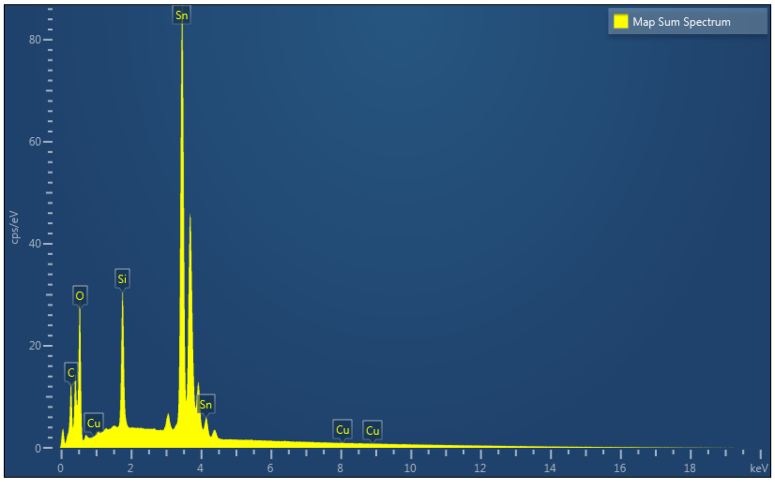

d

Element	Line Type	Wt%	Wt% Sigma	Atomic %
O	K series	28.01	0.11	69.68
Si	K series	5.71	0.03	8.10
Cu	K series	0.00	0.00	0.00
Sn	L series	66.27	0.10	22.22
Total:		100.00		100.00

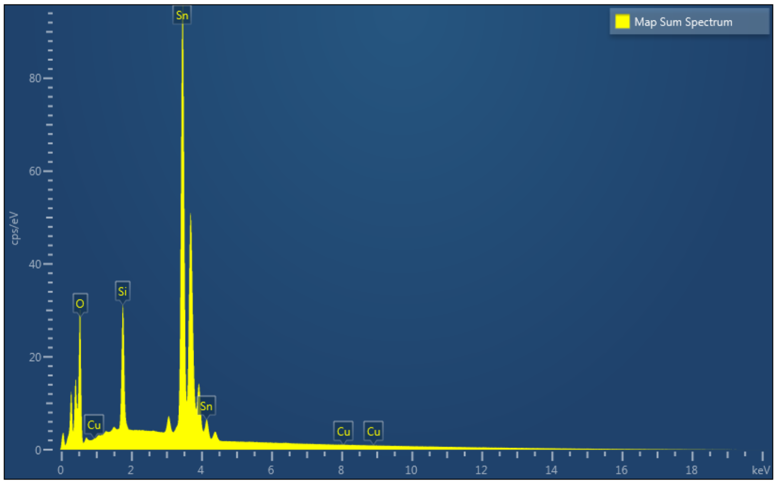

e

Element	Line Type	Wt%	Wt% Sigma	Atomic %
O	K series	27.23	0.07	69.18
Si	K series	5.35	0.02	7.74
Cu	K series	0.00	0.00	0.00
Sn	L series	67.41	0.07	23.08
Total:		100.00		100.00

f

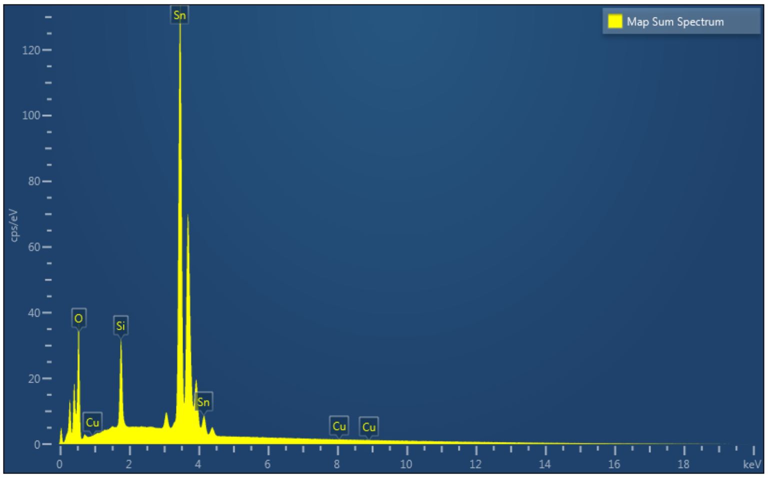

Element	Line Type	Wt%	Wt% Sigma	Atomic %
O	K series	24.69	0.10	67.50
Si	K series	3.99	0.02	6.22
Cu	K series	0.00	0.00	0.00
Sn	L series	71.31	0.10	26.28
Total:		100.00		100.00

Figure 5.15 SEM images of FTO electrodes before (a) and after (b) 24 hours of chronoamperometry. EDX spectra and elemental analysis of the FTO electrode surfaces before (c) after 6 hours (d), 12 hours (e), and 24 hours (f) of chronoamperometry, respectively. The Cu labels in the EDX spectra indicate where the Cu-based energies are expected, even though Cu is not observed on the electrode surface. The FTO electrodes used in (b), (d), (e), and (f) were rinsed for 1 minute following chronoamperometry.

Thus far, there is good evidence that **KNa-1** remains a soluble molecular species in solution and does not precipitate or electrodeposit even after extensive electrocatalytic OER. As previously discussed, Cu(II) shouldn't be soluble in strongly alkaline conditions. Specifically, Cu(II) should form insoluble $Cu(OH)_2$ under our experimental conditions (Figure 5.16). However, **KNa-1** is at the very least hydrolytically stable at pH 13. Along with our findings in Figure 5.10, we can rationalize **KNa-1** as polyoxoniobates ligating multiple copper ions to impart copper hydroxyl character, and thus thermodynamic stability, to protect these molecular polycuperates at high pH and high oxidation potentials (Figure 5.16).

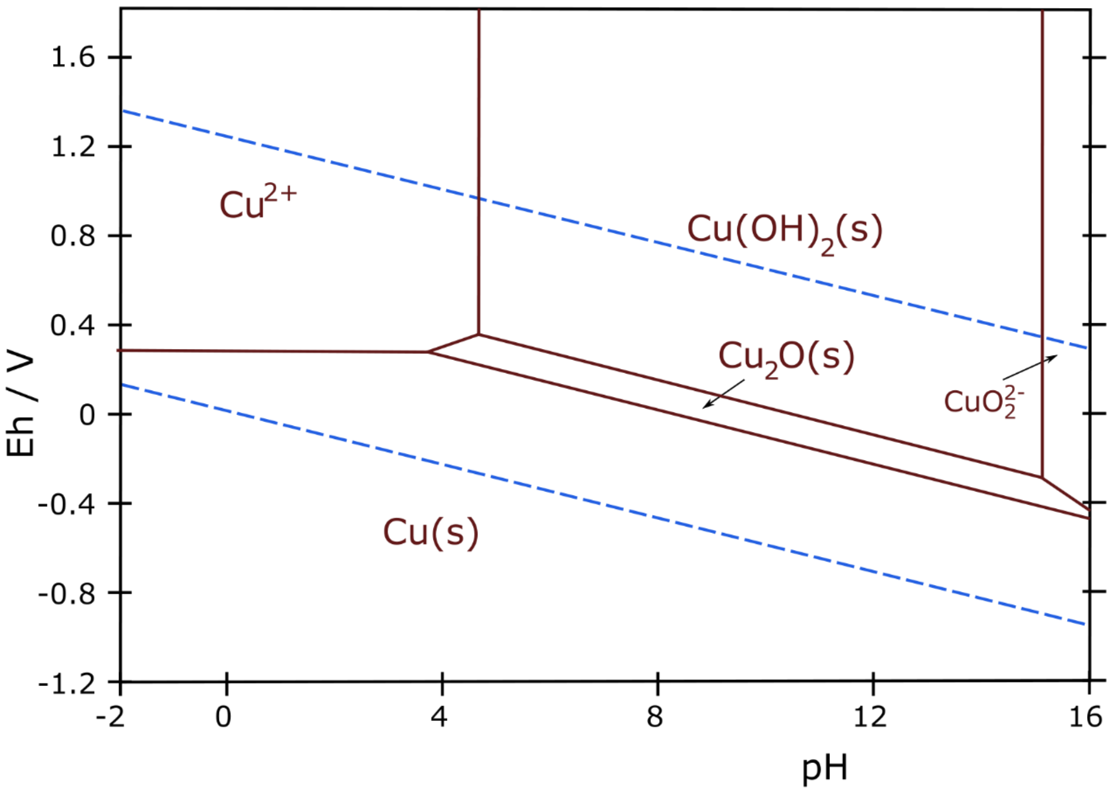

Figure 5.16 Pourbaix diagram of copper from strongly acidic to strongly basic pH values.[36]

Small-angle X-ray scattering

Despite apparently confirming the molecular nature of the active OER catalyst, we still do not have concrete evidence on the precise identity of the homogeneous electrocatalyst under our experimental conditions. It is unclear whether **KNa-1** remains electronically and structurally intact or if it is a pre-catalyst for another molecular OER electrocatalyst. Thus, we employ small-angle

X-ray scattering (SAXS) to investigate the stability and speciation of **KNa-1** in aqueous solutions relevant to water oxidation. The results indicate a difference in the stability of the cluster between aqueous conditions below pH 13 and at pH 13 (*vide infra*), and will be discussed separately. X-ray scattering curves of 1 mM **KNa-1** aged for 48 hours in water (unbuffered, pH 10.5), 0.1 M KCl, and 0.1 M sodium phosphate buffers at pH 11 and 12 are shown in Figure 5.17 and compared to the simulated data. In each case, the scattering curves are similar and closely match the simulated data, indicating that **KNa-1** retains the same structure in solution as determined by single-crystal X-ray diffraction. In water, the difference from other solutions observable at 0.02-0.06 Å^{-1} is due to an interference peak indicative of inter-particle repulsion. This interference is not observed in solutions with higher electrolyte concentrations due to electrostatic shielding of neighboring clusters.[45]

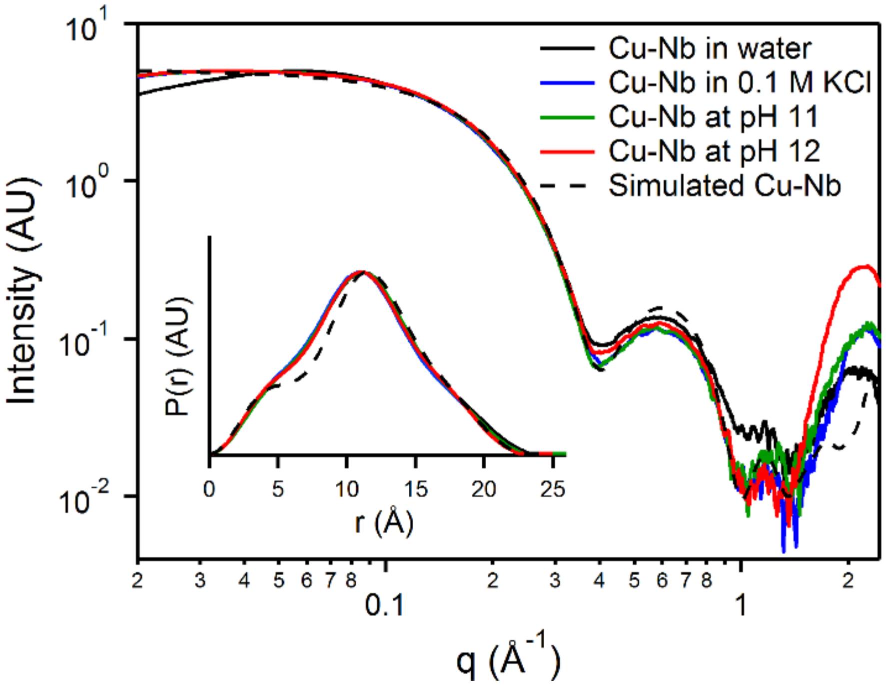

Figure 5.17 X-ray scattering curves of 1 mM **KNa-1** in various aqueous conditions after aging 48 hours, and the simulated scattering curve. Inset: Normalized pair-distance distribution function (PDDF) profiles.

Pair-distance distribution function (PDDF) profiles for **KNa-1** in each solution were determined by curve-fitting of the scattering curves using the Moore method (Figure 5.17 inset).[46] The PDDF profiles show negligible differences and the bell curve corresponds well to an approximate spherical shape, the closest simple shape to the determined X-ray crystal structure. The maximum linear extent, D_{max}, the distance at which the probability reaches zero, for each profile is 24-25 Å, which is quite close to the diagonal dimensions of the **KNa-1** cluster (Table 5.2). The radii of gyration, R_g, for **KNa-1** in each condition are also similar to each other; the simulated cluster has a smaller R_g because no associated countercations were assumed in its simulated scattering curve. Size distribution analyses of the scattering curves in Figure 5.17 were also very similar; for simplicity, only one analysis is reproduced here (Figure 5.18). Size distribution fitting of the scattering curve at pH 12 after aging 48 hours identifies a single population in solution with a mean diameter of 22 Å, indicating a monodisperse solution of **KNa-1** units. The similarities between scattering curves and associated analyses strongly support the conclusion that **KNa-1** is intact and stable under aqueous conditions at and below pH 12.

Table 5.2 Calculated form factor parameters for **KNa-1** in various aqueous conditions by SAXS

	PDDF Analysis‡		Guinier Analysis	Size Distribution
Medium†	R_g (Å)	D_{max} (Å)	R_g (Å)	Diameter (Å)
Water	9.16	25.3	9.50	23.1
0.1 M KCl	9.10	24.8	9.59	23.4
pH 11	9.05	24.6	9.58	23.3
pH 12	8.94	24.1	9.49	23.4
Simulated	8.54	22.5	9.22	22.5

† Parameters cannot be reported from conditions at pH 13 due to polydispersity

‡ All PDDF profiles were adequately fit using six Moore functions

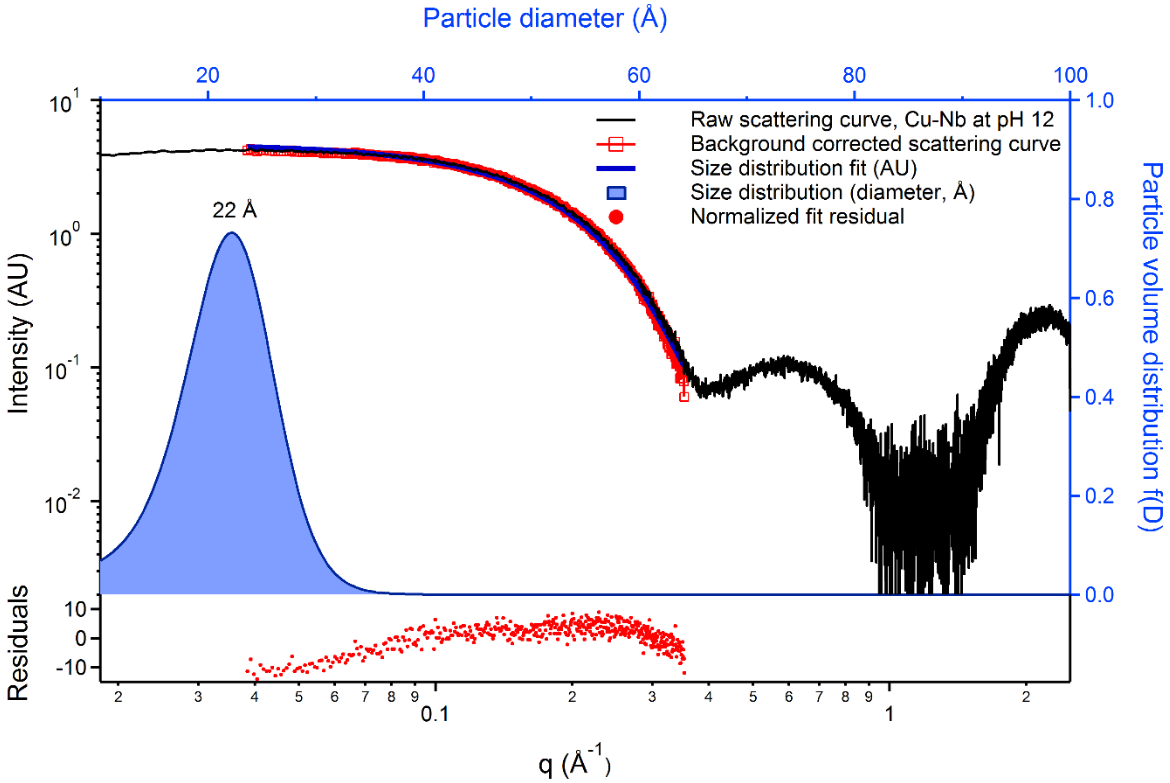

Figure 5.18 Size distribution analysis of the scattering curve of 1 mM **KNa-1** in 0.1 M sodium phosphate buffer, pH 12, after aging 48 hours.

The speciation of **KNa-1** in strongly alkaline solutions at pH 13 differs from those previously discussed. While **KNa-1** at or below pH 12 appears indefinitely stable, **KNa-1** dissolved in 0.1 M LiOH shows gradual changes over the course of several hours (Figure 5.19). The scattering curve at pH 13 shows a pronounced increase in intensity at low q indicative of the formation of larger species and general polydispersity accompanied by a broadening of the oscillation feature seen at ca. 0.4 Å^{-1}. This evolution appears to approach equilibrium after 48 hours, after which successive scattering curves are comparable. Long-term observation of solutions of **KNa-1** at pH 13 show no evidence of precipitation, so the observed polydispersity is likely due to molecular aggregation.

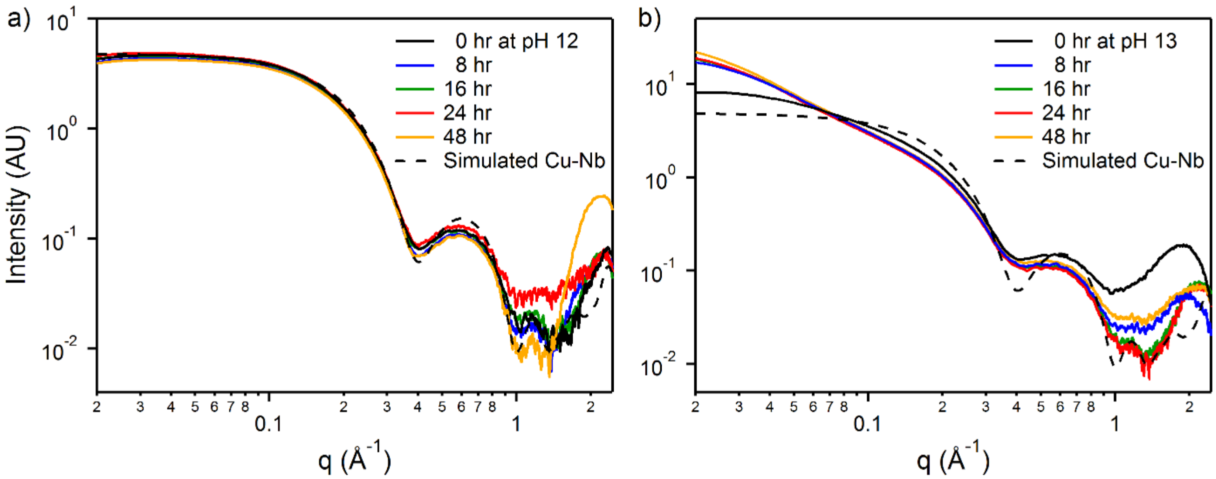

Figure 5.19 Time-dependent X-ray scattering curves of 1 mM **KNa-1** in a) 0.1 M sodium phosphate buffer, pH 12, and b) 0.1 M LiOH, pH 13.

Size distribution analysis of the scattering curve of **KNa-1** at pH 13 reveals a possible explanation for the observed polydispersity (Figure 5.20). The dominant population (86%) in solution remains a cluster with a mean diameter of 22 Å, consistent with the intact **KNa-1** unit. While this observation cannot discount smaller scale decomposition on the order of dissociation of a few individual bonds, the cluster size suggests massive rearrangement is not occurring. Furthermore, there is no evidence of smaller fragments (i.e. free $[Nb_6O_{19}]^{8-}$ or $[Nb_7O_{22}]^{9-}$ units) in solution, consistent with the observation of no copper oxide deposition during catalysis. Larger populations are observed at approximate multiples of the diameter of **KNa-1** at 43 Å, 62 Å, 79 Å, and 100 Å, with decreasing percentages of the total composition (Table 5.3). This pattern suggests that **KNa-1** forms a small population of oligomers at pH 13, but the monomeric unit remains the dominant species. Such a finding may also help to explain the change seen the FT-IR (Figure 5.9).

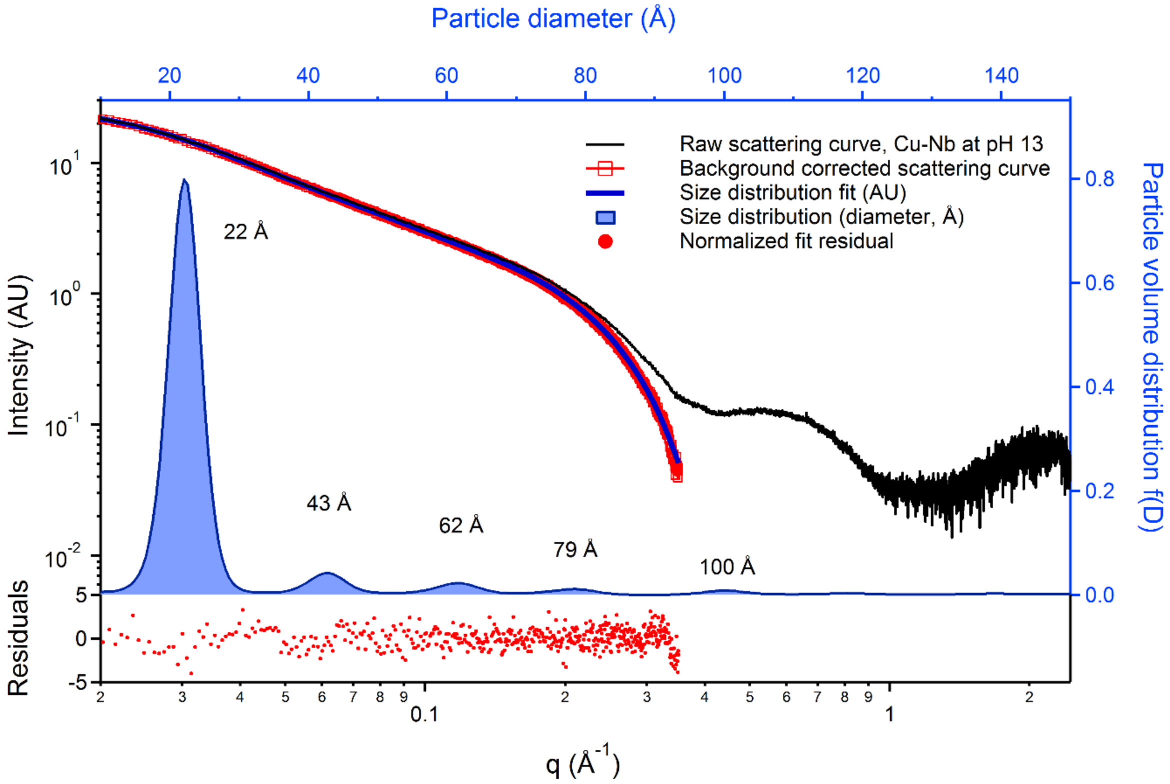

Figure 5.20 Size distribution analysis of the scattering curve of 1 mM **KNa-1** in 0.1 M LiOH, pH 13, after aging 48 hours.

Table 5.3 Size distribution analysis of **KNa-1** in various aqueous conditions by SAXS

Condition	Population diameter (Å), Percent of total population				
pH 12*	22, >99.9%				
pH 13	22, 86.0%	43, 5.7%	62, 3.5%	79, 1.7%	100, 1.2%
Pre-BE	22, 87.7%	44, 5.7%	66, 2.6%	91, 1.2%	105, 1.1%
Post-BE	22, 90.5%	46, 3.3%	57, 3.0%	86, 2.0%	133, 1.0%

* Analyses of all other aqueous conditions match those reported for pH 12

X-ray scattering curves were measured on 1 mM **KNa-1** solutions prior to and after electrochemical water oxidation catalysis in 0.1 M KOH for 24 hours to evaluate whether catalytic activity affects the previously observed speciation (Figure 5.21). Both scattering curves exhibit the oscillation feature at ca. 0.4 Å^{-1} and appear similar to late duration scattering curves of **KNa-1** in

0.1 M KOH (Figure 5.19). Size distribution analyses on both curves further support this similarity. The solution prior to catalysis is dominated by the monomeric population at 22 Å, followed by smaller populations of oligomers at mean diameters and percentages that closely match that observed in 0.1 M LiOH (Figure 5.22, Table 5.3). The solution after catalysis shows a very similar distribution, the only difference being an apparent blurring of the populations between 40 and 60 Å in diameter (Figure 5.23, Table 5.3). The dominant species, ranging from 86 to 90%, in all solutions at pH 13 is consistent with an intact **KNa-1** cluster.

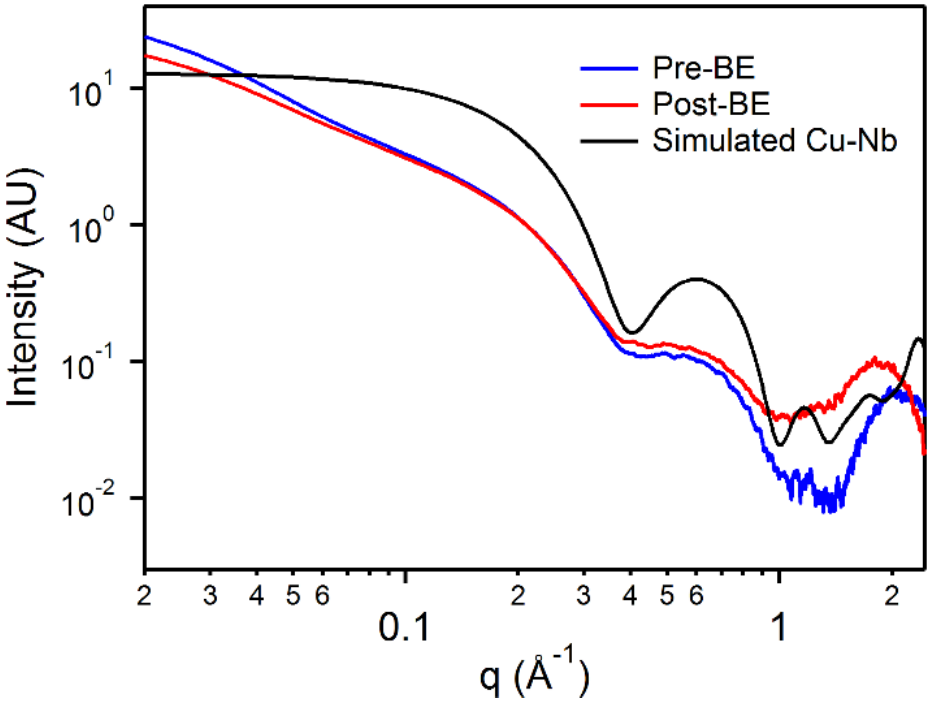

Figure 5.21 Scattering curves of 1 mM **KNa-1** in 0.1 M KOH, pH 13, prior to (blue, pre-BE) and after (red, post-BE) 24 hours of chronoamperometry at 1 V vs. Hg/HgO.

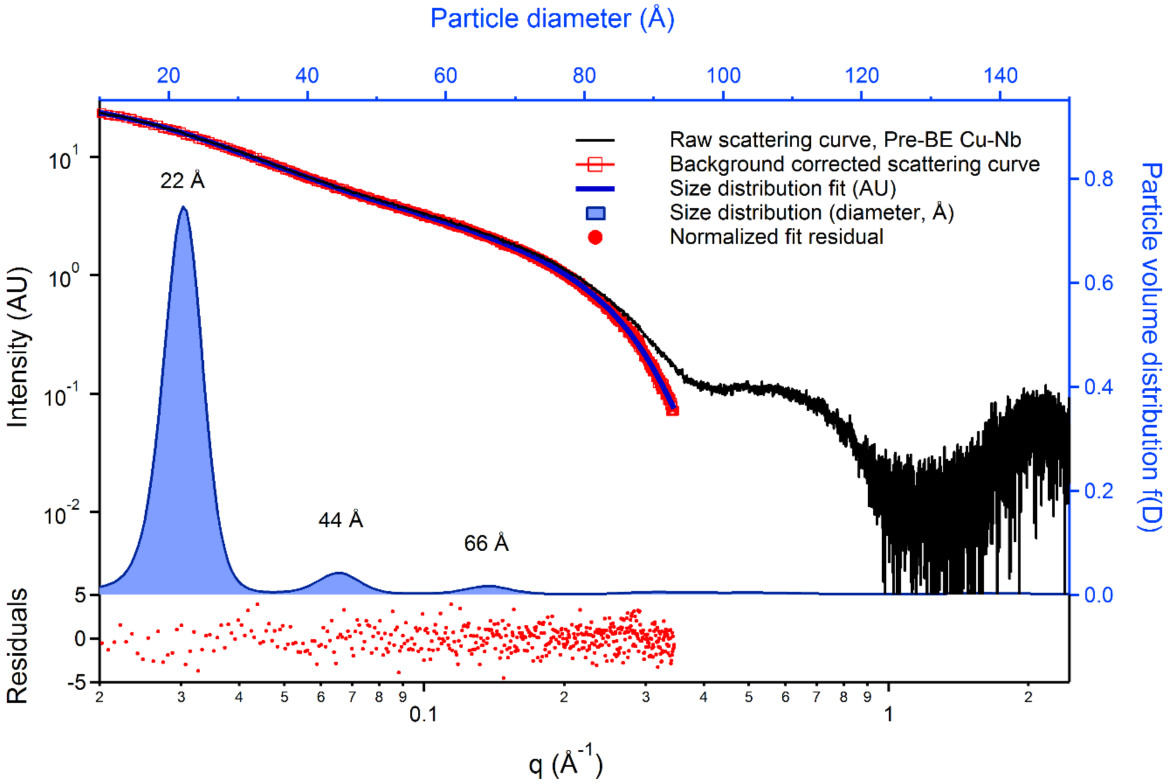

Figure 5.22. Size distribution analysis of the scattering curve of 1 mM **KNa-1** in 0.1 M KOH, pH 13, prior to 24 hours of chronoamperometry.

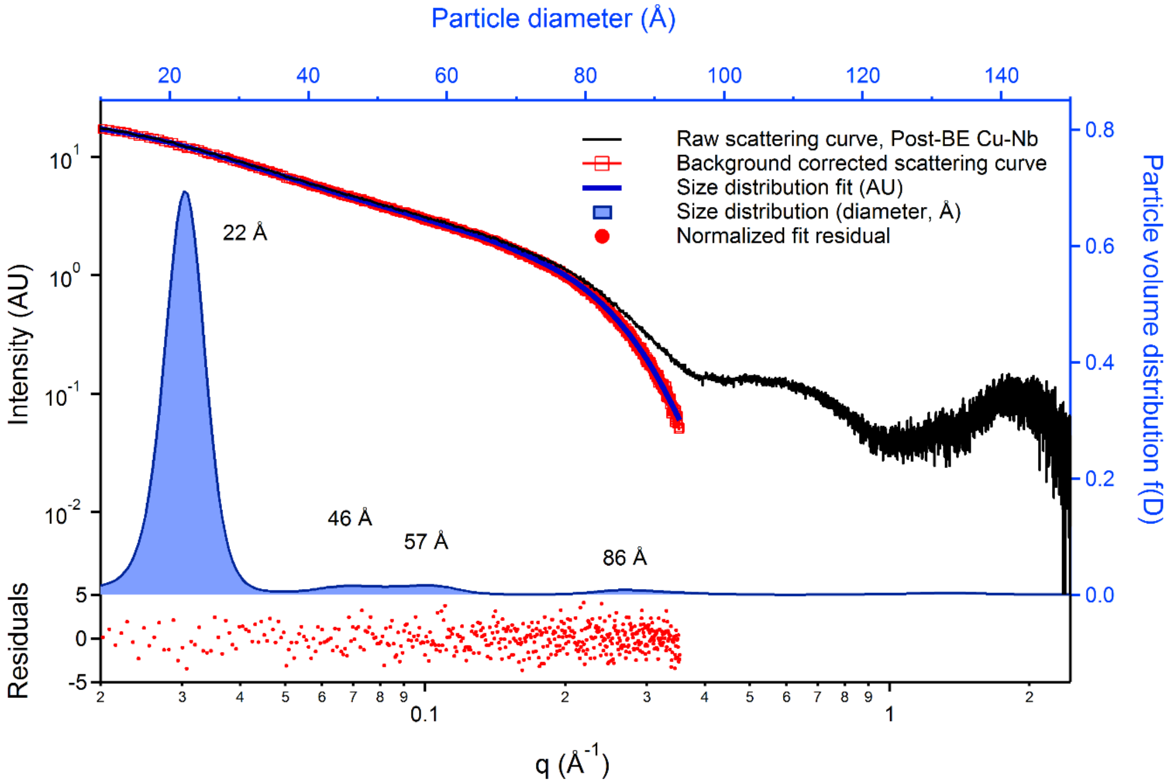

Figure 5.23. Size distribution analysis of the scattering curve of 1 mM **KNa-1** in 0.1 M KOH, pH 13, after 24 hours of chronoamperometry.

The speciation of **KNa-1** in alkaline solutions as observed by SAXS supports the conclusion that **KNa-1** is a molecular water oxidation catalyst. The observation of water oxidation at pH 12, where the monomeric **KNa-1** cluster is the only observed species, and pH 13, where the monomer is the dominant population, suggest that the monomer is responsible for the observed catalytic activity. Furthermore, the absence of electrodeposited copper oxides on the working electrode, combined with the lack of evidence for smaller fragments in the scattering data, support the conclusion that the polyoxoniobate cluster stabilizes copper-oxo species under alkaline conditions that would otherwise readily form insoluble copper oxides/hydroxides.

Experimental

General methods and materials

All reagents were used as purchased without further purification unless otherwise stated. Copper(II) sulfate anhydrous ($CuSO_4$, > 99.99%), barium chloride dihydrate ($BaCl_2 \cdot 2H_2O$, > 99%), sodium hydroxide (NaOH, > 85%) and potassium hydroxide (KOH, >99.99%) were purchased from Sigma-Aldrich. Hydrous niobium oxide (Nb_2O_5) was acquired from Reference Metals Company Inc. All solutions were prepared using Milli-Q nanopure water (18.2 MΩ.cm resistivity) unless stated otherwise. $K_7HNb_6O_{19} \cdot 13H_2O$ was synthesized and purified according to Nyman *et al*.[47] FTO glass (Pilkington TEC15, ~15Ω/sq resistance) was purchased from Hartford Glass Company, Inc.

Synthesis of $K_{16}Na_{12}[H_9Cu_{25.5}O_8(Nb_7O_{22})_8] \cdot 37.5H_2O$ (KNa-1).

KNa-1 was synthesized as previously described in the literature with modifications.[35] Typically, $K_7HNb_6O_{19} \cdot 13H_2O$ (1.38 g, 1.0 mmol) was dissolved in 30 mL DI water, and 5 mL of an aqueous solution of $BaCl_2 \cdot 2H_2O$ (0.24 g, 1.0 mmol) was added slowly while stirring until the solution became a white emulsion. A solution of $CuSO_4$ (0.16 g, 1.0 mmol) in 20 mL DI H_2O was then added dropwise. The pH of the green mixture was adjusted to 10–11 with 0.1 M NaOH, and then heated at 80 ^oC under stirring for 3 h. The solution was cooled to room temperature and centrifuged to remove the white precipitate. After standing at room temperature for 5 days, dark-green single crystals suitable for X-ray diffraction were collected. Yield: 0.56 g (16 % based on $K_7HNb_6O_{19} \cdot 13H_2O$).

Instrumentation

All UV-Vis spectroscopy was performed with an Agilent 8453 spectrometer at room temperature using a quartz cell with a 1 cm path length. The FT-IR spectra were recorded using 2% by weight KBr pellets in the range 4000−400 cm^{-1} on a Nicolet 6700 FT-IR spectrometer.

The electrochemical experiments were conducted with a Pine WaveDriver 20 Bipotentiostat. The three-electrode system was equipped with a working electrode, a platinum wire counter electrode, and Ag/AgCl (1 M KCl) reference electrode (CH-Instruments) (0.235 vs. NHE). Cyclic voltammetry experiments were conducted in a one-compartment cell with 10 mL of electrolyte solution, while controlled potential electrolysis measurements were conducted with a total of 10-20 mL of total electrolyte solution in a closed two-compartment anaerobic cell that was purged with N_2 for a minimum of 20 minutes prior to electrolysis (30 mL total volume, each compartment separated by a Nafion film without *iR* compensation). All experiments were performed at room temperature.

Scanning electron microscopy and energy dispersive X-ray spectroscopy (SEM-EDX) data was collected at the Clemson University Advanced Materials Center with three Hitachi transmission electron microscopes (STEM HD2000, TEM H7600T, and TEM 9500) and scanning electron microscopes (SEM 3400, SU-6600, and S4800) equipped with EDX.

XPS measurements were performed using a Thermo K-Alpha XPS. A monochromated aluminum Kα source (1486.6 eV) was used for excitation of photoelectrons. The base pressure of the analysis chamber was around 10^{-8} Pa during collection. Survey scan spectra were measured over a pass energy of 200 eV at 1eV energy steps. High resolution scans were performed over a pass energy of 50 eV at 0.1 eV energy steps. All samples were vacuum dried via Schlenk line at 60 °C before introduction into the XPS chamber. The Thermo K-Alpha flood gun was used for charge neutralization during all experiments. Analysis of all spectra were done using CasaXPS software (version 2.3.14).

Electrode pretreatment.

Glassy carbon (0.071 cm^2) disk electrode: Prior to the experiments, the glassy carbon electrode was polished for 5 minutes each with 0.3 µm, 0.05 µm, and 0.01 µm Al_2O_3 slurry in sequence. Followed by sonication water and isopropanol for 10 minutes each to remove debris. FTO (0.56 cm^2) electrodes: Prior to the experiments, the glass slides were cleaned by sonication in acetone, Milli-Q ultrapure water and isopropanol for ~20 min respectively, followed by drying at 60 °C in an oven for ~30 min. The glass slides then were stored in an air-tight glass bottle before use.

Small-Angle X-ray Scattering (SAXS)

Scattering curves were collected on an Anton Paar SAXSess instrument using Cu-K_α radiation (1.54 Å) with line collimation. The instrument was equipped with a wide-angle extension and 2D image plate for data collection in the range of q = 0.018-2.5 $Å^{-1}$. Solutions containing 1 mM **KNa-1** were sealed in 1.5 mm diameter glass capillary tubes (Hampton Research), placed under vacuum, and measured for 30 minutes each. Background solutions composed of the same solvent and buffer composition minus the analyte were also measured. Data collection and treatment (normalization, primary beam removal, background subtraction, desmearing, and smoothing) were performed using SAXSquant (Anton Paar) software. Data analyses were performed using the Irena macros within Igor Pro (WaveMetrics).[48] Pair-distance distribution function analyses were performed on each sample in the scattering region of ca. 0.03-0.9 $Å^{-1}$ using the Moore method.[46] Guinier analysis was performed on the region of ca. 0.09-0.2 Å^{-1}. Size distribution analyses were performed on the region of ca. 0.03-0.35 Å^{-1}. Simulated scattering data from 0-2.5 Å^{-1} was generated from the crystal structure using SolX v2.2.[49-50]

Conclusion

This chapter details the characterization of **KNa-1**, a molecular OER catalyst based on copper, which operates well under strong alkaline conditions. Electrochemical methods have derived a lower limit for the turnover over frequency (TOF) of 40 s^{-1}, a fast TOF that is, unfortunately, achieved at relatively high overpotentials. At η = ~ 800 mV, this homogeneous electrocatalyst achieves a Faradaic efficiency of 95% at a current density of 1 mA/cm^2 after 24 hours.

A number of characterization techniques including, UV-Vis spectroscopy, FT-IR, XPS, SEM-EDX, were used in addition to the suite of electrochemical techniques to characterize the structure, activity, and molecular stability of **1**. Questions regarding the exact nature of the active homogeneous electrocatalyst led us to employ Small-angle X-ray scattering (SAXS) to analyze aqueous solutions of **KNa-1**. Results indicate that the cluster is intact and is the only species present in solution at and below pH 12. At pH 13, limited oligomerization of **1** is observed, but we found no smaller fragments, which would indicate decomposition of the main polyanion unit or formation of copper oxyhydroxides. The dominant population remains the monomeric **1** polyanion (>85%). With all these characterization methodologies, we conclude that polyanion **1** remains intact under all evaluated conditions and is the main homogeneous electrocatalyst for OER.

Significantly, we showed that polyoxoniobates can function as stabilizing multi-dentate ligands under alkaline conditions for molecular metal-oxo/hydroxo species used as electrocatalysts. The stabilization of a homogeneous OER electrocatalyst using polyoxoniobates demonstrates one of the many potential assembly functions of such species. Additionally, the oligomerization behavior of the cuboid **1** cluster is an interesting phenomenon that has valuable prospects for further research, as it may provide insight on the behavior of analogous materials and molecular assembly.

References

1. McKone, J. R.; Lewis, N. S.; Gray, H. B., Will Solar-Driven Water-Splitting Devices See the Light of Day? *Chemistry of Materials* **2014,** *26* (1), 407-414.

2. Lauinger, S. M.; Yin, Q.; Geletii, Y. V.; Hill, C. L., Chapter Five - Polyoxometalate Multielectron Catalysts in Solar Fuel Production. In *Advances in Inorganic Chemistry*, van Eldik, R.; Cronin, L., Eds. Academic Press: 2017; Vol. 69, pp 117-154.

3. Suen, N.-T.; Hung, S.-F.; Quan, Q.; Zhang, N.; Xu, Y.-J.; Chen, H. M., Electrocatalysis for the oxygen evolution reaction: recent development and future perspectives. *Chemical Society Reviews* **2017,** *46* (2), 337-365.

4. Wang, L.-P.; Wu, Q.; Van Voorhis, T., Acid−Base Mechanism for Ruthenium Water Oxidation Catalysts. *Inorganic Chemistry* **2010,** *49* (10), 4543-4553.

5. Burke, M. S.; Kast, M. G.; Trotochaud, L.; Smith, A. M.; Boettcher, S. W., Cobalt-Iron (Oxy)hydroxide Oxygen Evolution Electrocatalysts: The Role of Structure and Composition on Activity, Stability, and Mechanism. *Journal of the American Chemical Society* **2015,** *137* (10), 3638-3648.

6. Chou, N. H.; Ross, P. N.; Bell, A. T.; Tilley, T. D., Comparison of Cobalt-based Nanoparticles as Electrocatalysts for Water Oxidation. *ChemSusChem* **2011,** *4* (11), 1566-1569.

7. Coggins, M. K.; Zhang, M.-T.; Chen, Z.; Song, N.; Meyer, T. J., Single-Site Copper(II) Water Oxidation Electrocatalysis: Rate Enhancements with HPO_4^{2-} as a Proton Acceptor at pH 8. *Angewandte Chemie International Edition* **2014,** *53* (45), 12226-12230.

8. Du, J.; Chen, Z.; Ye, S.; Wiley, B. J.; Meyer, T. J., Copper as a Robust and Transparent Electrocatalyst for Water Oxidation. *Angewandte Chemie International Edition* **2015,** *54* (7), 2073-2078.

9. Enman, L. J.; Stevens, M. B.; Dahan, M. H.; Nellist, M. R.; Toroker, M. C.; Boettcher, S. W., Operando X-Ray Absorption Spectroscopy Shows Iron Oxidation Is Concurrent with Oxygen Evolution in Cobalt–Iron (Oxy)hydroxide Electrocatalysts. *Angewandte Chemie International Edition* **2018,** *57* (39), 12840-12844.

10. Jiang, C. R.; Moniz, S. J. A.; Wang, A. Q.; Zhang, T.; Tang, J. W., Photoelectrochemical devices for solar water splitting - materials and challenges. *Chemical Society Reviews* **2017,** *46* (15), 4645-4660.

11. Kang, D.; Kim, T. W.; Kubota, S. R.; Cardiel, A. C.; Cha, H. G.; Choi, K. S., Electrochemical Synthesis of Photoelectrodes and Catalysts for Use in Solar Water Splitting. *Chemical Reviews* **2015,** *115* (23), 12839-12887.

12. Ndambakuwa, W.; Ndambakuwa, Y.; Choi, J.; Fernando, G.; Neupane, D.; Mishra, S. R.; Perez, F.; Gupta, R. K., Nanostructured nickel-cobalt oxide and sulfide for applications in supercapacitors and green energy production using waste water. *Surf. Coat. Technol.* **2021,** *410*, 10.

13. Osterloh, F. E., Inorganic nanostructures for photoelectrochemical and photocatalytic water splitting. *Chemical Society Reviews* **2013,** *42* (6), 2294-2320.

14. Peng, Z.; Jia, D.; Al-Enizi, A. M.; Elzatahry, A. A.; Zheng, G., From Water Oxidation to Reduction: Homologous Ni–Co Based Nanowires as Complementary Water Splitting Electrocatalysts. *Adv. Energy Mater.* **2015,** *5* (9), 1402031.

15. Pijpers, J. J.; Winkler, M. T.; Surendranath, Y.; Buonassisi, T.; Nocera, D. G., Light-induced water oxidation at silicon electrodes functionalized with a cobalt oxygen-evolving catalyst. *Proc Natl Acad Sci U S A* **2011,** *108* (25), 10056-61.

16. Qu, Y. T.; Li, Z. J.; Chen, W. X.; Lin, Y.; Yuan, T. W.; Yang, Z. K.; Zhao, C. M.; Wang, J.; Zhao, C.; Wang, X.; Zhou, F. Y.; Zhuang, Z. B.; Wu, Y.; Li, Y. D., Direct transformation of bulk copper into copper single sites via emitting and trapping of atoms. *Nat. Catal.* **2018,** *1* (10), 781-786.

17. Wang, Y.; Yang, C.; Huang, Y.; Li, Z.; Liang, Z.; Cao, G., Nickel induced electronic structural regulation of cobalt hydroxide for enhanced water oxidation. *Journal of Materials Chemistry A* **2020,** *8* (14), 6699-6708.

18. Yang, J. H.; Wang, D. G.; Han, H. X.; Li, C., Roles of Cocatalysts in Photocatalysis and Photoelectrocatalysis. *Accounts Chem. Res.* **2013,** *46* (8), 1900-1909.

19. Zhu, C. Z.; Wen, D.; Leubner, S.; Oschatz, M.; Liu, W.; Holzschuh, M.; Simon, F.; Kaskel, S.; Eychmuller, A., Nickel cobalt oxide hollow nanosponges as advanced electrocatalysts for the oxygen evolution reaction. *Chemical Communications* **2015,** *51* (37), 7851-7854.

20. Gerken, J. B.; Landis, E. C.; Hamers, R. J.; Stahl, S. S., Fluoride-Modulated Cobalt Catalysts for Electrochemical Oxidation of Water under Non-Alkaline Conditions. *Chemsuschem* **2010,** *3* (10), 1176-1179.

21. Yang, X. F.; Wang, A. Q.; Qiao, B. T.; Li, J.; Liu, J. Y.; Zhang, T., Single-Atom Catalysts: A New Frontier in Heterogeneous Catalysis. *Accounts Chem. Res.* **2013,** *46* (8), 1740-1748.

22. Folkman, S. J.; Soriano-Lopez, J.; Galán-Mascarós, J. R.; Finke, R. G., Electrochemically Driven Water-Oxidation Catalysis Beginning with Six Exemplary Cobalt Polyoxometalates: Is It Molecular, Homogeneous Catalysis or Electrode-Bound, Heterogeneous CoOx Catalysis? *Journal of the American Chemical Society* **2018,** *140* (38), 12040-12055.

23. Harriman, A.; Pickering, I. J.; Thomas, J. M.; Christensen, P. A., Metal oxides as heterogeneous catalysts for oxygen evolution under photochemical conditions. *Journal of the*

Chemical Society, Faraday Transactions 1: Physical Chemistry in Condensed Phases **1988,** *84* (8), 2795-2806.

24. Hunter, B. M.; Gray, H. B.; Müller, A. M., Earth-Abundant Heterogeneous Water Oxidation Catalysts. *Chemical Reviews* **2016,** *116* (22), 14120-14136.

25. Li, J.; Triana, C. A.; Wan, W.; Adiyeri Saseendran, D. P.; Zhao, Y.; Balaghi, S. E.; Heidari, S.; Patzke, G. R., Molecular and heterogeneous water oxidation catalysts: recent progress and joint perspectives. *Chemical Society Reviews* **2021,** *50* (4), 2444-2485.

26. Barnett, S. M.; Goldberg, K. I.; Mayer, J. M., A soluble copper–bipyridine water-oxidation electrocatalyst. *Nature Chemistry* **2012,** *4* (6), 498-502.

27. Chen, Z.; Kang, P.; Zhang, M.-T.; Stoner, B. R.; Meyer, T. J., Cu(II)/Cu(0) electrocatalyzed CO_2 and H_2O splitting. *Energy & Environmental Science* **2013,** *6* (3), 813-817.

28. Garrido-Barros, P.; Funes-Ardoiz, I.; Drouet, S.; Benet-Buchholz, J.; Maseras, F.; Llobet, A., Redox Non-innocent Ligand Controls Water Oxidation Overpotential in a New Family of Mononuclear Cu-Based Efficient Catalysts. *Journal of the American Chemical Society* **2015,** *137* (21), 6758-6761.

29. Kalantarifard, S.; Allakhverdiev, S. I.; Najafpour, M. M., Water oxidation by a nickel complex: New challenges and an alternative mechanism. *International Journal of Hydrogen Energy* **2020,** *45* (58), 33563-33573.

30. Luo, G.-Y.; Huang, H.-H.; Wang, J.-W.; Lu, T.-B., Further Investigation of a Nickel-Based Homogeneous Water Oxidation Catalyst with Two cis Labile Sites. *ChemSusChem* **2016,** *9* (5), 485-491.

31. Shaffer, D. W.; Xie, Y.; Concepcion, J. J., O–O bond formation in ruthenium-catalyzed water oxidation: single-site nucleophilic attack vs. O–O radical coupling. *Chemical Society Reviews* **2017,** *46* (20), 6170-6193.

32. Yu, L.; Lin, J.; Zheng, M.; Chen, M.; Ding, Y., Homogeneous electrocatalytic water oxidation at neutral pH by a robust trinuclear copper(ii)-substituted polyoxometalate. *Chemical Communications* **2018,** *54* (4), 354-357.

33. Yu, W.-B.; He, Q.-Y.; Ma, X.-F.; Shi, H.-T.; Wei, X., A new copper species based on an azo-compound utilized as a homogeneous catalyst for water oxidation. *Dalton Transactions* **2015,** *44* (1), 351-358.

34. Alibabaei, L.; Brennaman, M. K.; Norris, M. R.; Kalanyan, B.; Song, W.; Losego, M. D.; Concepcion, J. J.; Binstead, R. A.; Parsons, G. N.; Meyer, T. J., Solar water splitting in a molecular photoelectrochemical cell. *Proceedings of the National Academy of Sciences* **2013,** *110* (50), 20008-20013.

35. Niu, J.; Ma, P.; Niu, H.; Li, J.; Zhao, J.; Song, Y.; Wang, J., Giant Polyniobate Clusters Based on $[Nb_7O_{22}]^{9-}$ Units Derived from a Nb_6O_{19} Precursor. *Chemistry – A European Journal* **2007,** *13* (31), 8739-8748.

36. Haynes, W. M., Lide, D. R., & Bruno, T. J. , *CRC handbook of chemistry and physics: a ready-reference book of chemical and physical data.* . 97th ed.; CRC Press.: Boca Raton, Florida, 2016.

37. Zhang, M.-T.; Chen, Z.; Kang, P.; Meyer, T. J., Electrocatalytic Water Oxidation with a Copper(II) Polypeptide Complex. *Journal of the American Chemical Society* **2013,** *135* (6), 2048-2051.

38. Zhang, T.; Wang, C.; Liu, S.; Wang, J.-L.; Lin, W., A Biomimetic Copper Water Oxidation Catalyst with Low Overpotential. *Journal of the American Chemical Society* **2014,** *136* (1), 273-281.

39. Gerlach, D. L.; Bhagan, S.; Cruce, A. A.; Burks, D. B.; Nieto, I.; Truong, H. T.; Kelley, S. P.; Herbst-Gervasoni, C. J.; Jernigan, K. L.; Bowman, M. K.; Pan, S.; Zeller, M.; Papish, E. T., Studies of the Pathways Open to Copper Water Oxidation Catalysts Containing Proximal Hydroxy Groups During Basic Electrocatalysis. *Inorganic Chemistry* **2014,** *53* (24), 12689-12698.

40. Fu, L.-Z.; Fang, T.; Zhou, L.-L.; Zhan, S.-Z., A mononuclear copper electrocatalyst for both water reduction and oxidation. *RSC Advances* **2014,** *4* (96), 53674-53680.

41. Su, X.-J.; Gao, M.; Jiao, L.; Liao, R.-Z.; Siegbahn, P. E. M.; Cheng, J.-P.; Zhang, M.-T., Electrocatalytic water oxidation by a dinuclear copper complex in a neutral aqueous solution. *Angew Chem Int Ed Engl* **2015,** *54* (16), 4909-4914.

42. Chen, Z.; Meyer, T. J., Copper(II) Catalysis of Water Oxidation. *Angewandte Chemie International Edition* **2013,** *52* (2), 700-703.

43. Li, T.-T.; Cao, S.; Yang, C.; Chen, Y.; Lv, X.-J.; Fu, W.-F., Electrochemical Water Oxidation by In Situ-Generated Copper Oxide Film from [Cu(TEOA)(H_2O)$_2$][SO_4] Complex. *Inorganic Chemistry* **2015,** *54* (6), 3061-3067.

44. Liu, X.; Jia, H.; Sun, Z.; Chen, H.; Xu, P.; Du, P., Nanostructured copper oxide electrodeposited from copper(II) complexes as an active catalyst for electrocatalytic oxygen evolution reaction. *Electrochemistry Communications* **2014,** *46*, 1-4.

45. Putnam, C. D.; Hammel, M.; Hura, G. L.; Tainer, J. A., X-ray solution scattering (SAXS) combined with crystallography and computation: defining accurate macromolecular structures, conformations and assemblies in solution. *Q Rev Biophys* **2007,** *40* (3), 191-285.

46. Moore, P. B., Small-angle scattering. Information content and error analysis. *Journal of Applied Crystallography* **1980,** *13* (2), 168-175.

47. Nyman, M.; Alam, T. M.; Bonhomme, F.; Rodriguez, M. A.; Frazer, C. S.; Welk, M. E., Solid-state Structures and Solution Behavior of Alkali Salts of the $[Nb_6O_{19}]^{8-}$ Lindqvist Ion. *Journal of Cluster Science* **2006,** *17* (2), 197-219.

48. Ilavsky, J.; Jemian, P. R., Irena: tool suite for modeling and analysis of small-angle scattering. *Journal of Applied Crystallography* **2009,** *42* (2), 347-353.

49. Zhang, R.; Thiyagarajan, P.; Tiede, D. M., Probing protein fine structures by wide angle solution X-ray scattering. *Journal of Applied Crystallography* **2000,** *33* (3-1), 565-568.

50. Tiede, D. M.; Zhang, R.; Chen, L. X.; Yu, L.; Lindsey, J. S., Structural Characterization of Modular Supramolecular Architectures in Solution. *Journal of the American Chemical Society* **2004,** *126* (43), 14054-14062.

Chapter 6

Tafel Slope Analyses for Homogeneous Catalytic Reactions

Reproduced in part from Yin, Q.; Xu, Z.; Lian, T.; Musaev, D.G.; Hill, C.L.; Geletii, Y.V. Tafel Slope Analyses for Homogeneous Catalytic Reactions. *Catalysts* **2021**, *11*, 87.

Introduction

Tafel slope analysis has become increasingly popular in this era of solar fuels research and photoelectrochemistry. This chapter addresses the possibility of constructing Tafel plots for homogeneous catalytic multielectron redox processes and the usefulness of this approach. The model homogeneous reaction we have chosen for this study is the oxidation of water in equation 6.1.

Equation 6.1 is very unfavorable thermodynamically and requires an external source of energy such as electricity or light (e.g., solar). The overall reaction of water splitting, equation 6.3, includes two half-reactions, water oxidation and reduction, equations 6.1 and 6.2, respectively, which proceed in spatially separated sites:

$$2\ H_2O\ -\ 4\ e^- \longrightarrow O_2 + 4\ H^+ \qquad (6.1)$$

$$2\ H^+\ +\ 2\ e^- \longrightarrow H_2 \qquad (6.2)$$

$$2\ H_2O \longrightarrow O_2\ +\ 2H_2 \qquad (6.3)$$

The reverse reaction in equation 6.3 takes place in fuel cells to directly convert chemical energy into electricity.

In electrochemistry, the potential applied between the cathode and anode and the current is measured. Commonly, the empirically formulated Tafel relation in equation 6.4 is used to compare the electrocatalytic activities:

$$\eta = a + b \log(i), \qquad (6.4)$$

where $\eta = E - E_0$ is the difference between the electrode and standard potentials, i is the current density, and b is the Tafel slope.

The utility of Tafel slopes from a microkinetic analysis of aqueous electrocatalysis for energy conversion has been reported.[1,2] However, numerous simplifications and assumptions in the derivation of equation 6.4 leads to an incomplete description of the actual surface kinetics and makes the applicability of Tafel analysis questionable.[2,3,7,8] In many cases, homogeneous systems are simpler and easier experimentally for understanding the reaction mechanism. Therefore, we developed a protocol to construct Tafel-like plots for homogeneous reactions and studied the usefulness of such plots to better understand the reaction mechanism. In addition, while extensive mechanistic analyses of molecular redox systems have been conducted previously, many aspects still need to be precisely addressed.[9] Generally speaking, the Tafel-like plot is one among multiple approaches that link the kinetic and thermodynamic properties of such a catalytic system.

Both half reactions, equations 6.1 and 6.2, are complex multielectron processes catalyzed by transition metal complexes. Each one is routinely studied individually.[6,10–12] Stable homogeneous molecular catalysts are ideally suited for studies of the reaction mechanism and the relationship between reaction kinetics and thermodynamics. Indeed, previous studies on redox and chemical catalysts in different catalytic systems have already provided theoretical tools for mechanistic analyses.[9] More recently, Costentin and Savéant thoroughly analyzed the applicability of the Tafel equation to the homogeneous molecular catalysis of *electrochemical* CO_2 and O_2 reduction.[13] In this work, we describe a protocol for deriving a Tafel-like plot based on theoretical and experimental grounds to relate the reaction rate with the solution electrochemical potential for homogeneous water oxidation by $[Ru(bpy)_3]^{3+}$, catalyzed by the stable molecular tetraruthenium polyoxometalate $[Ru_4O_4(OH)_2(H_2O)_4(\gamma\text{-}SiW_{10}O_{36})_2]^{10-}$, **$Ru_4$POM**. This POM was the first fully inorganic (carbon-free), thus oxidatively robust, water oxidation catalyst (WOC), which is also hydrolytically stable over a wide pH range (pH 1–9).[14,15] Detailed electrochemical studies of this complex showed that the rates of electron exchange between an electrode and the complex is sluggish under typical catalytic turnover conditions.[14,16] As a result, neither the Tafel plot nor the exchange current density, i_0, can be measured experimentally. At the same time, the catalyst shows excellent activity in homogeneous aqueous solutions when stoichiometric oxidants such as Ce(IV) or $[Ru(bpy)_3]^{3+}$ are used. The question was posed as to whether data collected in homogeneous multielectron processes can be used to obtain a Tafel-like plot. This study addresses that question and aims to focus on the adaptation of an analog of traditional Tafel plots to the four-electron water oxidation process specific to homogeneous species.

Results and Discussion

Theoretical considerations

Here, we assume that water oxidation in homogeneous conditions proceeds through four fast Nernstian reversible electron transfer steps followed by the irreversible O_2 formation step, reactions 6.5–6.8, where C0 is the resting oxidation state of the catalyst, C, and C1–C4 are the one- to four-electron oxidized forms of the catalyst.

$$C0 - e \rightleftarrows C1 \qquad E^o_1 \qquad (6.5)$$

$$C1 - e \rightleftarrows C2 \qquad E^o_2 \qquad (6.6)$$

$$C2 - e \rightleftarrows C3 \qquad E^o_3 \qquad (6.7)$$

$$C3 - e \rightleftarrows C4 \qquad E^o_4 \qquad (6.8)$$

$$C4 + 2\,H_2O \longrightarrow C0 + O_2 + 4\,H^+ \qquad k_o \qquad (6.9)$$

If the equilibria are fast, then an applied and electrochemical solution potential, E, is linked via the Nernst equation, equations 6.10:

$$E - E^o_1 = (RT/F)\ln([C1]/[C0]) \qquad E - E^o_2 = (RT/F)\ln([C2]/[C1])$$

$$E - E^o_3 = (RT/F)\ln([C3]/[C2]) \qquad E - E^o_4 = (RT/F)\ln([C4]/[C3]) \qquad (6.10)$$

where R is the universal gas constant, T is the temperature, and F is the Faraday constant. The concentration of the catalyst in oxidation state $i = 0 - 4$ is described by a distribution function, equation 6.11:

$$\alpha_i = [Ci]/[Ct] \times [\exp(F(iE - \textstyle\sum_0^i E_i^o)/RT)]/[1 + \exp[F(E - \textstyle\sum_0^1 E_j^o)/RT] + \exp[F(2E - \textstyle\sum_0^2 E_j^o)RT] + \exp[F(3E - \textstyle\sum_0^3 E_j^o)/RT] + \exp[(4E - \textstyle\sum_0^4 E_j^o)/RT] \qquad (6.11)$$

where [Ct] = total concentration of the catalyst.

If a stoichiometric oxidant is used as a sacrificial electron acceptor, the Nernst law gives the applied potential equal to the solution potential. Here, we consider the case when $[Ru(bpy)_3]^{3+}$, Ru3, is an oxidant (Ru2 represents $[Ru(bpy)_3]^{2+}$). The electrochemical solution potential, E, created by this oxidant is:

$$E = E'_0 + 0.059 \times \log_{10} ([Ru3]/[Ru2]) = E'_0 + 0.059 \times \log_{10} \{[Ru3]/([Ru3]_o - [Ru2] + [Ru2]_o)\} \qquad (6.12)$$

where $E'_0 = 1.26$ V (SHE) is the standard reduction potential of the Ru3/Ru2 couple, and $[Ru3]_o$ and $[Ru2]_o$ are the initial concentrations of Ru3 and Ru2, respectively.

If the rate limiting step is reaction 6.9, then the reaction rate (current) is:

$$-d[Ru3]/dt = 4k_o[C4] = TOF_{app} \times [Ct] \qquad (6.13)$$

and the apparent turnover frequency (TOF_{app}) with respect to Ru3 consumption is:

$$TOF_{app} = 4\alpha_4 k_o \qquad (6.14)$$

Here, k_o is the rate constant for the oxidation of water. The value of the distribution factor, α_4 is time-dependent and can be determined from equations 6.10 and 6.11, and TOF_{app} is a kinetic parameter. The full equation linking TOF_{app} and apparent potential is complex, but can be simplified if k_o is known and $[Ru2]_o = 0$, equation 6.15:

$$\log_{10}(TOF_{app}) \approx \log_{10}(4k_o) + E'_0 + 0.059 \times \log_{10} ([Ru3]/([Ru3]_o - [Ru3])) - 4E \qquad (6.15)$$

At high applied potentials, [C4] ≈ [Ct] and TOF_{app} reaches a plateau with the value $4k_o$. This value is the maximum turnover frequency (TOF) achievable by a given catalyst. This is an intrinsic property of a catalyst and its associated turnover activity. However, TOF_0 of a certain catalytic system can be achieved at different potentials, E_{TOF}. As a result, the catalytic activity of two systems cannot be compared by a single number such as TOF_0. Two parameters, TOF_0 and E_{TOF}, are required to describe the catalytic activity. The slope of the Tafel-like plot at moderate potentials is a complex dependence of the catalyst reduction potentials and the Ru3 concentration. In our homogeneous catalytic system, Ru3 is used as a stoichiometric electron acceptor. Ru3 can also be generated in situ in a photoinduced reaction of Ru2 with persulfate, $S_2O_8^{2-}$, or electrochemically.

Homogeneous electrochemical reactions in the presense of an electron transfer catalyst

As the electron transfer from **Ru4POM** to the electrode is slow, we attempted to accelerate the overall reaction with the addition of an electron transfer catalyst. The stability of Ru3 is well documented to increase at lower pH. Therefore, the cyclic voltammetry (CV) was recorded at a slightly lower pH of 7.2. The CV of Ru3/Ru2 has an almost ideal shape with an anodic-cathodic peak separation of 69 mV and a ratio of anodic and cathodic current close to 1; $E_{1/2}$ = 1.26 V (versus SHE) in 80 mM sodium phosphate buffer at pH 7.2. The addition of 15 μM of **Ru_4POM** to 1.0 mM Ru2 results in a slight increase in anodic current (Figure 6.1), indicating that the reaction between Ru3 and **Ru_4POM** takes place. At higher concentration, **Ru_4POM** forms an insoluble adduct with Ru2, which does not allow CV measurements over a broad range of catalyst concentrations. A foot of the wave analysis cannot be applied, as no catalytic current is seen in this system.[17] The CV simulation with the SIM4YOU software package using the heterogeneous electron transfer reaction rate constant 0.065 cm s^{-1} (measured in 0.1 M H_2SO_4)[18] for Ru3 and a glassy carbon electrode (surface area is 0.0668 cm^2) is in good agreement with the experiment under the assumption of irreversible oxidation of Ru3 at the electrode at a potential of 1840 mV vs. SHE (Figure 1). The simulation results in the presence of **Ru$_4$POM** is also in reasonable agreement with the experiment when the reaction mechanism and rate constants described below are applied. Clearly, simple cyclic voltammograms do not provide much information on **Ru$_4$POM** redox potentials.

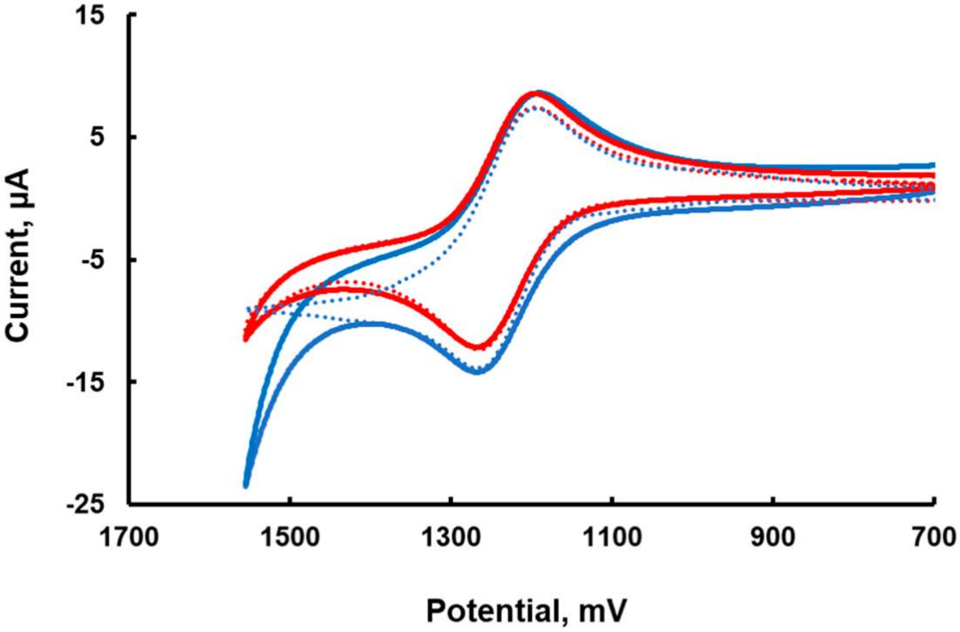

Figure 6.1 Cyclic voltammograms of 1.0 mM [Ru(bpy)$_3$]Cl$_2$ in 80 mM sodium phosphate at pH 7.2 (red) and in the presence of 15 μM **Ru$_4$POM** (blue); the simulated curves are dotted lines. Scan rate, 100 mV/s; potential versus SHE.

Linear sweep voltammetry

Linear sweep voltammetry (LSV) at very low scan rate with vigorous stirring of the solution is commonly used to obtain the dependence of the potential as a function of the logarithm of the current (Tafel equation). The experimental LSV curves are shown in Figure 6.2a. We then plotted the applied potential (in the range 900–1200 mV) as a function of the current normalized per concentration of added [**Ru$_4$POM**] (an analog of TOF) in Figure 6.2b.

The “Tafel slope” in the range of potentials between 900 and 1200 mV is ~120 mV/decade (Figure 6.2) for three different **Ru$_4$POM** concentrations. Based on the formal interpretation of the Tafel equation, this slope is consistent with $\alpha = 0.5$ and a one-electron process. However, as the theory of such measurements is not yet developed for a homogeneous WOC system, the meaning of this slope value is unclear.

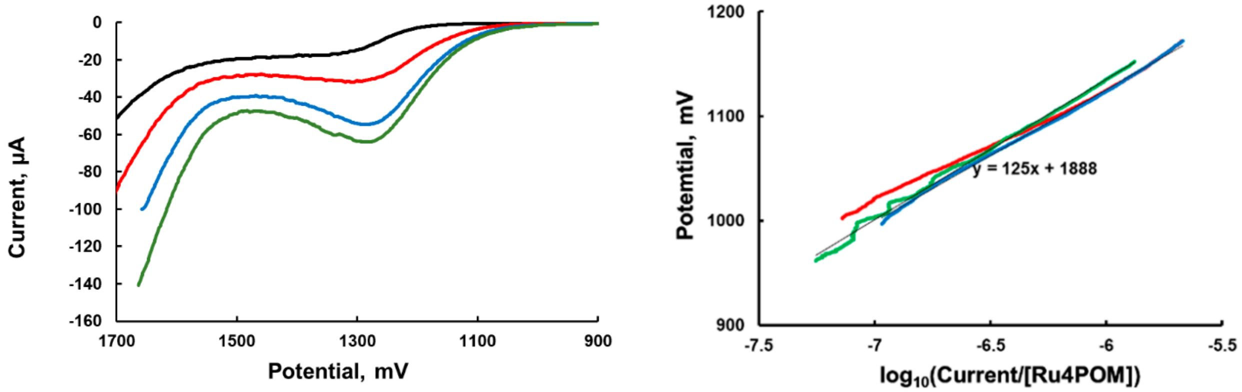

(**a**) (**b**)

Figure 6.2 (**a**) Linear sweep voltammograms with stirring at a scan rate 3.0 mV/s of 1.0 mM $[Ru(bpy)_3]Cl_2$ in 80 mM sodium phosphate at pH 7.2. [**Ru$_4$POM**]: 0 (black), 5 (red), 10 (blue), and 15 μM (green and orange); (**b**) Tafel plot in the range of potentials between 900 and 1200 mV.

Tafel plot from kinetic curves in homogeneous systems

The kinetics of water oxidation by Ru3 can be followed either by measuring oxygen formation or by the consumption/formation of Ru3/Ru2. The consumption of Ru3 can be followed by a decrease in absorbance at 670–680 nm ($\varepsilon = 420\ M^{-1}cm^{-1}$). [14] The reaction is fast and requires a stopped-flow instrument to collect high-quality kinetics data. The experimental details were described in our previous publications.[14,19] Both Ru2 and **Ru4POM** slightly absorb light at 680 nm, which must and can be taken into account for quantitative analysis of raw experimental data. Here for simplicity, a kinetic curve of [Ru3] consumption versus time is the decrease in absorbance at 680 nm. At a given time *t*, the reaction rate can be approximated as $d[Ru3]/dt \approx ([Ru3]_{(t - \Delta t)} - [Ru3]_{t + \Delta t)})/2\Delta t$ and $TOF_{app} = (d[Ru3]/dt)/[Ct]$ can be quantified ([Ct] is the total concentration of **Ru4POM**). We make the reasonable assumption, based on our earlier studies, that the simplified reaction mechanism are reactions 6.5–6.9. If reversible reactions are in equilibrium and [Ct] << [Ru3], then the electrochemical solution potential at time *t* can be calculated from the Nernst equation $E = E'_0 + 0.059 \times \log_{10}(([Ru3]_t/([Ru3]_0 - [Ru3]_t))$, where $E'_0 = 1.26$ V is the standard reduction potential of the [Ru3]/[Ru2] couple, and $[Ru3]_0$ is the initial concentration of Ru3. As Ru3/Ru2 and **Ru4POM** have large and opposite charges, their reduction potentials and the rates of their intermolecular reactions are ionic-strength-dependent. In order to keep pH constant, the use of buffered solutions is required. However, even low concentrations of sodium phosphate buffer (e.g., 25 mM) create a high ionic strength (μ ~ 75 mM). Therefore, in this work, we use the experimentally determined value of the reduction potential for the Ru2/Ru3 couple as the reference point in all calculations (e.g., 1.06 V versus 3.0 M NaCl Ag/AgCl reference electrode). We define TOF as (d[Ru3]/dt)/[Ct]. This procedure converts a single kinetic curve to the dependence of TOF on applied potentials.

The self-decomposition of Ru3 is relatively slow at pH 7.0–8.0, and the O_2 yield approaches 80% of the theoretical value at [**Ru4POM**] > 5 μM. Therefore, the kinetics of $[Ru(bpy)_3]^{3+}$ consumption can be considered as the kinetics of water oxidation. The beginning of kinetic curves (up to 15% conversion) has the highest Ru3/Ru2 ratio, which quickly changes with time and makes the rate measurements problematic.

The typical kinetic curves and the corresponding Tafel-like plots are shown on Figure 6.3. The initial rates are commonly used to study the reaction kinetics. In this work, we did not use this approach, due to two major problems. First, if Ru2 is not added in the reaction mixture, the rate quickly changes at very low conversions, creating uncertainty in the definition of the initial rate. Secondly, in the early stage, small experimental uncertainties in Ru2 concentration will lead to significant errors in [Ru3]/[Ru2] ratio.

The experimental $\log_{10}$(TOF) dependence on the electrochemical solution potential is weakly dependent on catalyst concentration and is not linear. In order to interpret the data, we build a kinetic model of homogeneous processes, performed the fitting of kinetics curves, and then simulated the Tafel plot. It appeared that the simulated Tafel plots are weakly dependent on parameters obtained from fitting. Therefore, we had to narrow the ranges of variable parameters using additional sets of experimental data. In this respect, differential pulse voltammetry could be helpful to estimate the oxidation potentials of **Ru$_4$POM**.

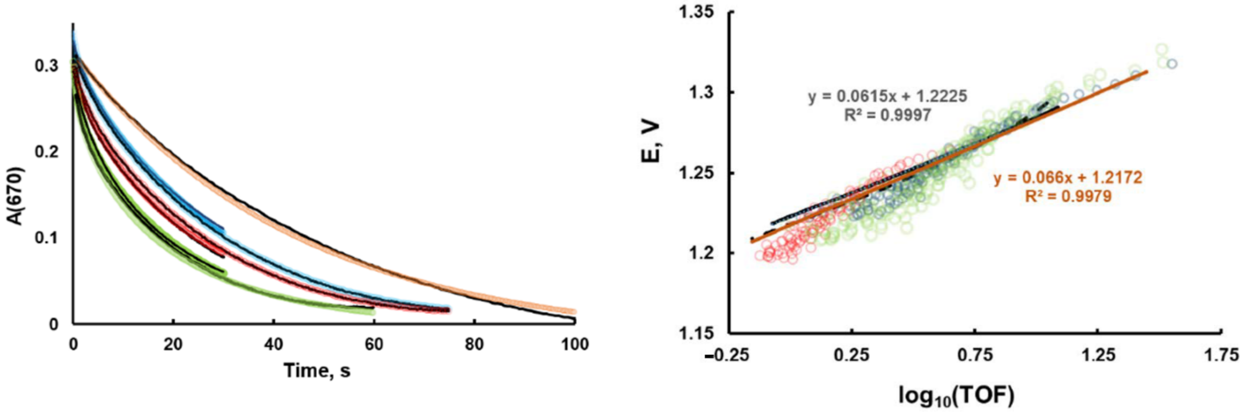

(**a**) (**b**)

Figure 6.3. (**a**) The kinetics of $[Ru(bpy)_3]^{3+}$ consumption measured at 670 nm. Sodium borate buffer (25 mM) at pH 8.0, 0.85 mM $[Ru(bpy)_3]^{3+}$, **Ru$_4$POM** – 0 (orange), 2.5 (blue), 5.0 (red), and 10 μM (green). The fitting using COPASI software to the mechanism in reactions 6.16–6.22 is in solid lines;[20] (**b**) turnover frequency (TOF) and potential are calculated as described in the text. The brown line is calculated using equation 6.15. The black line is generated by COPASI software with the same parameters as in (**a**).

Differential pulse voltammetry

Differential pulse voltammetry (DPV) has two features: The effect of the charging current can be minimized and only faradaic current is extracted. This technique is well suited for electrochemical examination of **Ru$_4$POM**, which has a low rate constant of electron transfer to electrode; however, like other electroanalytic techniques, DPV requires the use of a high electrolyte concentrations. Indeed, the DPV peaks significantly increase with an increase in $NaNO_3$ electrolyte concentration in 80 mM sodium borate buffer at pH 8.0 and also shift to lower potentials (Figure 6.4). The first peak becomes visible at 0.5 M $NaNO_3$ at ~0.65 V and shifts to a lower potential at 0.75 M $NaNO_3$. The width of the peak is around 90 mV, which is consistent with the one-electron transfer process (theoretical value 90 mV). The second peak has a width of about 45 mV and thus is very likely a two-electron process. At low ionic strength, the potential of the second peak is in the range of 1.0–1.1 V vs. Ag/AgCl.

We considered studying the kinetics of water oxidation at elevated concentrations of electrolyte in order to have the similar conditions to those used in electrochemical studies. However, the rate of water oxidation by Ru3 decreases with an increase in electrolyte concentration due to ionic strength effects, but the rate of Ru3 self-decomposition remains unchanged and becomes the predominant kinetic event. As such, the redox potentials measured by DPV could be extrapolated to low ionic strength to estimate the possible range of **Ru_4POM** potentials.

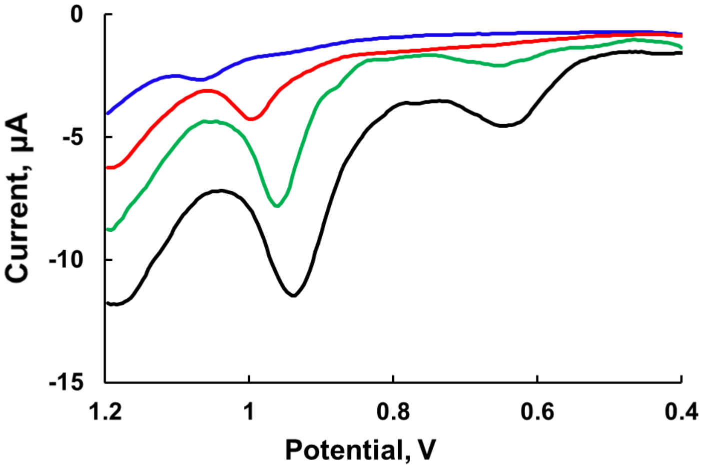

Figure 6.4 Differential pulse voltammetry curves of 1.0 mM **Ru_4POM** in 80 mM sodium borate buffer at pH 8.0 at varying concentrations of $NaNO_3$: 0.15 M (blue), 0.25 M (red), 0.5 M (green), and 0.75 M (black). Differential pulse voltammetry (DPV) parameters: V (mV/s) = 20, sample width (ms) = 17, pulse amplitude (mV) = 50, pulse width (ms) = 50, pulse period (ms) = 200, quiet time (s) = 2.

Kinetic model of homogeneous water oxidation by $[Ru(bpy)_3]^{3+}$ catalyzed by Ru_4POM

Having information on the range of redox potentials of **Ru_4POM** and making minimal assumptions, the mechanism in reactions 6.16–6.22 is proposed:

$C0 + Ru3 \leftrightarrows C1 + Ru2$; $k_1 = 1x10^{10}$; $k_{-1} = 10\ M^{-1}s^{-1}$; $K_1 = 1x10^9$; $\Delta E_1 = -0.61$ V (6.16)

$C1 + Ru3 \leftrightarrows C2 + Ru2$; $k_2 = 1x10^{10}$; $k_{-2} = (4.6 \pm 8) \times 10^5 M^{-1}s^{-1}$; $K_2 = 2.2x10^4$; $\Delta E_2 = -0.26$ V (6.17)

$C2 + Ru3 \leftrightarrows C3 + Ru2$; $k_3 = 1x10^{10}$; $k_{-3} = (5.4 \pm 9) \times 10^5 M^{-1}s^{-1}$; $K_3 = 1.8x10^4$; $\Delta E_3 = -0.26$ V (6.18)

$C3 + Ru3 \leftrightarrows C4 + Ru2$; $k_4 = (1.5 \pm 0.8) \times 10^7$; $k_{-4} = (8.0 \pm 4) \times 10^8 M^{-1}s^{-1}$; $K_4 = 0.2$; $\Delta E_4 = 0.10$ V (6.19)

$C4 \rightarrow C0 + O_2$; $k_0 = 18 \pm 2\ s^{-1}$ (6.20)

$Ru3 \rightarrow Ru_x$ $k_d = 0.0023 \pm 0.0005\ s^{-1}$ (6.21)

$10\ Ru3 + Ru_x \rightarrow 10\ Ru2 + Pr$ $k_{dd} > 1 \times 10^5\ M^{-1}s^{-1}$ (6.22)

The latter two reactions (6.21 and 6.22) are added to describe the rate and stoichiometry of the Ru3 self-decomposition reaction in the absence of a catalyst. The values were determined from the fitting of five kinetic curves and assuming the rate law for reaction 6.21 as $d[Ru3]/dt = -k_{dd}[Ru3][Ru_x]$. It appeared that the overall reaction rate and O_2 yield are independent of k_{dd}, if $k_{dd} > 1 \times 10^5\ M^{-1}\ s^{-1}$. We assumed that the very thermodynamically favorable reactions between two reactants with opposite charges proceed with the diffusion-controlled rate constants $1 \times 10^{10}\ M^{-1}s^{-1}$. The optical density at 670 nm was calculated as $A_{670} = 420 \times [Ru3] + 20 \times [Ru2]$. The results of the fitting are strongly dependent on dioxygen yield over the reaction time. Therefore, we used an additional set of experimental data. The dioxygen yield at 20 ± 2 s was measured to be 41, 60, and 85 µM in the presence of 2.5, 5.0, and 10 µM **Ru_4POM**, respectively. The calculated values of O_2 were the same as the experimental ones within a 5% range. For each concentration of **Ru_4POM**, two kinetic curves with different reaction times were used. The results of the fitting are given in Figure 6.3 and the values of the parameters are given in reactions 6.16–

22. The values of the variable parameters are highlighted in italics. The standard deviations are generated by the fitting software. As expected, the values of rate constants extracted by fitting have a large error range due to the low number of experimental curves used in fitting. The increase in the numbers of curves requires much longer computing time and results in only a slight decrease in accuracy of the extracted parameters. As the focus of this work is not the study of the explicit reaction mechanism, we did not fit a large set of experimental curves.

It is important to note that the Tafel-like plot cannot be used to confirm a specific kinetic model. However, it can provide additional information about the activity of a catalytic system.

Comparison of different homogeneous catalytic systems using Tafel-like plots

First, we used the kinetic data on O_2 evolution in water oxidation by Ce(IV) under acidic conditions catalyzed by **Ru_4POM**.[15] The experiment was performed in unbuffered 1.1 mM Ce(IV) solution. The estimated pH was 2.5. The standard redox potential of the Ce(IV)/Ce(III) couple was taken to be 1.5 V.[21–23] The value of the overpotential was calculated as a difference between the Nernstian electrochemical solution potential ($E = 1.5 + 0.059 \times \log([Ce(IV)]/[Ce(III)])$) and the standard oxidation potential of water ($E = 1.24 - 0.059 \times pH$). We digitized the data in Figure S10 from Sartorel *et al*.[15] and obtained the Tafel plot in Figure 6.5 (blue circles). Based on our kinetic model, we simulated the dependence of TOF for O_2 formation as a function of overpotential at pH 8.0 (Figure 6.5 red circles). As expected, both sets of data form almost a straight line with a slope of 67 mV per decade, which describes the catalytic activity of **Ru_4POM** over a wide range of conditions.

Finally, we collected stopped-flow data for another well-established homogeneous WOC, $[Co_4(H_2O)_2(PW_9O_{34})_2]^{10-}$ (**Co_4P_2**),[24] in 80 mM sodium borate buffer at pH 8.0 under conditions similar to those for **Ru_4POM**. The data were processed in the same way as described above, where the TOF for O_2 formation is equal to 1/4 of the TOF for Ru3 consumption, and plotted in Figure 6.5. The **Co_4P_2** is more active than **Ru_4POM** at overpotentials lower than 0.44 V, while it is lower at overpotentials higher than 0.44 V. The differences in Tafel slopes indicate that the rate-determining steps and/or the corresponding WOC reaction mechanism are different in these two systems.

In order to understand how the reaction parameters in reactions 16–22 affect the Tafel slope, we simulated the Tafel slope using COPASI and then observed the effects of changing each of the parameters within a range of 10^4–10^6 from the fitted values of **Ru_4POM**. We have found that if the equilibrium of the reaction in reaction 19 is shifted to the left side (corresponding to the condition that the first oxidation potential is very high), then the Tafel slope becomes 30 mV/decade. This leads us to believe that the first oxidation potential of **Co_4P_2** is higher and the step depicted in equation 19 becomes rate-determining instead.

Here, it is worth mentioning that experimental slopes in Figure 6.3 are slightly higher than the theoretical 30 and 60 mV/decade. The TOF was also calculated based on the rate of Ru3 consumption, which includes the Ru3 self-decomposition side reaction that we deemed negligible for our analysis.

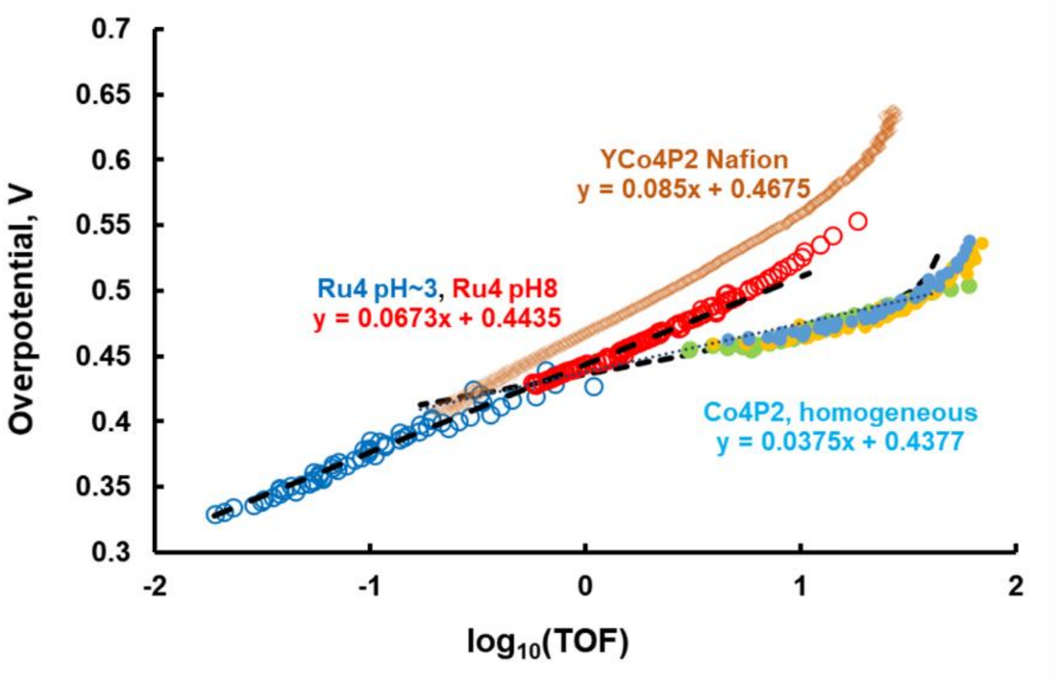

Figure 6.5 Tafel-like plots for water oxidation catalyzed by soluble **Ru_4POM** and **Co_4P_2** (completely homogeneous catalysts) derived using the described methodology compared to heterogenized POM Tafel plots measured via electrochemistry. Conditions for **Co_4P_2** system: 80 mM sodium borate buffer at pH 8.0, 0.34 mM Ru3, 2.5 (light blue), 5 (green), 10 (yellow) µM **Co_4P_2**, 24 °C.

Tafel slope for heterogeneous Co_4P_2 complex

One of the reasons for performing a Tafel-like analysis on the homogeneous catalysts is to make comparisons to the analogous heterogeneous catalysts where accessible. Various different counter-cation variants of **Co_4P_2** were heterogenized via a 5 wt% Nafion mixture and drop-casted onto a glassy carbon electrode in order to measure their Tafel behavior. These Tafel plots are shown in Figure 4.15. They all exhibit similar Tafel slopes of about 80 mV/decade, which is greater than the 60 mV/decade typically observed for amorphous cobalt oxides. This suggests either a different WOC mechanism or different cobalt-centered active species are involved in with the two types of cobalt-containing WOCs. Nonetheless, it is likely that all these variants of **Co_4P_2** have the same rate-determining step given their similar Tafel slopes.

As the current in these electrochemical experiments can be directly converted to TOF (four electrons per turnover), we can then compare the Tafel plots of the heterogenized **Co_4P_2** to those of the homogeneous **Co_4P_2** (Figure 6.5). We note that these samples have similar electroactive surface areas as measured by capacitive current. The differences in exchange current density must therefore be a result of counterion effects. In this case, as they follow the expected trend of lower Lewis acidity, giving rise to higher catalytic currents, we can generally attribute the observed trend to their Lewis acid–base chemistry.

Experimental

All common synthetic chemicals were reagent grade and purchased through commercial sources such as Sigma-Aldrich and VWR and used without further purification. Synthesis of **Ru_4POM** and **Co_4P_2** was performed following exact literature procedures and recrystallized from aqueous solution.[14,24] Synthesis of the $[Ru(bpy)_3]^{3+}$ source, $[Ru(bpy)_3](ClO_4)_3$, was obtained by oxidizing $[Ru(bpy)_3]Cl_2$ using PbO_2 in 0.5M H_2SO_4 and precipitating by addition of $HClO_4$.[25] The product was then dried and stored in a refrigerator (4 °C).

Stopped-flow UV-Vis spectroscopy

Stopped-flow UV-Vis spectroscopy was performed on a Hi-Tech KinetAsyst Stopped Flow SF-61SX2 instrument equipped with a diode array detector operating between wavelengths ranging from 400 to 700 nm. One of the feeding syringes was filled with a solution of $[Ru(bpy)_3]^{3+}$ and the second with a freshly prepared buffer solution containing the catalyst. The consumption of $[Ru(bpy)_3]^{3+}$ was followed by a decrease in absorbance at 670 nm ($\varepsilon_{670} = 4.2 \times 10^2$ M^{-1} cm^{-1}) with an optical path length of 10 mm. The data were acquired and treated using KinetAsyst™ 3.0 software. Consequent analysis of the resulting kinetic data were performed using Excel and the COPASI software package.[20]

Electrochemistry

Electrochemical analyses were carried out using standard three-electrode measurements on a Pine Research Instrument WaveDriver 20 bipotentiostat and a BAS CV-50W potentiostat. All potentials were measured using glassy carbon electrodes against 1 M KCl Ag/AgCl reference electrodes (+0.235 V vs. NHE) purchased from CH Instruments. The counter electrodes were either a platinum wire or a graphite rod. Electrochemical cells were either cylindrical or conical electrochemical glassware or three-necked round-bottom flasks. All electrochemical measurements were done with the reference and working electrodes in proximity and clear from obstructions that would hinder contact with the reaction solution.

Conclusion

We describe a protocol to obtain Tafel-like plots for two different homogeneous catalytic systems based on kinetic and thermodynamic data. These plots visualize the activity of different catalysts under different solution overpotential conditions and allow for the ready comparison of their activity with each other, as well as with heterogeneous catalysts whose Tafel plots can be obtained using a traditional electrochemical setup. The resulting Tafel slopes indicate that the reaction mechanisms in water oxidation catalyzed by **Ru_4POM** and **Co_4P_2** are likely different with distinct rate-determining steps. In fact, from the previous chapters, we can conclude that **Co_4P_2** undergoes a generalized WNA pathway (Figure 1.2) with the rate determining step being the peroxo-forming step. Whereas, **Ru_4POM** likely undergoes four sequential oxidations aided by PCET and primarily experience an intramolecular I2M pathway.

This establishes a template with which molecularly discrete homogeneous WOCs can be directly compared to each other, regardless of the oxidant used, and addresses one of the biggest issues in WOC development: that of how to compare the catalytic reactivity of homogeneous and heterogeneous systems. In the future, we hope to expand upon this work and show further utilization of these protocols to elucidate the reaction mechanisms of other WOC systems.

References

1. Bard, A.J.; Faulkner, L.R. *Electrochemical Methods: Fundamentals and Applications*, 2nd ed.; John Wiley & Sons: Hoboken, NJ, USA, 2000.
2. Shinagawa, T.; Garcia-Esparza, A.T.; Takanabe, K. Insight on Tafel slopes from a microkinetic analysis of aqueous electrocatalysis for energy conversion. *Sci. Rep.* **2015**, *5*, 13801, doi:10.1038/srep13801.
3. Hu, J.-M.; Zhang, J.-Q.; Cao, C.-N. Oxygen evolution reaction on IrO2-based DSA® type electrodes: Kinetics analysis of Tafel lines and EIS. *Int. J. Hydrogen Energy* **2004**, *29*, 791–797, doi:10.1016/j.ijhydene.2003.09.007.
4. Anantharaj, S.; Ede, S.R.; Karthick, K.; Sam Sankar, S.; Sangeetha, K.; Karthik, P.E.; Kundu, S. Precision and correctness in the evaluation of electrocatalytic water splitting: Revisiting activity parameters with a critical assessment. *Energy Environ. Sci.* **2018**, *11*, 744–771, doi:10.1039/C7EE03457A.
5. de Chialvo, M.R.G.; Chialvo, A.C. Hydrogen evolution reaction: Analysis of the Volmer-Heyrovsky-Tafel mechanism with a generalized adsorption model. *J. Electroanal. Chem.* **1994**, *372*, 209–223, doi:10.1016/0022-0728(93)03043-O.
6. Walter, M.G.; Warren, E.L.; McKone, J.R.; Boettcher, S.W.; Mi, Q.; Santori, E.A.; Lewis, N.S. Solar Water Splitting Cells. *Chem. Rev.* **2010**, *110*, 6446–6473, doi:10.1021/cr1002326.
7. Li, D.; Lin, C.; Batchelor-McAuley, C.; Chen, L.; Compton, R.G. Tafel analysis in practice. *J. Electroanal. Chem.* **2018**, *826*, 117–124, doi:10.1016/j.jelechem.2018.08.018.
8. Marshall, A.T.; Vaisson-Béthune, L. Avoid the quasi-equilibrium assumption when evaluating the electrocatalytic oxygen evolution reaction mechanism by Tafel slope analysis. *Electrochem. Commun.* **2015**, *61*, 23–26, doi:10.1016/j.elecom.2015.09.019.

9. Savéant, J.-M. Molecular Catalysis of Electrochemical Reactions. Mechanistic Aspects. *Chem. Rev.* **2008**, *108*, 2348–2378, doi:10.1021/cr068079z.

10. Lauinger, S.M.; Yin, Q.; Geletii, Y.V.; Hill, C.L. Chapter Five—Polyoxometalate Multielectron Catalysts in Solar Fuel Production. In *Advances in Inorganic Chemistry*; van Eldik, R., Cronin, L., Eds.; Academic Press: Cambridge, MA, USA, 2017; Volume 69, pp. 117–154.

11. Sumliner, J.M.; Lv, H.; Fielden, J.; Geletii, Y.V.; Hill, C.L. Polyoxometalate Multi-Electron-Transfer Catalytic Systems for Water Splitting. *Eur. J. Inorg. Chem.* **2014**, *2014*, 635–644, doi:10.1002/ejic.201301573.

12. Roger, I.; Shipman, M.A.; Symes, M.D. Earth-abundant catalysts for electrochemical and photoelectrochemical water splitting. *Nat. Rev. Chem.* **2017**, *1*, 0003, doi:10.1038/s41570-016-0003.

13. Costentin, C.; Savéant, J.-M. Homogeneous Molecular Catalysis of Electrochemical Reactions: Catalyst Benchmarking and Optimization Strategies. *J. Am. Chem. Soc.* **2017**, *139*, 8245–8250, doi:10.1021/jacs.7b02879.

14. Geletii, Y.V.; Besson, C.; Hou, Y.; Yin, Q.; Musaev, D.G.; Quiñonero, D.; Cao, R.; Hardcastle, K.I.; Proust, A.; Kögerler, P.; et al. Structural, Physicochemical, and Reactivity Properties of an All-Inorganic, Highly Active Tetraruthenium Homogeneous Catalyst for Water Oxidation. *J. Am. Chem. Soc.* **2009**, *131*, 17360–17370, doi:10.1021/ja907277b.

15. Sartorel, A.; Carraro, M.; Scorrano, G.; Zorzi, R.D.; Geremia, S.; McDaniel, N.D.; Bernhard, S.; Bonchio, M. Polyoxometalate Embedding of a Tetraruthenium(IV)-oxo-core by Template-Directed Metalation of $[\gamma\text{-SiW}_{10}O_{36}]^{8-}$: A Totally Inorganic Oxygen-Evolving Catalyst. *J. Am. Chem. Soc.* **2008**, *130*, 5006–5007, doi:10.1021/ja077837f.

16. Lee, C.-Y.; Guo, S.-X.; Murphy, A.F.; McCormac, T.; Zhang, J.; Bond, A.M.; Zhu, G.; Hill, C.L.; Geletii, Y.V. Detailed Electrochemical Studies of the Tetraruthenium Polyoxometalate Water Oxidation Catalyst in Acidic Media: Identification of an Extended Oxidation Series using Fourier Transformed Alternating Current Voltammetry. *Inorg. Chem.* **2012**, *51*, 11521–11532, doi:10.1021/ic301370y.

17. Costentin, C.; Drouet, S.; Robert, M.; Savéant, J.-M. Turnover Numbers, Turnover Frequencies, and Overpotential in Molecular Catalysis of Electrochemical Reactions. Cyclic Voltammetry and Preparative-Scale Electrolysis. *J. Am. Chem. Soc.* **2012**, *134*, 11235–11242, doi:10.1021/ja303560c.

18. Martin, C.R.; Rubinstein, I.; Bard, A.J. The heterogeneous rate constant for the Ru(bpy)33+/2+ couple at a glassy carbon electrode in aqueous solution. *J. Electroanal. Chem. Interfacial Electrochem.* **1983**, *151*, 267–271, doi:10.1016/S0022-0728(83)80439-2.

19. Vickers, J.W.; Sumliner, J.M.; Lv, H.; Morris, M.; Geletii, Y.V.; Hill, C.L. Collecting meaningful early-time kinetic data in homogeneous catalytic water oxidation with a sacrificial oxidant. *Phys. Chem. Chem. Phys.* **2014**, *16*, 11942–11949, doi:10.1039/C3CP55406F.

20. Hoops, S.; Sahle, S.; Gauges, R.; Lee, C.; Pahle, J.; Simus, N.; Singhal, M.; Xu, L.; Mendes, P.; Kummer, U. COPASI—A COmplex PAthway SImulator. *Bioinformatics* **2006**, *22*, 3067–3074, doi:10.1093/bioinformatics/btl485.

21. Bilal, B.A.; Müller, E. Thermodynamic Study of Ce4+ /Ce3+ Redox Reaction in Aqueous Solutions at Elevated Temperatures: 1. Reduction Potential and Hydrolysis Equilibria of Ce4+ in HCIO4 Solutions. *Z. Nat. A* **1992**, *47*, 974–984, doi:10.1515/zna-1992-0908.

22. Bouchaud, B.; Balmain, J.; Bonnet, G.; Pedraza, F. pH-distribution of cerium species in aqueous systems. *J. Rare Earths* **2012**, *30*, 559–562, doi:10.1016/S1002-0721(12)60091-X.

23. Hayes, S.A.; Yu, P.; O’Keefe, T.J.; O’Keefe, M.J.; Stoffer, J.O. The Phase Stability of Cerium Species in Aqueous Systems. *J. Electrochem. Soc.* **2002**, *149*, C623, doi:10.1149/1.1516775.

24. Yin, Q.; Tan, J.M.; Besson, C.; Geletii, Y.V.; Musaev, D.G.; Kuznetsov, A.E.; Luo, Z.; Hardcastle, K.I.; Hill, C.L. A Fast Soluble Carbon-Free Molecular Water Oxidation Catalyst Based on Abundant Metals. *Science* **2010**, *328*, 342–345, doi:10.1126/science.1185372.

25. Shafirovich, V.Y.; Khannanov, N.K.; Strelets, V.V. Chemical and Light-Induced Catalytic Water Oxidation. *New J. Chem.* **1980**, *4*, 81–84.